

# Sheffield Hallam University

*MALDI-MS imaging for direct drug distribution analysis.*

TRIM, Paul James.

Available from the Sheffield Hallam University Research Archive (SHURA) at:

<http://shura.shu.ac.uk/20455/>

## A Sheffield Hallam University thesis

This thesis is protected by copyright which belongs to the author.

The content must not be changed in any way or sold commercially in any format or medium without the formal permission of the author.

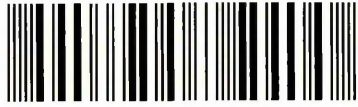
When referring to this work, full bibliographic details including the author, title, awarding institution and date of the thesis must be given.

Please visit <http://shura.shu.ac.uk/20455/> and <http://shura.shu.ac.uk/information.html> for further details about copyright and re-use permissions.

Learning and Information Services  
Adsetts Centre, City Campus  
Sheffield S1 1WD

26545

101 963 640 8



**REFERENCE**

ProQuest Number: 10701101

All rights reserved

INFORMATION TO ALL USERS

The quality of this reproduction is dependent upon the quality of the copy submitted.

In the unlikely event that the author did not send a complete manuscript and there are missing pages, these will be noted. Also, if material had to be removed, a note will indicate the deletion.



ProQuest 10701101

Published by ProQuest LLC (2017). Copyright of the Dissertation is held by the Author.

All rights reserved.

This work is protected against unauthorized copying under Title 17, United States Code  
Microform Edition © ProQuest LLC.

ProQuest LLC.  
789 East Eisenhower Parkway  
P.O. Box 1346  
Ann Arbor, MI 48106 – 1346

**MALDI-MS Imaging for Direct Drug Distribution Analysis.**

**Paul James Trim.**

**A thesis submitted in partial fulfilment of the requirements of Sheffield Hallam  
University for the degree of Doctor of Philosophy**

**October 2009**



## Acknowledgements

I would like to thank my supervisor Prof. Malcolm Clench, for giving me the opportunity to undertake this work and for all of his help and support throughout my PhD.

This PhD was supported by a BBSRC CASE Studentship in collaboration with GlaxoSmithKline and Sheffield Hallam University.

I would also like to thank Dr. Peter Marshall (GSK) and Andy West (GSK), for their support throughout this project.

This work would not have been possible without the help, support and guidance from Dr Marten Snell and Emmanuelle Claude from Waters Corporation in Manchester, who have provided their time and knowledge with the Synapt HDMS, and everyone at Quotient Bioresearch (Rushden). Especially Dr Andrew McEwen, Claire Henson, Jenny Avery, Bryn Flinders, Kelly Hearn, Chris Brown and Andrew McCollin.

Of Course thank you to the Mass Spec Group at Sheffield Hallam University for the knowledge sharing and friendship throughout, many thanks Dr Marie-Claude Djidja, Dr David Anderson, Dr Caroline Earnshaw, Dr Tasneem Muharib, Philippa Hart, Laura Cole, Salem Omer, Dr Jill Newton, Dr Simona Francese and my second supervisor Dr Alessandra Princivalle.

Last but in no way least thanks to all my family and friends who have supported me throughout my studies and a special thank you to my partner Rachel, my dear friends Richard and Allison and of course my two god daughters Jasmin and Nicole for their welcome interruptions and endless entertainment.

## Abstract

MALDI Imaging has gained huge interest in the past few years with an ever increasing population of specialists choosing to investigate samples using MALDI imaging, including growing interest and financial backing from pharma and contract research organisations.

Presented within this thesis is the development and application of MALDI imaging techniques for a variety of analytical problems. The use of various software packages have been employed in the interpretation of the data acquired from MALDI experiments including, the use of statistical analysis for the identification of ion of interest from 6 distinct brain regions and also for the identification of ions of interest associated with small molecule tumour markers.

The advantages of MALDI-IMS-MSI as a further separation stage within MALDI-MSI have been shown. Demonstrated is a method for MALDI-IMS-MS imaging of endogenous lipids in healthy tissue and tumours, also demonstrated is the application of MALDI-IMS-MS to xenobiotic distribution studies, it has been clearly shown that ion mobility separation within MALDI-MSI experiments can improve the analysis of xenobiotics by removing any interfering ions.

With instrumentation development for MALDI a high repetition rate Nd:YVO<sub>4</sub> laser has been assessed as a possible method for decreasing acquisition time

<b>1. Introduction</b>	<b>1</b>
1.1. Drug Discovery	2
1.1.1. Target Identification	2
1.1.2. Lead Optimisation	3
1.1.3. Phase I Clinical Trials	4
1.1.4. Phase II Clinical Trials	5
1.1.5. Phase III Clinical Trials	5
1.2. Drug Distribution Studies	5
1.2.1. Quantitative Whole Body Autoradiography (QWBA)	6
1.3. Mass Spectrometry Instrumentation	8
1.3.1. Ionisation Sources	9
1.3.1.1. Electrospray Ionisation (ESI)	10
1.3.1.2. Desorption Electrospray Ionisation (DESI)	11
1.3.1.3. Matrix Assisted Laser Desorption Ionisation (MALDI)	14
1.3.1.3.1. Microprobe MALDI	14
1.3.1.3.2. Microscope MALDI	15
1.3.1.4. Secondary Ion Mass Spectrometry (SIMS)	16
1.3.2. Mass Analysers	17
1.3.2.1. Quadrupole (Q)	18
1.3.2.2. Time Of Flight (TOF)	18
1.3.2.3. Tandem Instruments	20
1.3.3. MALDI Lasers	21
1.3.3.1. Nitrogen Lasers	21
1.3.3.2. Nd:YAG Lasers	21
1.3.3.3. Nd:YVO4 Lasers	22
1.3.3.4. Infra Red Lasers	22
1.3.3.5. IR and UV combined Laser	23
1.3.3.6. Multi-Frequency Lasers	23
1.3.4. Instruments	24
1.3.4.1. Q-Star Pulsar-i	24
1.3.4.2. Synapt HDMS	25
1.3.5. Ion Mobility Separation	27
1.3.5.1. Drift Time Ion Mobility Spectrometry (DTIMS)	27
1.3.5.2. Aspiration Ion Mobility Spectrometry (IMCell)	29
1.3.5.3. Differential Mobility Spectrometry (DMS)	29
1.3.5.4. Travelling Wave Ion Mobility Spectrometry (T-WAVE IMS)	30
1.4. MALDI Introduction	35
1.5. Matrices For MALDI-MS	38
1.6. Matrix Application	42
1.6.1. Manual Spotting	42
1.6.2. Manual Spray	42
1.6.3. Sublimation	44
1.6.4. Automated Pneumatic Spraying	45
1.6.5. Vibrational Vapourisation	46

1.6.6. Acoustic Droplet Ejection .....	47
1.6.7. Ink-Jet Printers.....	48
1.7. Desorption and Ionisation in MALDI.....	50
1.7.1. Desorption.....	50
1.7.2. Ion Formation in MALDI.....	51
1.8. Scope of this Thesis.....	57
1.8.1. Imaging Lipids.....	57
1.8.2. Imaging Xenobiotic Compounds.....	59
1.9. Aims of this Project.....	60
1.10. References.....	62
<b>2. Chapter 2 - MALDI-MS Imaging of Lipids in Rat Brain Tissue with Integrated Unsupervised and Supervised Multivariate Statistical Analysis.....</b>	<b>70</b>
2.1. Introduction.....	71
2.1.1. Lipids.....	71
2.1.2. MALDI Statistical Analysis.....	77
2.1.3. Brain Tissue Analysis.....	79
2.2. Experimental.....	81
2.2.1. Preparation of Tissue Sections for MALDI-MS Analysis.....	81
2.2.2. Sample Preparation.....	84
2.2.3. Mass Spectrometric Analysis.....	84
2.2.4. Principle Components Analysis.....	85
2.2.5. Image Processing.....	87
2.2.6. Profile Data Acquisition.....	87
2.3. Results and Discussion.....	88
2.3.1. PCA Analysis.....	88
2.3.2. Image Analysis.....	91
2.3.3. Lipid Analysis.....	93
2.3.4. Profile Data Analysis.....	98
2.4. Conclusions.....	103
2.5. References.....	104
<b>3. Chapter 3 - Matrix Assisted Laser Desorption Ionisation – Ion Mobility Separation – Mass Spectrometry Imaging of Small Molecules.....</b>	<b>105</b>
3.1. Introduction.....	106
3.1.1. A New Dimension in MALDI Imaging.....	106
3.1.2. MALDI Imaging of Small Molecules .....	106
3.1.2.1. Lipidomics.....	106
3.1.2.2. Xenobiotic Imaging.....	107
3.1.2.3. MALDI-Ion Mobility –MS.....	109
3.1.3. MALDI Synapt HDMS System.....	112
3.2. Experimental Methods.....	114
3.2.1. Organ Sample Preparation.....	114

3.2.2. Large Tissue Section Preparation.....	114
3.2.3. Matrix Application.....	115
3.2.4. Mass Spectrometric Imaging.....	115
3.2.5. Ion Mobility Data Analysis.....	116
3.2.6. Image Visualisation.....	117
3.2.7. Mass Resolution.....	117
3.3. Results.....	118
3.3.1. Lipid Analysis .....	118
3.3.2. Removal Of Matrix Interference.....	121
3.3.3. Separation of Ions of Interest.....	126
3.3.4. Separation of endogenous and xenobiotic species.....	134
3.4. Conclusion.....	134
3.5. References.....	136
<b>4. Chapter 4 - Matrix Assisted Laser Desorption Ionisation - Ion Mobility Separation - Mass Spectrometry Imaging of Vinblastine in Whole Body Tissue Sections.....</b>	<b>137</b>
4.1. Introduction.....	138
4.1.1 MALDI-MSI.....	138
4.1.2 Xenobiotic Imaging.....	139
4.1.3 MALDI-IMS-MS.....	142
4.1.4 Synapt HDMS.....	143
4.1.5 Vinblastine.....	146
4.2. Experimental.....	148
4.2.1. Preparation of Tissue Sections .....	148
4.2.1.1. Sample Preparation for Non Radiolabelled Vinblastine.....	148
4.2.1.2. Sample Preparation for Radiolabelled 3H Vinblastine.....	148
4.2.1.3. Sample Oxidation.....	149
4.2.1.4. Sample Preparation .....	149
4.2.1.5. MALDI Imaging Section Handling.....	151
4.2.1.6. Mass Spectrometric Analysis .....	151
4.2.1.7. Quantitative Whole Body Autoradiography (QWBA) tissue handling, Imaging and quantitation.....	155
4.2.1.8. Tissue Spiking.....	156
4.3. Results and Discussion.....	157
4.3.1. MALDI.....	157
4.3.2. Whole Body Autoradiography.....	161
4.4. Conclusions.....	169
4.5. Reference.....	171

<b>5. Chapter 5 - Lipid Distribution within HCT 116, Tumour Margin and Surrounding Tissue, and the Effects of a Chemotherapeutic drug administration on Lipids.....</b>	<b>173</b>
5.1. Introduction.....	174
5.1.1. Role of lipids in cellular processes within cancer.....	174
5.1.2. Tumour Xenograft methodology .....	180
5.1.3. Vinblastine.....	181
5.1.4. Principle Component Analysis (PCA) in MALDI.....	184
5.2. Methodology.....	185
5.2.1. Sample Preparation HCT 116 .....	185
5.2.2. Xenograft sectioning.....	186
5.2.3. Matrix Coating.....	186
5.2.4. QStar Pulsar-i Image accusation.....	187
5.2.5. Synapt Image accusation.....	187
5.2.6. PCA-DA Data Processing.....	188
5.2.7. Image processing.....	189
5.2.8. Histological staining.....	190
5.2.9. PPM mass error calculations .....	191
5.3. Results and discussion.....	191
5.4. Conclusion.....	211
5.5. References.....	213
<b>6. Chapter 6 - High Repetition Solid State Laser and Raster Imaging for High Throughput, High Resolution MALDI-Imaging.....</b>	<b>214</b>
6.1. Introduction.....	215
6.1.1. How Lasers Work.....	215
6.1.2. Lasers in Use for MALDI.....	222
6.1.3. Raster imaging V's Conventional imaging.....	231
6.2. Methodology.....	233
6.2.1. Sample Preparation (Numbers).....	233
6.2.2. Sample Preparation (Brain tissue).....	234
6.2.3. Vinblastine Profile and fragmentation due to laser repetition rate.....	235
6.2.4. Mass spectrometric profiling and imaging.....	235
6.2.5. Image Processing.....	236
6.3. Results and discussion.....	236
6.4. Conclusion.....	251
6.5. Reference.....	253

---

<b>7. Chapter 7 – Conclusions and Futures Work.....</b>	<b>255</b>
7.1. Conclusions.....	256
7.2. Future Work .....	258
<b>8. Chapter 8 – Posters, Publications and Conference Attendance.....</b>	<b>260</b>
8.1. Poster Presentation.....	261
8.2. Presentation.....	262
8.3. Peer Review Publications.....	263
8.4. Conference Attendance.....	267

## List of Figures

### 1.0 Chapter 1 - Introduction

1.1	Schematic representation of the drug discovery process and approximate times involved at each stage. (Ashburn and Thor 2004).....	2
1.2	QWBA image showing radiolabel distribution within three rat whole body tissue section, also shown are a series of spiked blood samples for calibration. ( <a href="http://www.biospacelab.com">www.biospacelab.com</a> ).....	7
1.3	Simplified schematic of a mass spectrometer.....	9
1.4	schematic of an electrospray ionisation source. ( <a href="http://www.chm.bris.ac.uk">www.chm.bris.ac.uk</a> ).....	10
1.5	Schematic of the droplet desolvation during ESI. ( <a href="http://www.chm.bris.ac.uk">www.chm.bris.ac.uk</a> ).....	11
1.6	DESI instrumentation schematic showing the electrospray source directed at the sample and not directly into the mass spectrometer as in ESI. (Takats et al 2004).....	12
1.7	Schematic of the pattern from an imaging DESI experiment, showing the possible spread of analytes due to the electrospray.....	13
1.8	Schematic representation of a microprobe MALDI setup. (Klerk et al., 2009).....	15
1.9	Schematic representation of a microscope MALDI setup. (Klerk et al., 2009).....	16
1.10	Schematic representation of the generation of secondary ions within SIMS. (Castner 2003).....	17
1.11	schematic of a quadrupole mass analyser red ion is of the correct mass to charge and is able to exit the quadrupole, the yellow ion is a different mass to charge that ends up being neutralised on the metal rods.....	18
1.12	Schematic of the TOF portion of a Synapt HDMS system (Waters Corporation, Manchester, UK) showing the flight path of ions in the time of flight tube when in V or W mode of operation.....	20
1.13	Schematic of an Applied Biosystems/MDS Sciex hybrid quadrupole time-of-flight instrument (Q-Star Pulsar-i). Adapted from Baldwin et al., 2001.....	25
1.14	Schematic of the Synapt HDMS system (Waters Corporation, Manchester, UK) (Oppenheimer et al 2009).....	26
1.15	Schematic of the Tri Wave IMS cell within the Synapt HDMS (Waters, Manchester, UK) shown are the locations of the three travelling wave stacked ring ion guides (TW-SRIG). (Pringle et al., 2006).....	30
1.16	a) A computer model of the SRIG which forms the T-WAVE IMS cell. The potential gradient exists across the aperture and increases markedly near the electrode walls.	



	b) The same SRIG animation but from a different angle showing the waves that form which the ions “surf”. (Giles et al., 2004).....	32
1.17	SIMION plots of the ion trajectory within the T-WAVE IMS cell showing the ion surfing the wave and then rolling over the top of the wave and being collected by the following wave. (Giles et al., 2004).....	33
1.18	Ion Mobility separation of singly charged and multiply charged peptides. (Pringle et al., 2007).....	34
1.19	Kidney section after manual spray coating with $\alpha$ CHCA matrix.....	43
1.20	Image of the apparatus required for matrix sublimation. (Hankin et al., 2007).....	45
1.21	SunCollect matrix spotter/sprayer. ( <a href="http://www.sunchrom.de/pdf/SunChrom%20SunCollect_english.pdf">http://www.sunchrom.de/pdf/SunChrom%20SunCollect_english.pdf</a> ).....	45
1.22	ImagePrep matrix applicator. ( <a href="http://www.bdal.com/uploads/media/ImagePrep-2008-eBook.pdf">http://www.bdal.com/uploads/media/ImagePrep-2008-eBook.pdf</a> ).....	46
1.23	Portrait 630 multi reagent spotter. ( <a href="http://www.labcyte.com/portrait@_630_spotter/default.92.html">http://www.labcyte.com/portrait@_630_spotter/default.92.html</a> ).....	48
1.24	ChIP matrix printer ( <a href="http://www.shimadzu-biotech.net/pages/products/2/chip.php">http://www.shimadzu-biotech.net/pages/products/2/chip.php</a> ).....	49
1.25	Schematic representation of photoexcitation and energy pooling.....	56

## 2.0 Chapter 2 - MALDI-MS Imaging of Lipids in Rat Brain Tissue with Integrated Unsupervised and Supervised Multivariant Statistical Analysis.

2.1	Generic structures of several lipid species. a) Fatty acids, b) Glycerolipids, c) Glycerophospholipids, d) Shingolipids, e) Sterols, f) Prenols, g) Saccharolipids, h) polyketides.....	73-76
2.2	Phosphatidycholine structure.....	77
2.3	Schematic diagram of the brain regions selected for the PCA. The 6 highlighted regions of the brain displayed illustrate where each of the 10 MALDI mass spectra were acquired for subsequent multivariate analysis.....	81
2.4	Image of a rat brain mounted on cork using OCT.....	83
2.5	Spectra obtained from OCT contaminated sample, OCT related peaks appear as a polymer with peaks at regular m/z 44 intervals.....	83
2.6	a) Unsupervised scores plot generated from the PCA, scores plot of PC1 verses PC2 using pareto scaling with the points from each of the six regions of the brain encircled as a visual aid no statistical significance should be drawn from these visual aids. b) Unsupervised loadings plot generated from the PCA, loadings plot of PC1 verses PC2 using pareto scaling, showing possible ions of interest including the ions predominantly responsible for the	

- separation of white and grey matter brain regions m/z 788.48 and m/z 734.45 respectively shown in red and showing the ion of interest m/z 762.47. c Supervised scores plot generated from the PCA, scores plot of PC1 verses PC2 using pareto scaling with the points from each of the six regions of the brain encircled as a visual aid no statistical significance should be drawn from these visual aids. d) Supervised loadings plot generated from the PCA, loadings plot of PC1 verses PC2 using pareto scaling, showing possible ions of interest including the ions predominantly responsible for the separation of white and grey matter brain regions m/z 788.48 and m/z 734.45 respectively shown boxed in red and showing the ion of interest m/z 762.47 shown to have a positive PC1 and a Positive PC2 which corresponds to the grey cerebellar cortex region in the scores plot, and m/z 772.46 which has a positive PC1 and a negative PC2 which relates to the Hippocampal formation in the scores plot.....89-90
- 2.7 a) 2D ion density map of m/z 734.45 which has a highly positive PC1 loading and has been shown to be associated predominantly with regions of grey matter within the brain. b) 2D ion density map of m/z 788.48 which has a highly negative PC1 loading and has been shown to be associated predominantly with regions of white matter within the brain. c) 2D ion density map overlay of m/z 734.45 (GREEN) which has a highly positive PC1 loading and has been shown to be associated predominantly with regions of grey matter within the brain with overlaid 2D ion density map produced from imaging ion m/z 788.48 (RED) which has a highly negative PC1 loading and has been shown to be associated predominantly with regions of white matter within the brain. complimentary images can be seen areas shown in yellow are areas associated to both white and grey matter. d) 2D ion density map of ion m/z 762.47 which has a positive PC1 loading and a positive PC2 loading and is shown to be elevated in the region of the brain relating to the grey cerebellar cortex. e) 2D ion density map of m/z 772.40 which has a positive PC1 loading and a negative PC2 loading and is shown to be elevated within the grey cerebellar cortex, a section of the cerebral cortex, partially in the thalamus and especially in the hippocampal formation. The area with the highest intensity includes the striatum, ventral pallidum and other ventral nuclei that have not been included in the PCA analysis within this work.....92
- 2.8 Total mass spectra obtained with the phospholipid region enlarged and inset, shown with the tentative phospholipid

	assignments according published phospholipid data (Jackson et al., 2005) Peaks have been assigned to the following phosphatidylcholines, PC 32:0 [M+H] <sup>+</sup> at m/z 734.45, PC 34:1 [M+H] <sup>+</sup> at m/z 760.46, PC 34:0 [M+H] <sup>+</sup> at m/z 762.47, PC 32:0 [M+K] <sup>+</sup> at 772.40 and PC 36:1 [M+H] <sup>+</sup> at m/z 788.48.....	94
2.9	a) Single spectra showing the lipid region with spectral location inset, taken from the cerebral cortex (grey matter) tentative lipid assignments are given for the prominent lipids.....	95
2.10	Single spectra showing the lipid region with spectral location inset, taken from the corpus callosum (white matter) tentative lipid assignments are given for the prominent lipids.....	96
2.11	Combined Profile obtained from areas of white and gray cerebellar cortex, using the Portrait multi reagent spotter for matrix printing. The array of data within the lipid rich region of the spectra can be seen.....	98
2.12	Enhanced view of the lipid region within figure 2.10. Several lipid species have been tentatively identified based on their mass.....	99
2.13	MALDI spectra obtained from a gray matter brain tissue using the Portrait multi reagent spotter for matrix printing.....	101
2.14	MALDI spectra obtained from white matter brain tissue using the Portrait multi reagent spotter for matrix printing.....	102

### 3.0 Chapter 3 - Matrix Assisted Laser Desorption Ionisation – Ion Mobility Separation – Mass Spectrometry Imaging of Small Molecules.

3.1	2D MALDI-ion mobility-TOFMS plot showing the familial trend lines associated with ion molecule class taken from Jackson et al., 2007.....	110
3.2	Schematic of the instrument configuration of the MALDI Synapt HDMS system (Water Corporation, Manchester, UK).....	112
3.3	schematic of the inside of the ion mobility cell within the Synapt HDMS instrument (Water Corporation, Manchester, UK), shown are ions “surfing” the travelling wave along the stacked ring ion guides. ( <a href="http://www.youtube.com">www.youtube.com</a> ).....	113
3.4	Driftscope plot of m/z700 – 750 indicating the possible separation of lipid classes and chemical noise and matrix ions.....	119
3.5	Mass spectra obtained from each of the 3 regions highlighted in Figure 3.4 and a total mass spectra of the same region without IMS.....	120

3.6	a) MALDI mass spectrum of rat kidney in the region $m/z$ 400 – 405, showing two overlapping peaks selected for imaging. b) 2D ion plot of ion $m/z$ 402.012 showing primary distribution of this ion within the kidney, and some surrounding signal. c) 2D ion plot of ion $m/z$ 402.072 showing its spatial distribution primarily in the surrounding matrix, and not in the kidney tissue.....	122
3.7	a) drift scope plot with the highlighted region of interest. b) mobilogramme of the two ions encircled in (a). c) mass spectra extracted from the mobilogramme showing the different ions associated with the differences in drift time.....	125
3.8	a) MALDI-MS image of $m/z$ 402.01 in a rat kidney section obtained a) with ion mobility separation on, b) without ion mobility separation. The ion mobility separation has removed the interference surrounding the kidney caused by the interference from the unresolved $m/z$ .....	126
3.9	Partial MALDI mass spectrum obtained from a tissue section containing a DU145 tumour xenograph, highlighted is a peak at $m/z$ 527.92 with a shoulder of a second peak. Inset is the 2D ion plot of peak $m/z$ 527.92.....	127
3.10	Driftscope plot of the same mass region as shown in Figure 3.9, encircled is the ions that account for the peak at $m/z$ 527.92 there are at least 2 ions which are accounting for this peak.....	128
3.11	Mobilogramme from the peak at $m/z$ 527.9, this shows two different drift times associated with this mass range.....	129
3.12	a) MALDI mass spectra obtained after ion mobility separation showing the ions accounting for the faster drift time. b) Mass spectra accounting for the peak with the slower drift time shown in Figure 3.11.....	130
3.13	Mass spectra of the overlapping ions at $m/z$ 527.916 and 528.035 after ion mobility separation showing the measurements at FWHM.....	131
3.14	a) 2D ion plot of the ion mobility separated ion at $m/z$ 527.916. b) 2D ion plot of the ion mobility separated ion at $m/z$ 528.035 each of these two ions have very different distributions within the tissue. c) 2D ion plot of $m/z$ 527.8 - 528.0 without ion mobility separation.....	133

- 4.0 Chapter 4 - Matrix Assisted Laser Desorption Ionisation - Ion Mobility Separation - Mass Spectrometry Imaging of Vinblastine in Whole Body Tissue Sections.**
- 4.1 Schematic of the MALDI HDMS SYNAPT system, this instrument has a quadrupole orthogonal acceleration time-of-flight geometry and is equipped with an ion mobility separation device located between the quadrupole and the time-of-flight analyser. The ion mobility separator used consists of three consecutive travelling wave regions: The Trap T-Wave, Ion Mobility separation T-Wave and the transfer T-wave. Collision induced dissociation can be achieved in either or both the trap or transfer T-wave. (Waters, Manchester, UK)..... 145
- 4.2 Structures of Vinblastine ( $C_{46}H_{58}N_4O_9$ , mono isotopic mass 810.420) and vincristine ( $C_{46}H_{56}N_4O_{10}$  mono isotopic mass 824.400) structures. These compounds are chemical analogues of each other with a difference on one group between a  $CH_3$  and  $COH$ . Indicated is the difference between the two molecules.....147
- 4.3 a) Optical image of the whole body section used for the MALDI imaging experiments, showing the anatomical features and their relative locations within the section before matrix coating. b) MALDI-MSI image of the same tissue section, highlighting the anatomical features by imaging the distribution of specific ions, the varying colour is only an aid to visual identification and not intended to show relative ion intensity..... 150
- 4.4 a) MALDI-IMS-MS/MS transfer dissociation pattern of vinblastine spot on tissue, viewed within "DriftScope" showing the separation of vinblastine from endogenous lipid  $m/z$  811. Two distinct product ion patterns are seen with different drift times, vinblastine has a shorter drift time (4.8-5.6ms) compared to that of the endogenous lipid (5.8-6.5ms). b) Product ion mass spectrum arising from the drift time of 4.8-5.6ms, from the known dissociation pattern of vinblastine it can be seen that this drift time relates to vinblastine. c) Product ion mass spectrum arising from the longer drift time 5.8-6.5ms, this clearly is derived from an endogenous PC lipid as indicated by the intense and characteristic product ion at  $m/z$  184 corresponding to the PC head group  $(H_2PO_4CH_2CH_2N(CH_3)_3)^+$ .....154
- 4.5 Chemical structure of vinblastine and the main dissociation pathways leading to the formation of the observed product ions in the MS/MS spectrum.

	(Favretto et al., 1998).....	155
4.6	Total MALDI-MS mass spectrum of vinblastine spotted on tissue, showing the complexity of signals around the mass of vinblastine $m/z$ 811.4. This region includes ions from alkali metal adducts and singly charged species of several lipids, as well as ions from other species such as matrix related ions.....	158
4.7	MALDI-MS/MS Images from the thoracic and abdominal cavities showing the distribution of the precursor and product ions of vinblastine. a) $m/z$ 811.4, b) $m/z$ 811-793, c) $m/z$ 811-751, d) $m/z$ 811-733, e) $m/z$ 811-719, f) $m/z$ 811-691, g) $m/z$ 811-649, h) $m/z$ 811-524, i) $m/z$ 811-355. (For organ identification see Figure 4.3b).....	159
4.8	"DriftScope" plot of the data obtained from the vinblastine dosed whole body MALDI-IMS-MS/MS imaging, showing the complexity of signals within the data set, numerous ions can be seen with various drift times.....	160
4.9	Comparison of $m/z$ 811 and $m/z$ 811-751 using MALDI-IMS-MS/MS and conventional MALDI-MS/MS clearly demonstrates the advantages of ion mobility separation within MALDI xenobiotic imaging. Indicated is the main difference with the distribution of the ion of interest within the renal pelvis, c) shows the whole body autoradiography plot of a corresponding section from a tritiated vinblastine dose, it can be seen that there is almost no signal in the renal pelvis, confirming the results of the MALDI-IMS-MS/MS.....	161
4.10	MALDI-MSI image of an axial brain section of a rat after $6\text{mgkg}^{-1}$ IV dose of vinblastine, imaged is the distribution of the product ion of vinblastine at $m/z$ 355, overlaid onto a background of an endogenous lipid, showing that vinblastine is only present in the ventricle.....	163
4.11	a) Whole body autoradiograph showing the distribution of $^3\text{H}$ in a 1 hour post dose Rat dosed with $6\text{mg/kg}$ IV $^3\text{H}$ Vinblastine. b) shows the areas selected for analysis and quantification using the "SeeScan" software.....	165
4.12	Enhanced images of the kidney from the whole body sections, before and after imaging. a) an optical image of the kidney from the whole body section dosed at $6\text{mgKg}^{-1}$ IV vinblastine before matrix application. b) the same tissue section as shown in 4.12a but imaged by MALDI-IMS-MS showing the distribution of vinblastine within the kidney, with the highest intensity (white) showing a broken ring of intensity between the cortex and medulla.	

c) optical image of the kidney within the whole body section dosed with  $^3\text{H}$  Vinblastine. d) Whole Body auto radiography of the tissue section shown in 4.12c, indicated is the broken ring of slightly higher intensity (white) between the cortex and medulla is indicated..... 168

## 5.0 Chapter 5 - Lipid Distribution within HCT 116, Tumour Margin and Surrounding Tissue, and the Effects of a Chemotherapeutic drug administration on Lipids.

5.1	schematic structure of a) sphingosine, b) sphinganine.....	176
5.2	The biosynthetic pathway of certain sphingolipids (Modrak et al., 2006).....	177
5.3	Some of the roles of sphingolipids within cancer growth regulation and therapy (Ogretmen 2006).....	179
5.4	100x magnification of HCT 116 cells in culture (Brattain et al., 1981).....	181
5.5	Structure of vinblastine.....	182
5.6	Structure of desacetylvinblastine the major metabolite of vinblastine.....	183
5.7	MALDI MS profile of vinblastine showing the $[\text{M}+\text{H}]^+$ peak at $m/z$ 811.4 and the associated peak at $m/z$ 809.4.....	183
5.8	Proposed structure for the ion observed at $m/z$ 809.4. Highlighted in red is the bond believed to have changed from the original vinblastine structure.....	184
5.9	a) H&E stained section of the Control, non-dosed tumour section after MALDI imaging. b) H&E stained section of the dosed tumour xenograft after MALDI imaging, c) A magnified image of the control tissue section showing the 3 distinctively different tissue regions.....	192
5.10	a) Scores plot showing the PCD-DA for 10 spectra from each of the 3 different tissue regions from the dosed and the non-dosed tissue sections, the separation of the groups of spectra can be seen. b) Loadings plot showing the ions contributing to the separation of the spectra in the scores plot, highlighted are the ions of interest imaged in figure 5.11.....	194
5.11	2D ion plots showing the distribution of some of the ions of interest within the tissue sections selected from the loadings plot, with the corresponding H&E stained tissue section. Identifications have been made based on MS/MS data analysis.....	195
5.12	Product ion mass spectrum for $m/z$ 756 and the interpretation identifying this ion as PC 32:0 $[\text{M}+\text{Na}]^+$ .....	196
5.13	Product ion mass spectrum for $m/z$ 734	

	and the interpretation identifying this ion as PC 32:0 [M+H] <sup>+</sup> Fatty acid chains shown is only one option for this configuration, based on the mass.....	196
5.14	Product ion mass spectrum for m/z 758 and the interpretation identifying this ion as PC 34:2 [M+H] <sup>+</sup> : Note the fatty acid chains shown are only one option for this configuration, based on the mass.....	197
5.15	Product ion mass spectrum for m/z 760 and the interpretation identifying this ion as PC 34:1 [M+H] <sup>+</sup> Fatty acid chains shown is only one option for this configuration, based on the mass.....	197
5.16	2D ion plots of the m/z values listed in Table 5.2.....	200
5.17	2D ion plots of the m/z values listed in Table 5.3.....	203
5.18	2D ion plots of the m/z values listed in Table 5.3.....	204
5.19	2D ion plots of the m/z values listed in Table 5.3.....	205
5.20	2D ion plots of possible phosphatidylcholine (PC) lipids species listed in Table 5.4.....	207
5.21	DriftScope plot from the imaging data acquired from a portion of a 6Hr post dose tumour tissue section. Familial trend lines can be seen.....	209
5.22	a) DriftScope plot of the region in which Vinblastine ions can be seen, encircled is an ion associated with vinblastine at m/z 809.4 and also encircled is the interfering ion. b) Mass spectrum showing the overlapping peaks of interest. c) Ion mobility separated 2D ion plot of the vinblastine associated ion m/z 809.4. d) Biomap image created without ion mobility separation, clearly showing the effect of ion masking due to interference. e) Biomap image of the interfering ion after ion mobility separation.....	210

## 6.0 Chapter 6 - High Repetition Solid State Laser and Raster Imaging for High Throughput, High Resolution MALDI-Imaging.

6.1	Electron configuration with respect to energy levels, this configuration would be written as 1s <sup>2</sup> , 2s <sup>2</sup> p <sup>6</sup> , 3s <sup>2</sup> p <sup>6</sup> d <sup>10</sup> , 4s <sup>2</sup> p <sup>6</sup> .....	216
6.2	A graphical shell model representation of the electron rings within nitrogen and neodymium. Each shell represents an energy level.....	217
6.3	The energy levels within a N <sub>2</sub> molecule responsible for the generation of a photon at 337nm. ( <a href="http://www.fineartradiography.com/hobbies/lasers/nitrogen/">http://www.fineartradiography.com/hobbies/lasers/nitrogen/</a> ).....	219
6.4	The energy levels within a Nd atom responsible for the generation of a photon at 1064nm. ( <a href="http://stwww.weizmann.ac.il/Lasers/laserweb/Ch-6/C6s2t2p2.htm">http://stwww.weizmann.ac.il/Lasers/laserweb/Ch-6/C6s2t2p2.htm</a> )	



	(Pumped at 0.808 $\mu$ m).....	219
6.5	A typical N2 laser spot, showing multiple maxima throughout the laser spot a) in a 2d plane showing laser spot b) showing a laser spot in 3D also showing the multiple maxima throughout the laser spot and c) showing the random nature of the maxima as they change over 8 consecutive shots (Holle et al., 2006).....	227
6.6	The Gaussian distribution of a typical Nd:YAG laser. (Holle et al., 2006).....	228
6.7	Teem Nd:YAG laser spot profiles at (a) 25% and (b) 100% laser power, showing multiple maxima throughout the laser spot after it has been passed through a 100 $\mu$ m fibre optic.....	229
6.8	The structured beam profile of a single shot from the Nd:YAG "smart beam™" laser (Holle et al., 2006).....	230
6.9	The Gaussian spot profile of an Nd:YVO4 laser before entering the fibre optic cable.....	231
6.10	The three imaging modes that can be used within the oMALDI Server 5.1 software (Applied Biosystems/MDS Sciex, Concord, Ontario, Canada).....	232
6.11	The differences between the matrix ablation using raster imaging compared to conventional spot to spot imaging. Reproduced from Simmons 2008.....	233
6.12	The printed numbers mounted on to an Opti TOF target plate, after being coated in $\alpha$ CHCA matrix, prior to imaging.....	234
6.13	Brain image, imaged using raster imaging. Total acquisition time for the image at 150 $\mu$ m resolution took ~37mins.....	238
6.14	The distribution of matrix related ions over 1-20KHz laser repetition rate, a) the distribution of the molecular ion of the matrix $\alpha$ CHCA (M+H) <sup>+</sup> at m/z 190, b) the distribution of the ion of matrix minus water (M-H <sub>2</sub> O) <sup>+</sup> at m/z 172, c) the distribution of the sodiated matrix adduct (M+Na) <sup>+</sup> at m/z 212 and d) the distribution of the potassiated matrix adduct (M+K) <sup>+</sup> at m/z 228.....	240
6.15	The distribution of two different ions over 1-20KHz laser repetition rates. a) The distribution of m/z 134 this ion demonstrates the effect of matrix suppression. b) The distribution of the ink related ion m/z 325.....	241
6.16	The distribution of a) m/z 134 normalised against the matrix ion m/z 190 at laser repetition rates 1-10KHz, b) m/z 134 normalised against the matrix ion m/z 190 at laser repetition rates 10-20KHz,	

	c) m/z 325 normalised against the matrix ion m/z 190 at laser repetition rates 1-10KHz and d) m/z 325 normalised against the matrix ion m/z 190 at laser repetition rates 10-20KHz.....	243
6.17	The relationship between the laser repetition rate, average power and energy for the Elforlight spot series laser (Elforlight Ltd. Daventry, UK. Private communication)....	244
6.18	Chart showing the laser power selected for the conventional MALDI analysis of $\alpha$ CHCA. An attempt was made to maintain a similar signal for ion m/z 414, also shown are the ion counts for a series of matrix related ions at m/z 172, 190 and 212.....	245
6.19	graph showing the mean ion count of 5 replicate measurements showing matrix ions and vinblastine associated ions.....	248
6.20	The ratio of m/z 811.4 the protonated molecule of vinblastine compared to possible fragment ions. Little difference between different laser repetition rates, is observed. Note: m/z 809 has not been shown due to the possibility that this ion is not a fragment of the parent but a vinblastine related ion.....	249

## List of Tables

<b>1.0</b>	<b>Chapter 1 - Introduction</b>	
1.1	Some matrices commonly used for MALDI-MS including their structure and an example of what they have been used for the analysis of. This is not an exhaustive list and there are novel matrices or matrix combinations being reported every year.....	40
1.2	Quick guide to some of the available matrix coating techniques showing some of the advantages and disadvantages. (adapted from Kaletas et al., 2009.).....	50
<b>2.0</b>	<b>Chapter 2 - MALDI-MS Imaging of Lipids in Rat Brain Tissue with Integrated Unsupervised and Supervised Multivariate Statistical Analysis.</b>	
2.1	List of statistical processing methods used within MALDI-MS imaging data processing with advantages and disadvantages. (Van den berg et al., 2006).....	78
2.2	Comparison of the observed lipid masses and the calculated mass.....	94
2.3	Comparison of the theoretical and measured mass taken from the spectra shown in figure 2.11. Identified are the possible Lipids species and the PPM mass error. All the PPM mass errors are below 10PPM.....	100
<b>4.0</b>	<b>Chapter 4 - Matrix Assisted Laser Desorption Ionisation - Ion Mobility Separation - Mass Spectrometry Imaging of Vinblastine in Whole Body Tissue Sections.</b>	
4.1	The sample oxidation data following administration of <sup>3</sup> H radiolabelled Vinblastine. Concentrations of radioactivity are greatest in all tissues and plasma except in the brain at 1 hour post dose. Highest concentrations of radioactivity were measured in the kidney at 30.2µg equiv/g 1 hour post dose.....	162
4.2	Tissue concentrations of radioactivity calculated from the WBA image using "SeeScan" software from the known standards and the calculated µg equiv/g of the drug or metabolite. (BLQ - Below Limit of Quantification).....	166
<b>5.0</b>	<b>Chapter 5 - Lipid Distribution within HCT 116, Tumour Margin and Surrounding Tissue, and the Effects of a Chemotherapeutic drug administration on Lipids.</b>	
5.1	The percentage variance and total variance accounted for by each principle component	

	selected by the PCA DA software.....	195
5.2	List of possible Sphingolipid species and whether they were detected within different tissue regions of the dosed and non dosed tissue sections. An arbitrary visual scale was used with the following indications of relative abundance, Very low to no signal observed is shown by a (-), low relative abundance is shown by (+), followed by (++) which denotes medium relative abundance, and a relatively high abundance is shown by (+++) and a very high abundance is denoted by (+++). This table is just as a visual comparison for a range of lipids throughout each tissue region. All data used in the compilation of this table is from data normalised against the matrix ion m/z 190. (# Possible lipid species not confirmed by MS/MS) SPPC = sphingosylphosphorylcholine, PAF = Platelet activating factor, LPC = Lyso phosphitidylcholine. PPM mass errors have been calculated and displayed, Red- >20ppm, Yellow - 10-20ppm, Green - <10ppm.....	199
5.3	List of possible Sphingomyelin (SM) species and whether they were detected within different tissue regions of the dosed and non dosed tissue sections. An arbitrary visual scale was used with the following indications of relative abundance, Very low to no signal observed is shown by a (-), low relative abundance is shown by (+), followed by (++) which denotes medium relative abundance, and a relatively high abundance is shown by (+++) and a very high abundance is denoted by (+++). This table is just as a visual comparison for a range of lipids throughout each tissue region. All data used in the compilation of this table is from data normalised against the matrix ion m/z 190. PPM mass errors have been calculated and displayed, Red- >20ppm, Yellow - 10-20ppm, Green - <10ppm.....	201-202
5.4	List of possible PC lipid species and whether they were detected within different tissue regions of the dosed and non dosed tissue sections. An arbitrary visual scale was used with the following indications of relative abundance, (<0.1au) very low to no signal observed (-), (0.1-1au) low relative abundance (+), (1-5au) medium relative abundance (++) , (>5au) relatively high abundance (+++). This table is just as a visual comparison for a range of lipids throughout	

each tissue region. All data used in the compilation of this table is from data normalised against the matrix ion m/z 190. (# possible lipid species not confirmed by MS/MS). PPM mass errors have been calculated and displayed, Red- >20ppm, Yellow - 10-20ppm, Green - <10ppm.....206

**6.0 Chapter 6 - High Repetition Solid State Laser and Raster Imaging for High Throughput, High Resolution MALDI-Imaging.**

6.1 The values for each of the 5 acquisitions for each laser repetition rate used and the laser power selected.....246

6.2 The intensity values of some matrix ions and vinblastine associated ions over 5 replicate measurements over 5 different laser repetition rates.....247

6.3 The survival yields of vinblastine using different laser repetition rates using the parent ion m/z 811.4 as the  $I_m$  and the fragment ion m/z 355 as  $I_f$ .....250

## Abbreviations

µg	Microgram
µJ	Micro Joules
µl	Microlitre
µm	Micrometer
ADME	Absorption, Distribution, Metabolism, Excretion.
CCA	Canonical Correction Analysis
CMC	Carboxy Methyl Cellulose
DA	Discriminant Analysis
DART	Direct Analysis in Real Time
DESI	Desorption Electrospray Ionisation
Er:YAG	Erbium-Yttrium Aluminium Garnet
ESI	ElectroSpray Ionisation
FBS	Foetal Bovine Serum
g	Gram
GC	Gas Chromatography
HDMS	High Definition Mass Spectrometry
HPLC	High Performance Liquid Chromatography
Hz	Hertz
IMS	Ion Mobility Separation
IR	Infra-Red
k	instrument related constant
Kg	Kilogram
KHz	Kilohertz
KV	Kilovolts
LC	Liquid Chromatography
LDI	Laser Desorption Ionisation
LSC	Liquid Scintillation Counting
m	Mass
m/z	Mass divided by Charge
MALDI	Matrix Assisted Laser Desorption Ionisation
mg	Milligram
Min	Minute
mM	MilliMolar

MS	Mass Spectrometry
MSI	Mass Spectrometry Imaging
N <sub>2</sub>	Nitrogen
NCE	New Chemical Entities
Nd:YAG	Neodymium-Yttrium Aluminium Garnet
Nd:YLF	Neodymium-
Nd:YVO <sub>4</sub>	Neodymium- Yttrium Vanadate
NDE	New Drug Entities
ng	Nanogram
nl	Nanolitres
nm	Nanometers
ns	Nanoseconds
oC	Degrees Centigrade
OCT	Optimum Cutting Temperature
OPO	Optical Parametric Oscillator
PC	Phosphatidylcholine
PCA	Principle Components Analysis
ps	Picoseconds
Q	Quadrupole
QWBA	Quantitative Whole Body Autoradiography
SIMS	Secondary Ion Mass Spectrometry
SM	Sphingomyelin
SY	Survival Yield
t	Time
TFA	Trifluoroacetic acid
TIC	Total Ion Count
TOF	Time Of Flight
UV	Ultra Violet
UV	Ultra-Violet
Vis	Visible
WBA	Whole Body Autoradiography
z	Charge
α-CHCA	alpha - cyano-4-hydroxycinnamic acid

# CHAPTER 1

---

## Introduction



## 1.0 Introduction

### 1.1 Drug Discovery

#### 1.1.1 Target Identification.

The initial stage in the drug discovery process is the identification of a medical need for the development of a drug compound based on the lack of current methodology in the treatment or a lack of existing effective drugs. Once a medical need has been identified the drug development process starts. Figure 1.1 shows a schematic of the common steps involved with the drug discovery and development process from the identification of possible targets until a completed drug can be distributed into the market. This entire process takes several years to complete and only a few of the initial compounds make it to market. Typically <10% are finally marketed (Ashburn and Thor 2004).

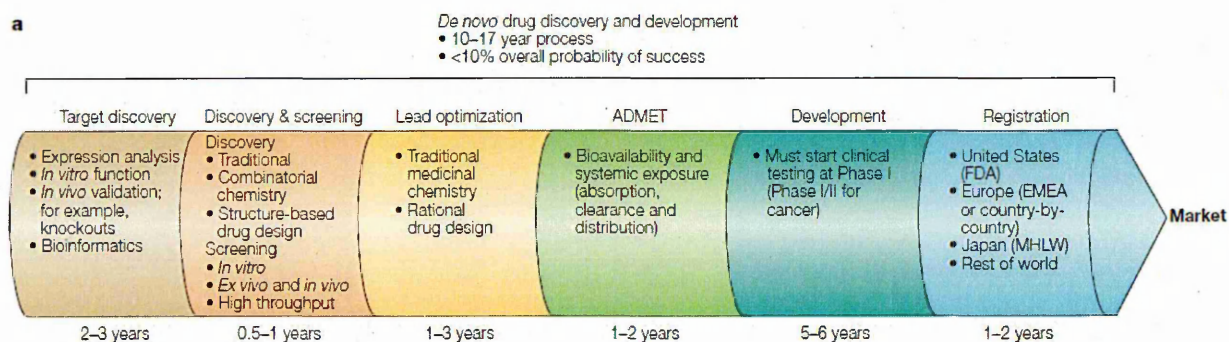


Figure 1.1 Schematic representation of the drug discovery process and approximate times involved at each stage. (Ashburn and Thor 2004).

The first stage, once a medical need has been identified, is to find disease modifying targets (Lindsay 2003). Possible drug targets are usually a single gene, gene product or molecular mechanism (Sams-Dodd 2005). Once a possible target has been identified it needs to be validated. Target validation

involves the determination of the therapeutic value of the target within a specified patient population. If the target is deemed a viable target then a high throughput screening assay is developed. The use of high throughput screening allows for rapid analysis of possible target specific compounds from compound libraries and the identification of possible lead compounds.

### **1.1.2 Lead Optimisation**

If a lead compound is identified this compound then needs to be optimised. Lead optimisation may involve the manipulation of the lead compound structure, or assessment of any structural isomers, using high throughput screening, until a compound that has the optimum specificity towards the target is found. Lead optimisation can involve the lead compound/s undergoing modification or synthesis. In order to improve target interaction, specificity, efficacy, reduce toxicity and improve pharmacokinetics and pharmacodynamics.

There is currently a requirement to use *in vivo* studies within certain areas of the drug discovery process, including toxicity and distribution studies. More and more, pharma are trying to use alternative *in vitro* studies to reduce the number of animal experiments. Repeat dose toxicity studies currently have to be carried out *in vivo* for both rodent and non rodent (commonly initially rabbit) species for a period of time consistent with the planned duration of clinical studies (Ng 2004). Possible metabolites of new chemical entities (NCE) are commonly characterised using several techniques including: LC/MS, HPLC/MS, GC/MS, UV/Vis spectroscopy etc (Zhang *et al.*, 2009). There is

scope within this field for the application of imaging technologies, and specifically MALDI imaging for the identification and analysis of the spatial distribution of NCEs and their metabolites. This could add additional spatial information within the metabolite identification experiments (Sugiura and Setou 2009).

When a lead compound has been shown to be a successful compound in the *in vitro* and *in vivo* animal studies it is required to enter clinical trials.

The final lead compound needs to be placed into a drug design. The drug design markedly differs depending on the possible market for the drug and more importantly the absorption, distribution, metabolism and excretion (ADME) properties of the compound. These can all be altered depending on the drug's formulation and route of administration. Factors that need to be considered are possible routes of administration, and initial dose formulation (Ricaurte *et al.*, 1988).

### **1.1.3 Phase I clinical trials.**

Phase I clinical trials are primarily designed to assess the safety of the drug within healthy human volunteers. A small group of healthy human volunteers receive a single dose or a dosing regime of the drug. The pharmacokinetics and pharmacodynamics of the test compound are assessed and any physiological or behavioural effects are assessed.

### **1.1.4 Phase II clinical trials**

Phase II Clinical trials involves either open label, blind or double blind trials, on the relevant disease group. Part of the group will receive the new test compound possibly with different dosing regimes and the other members of the group will receive a placebo or the current standard treatment depending on the patient risk if they receive only the placebo. The data obtained in phase II aids in the development of the most effective dosing regimes and the effectiveness of the treatment.

### **1.1.5 Phase III clinical trials.**

Phase III is an extension of phase II and involves a much wider group compared to phase II. Normally over several locations. This allows more extensive assessment of the safety and efficacy and allows extensive statistical analysis of the obtained data. And a comparison of efficacy with current treatments can be made.

At this stage if the drug benefits and efficacy far outweigh any safety or side effects, the full data is presented to the regulatory authorities for assessment and approval. Once approved the drug can be marketed.

## **1.2 Drug distribution studies.**

Current drug distribution studies are primarily carried out using quantitative whole body autoradiography (QWBA), and organ homogenate analysis using liquid scintillation counting (LSC). QWBA has taken over from more conventional animal dissection and determination of tissue homogenate composition (Solon and Kraus 2002). The pharmacokinetic data obtained

using QWBA are utilised in the prediction of the exposure of human volunteers to isotope labelled compounds during radioisotope mass balance studies. These studies are a requirement for new compounds (Solon and Lee 2002)

### **1.2.1 Quantitative Whole Body Autoradiography (QWBA)**

This is the most common way for determining the distribution of xenobiotics within whole body animal studies, and is utilised routinely within preclinical drug development studies (Coe 2000).

QWBA involves the synthesis of a drug compound which contains a radiolabel predominantly carbon 14 or tritium. Tritium labelled new drug entities (NDE) are easier and quicker to obtain (Potchoiba and Nocerini 2004). One problem with using tritium is that a percentage of the radiolabel may be lost during the freeze drying process as tritiated water. Radio labelling developmental drug compounds can be an expensive process (Ulberg 1954)

An animal is dosed with the labelled compound and sacrificed after a set time period, the animal is then frozen within a block of carboxymethyl cellulose (CMC) (QWBA methodology is covered further in Chapter 4 of this thesis). The animal is then sectioned using a whole body cryotome. The sections are placed onto a radiation sensitive plate and stored for a desired amount of time after they have been freeze dried. The radio sensitive plates are then automatically read using a plate reader. Using software the concentration of the known standards can be entered and the quantification of the radiolabel

and hence compound concentration can be calculated (Potchoiba *et al* 1997, Potchoiba *et al* 2004).

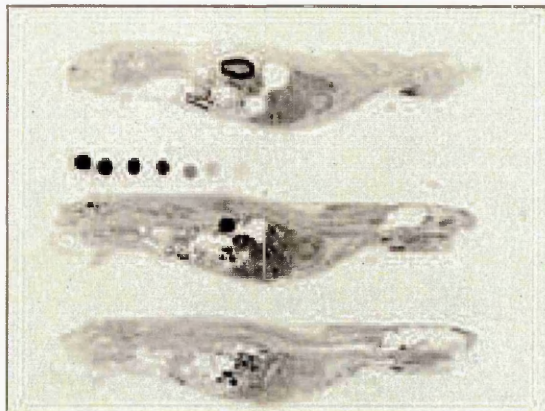


Figure 1.2 QWBA image showing radiolabel distribution within three rat whole body tissue section, also shown are a series of spiked blood samples for calibration. ([www.biospacelab.com](http://www.biospacelab.com))

Maas *et al.*, 2000 presented work recommending the standardisation of QWBA methodology. Within this work they assessed several parameters that are variable within QWBA analysis. They proposed that the optimum thickness for QWBA analysis was between 25-50 $\mu$ m. This was recommended due to the  $\mu$ g equivalents/g calculations from the detected radioactivity. The quantification was carried out using spiked blood standards included into the CMC block prior to sectioning to create a standard curve. One of the reasons for recommending this tissue section thickness is due to tissue self absorption of the radioactivity. This is highest within bone tissue, which is expected due to its density. They also recommend the orientation of the samples to be vertical to the scanning direction to reduce flaring from areas of high concentration, this can mask areas of lower intensity. Temperature should be maintained constant preferably at a low temperature

and the sample should be stored in a shielded box to reduce the background signal. Also scanning acquisition should be performed as soon as possible due to non linear fading of intensity over time.

The main limitations with the use of QWBA is the fact that only the radiolabel can be imaged, hence, this technique is unable to differentiate between parent compound and metabolites. Therefore in combination with this technique another animal receives a cold dose of the drug compound from which the organs of interest can be harvested and analysed to obtain the compound or metabolite identification and further quantification through various techniques, mainly a form of LC-MS, is used.

MALDI-MSI is a relatively new method which potentially addresses some of the issues arising from QWBA.

### **1.3 Mass spectrometry Instrumentation**

Mass Spectrometry (MS) is an invaluable tool in biomedical research. It is used in the characterisation and structural elucidation of molecules and elements, as well as in qualitative and quantitative sample composition studies.

Mass spectrometers have at least three regions, an ionisation source to produce ions from a sample. Mass analysers or selectors to separate the ions based on their mass-to-charge, and finally a detector to measure the ions abundance and record the data.

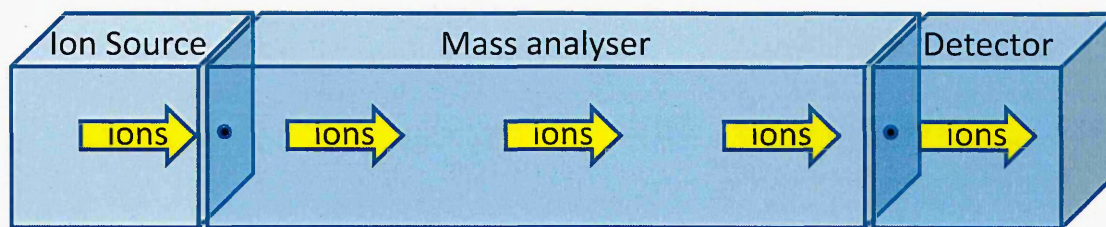


Figure 1.3 Simplified schematic of a mass spectrometer.

### 1.3.1 Ionisation sources

There are several ionisation sources used within mass spectrometry. Different ion sources are used for different techniques. Each ion source has different characteristics including but not limited to mass range, fragmentation, sample depth penetration, sample destruction and spatial resolution (if required for an imaging technique). Another consideration when choosing an ionisation source is the type of sample that requires analysis e.g. Solid, liquid or gas.

Some of the ion sources used within mass spectrometry include radioactive ionisation, corona discharge ionisation (Ross and Bell 2002), photoionisation (Cooper *et al.*, 2002), electrospray ionisation (ESI) (Postle *et al.*, 2007), secondary electrospray ionisation, laser desorption ionisation (LDI) (Benazouz *et al.*, 1999), Surface enhanced - LDI (Hinshelwood *et al.*, 1999) and matrix assisted laser desorption ionisation (MALDI). Within Biological mass spectrometry the most common ionisation source used is ESI (which is usually coupled to a separation technique e.g. HPLC).



### 1.3.1.1 Electrospray ionisation (ESI)

ESI is one of the most common ion sources used within biological mass spectrometry, and is often coupled to HPLC systems (high performance liquid chromatography). Figure 1.4 shows a schematic of an ESI source. In one embodiment the source has a capillary which carries the sample solution into it at range of flow rates from several  $\mu\text{L}/\text{min}$  down to a few  $\text{nL}/\text{min}$ .

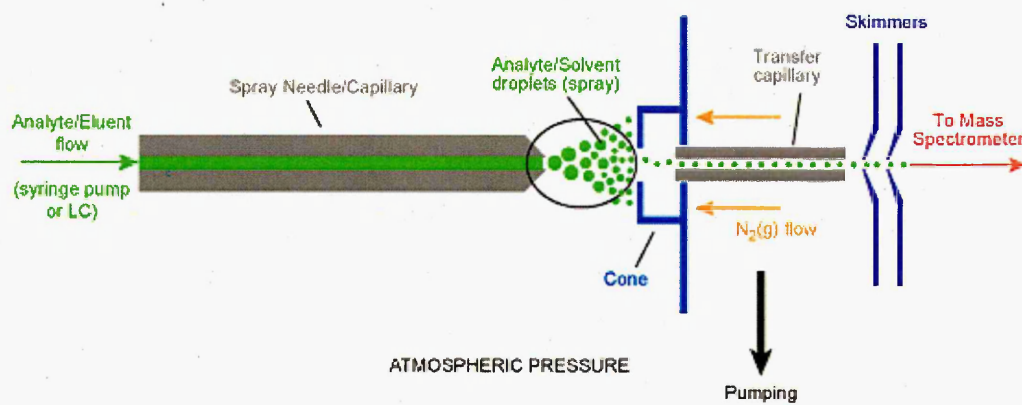


Figure 1.4 schematic of an electrospray ionisation source. ([www.chm.bris.ac.uk](http://www.chm.bris.ac.uk))

A high voltage is applied to the capillary typically in the range of 2-5kV. This applied potential voltage causes the positively charged ions in the solution to accumulate at the tip forming a cone called a Taylor cone (Figure 1.5). This then starts budding and forms a spray/mist of multiply charged droplets. These droplets undergo solvent evaporation and hence size reduction. There is a critical point at which the droplet undergoes fission due to the charge repulsion overcoming the surface tension of the droplet this is known as the Rayleigh limit. This process can occur numerous times until the resulting ions are fully desolvated this occurs at atmospheric pressures. This process is

depicted in figure 1.5. ESI often results in multiply charged ions compared with MALDI which predominantly results in singly charged ions. For further information on ESI, Gaskell 1997 has presented an excellent review.

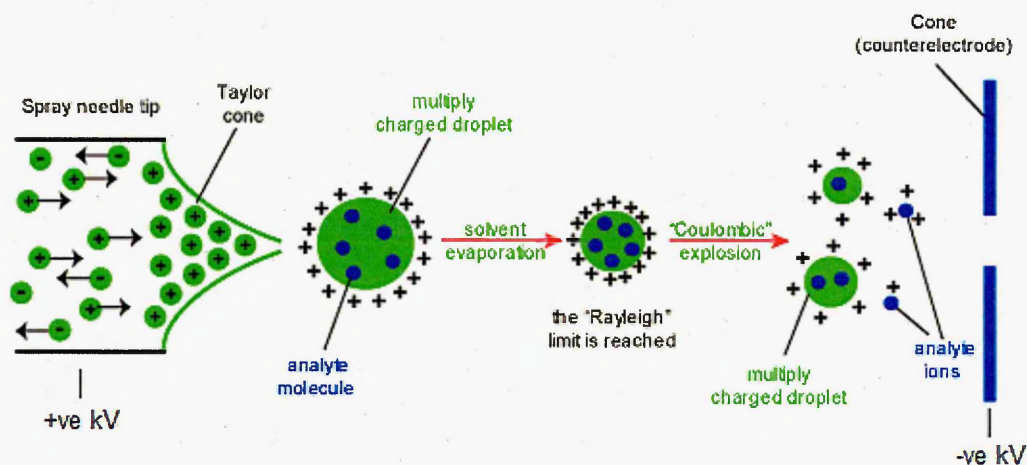


Figure 1.5 Schematic of the droplet desolvation during ESI. ([www.chm.bris.ac.uk](http://www.chm.bris.ac.uk))

### 1.3.1.2 Desorption ElectroSpray Ionisation Source (DESI).

ESI has recently been adapted into DESI (Desorption Electrospray Ionisation) (Takats *et al.*, 2004) this involves desorbing ions from a sample surface with an ESI source. A schematic of the instrument arrangement is shown in figure 1.6

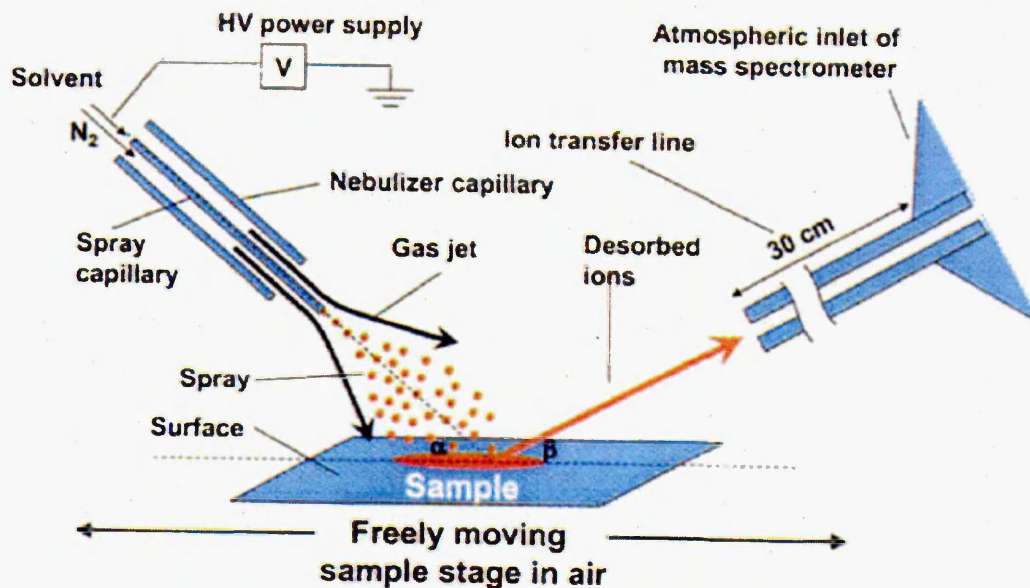


Figure 1.6 DESI instrumentation schematic showing the electrospray source directed at the sample and not directly into the mass spectrometer as in ESI. (Takats et al 2004)

The sample is impacted by charged droplets and ions from the solvent in the electrospray. The impact of these results in the production of gaseous ions of the sample originally on the sample surface. The resulting mass spectra are similar to ESI mass spectra with singly and multiply charged ions. DESI can be used for the detection of small molecules and proteins and peptides. By varying the solvent composition from the ESI source within DESI, analytes can be selectively analysed, or with varying sensitivity.

Takats *et al.*, 2005 have adapted this ionisation source for spatial analysis and imaging, although only the theory with no images has been presented. They also demonstrate the use of this technique for the detection of explosives for forensics. The authors present evidence for both charge transfer and droplet pick up mechanisms for the ionisation process in DESI. Imaging DESI has now been shown by many groups. Wiseman *et al.*, 2006

have demonstrated rat brain tissue lipid imaging using DESI. DESI imaging involves acquiring a DESI mass spectrum at a location which is then stored as a pixel within the image. The sample is then moved left or right relative to the source depending on the instrument configuration, and another mass spectrum is recorded. This process is repeated across the sample area. Once one line is completed the sample is moved towards the MS inlet, this reduces the possibility of analysing material redistributed in the direction of the electrospray flow (Figure 1.7).

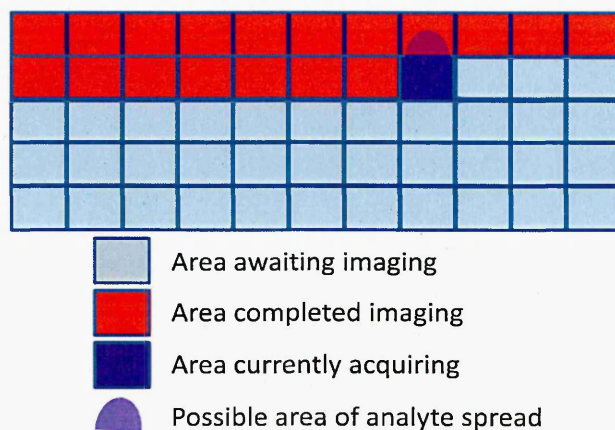


Figure 1.7 Schematic of the pattern from an imaging DESI experiment, showing the possible spread of analytes due to the electrospray.

DESI has recently been used for whole body imaging by Kertesz *et al.*, 2008 and has been compared to whole body autoradiography which is the standard for whole body tissue imaging for drug distribution studies, as previously described.

### **1.3.1.3 Matrix assisted laser desorption ionisation (MALDI)**

Matrix Assisted Laser Desorption Ionisation (MALDI) was introduced in the late 1980's (Karas *et al.*, 1985, Tanaka *et al.*, 1988) as a soft ionisation technique intended for extending MS analysis to large biomolecules. The conventional MALDI-MS technique has since been developed into an imaging technology. MALDI-MS imaging (MALDI-MSI) has been used in a wide variety of applications since the first full paper (Caprioli *et al.*, 1997).

MALDI is a relatively soft ionisation technique producing predominantly singly charged ions (Karas *et al.*, 2000). MALDI is a two stage process involving the desorption/ablation event followed by ionisation of the analytes. These two events will be discussed further later in this introduction. Usually a sample is coated with a matrix (predominantly an organic acid) which absorbs radiation within the wavelength of the laser used within the experiment, commonly UV lasers. The desorption and ionisation within MALDI is predominantly done under vacuum conditions compared to ESI which is at atmospheric pressure. The sample once coated with the matrix is then placed in the instrument where the sample is irradiated by a laser.

There are two modes of operation for MALDI MSI, these are microprobe and microscope mode (Luxembourg *et al.*, 2004 and Klerk *et al.*, 2009).

#### **1.3.1.3.1 Microprobe MALDI.**

Microprobe mode MALDI involves irradiating a small area/pixel with a laser and recording the resulting mass spectra for each position defined by the user. After image acquisition is complete ions are selected and an image is



reconstructed as a 2D ion density map based on the ion intensity at each location. This is the mode all experiments within this thesis have been carried out using. Figure 1.8 shows a representation of microprobe mode MALDI imaging experiment.

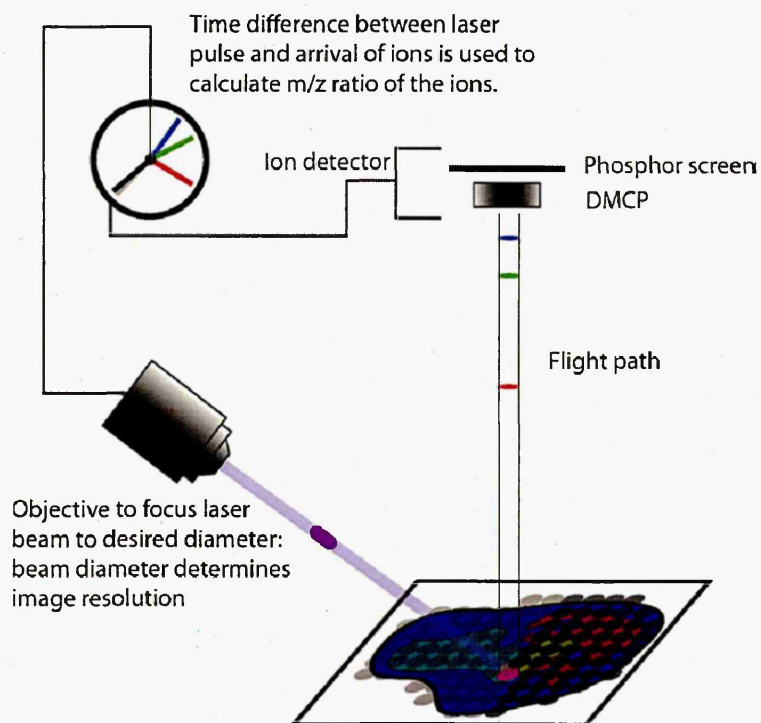


Figure 1.8 Schematic representation of a microprobe MALDI setup. (Klerk et al., 2009)

### 1.3.1.3.2 Microscope MALDI.

Microscope MALDI involves irradiating the entire area that is to be imaged. This results in the generation of ions from the sample which retain their spatial distribution and are detected using a 2D position sensitive detector. Figure 1.9 shows a representation of a microscope mode MALDI experiment.

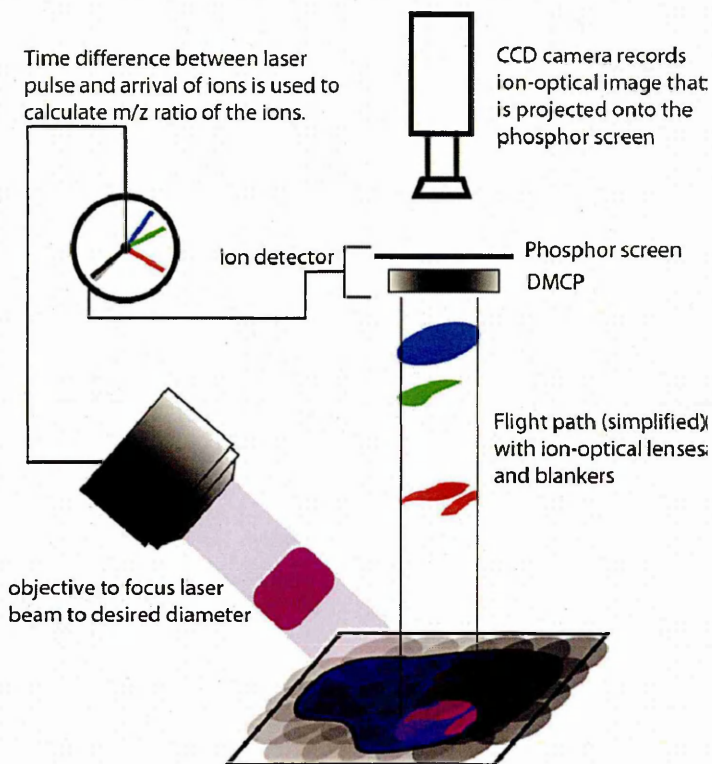


Figure 1.9 Schematic representation of a microscope MALDI setup. (Klerk et al., 2009)

#### 1.3.1.4 SIMS (Secondary Ion Mass Spectrometry).

SIMS imaging is a complimentary technique to MALDI MSI. SIMS imaging currently has a much higher spatial resolution compared to MALDI however the effective mass range is much smaller than achievable using MALDI (Heeren et al 2008, Monroe et al 2008).

SIMS involves the generation of ions from a sample by bombarding the sample with a primary ion beam generated by an ion gun. The primary ion beam is focused onto the sample and penetrates the surface. This causes the ionisation and sputtering of some of the sample surface into the surround. These ions then pass through various ion optics and into a mass analyser commonly a TOF MS (Zheng et al., 2008). A schematic of ion formation in SIMS is shown in figure 1.10.

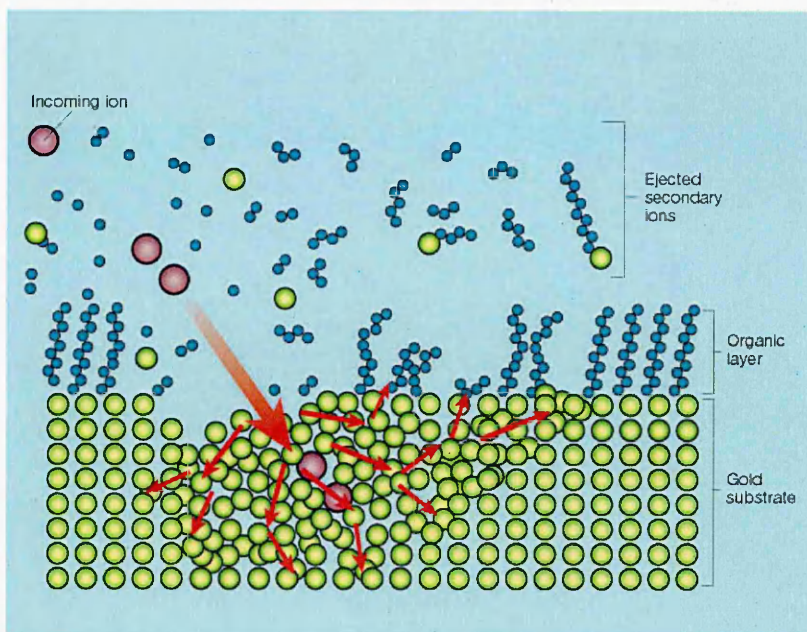


Figure 1.10 Schematic representation of the generation of secondary ions within SIMS. (Castner 2003)

SIMS and MALDI data sets have been combined from the same tissue section by Eijkel *et al.*, 2009. The possible benefits from the correlation of both imaging techniques was demonstrated, including the high spatial resolution obtainable by SIMS. They used principle component analysis (PCA) and canonical correlation analysis (CCA) to extract information on the spatial distributions of different ions of interest and combine the two data sets.

### 1.3.2 **Mass analysers**

There are several possible analysers that can be used within mass spectrometry including ion traps (Beaudry *et al.*, 2009), Fourier transform ion cyclotron (Irungu *et al.*, 2008) and magnetic sector (Bereman *et al.*, 2008). These analysers will not be covered in the scope of this introduction. The mass analysers covered within this thesis will include quadrupole (Q) and time of flight (TOF) analysers and tandem mass analysers.



### 1.3.2.1 *Quadrupole*

Quadrupole mass filters are commonly used on smaller instruments or in conjunction with other mass analysers as a tandem instrument (Morris *et al.*, 1997). Quadrupole mass filters consist of 4 metal rods connected in pairs running parallel to each other. Across these rods an RF voltage is applied in pairs along with a DC voltage which is applied along the length of the quadrupole. Applying these voltages and by varying the RF voltages ions can be selected to transverse the quadrupole. Ions which are not the correct mass-to-charge end up colliding with the metal poles.

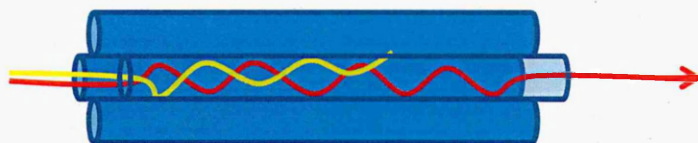


Figure 1.11 schematic of a quadrupole mass analyser red ion is of the correct mass-to-charge and is able to exit the quadrupole, the yellow ion is a different mass-to-charge that ends up being neutralised on the metal rods.

### 1.3.2.2 *Time of flight*

Time of flight (TOF) mass analysis is a very common form of mass analysis used within MALDI experiments. TOF mass analysers accurately measure the time it takes an ion to transverse a field free drift tube, after the ions have been accelerated using a voltage. Because each ion has the same kinetic energy larger ions travel slower than smaller ions. The simplified equation

showing the relationship between time and mass/charge ratio is shown below in equation 1.1

$$t = k \sqrt{\frac{m}{z}}$$

*Equation 1.1 Equation showing the relationship between time and mass-to-charge within a TOF analyser,  $t$  = time taken to transverse the drift tube,  $k$  = is an instrument related constant calculated by the total length of the drift tube divided by the square root of twice the voltage applied to accelerate the ions into the flight tube,  $m$  is the mass of the ion and  $z$  is the charge on the ion.*

There are two ways in which the TOF analyser is orientated compared to the ions original direction of motion these are linear or axial and orthogonal.

Linear or axial TOF ions are accelerated in their original direction of travel into the TOF analyser. One of the issues with this arrangement is that any slight variation in the initial sample height may alter their effective time of flight and hence could reduce the mass resolution of the instrument.

Orthogonal TOF instruments accelerate the ions into the drift tube at  $\sim 90^\circ$  to their original direction of travel hence removing any experimental differences in the original starting height of the ions.

Also the mass resolution can further be improved with the use of reflectron TOF (Franzen 1997). Reflectron TOF instruments use a set of ring electrodes each with increasing potential voltage which reflects the ion back down the length of the flight tube doubling the length the ions have to travel. This also corrects for any differences with the kinetic energy for ions with the same mass-to-charge. Ions with a higher kinetic energy travel further into the reflectron and hence travel a slightly longer flight path to ions with a lower

kinetic energy. Some of the many commercial TOF analysers can be run in "V" or "W" mode this represents the flight path of the ions, by using this method the distance for TOF separation can be doubled within the same length flight tube. (Figure 1.12)

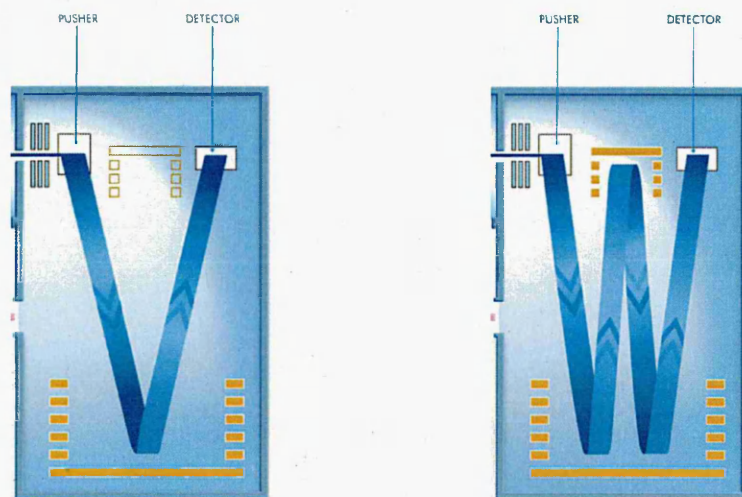


Figure 1.12 Schematic of the TOF portion of a Synapt HDMS system (Waters Corporation, Manchester, UK) showing the flight path of ions in the time of flight tube when in "V" or "W" mode of operation.

### 1.3.2.3 Tandem instruments

There are two types of tandem instruments. These are tandem in time which account for ion trap mass spectrometers, which can trap ions and then selectively release them. The second type is tandem in space which involve multiple mass analysers. Tandem in Space is the type of mass spectrometers covered briefly within this thesis.

Several commercial instruments are tandem instruments which contain two mass analysers. Both instruments used throughout this thesis are Q-TOF hybrid instruments. This means the instrument has a quadrupole mass

analyser (or hex/octo-pole) followed by a TOF mass analyser. Other tandem instruments include TOF-TOF (Falkner *et al.*, 2007) or another arrangement is triple quads, which employ Q1 and Q3 as mass selectors or mass analysers and Q2 as a collision cell.

### **1.3.3 MALDI Lasers**

There are essentially only a few lasers used within MALDI instruments. The two most common lasers used are the N<sub>2</sub> lasers and the Nd:YAG lasers. However IR lasers have been used.

#### **1.3.3.1 N<sub>2</sub> lasers**

This is traditionally the most common MALDI laser and one of the cheapest laser options for MALDI. This laser has an output of 337nm which is suitable for many MALDI matrices. One problem with N<sub>2</sub> lasers is the limited repetition rate, normally 20Hz-50Hz. N<sub>2</sub> lasers were initially the most common laser used within MALDI due to their relatively low cost and previously were much smaller than other laser options.

#### **1.3.3.2 Nd:YAG lasers**

Matrix assisted laser desorption was first reported using a frequency quadrupled Nd:YAG laser at 266nm (Karas *et al.*, 1985). Since then the further development of these lasers, allowing the size and cost to be reduced has enabled the inclusion of this laser system as a direct replacement for conventional N<sub>2</sub> laser systems. Frequency tripled Nd:YAG lasers have a

wavelength output of 355nm. This laser system allows repetition rates between 200Hz-2KHz.

### **1.3.3.3 Nd:YVO<sub>4</sub> lasers**

Frequency tripled Nd:YVO<sub>4</sub> lasers also have a wavelength of 355nm but allow much higher repetition rates with the possibility of reaching 100 KHz repetition rates. The use of a Nd:YVO<sub>4</sub> laser forms part of this thesis. This laser was used for high repetition rate MALDI imaging, allowing the use of raster imaging whilst maintaining a significant number of laser shots per pixel (Further work on this laser can be seen in Chapter 6 of this thesis). Tojo *et al.*, 2008 have also presented work using a Nd:YVO<sub>4</sub> laser for MALDI, within this work the authors demonstrate the characteristics of a Nd:YVO<sub>4</sub> laser, but they have not shown any results using this laser for MALDI.

### **1.3.3.4 Infra Red lasers**

Infra red lasers have also been employed for MALDI analysis, the first results published from an IR MALDI experiment were from Overberg *et al.*, 1990, within in this work they utilise a Er:YAG laser at 2.94µm wavelength, the same group also presented work using a CO<sub>2</sub> laser in 1991 (Overberg *et al.*, 1991).

IR MALDI has been used for a variety of applications since its development especially large biomolecules including intact proteins. (Berkenkamp *et al.*, 1997)

IR LDI and IR MALDI all rely on the absorption of photons at IR laser wavelengths by O-H, C-H, N-H, C-O and C=O bond stretching and bending.

A lot of IR MALDI experiments utilise glycerol as a matrix.

IR MALDI is a softer ionisation than UV-MALDI producing less metastable ion fragmentation (Dreisewerd *et al.*, 2003).

#### **1.3.3.5 IR and UV combined lasers.**

Huang *et al.*, 2008 have reported the use of a combined IR-LD and UV-MALDI instrument. Within this work the use of a pulsed optical parametric oscillator (OPO) IR laser, which has a tuneable wavelength was described. They utilised two wavelengths 2.94 $\mu\text{m}$  and 3.05 $\mu\text{m}$  to ablate the sample and this was then followed by a UV laser pulse at 351nm to ionise the plume generated by the IR laser. The UV laser was fired 50 $\mu\text{s}$  after the IR laser parallel to the sample. Different delay times between the two laser shots markedly changed the ion signals and this time delay is clearly a critical step, as would be expected due to the plume expansion.

The use of IR MALDI / LDI has also been reported with an ion mobility cell by Woods and Jackson 2006. Within this work they also describe the use of a OPO IR laser and for comparison a Nd:YLF laser for UV MALDI. Comparison of both UV and IR spectra showed that the IR MALDI resulted in less fragmentation of the analyte, they also showed that IR MALDI and IR LDI are similar for the analysis of phospholipids in rat brain tissue.

#### **1.3.3.6 Multi-frequency lasers**

Su *et al.*, 2006 presented some initial experiments using a multi-frequency laser within a MALDI experiment. The multi-frequency laser used within this work emits multiple wavelengths including 355nm. It was shown that using

$\alpha$ CHCA as a matrix similar results were obtainable using a 355nm laser and the multi-frequency laser, this was also true with the use of SA as the matrix. However with activated charcoal a more intense peak of cytochrome C was observed at  $m/z$  12327 using the multi-frequency laser compared to a 355nm Nd:YAG laser.

### 1.3.4 Instruments

#### 1.3.4.1 Q-Star Pulsar-*i*

In this thesis, for small molecule MALDI-MSI one of the main instruments used was an Applied Biosystems/MDS Sciex hybrid quadrupole time-of-flight instrument (Q-Star Pulsar-*i*) fitted with an orthogonal MALDI ion source. Three different lasers have also been used during the course of this work: a 337nm N<sub>2</sub> laser, a 355nm frequency tripled 1 KHz Nd:YAG laser (Chapter 2) and a 355nm frequency tripled 1-20 KHz Nd:YVO<sub>4</sub> laser (Chapter 6). The Q-Star itself has a MALDI source, to create the ions, followed by a quadrupole mass filter for precursor ion selection, followed by a 2-D quadrupole ion trap which gates ions into the orthogonal reflectron TOF for mass analysis. The 2D quadrupole ion trap also acts as a collision cell.

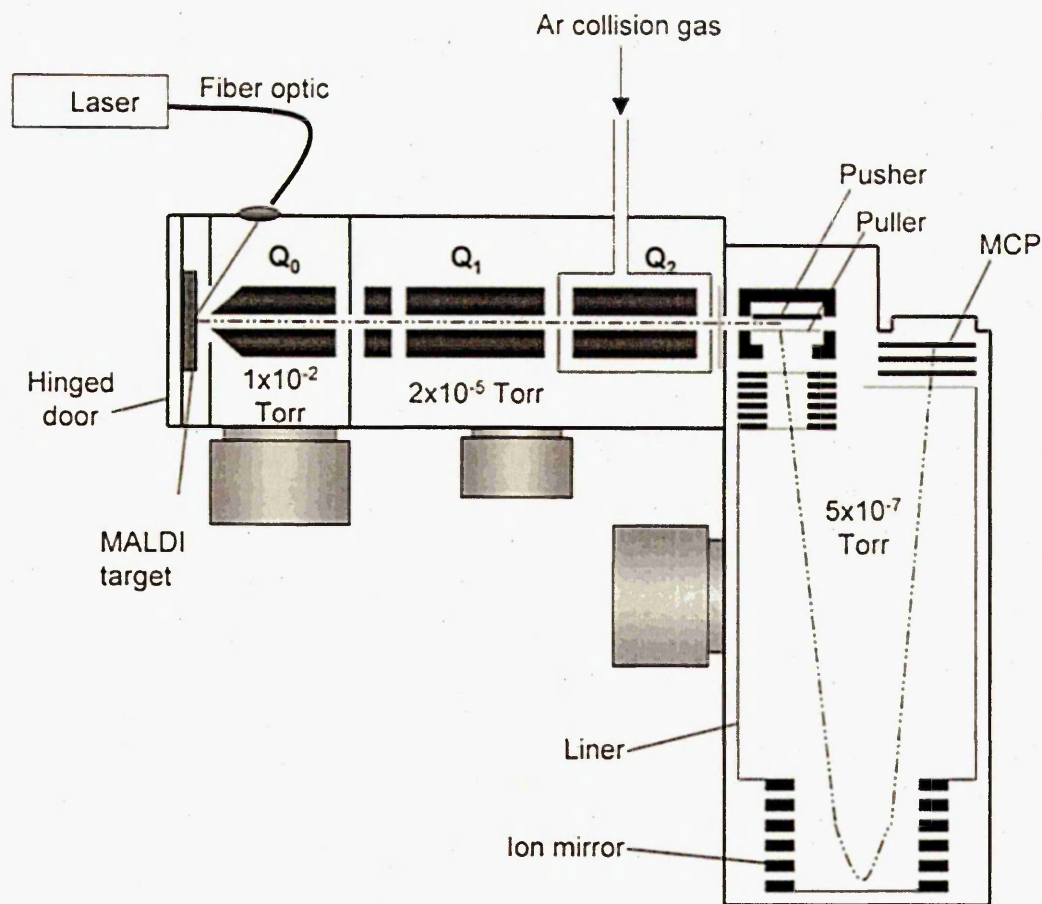


Figure 1.13 Schematic of an Applied Biosystems/MDS Sciex hybrid quadrupole time-of-flight instrument (Q-Star Pulsar-i). Adapted from Baldwin et al., 2001.

### 1.3.4.2 MALDI Synapt HDMS

A Waters “Synapt” HDMS system was used for MALDI - ion mobility separation – MSI, within this thesis (Chapters 3, 4 & 5). The Synapt HDMS system is a MALDI hybrid quadrupole/travelling wave IMS/oa-ToF instrument.

A schematic of this instrument is shown in figure 1.14.



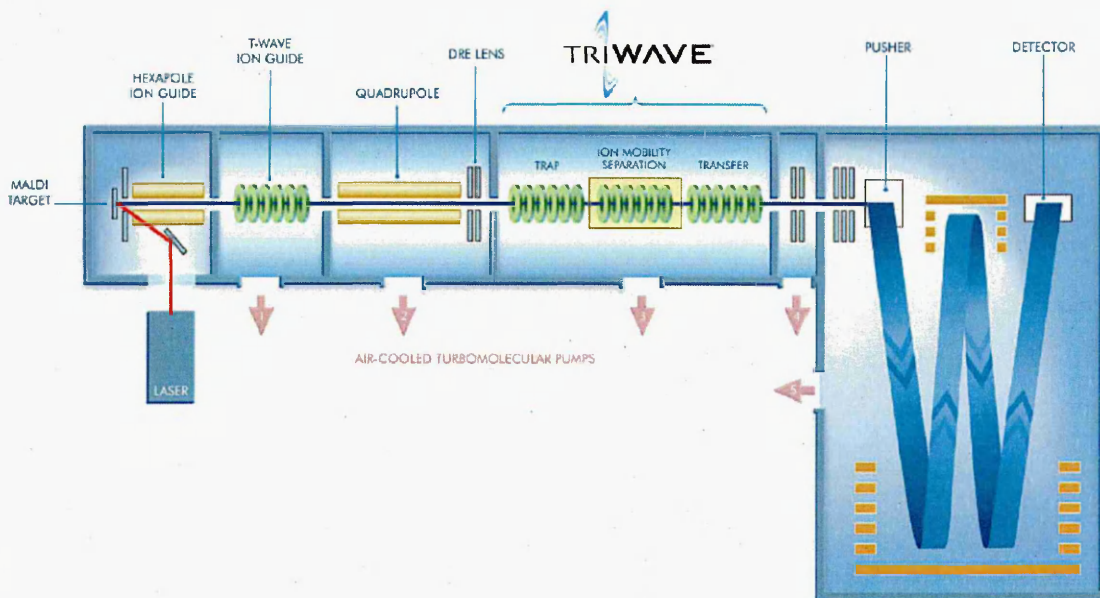


Figure 1.14 Schematic of the Synapt HDMS system (Waters Corporation, Manchester, UK) (Oppenheimer et al 2009).

Within this instrument the region of the instrument responsible for the ion mobility is the Tri-Wave region. This region comprises of three distinct parts the "Trap" acts as an ion guide and the last set of electrodes gate the ions into the travelling wave ion mobility separation (T-WAVE IMS) cell, releasing a packet of ions into the T-WAVE IMS cell which then undergo ion mobility separation (this will be covered further later in this introduction). Once the ions have been separated within the T-WAVE IMS cell they enter the "Transfer" region which is another ion guide which transfers the ions into the TOF analyser. This can be operated in "V" or "W" reflectron modes as previously described.

### 1.3.5 Ion Mobility Separation.

The addition of ion mobility separation (IMS) adds another dimension of separation to mass spectrometric analysis. Conventional mass spectrometers can only separate ions based on their mass-to-charge whereas ion mobility either separates purely on averaged collisional cross sectional area within traditional IMS drift tubes, or by their averaged collisional cross sectional area to charge within the travelling wave IMS. This additional dimension of separation has proved to be highly advantageous within mass spectrometry. The use of ion mobility itself has also markedly grown over the past decade and during 2008 there were over 50,000 stand alone ion mobility spectrometers throughout the world employed for the detection of explosives, drugs and chemical warfare agents (Kanu *et al.*, 2008). IMS and mass spectrometry complement each other very well and IMS can now be incorporated into nearly all mass spectrometers if it is desired.

There are four types of IMS used within mass spectrometry they will each be briefly discussed here, and a more in-depth discussion will be made of the travelling wave IMS, which was extensively used in the work reported in this thesis.

#### **1.3.5.1 Drift Time Ion Mobility Spectrometry (DTIMS)**

DTIMS is performed by measuring the time taken for an ion to “drift” through a drift tube which contains a buffer gas and a low electric field, in these conditions the velocity of the ion is directly proportional to the electric field and this proportionality constant is called the ion mobility constant “K” and is related to the average collisional cross section by equation 1.2.

$$K = \left( \frac{3q}{16N} \right) \left( \frac{2\pi}{kT} \right)^{\frac{1}{2}} \left( \frac{m+M}{mM} \right)^{\frac{1}{2}} \left( \frac{1}{\Omega} \right)$$

Equation 1.2 Ion mobility constant "K" equation where  $q$  is the charge on the ion,  $N$  is the number density of the buffer gas,  $k$  is Boltzmann's constant,  $T$  is the absolute temperature,  $m$  is the mass of the buffer gas,  $M$  is the mass of the ion and  $\Omega$  is average collisional cross section

There are two types of DTIMS the first of these is ambient pressure drift time ion mobility spectrometry (APIMS). Incorporation of APIMS into mass spectrometers has the advantage of high IMS resolving power but this is at the cost of a low duty cycle and reduced sensitivity. APIMS is commonly employed as a field instrument for the detection of explosives, drugs and chemical warfare agents (Kanu *et al.*, 2008).

The other type of DTIMS is reduced pressure drift time ion mobility spectrometry (RPIMS), using reduced pressure drift tubes allowed for more efficient transfer of ions from the drift tube into the mass spectrometer or vice-versa as the RPIMS can be placed before or after the mass spectrometer. This means that it can perform IMS prior to mass analysis or mass selected ion can be subjected to IMS to determine their average collisional cross section.

### 1.3.5.2 Aspiration Ion Mobility Spectrometry (IMCell)

Within an IMCell the mobility of each ion is determined by the distance it travels in the direction of the electric field before it collides with an electrode ring. This movement is orthogonal to a flow of buffer gas and hence the buffer gas deflects the ions from their flight path. Since the ions can travel both directions within the electric field this allows the IMS of both positive and negative ions simultaneously.

### **1.3.5.3 Differential Mobility Spectrometry (DMS)**

DMS utilises two electrodes, between these a dispersion voltage (DV) is applied. In one direction the electric field strength is twice the strength of the other direction but the duration of the electric field is only half the time of the other direction, and the field direction is alternated. Ions are introduced orthogonally to the field direction in a flow of buffer gas. The effect of a DV causes separation of the ions depending on their different mobility's within each field. Within the drift tube an additional voltage is then scanned on one electrode, this is the compensation voltage (CV). This CV causes ions with different mobilities to be transferred into a mass spectrometer for mass spectrometric analysis. This type of analysis has been called many different names including alternating field IMS (AFIMS), Field ion spectrometry (FIS). It is sold commercially by Thermo Scientific as high field asymmetric waveform ion mobility spectrometry (FAIMS) (Kolakowski and Mester 2007).

### **1.3.5.4 Travelling Wave Ion Mobility Spectrometry (T-WAVE IMS)**

Within a T-WAVE IMS cell a sequential series of low voltage waves propel the ions through a drift tube filled with a buffer gas and hence separate the ions based on the averaged collisional cross sectional area to charge.

Within T-WAVE IMS instruments it takes milliseconds for ions to travel along the IMS and it takes microseconds for the TOF MS analysis so the two parts can marry up together producing hundreds of TOF MS spectra for each IMS run therefore the sensitivity of the MS is not compromised by the duty cycle of the IMS.

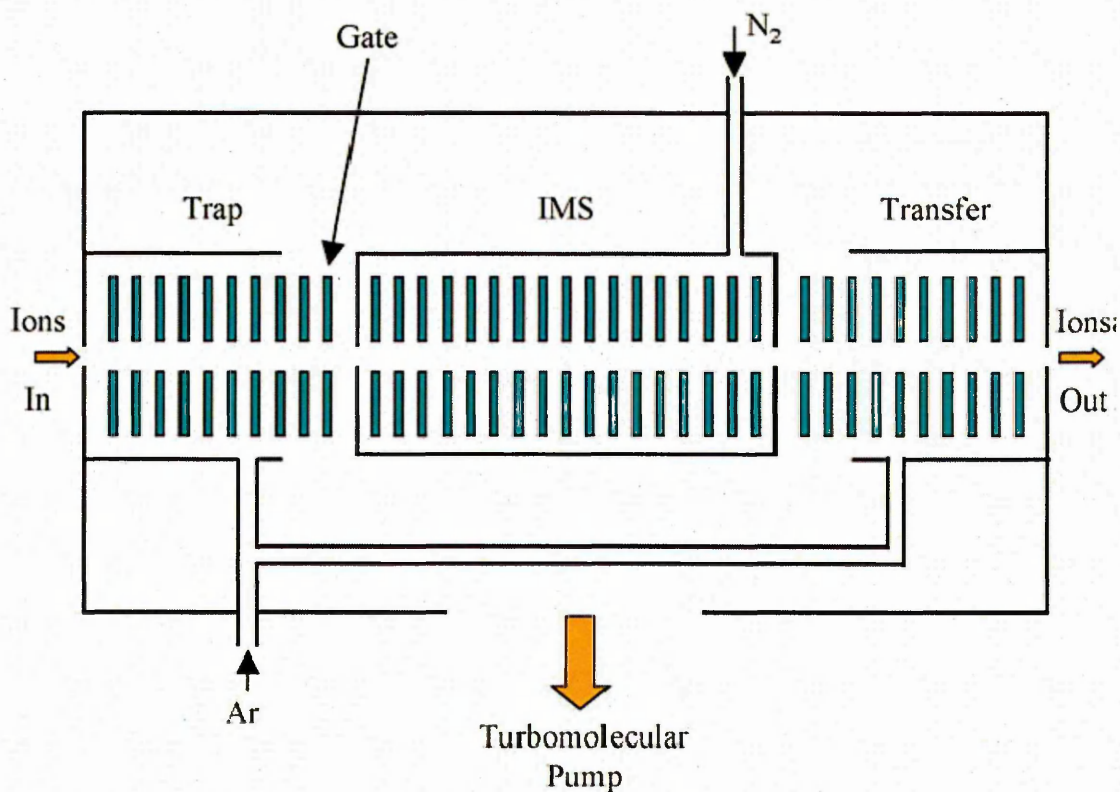


Figure 1.15 Schematic of the Tri Wave IMS cell within the Synapt HDMS (Waters, Manchester, UK) shown are the locations of the three travelling wave stacked ring ion guides (TW-SRIG). (Pringle et al., 2006)

Chapter 1

Within the T-WAVE IMS cell the electrodes are connected in repeat sections of six pairs of electrodes. Each ring electrode has two voltages applied to form the travelling wave, a radially confining RF voltage (to reduce scattering effects), and the travelling wave voltage, a third DC bias voltage can be applied for fragmentation if required this is done within the SYNAPT in the trap and transfer regions. The T-WAVE IMS cell contains 61 electrodes and has a total length of 185mm, flanked each side by the trap and transfer travelling wave ion guides (TWIG or TW-SRIG) consisting of 33 electrodes and 100mm in length. All the electrodes have 1.5mm centre to centre spacing with ion transmission apertures of 5mm and each electrode is 0.5mm thick. The T-WAVE IMS is operated with gas pressures up to 1mbar with waves of up to 25V with velocities ~300-600m/s (*Pringle et al., 2006*). These waves can be computer modelled to demonstrate how the T-WAVE IMS works. Figure 1.16a shows a computer model of the SRIG which forms the T-WAVE IMS cell. The potential gradient exists across the aperture and increases markedly near the electrode walls. Figure 1.16b shows the same SRIG animation but from a different angle showing the waves that form which the ions "surf" (*Giles et al., 2004*).

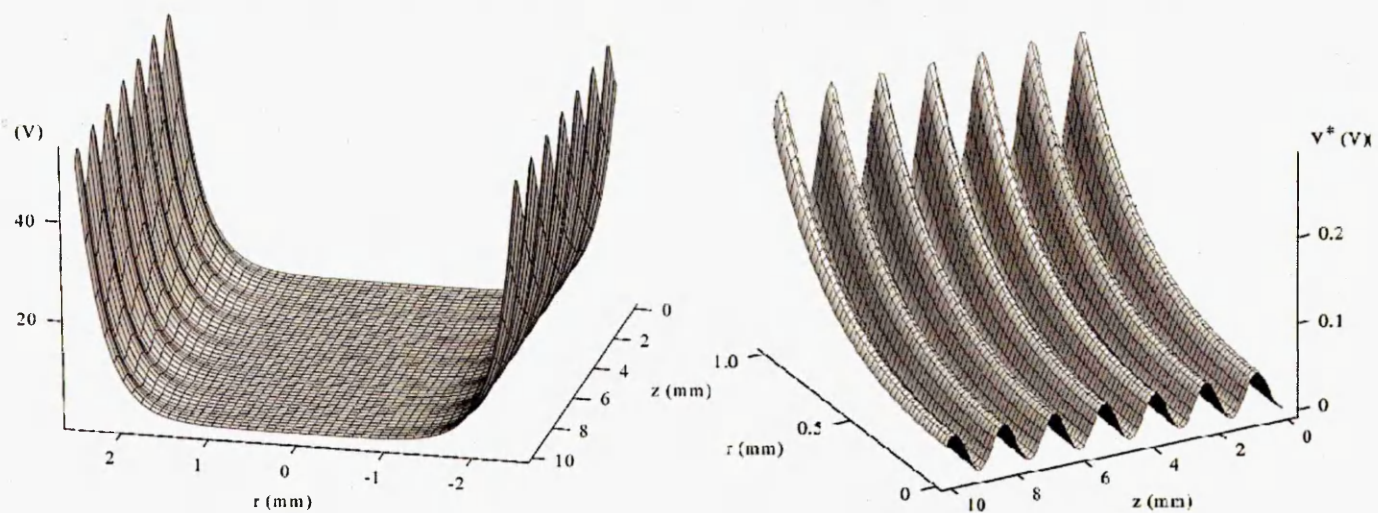


Figure 1.16 a) A computer model of the SRIG which forms the T-WAVE IMS cell. The potential gradient exists across the aperture and increases markedly near the electrode walls. b) The same SRIG animation but from a different angle showing the waves that form which the ions “surf”. (Giles et al., 2004)

Figure 1.17 Shows a series of SIMION plots demonstrating how the ions surf the travelling wave and then roll over the top of the wave and get collected by the following wave, this process is repeated numerous times. The number of times each ion rolls over the top of the wave is dependent on the wave characteristics (Height and Speed) and also on the effective drag caused by the surrounding gas. Hence the ions are separated based on their average collisional cross sectional area because all the ions experience the same wave characteristics, but the number of collisions between the ions and the background gas changes based on their average collisional cross sectional area.



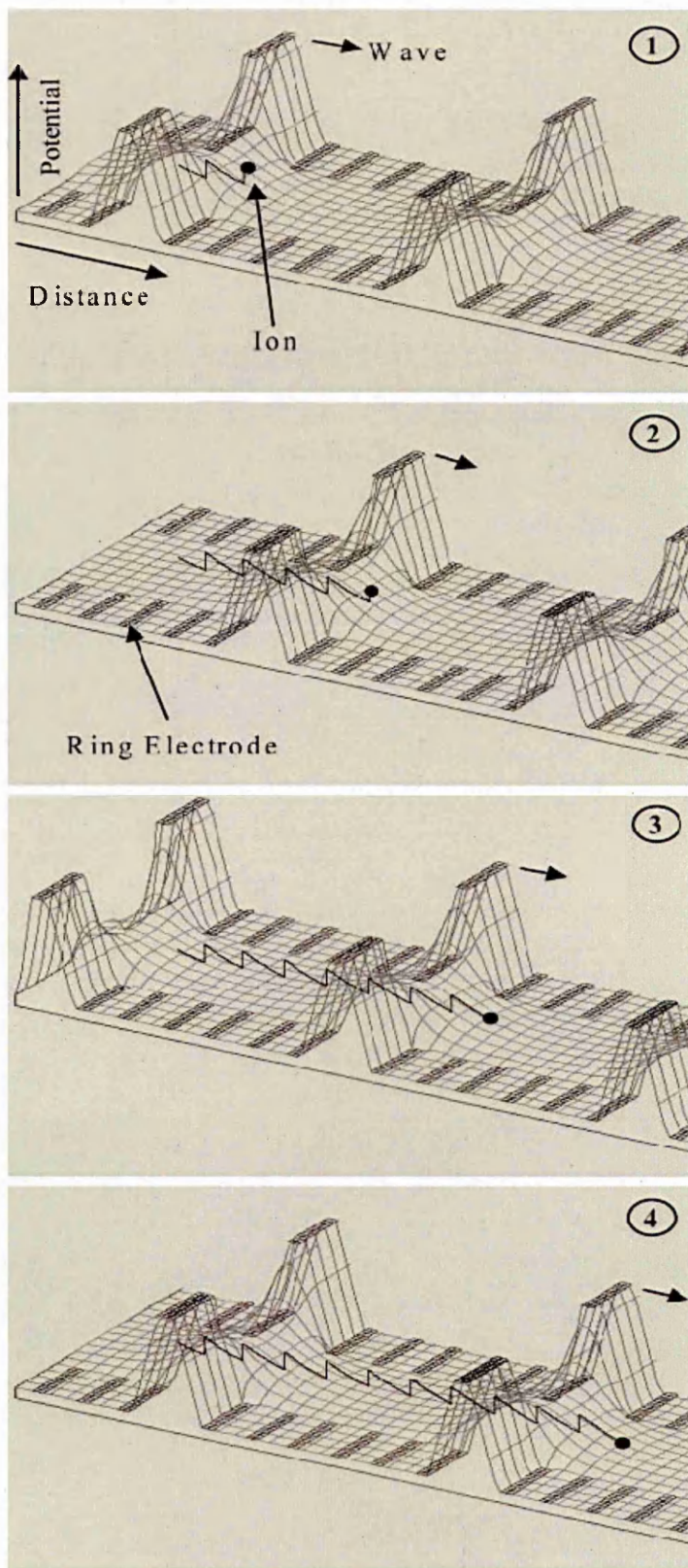


Figure 1.17 SIMION plots of the ion trajectory within the T-WAVE IMS cell showing the ion surfing the wave and then rolling over the top of the wave and being collected by the following wave. (Giles et al., 2004)



Results obtained from T-wave IMS TOF MS instruments often show trend lines, when the mobility drift time is plotted against the  $m/z$ . Classes of ions regularly follow a trend line (Jackson *et al.*, 2007), these trend lines can be due to structural differences and hence differences in the average collisional cross sections of isobaric ions. Trend lines are also formed by charge states of ions because multiply charged ions travel through the T-wave IMS faster than isobaric singly charged ions (Pringle *et al.*, 2007).

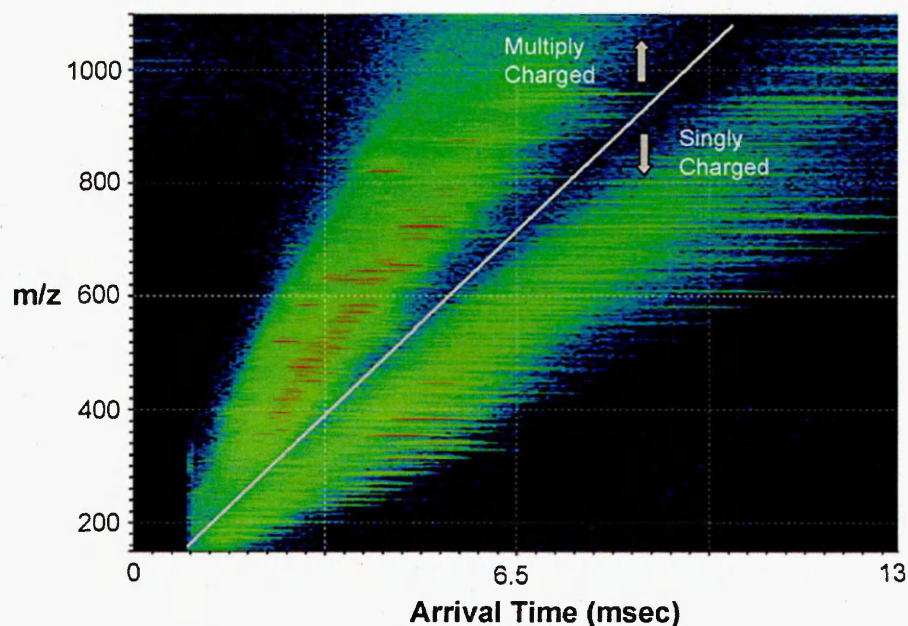


Figure 1.18 Ion Mobility separation of singly charged and multiply charged peptides. (Pringle *et al.*, 2007)

Initially T-wave IMS gave one of the lowest resolutions of IMS instruments but recent advances in the T-wave IMS which have been incorporated in the SYNAPT G2 (Waters corporation, Manchester, UK) have markedly improved the ion mobility resolution. This has been achieved within the T-Wave IMS cell by increasing the length of the cell and increasing the operating pressure

within the T-Wave IMS by using a helium filled entry cell. (www.waters.com)

This results in increased numbers of collisions between ions travelling within the cell and the buffer gas, increasing the ion mobility resolution.

#### 1.4 MALDI Introduction

Biological samples for MALDI-MSI are usually in the form of thin tissue sections. In preparation for MALDI MSI analysis these tissue sections are coated with an organic acid matrix solution. The organic acid co-crystallises with analytes on the tissue surface and in the same way as with conventional MALDI the matrix is ablated from the surface along with the associated analyte molecules by means of a pulsed laser. Matrices are chosen that absorb electromagnetic radiation at the specific wavelength of the laser e.g. a  $N_2$  laser with a wavelength of 337nm, or a frequency tripled Nd:YAG laser with a wavelength of 355nm (Demirev *et al.*, 2005).

When acquiring a mass spectrometric image using microprobe mode MALDI, the laser is fired at the sample for a pre-selected length of time at a series of predetermined points. At each x, y coordinate, a full scan mass spectrum is recorded or ms/ms if required. Images are then produced by plotting the spatial dimensions against the relative abundance of a selected ion (Prideaux *et al.*, 2007). A slight variation of this method is the use of "dynamic Pixel". Dynamic pixel moves the target plate during each acquisition within the defined spatial resolution (Simmons 2008). A further development on this method is the use of continuous raster imaging, this method markedly improves the image acquisition time. This is achieved by continuously firing the laser at the target for a complete row of the image, during which the

software collates the acquired data at known intervals depending on the spatial resolution requested and the sampling speed selected, only at the end of each row is the laser stopped and then moved to the start position of the next row.

Two of the most important steps in acquiring a MALDI-MS image are sample acquisition and preparation. Techniques employed should ensure that the spatial localisation and integrity of the analyte compounds are maintained. Schwartz *et al.*, 2003 recommended that the tissue should be surgically removed and the native shape of the tissue preserved. Once the tissue has been removed it must be snap frozen, there are a number ways to achieve this. These include, wrapping the tissue lightly in aluminium foil and slowly submerging the tissue in to liquid nitrogen (Schwartz *et al.*, 2003, Chaurand *et al.*, 2005, Reyzer and Caprioli 2005), direct tissue freezing by placing the tissue in powdered dry ice (Sugiura *et al.*, 2006), and submerging the tissue in dry ice cooled hexane (Hsieh *et al.*, 2006) for 15-30 seconds. An alternative method is to use isopentane cooled to  $-30^{\circ}\text{C}$  for 15-20 seconds (Wang *et al.*, 2005). Within the work reported here a similar technique to that of Wang *et al.*, 2005 was used, this involves liquid nitrogen cooled isopentane into which the fresh tissue is submerged for 15-20 seconds. After snap freezing the frozen tissue is stored at  $-80^{\circ}\text{C}$ . At this temperature tissue can be stored for long periods of time. It has been shown by Schwartz *et al.*, 2003 that tissue stored in this way shows no significant degradation for at least a year.

When required tissue is sectioned in a cryostat between -5 to -25°C (Schwartz *et al.*, 2003). The thickness of the tissue sections used for MALDI-MS imaging have been shown (Sugiura *et al.*, 2006) to make a significant difference to the images obtained from high molecular weight proteins. Within this work a tissue section thickness of 5µm is recommended, for ionisation and detection of high molecular weight proteins. Two main reasons have been described to explain this effect; the first is that charging effects are lower in thinner tissue sections, the second is the washing of thicker tissue sections to remove the salts and lipids which reduce the spectra quality of high molecular weight proteins is not sufficient in thicker sections. In contrast Schwartz *et al.*, 2003 state that tissue sections 10-20µm thick are optimal due to thicker sections being more robust and easier to handle.

Schwartz *et al.*, 2003 also claim that the way in which tissue sections are thaw mounted affects the spectral quality. Thaw mounting tissue by pressing a room temperature target plate onto the section and thaw mounting the tissue on the target is one method, however this leaves a residue of ice crystals on the cryostat surface possibly leaving soluble proteins behind. The method preferred by Schwartz *et al.*, 2003 is to cool the target plate down in the cryostat and then place the frozen section on the cooled target plate using an artist brush, and then warming both up which results in the section being thaw mounted without loss of any analytes.

Some applications require tissue sections to be washed to remove some of the salt and lipids from the tissue surface prior to matrix deposition. The

methodology for this step varies considerably between different experiments and this step also needs optimising for each project. When imaging proteins it has been found (Chaurand *et al.*, 2006) that the best washing step was to wash with, 70% ethanol followed by 90% ethanol: 9% glacial acetic acid: 1% deionised water (v:v:v). Whereas they had previously reported (Chaurand *et al.*, 2004) that the best method was not to wash the tissue at all but to place it in a desiccator for 1-2 hours. In lipid studies (Woods and Jackson 2006) no washing step was employed.

## 1.5 Matrices for MALDI MS

There are several matrices used for MALDI MS and each has different applications. Matrix selection is a critical parameter for imaging experiments and there are a wide selection of matrices available for this application. The three most common matrices used for imaging are  $\alpha$ CHCA, mainly for low molecular weight peptides, (Schwartz *et al.*, 2003), sinapinic acid, for higher molecular weight proteins, and DHB for lipids (Jackson *et al.*, 2007). These matrices are also used for many other applications. As well as these common matrices several groups have reported the possible benefits of combining different matrices. Laugesen and Roepstorff 2003 reported the combination of DHB and  $\alpha$ CHCA for the analysis of peptides and proteins. The use of solid ionic matrices have also recently been reported. Snovida *et al.*, 2008 have demonstrated the combination of DHB with aniline or N,N-Dimethylaniline for carbohydrate analysis. Aniline has also been combined with  $\alpha$ CHCA for a variety of applications by Calvano *et al.*, 2009.

Guo and He., 2007 have used  $\alpha$ CHCA and 9-AA (9-aminoacridine) for the analysis of various small molecules including, PCs and IPs (inositol phosphates). This was found to reduce the background noise in the experiment as well as to allow switching between polarities without further sample preparation. Kim *et al.*, 2005 have shown that the combination of  $\alpha$ CHCA with nitrilotriacetic acid also reduces the background noise of the matrix adducts. Another method for reducing the chemical noise created by  $\alpha$ CHCA matrix clusters has been demonstrated for conventional MALDI analysis by Smirnov *et al.*, 2004. Within this work the authors washed the matrix/sample co-crystallised spots with either water or ammonium salt solutions, this helps to remove the alkali matrix salts from the sample due to their higher solubility in water compared to the  $\alpha$ CHCA crystals. They also report the inclusion of monoammonium phosphate into the matrix solution which suppressed the formation of matrix clusters and improved sensitivity.

There have been many other matrices reported some of which are shown in table 1.1

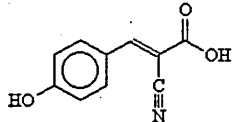
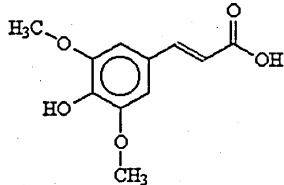
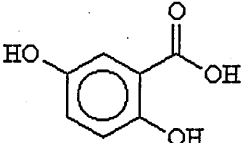
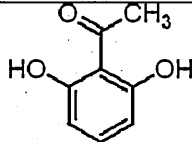
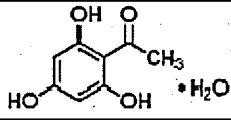
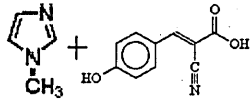
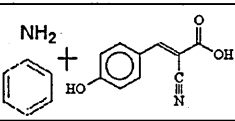
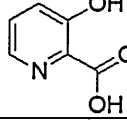
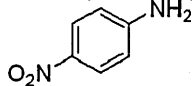
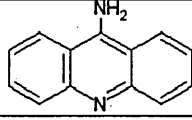
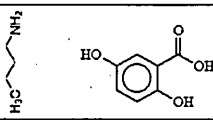
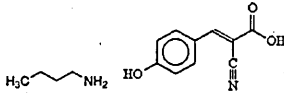
Matrix	Structure	Application	Reference
$\alpha$ CHCA		Peptides, Small Proteins and lipids	Guo and He 2007, Schwartz <i>et al.</i> , 2003
SA		Proteins, Peptides and lipids	Beavis <i>et al.</i> , 1989a, Beavis <i>et al.</i> , 1989b
DHB		Proteins, peptides and lipids	Strupat <i>et al.</i> , 1991, Jackson <i>et al.</i> , 2007
DHA		Lipids	Jackson <i>et al.</i> , 2005b
THAP		Oligonucleotides	Gyemant <i>et al.</i> , 2001
ImCHCA (1-methylimidazole-CHCA)		Gangliosides	Chan <i>et al.</i> , 2009
ANI-CHCA (Aniline-CHCA)		Amino acids, peptides, proteins, lipids.	Calvano <i>et al.</i> , 2009.
3-HPA		ssDNA oligomers, peptides and glycoproteins	Wu <i>et al.</i> , 1992, Tang <i>et al.</i> , 1994.
4-NA (4-nitroaniline)		Lipids, other small molecules	Batoy <i>et al.</i> , 2008
9-AA (9-Amino acrodine)		Lipids, other small molecules	Guo and He 2007
Graphite	C	Cerebrosides	Cha and Yeung 2007
DHBB (2,5-dihydroxy-benzoic acid butylamine)		Pullulans (polysaccharides)	Schnoll-Bitai <i>et al.</i> , 2008.
CICCA (4-chloro-alpha-cyanocinnamic acid)		Phosphatidylethanolamine Chloramines	Jaskolla <i>et al.</i> , 2009.

Table 1.1 Some matrices commonly used for MALDI-MS including their structure and an example of their applications. This is not an exhaustive list as novel matrices and matrix combinations are reported every year.

Matrix selection is also influenced by the laser type to be used. For example, when a 355nm laser is used, because of the absorption profiles of SA and DHB, poor desorption/ionisation results (Allwood *et al.*, 1996).

Matrices that are currently employed within MALDI-MS have been shown to change their absorption wavelengths when dry compared to when they are in solution. These matrices generally shift the absorption profile towards longer wavelengths when dry compared to in solution (Wu *et al.*, 1993). The absorption profile of 3-HPA has an absorption maxima at approximately 308nm and hardly absorbs at 355nm when in solution, but when 3-HPA is a dry powder it shows good absorption/ionisation performance at wavelengths between 266-355nm. Horneffer *et al.*, 1999 showed that various positional isomers of DHB nearly all showed an absorption shift towards longer wavelengths when dry compared to in solution. This shift in the absorption profiles of matrices can be very important within MALDI-MS, since generally spectrum quality increases with absorption until a level where the spectrum quality compared to absorption level out.

Matrices are chosen that absorb electromagnetic radiation at the specific wavelength of the laser and ionisation is generally thought to occur in a two stage process, firstly by a collective absorption and ablation event of the matrix and analyte, followed by an active role of the matrix in the ionisation of the analytes (Glückmann *et al.*, 2001). The desorption and ionisation events within MALDI will be further discussed later in this introduction.



## **1.6 Matrix application**

### **1.6.1 Manual spotting**

Manual spotting of matrix is not used for imaging experiments due to the low spatial resolution obtainable by manual spotting caused by analyte spreading. This technique is generally used for profiling experiments (Schwartz *et al.*, 2003, Chaurand *et al.*, 2005, Reyzer *et al.*, 2005, Chaurand *et al.*, 2004, Chaurand *et al.*, 2006, Woods and Jackson 2006). Manual spotting does tend to provide higher sensitivity compared to a matrix sprayed section. This is most likely due to the time that the analyte has to co-crystallise with the matrix. Generally with spotting experiments the drying time is much longer than spray coating, and due to the volume of matrix spotted generally the analyte can be redistributed within the spot and hence a larger area is used to form the co-crystals.

Matrix application is one of the most important stages in imaging experiments a uniform matrix coating is required for reliable imaging experiments, this can be achieved using several techniques.

### **1.6.2 Manual Spray**

Manual spray coating is probably the cheapest method available for the application of matrix for MALDI MSI. As well as being one of the cheapest methods it is also one that can give some excellent results. Hence manual spray coating is one of the preferred methods for MALDI imaging (Prideaux *et al.*, 2007, Schwartz *et al.*, 2003, Chaurand *et al.*, 2005, Reyzer *et al.*, 2005,

Hsieh *et al.*, 2006, Hsieh *et al.*, 2007, Chaurand *et al.*, 2004, Jackson *et al.*, 2007), because it forms a uniform matrix deposition. However, the results depend on the operator, and therefore, reproducibility between operators may be poor. A skilled operator can make this one of the best and most reliable methods of matrix coating. The key aspect to observe and control when manual spray coating, is the wetness of the sample. There is a fine balance between sufficiently wetting the sample, allowing for matrix and analyte co-crystallisation, and allowing sufficient time to allow this process to occur increasing the sensitivity of the technique. If the sample is too wet, analyte redistribution can occur resulting in reduced spatial resolution and the integrity of the imaging results is affected. Figure 1.19 shows a kidney section manually spray coated with  $\alpha$ CHCA. An even matrix coating can clearly be seen across the sample.



*Figure 1.19 Kidney section after manual spray coating with  $\alpha$ CHCA matrix.*

### 1.6.3 Sublimation

Sublimation as a method of matrix application has been shown (Hankin *et al.*, 2007) to be suitable for matrix deposition when imaging phospholipids in brain tissue. The benefits of matrix coating when using vacuum sublimation have been described (Jaskolla *et al.*, 2009), compared to conventional dried droplet preparations. Using scanning electron microscopy (SEM) the matrix surface after application was imaged.

The method employed (Hankin *et al.*, 2007) used dry matrix (~300mg) placed in the bottom of a flask, inside the flask a cooling finger was placed until it rested about 1 inch above the matrix. At the end of this the section to be matrix coated was placed and maintained at 15°C. The whole unit was placed under a low vacuum pressure 0.05Torr, and the base of the flask where the matrix was then slowly heated to 120°C and held at that temperature for approximately 15-20mins. This resulted in the sublimation of the matrix, giving a fine coating of matrix on the sample without the use of solvents. This completely removes the possibility of analyte redistribution. They also demonstrated that good homogeneous matrix crystallisation on a glass slide can be achieved using this method and have shown that this method can improve the signal of a glycerophosphocholine 16:0/18:0 spot on a glass slide compared to electro-sprayed matrix. Images obtained using this method has shown good correlation to stained tissue sections. Figure 1.20 shows the set up required for matrix sublimation.

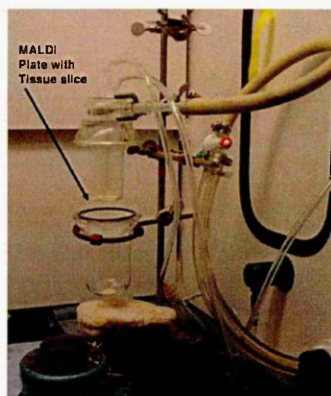


Figure 1.20 Image of the apparatus required for matrix sublimation. (Hankin et al., 2007)

#### 1.6.4 Automated Pneumatic Spraying

An example of an automated pneumatic sprayer is the SunCollect MALDI Spotter (KR Analytical Ltd) (Figure 1.21). This instrument can be operated in two modes and depending on the operation required it can be utilised as a spotting device which can spot volumes  $>10\text{nl}$  per spot, the solution is deposited via a capillary on an X, Y, Z movable arm. This can also be exchanged in a few minutes with the addition of a compressed air line into a sprayer.

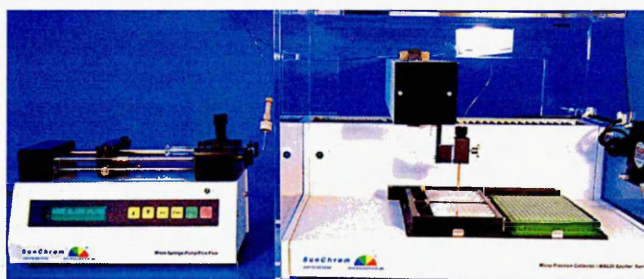


Figure 1.21 SunCollect matrix spotter/sprayer

[http://www.sunchrom.de/pdf/SunChrom%20SunCollect\\_english.pdf](http://www.sunchrom.de/pdf/SunChrom%20SunCollect_english.pdf)

The SunCollect is best suited to MALDI imaging when used as a sprayer (Wolstenholme *et al* 2009). Automated sprayers have the advantage of reproducible matrix application, with visually improved homogeneous matrix covering compared to manual spraying. Homogeneous matrix coverage is only one of the critical parts of MALDI sample preparation. Another is the time allowed for the formation of matrix analyte co-crystallisation, which is controlled by the duration of the drying time. Due to the limited drying time obtained using automated pneumatic sprayers the time allowed for analyte matrix co-crystallisation is limited, reducing the sensitivity for some analytes.

### 1.6.5 Vibrational Vapourisation

An example of matrix coating using vibrational vapourisation is the ImagePrep (Bruker Daltonics, Germany). This instrument utilises vibrational vaporisation technology to form a cloud of matrix which is left to settle on the sample surface (Kaletas *et al.*, 2009).



Figure 1.22 ImagePrep matrix applicator.

<http://www.bdal.com/uploads/media/ImagePrep-2008-eBook.pdf>

Using this technology a spatial resolution determined by the matrix crystal size formed by the droplets is  $<50\mu\text{m}$ . The average crystal size created using

this vaporisation technology is  $\sim 20\mu\text{m}$  (Kaletas *et al.*, 2009). The image prep has an optical sensor which measures the amount of light that is scattered from the matrix crystals on the sample slide. Using this method the amount of matrix deposited onto the sample can be controlled. This system also allows for monitoring of the wetness and drying rate of the matrix. During matrix application the matrix becomes wet on the surface of the sample resulting in the scattered light intensity fading, as the matrix crystals form and the matrix layer dries the amount of light scattered increases, when the matrix layer is completely dry this is a direct indication of the thickness of the matrix layer.

### **1.6.6 Acoustic Droplet Ejection.**

An example of the use of acoustic droplet ejection technology for matrix application is the Portrait 630 reagent multi spotter (Labcyte Inc. CA) (Figure 1.23) is a Matrix spotter which deposits 170pL droplets by using acoustic ejection technology ([www.labcyte.com](http://www.labcyte.com), Kaletas *et al.*, 2009). One of the major advantages of this instrument is the fact that there are no tips, nozzles or capillaries that can become blocked or add contamination to a sample. Using this technology allows the Portrait to spot any concentration of matrix. The only limiting factor is the solubility of the matrix. If it can be dissolved into solution then effectively the Portrait can spot it.



Figure 1.23 Portrait 630 multi reagent spotter.

([http://www.labcyte.com/portrait@\\_630\\_spotter/default.92.html](http://www.labcyte.com/portrait@_630_spotter/default.92.html))

The Portrait records the position of each spot within an experiment. The number of droplets per spot per cycle can be set along with the delay/drying times between each drop or cycle. Using this system allows the deposition of almost any solution and with the accurate location of each spot recorded within the method file allows for an enzyme to be printed, incubated and then the application of a MALDI matrix in exactly the same location. This prevents the possibility of analyte migration throughout a sample because the matrix is applied in discrete spots. Unfortunately this instrument is currently the most expensive available on the market, retailing at approximately £120,000 in 2009.

### **1.6.7 Ink-Jet Printers.**

An advanced ink-jet printer used for the application of matrix is the CHIP-1000 Chemical Printer (Shimadzu Corporation, Tokyo.) (Figure 1.24). This is a matrix printer which deposits 87pL droplets using a Piezo printing head (Kaletas *et al.*, 2009). The CHIP-1000 records the location of each spot and can reprint matrix and enzymes in the same location.



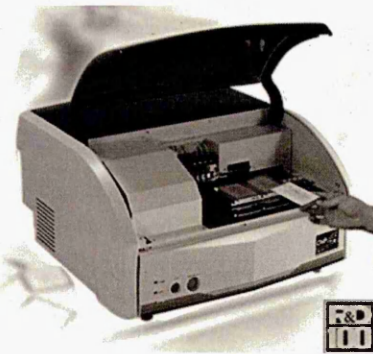


Figure 1.24 ChIP matrix printer

<http://www.shimadzu-biotech.net/pages/products/2/chip.php>

One of the major drawbacks with the CHIP-1000 is the use of a fine printer head which can block depending on the matrix concentration and the solvent used. The matrix concentration that can reliably be used is  $<10\text{mg/ml}$ .

There have also been reports of “homemade” ink-jet matrix printers (Baluya *et al.*, 2007) for MALDI matrix application. Better quality and more reproducible mass spectral images compared to electrospray and airbrush matrix application methods were obtained.

A quick reference table is shown below for some of the Matrix coating techniques.



Technique	Droplet diameter	Advantages	Disadvantages
Droplet deposition by hand	Variable, mostly large (>900 $\mu\text{m}$ )	Fast, simple, cheap	No spatial information, poor reproducibility
Pneumatic nebulization (airbrush)	Variable, mostly small (aerosols)	Fast, simple, homogenous layer, cheap	Limited environmental control, low concentrations of matrix solution can be used, quality varies from person to person, droplet size not constant
SunCollect	Variable, mostly small (aerosols)	Fast, simple, homogenous layer, cheap, removes personal variation, flow rate control.	Limited environmental control, low concentrations of matrix solution can be used, limited drying/co-crystallisation time
ChIP	$\sim 150 \mu\text{m}$ (100 $\mu\text{L}$ )	Uniform droplets, precision of placement, conditions can be controlled, automated, high signal quality, reproducible	Slow, nozzle tip clogging, expensive
Portrait 630 reagent multi-spotter	180-230 $\mu\text{m}$ (170 $\mu\text{L}$ )	Uniform droplets, precision of placement, automated, no clogging, fast, good reproducibility	Matrix applied as droplets, expensive.
ImagePrep	Variable, but small ( $\sim 20\text{-}50 \mu\text{m}$ )	Conditions can be varied and controlled, automated, homogenous layer	Slow, small area, membrane clogging, droplet size not constant, expensive
Sublimation	Very small	Cheap, very homogenous, high purity of organic matrix, reproducible, fast	Limited time for analyte-matrix interaction, only lipids detected so far

Table 1.2 Quick guide to some of the available matrix coating techniques showing some of the advantages and disadvantages. (adapted from Kaletas et al., 2009.)

## 1.7 Desorption and Ionisation in MALDI

### 1.7.1 Desorption

Desorption is the process of solid to gas phase transition. The emitted material contains few particles, droplets or clusters. However in MALDI, ablation is possibly a better description of the process, because at ablative laser fluences sample overheating and subsurface nucleation occurs leading to phase explosion (Knockenmuss 2006). The ablation process is explained

thus; when the energy density is large enough, an explosive transition from a solid phase into a gas phase occurs. This causes a "gas jet" with a large initial ion velocity and velocity spread (Karas *et al.*, 2000 & Karas *et al.*, 2003). This initial ion velocity is partially matrix dependent and to a lesser extent analyte size dependent. Peak sample temperatures achieved during laser ablation can be between 600-1200K (Knockenmuss 2006). After the initial irradiation, the desorbed/ablated material rapidly cools and then more slowly as the gas plume undergoes a dramatic density reduction from a solid phase to high vacuum conditions within the mass spectrometer. The ablated material contains particles, clusters, molecules and ions. Particles are large aggregates of molecules similar to the bulk material, whereas clusters are small aggregates of molecules which may have different properties to the bulk material. Particles may not vaporise and hence are not normally analysed within MALDI (Knockenmuss 2006).

### **1.7.2 Ion Formation in MALDI**

The ionisation process in MALDI is still not fully understood, ionisation was originally thought to be achieved purely by a proton transfer reaction, however it is now thought to be a very complex process involving several processes. It is generally accepted that not one mechanism can account for the observed signal but several mechanisms all contribute to overall ion formation and detection.

Ionisation in MALDI is generally thought to occur as a two stage process, including the desorption and primary ionisation of the sample during and

shortly following the laser irradiation (Knocknemuss 2006). This process is thought to result in the formation and ejection of particles, clusters and molecules from the sample into the surroundings (Karas *et al.*, 2000, Dreisewerd 2003, Knockenmuss 2006). This stage is followed by secondary ion-molecule thermodynamic and kinetic reactions.

One phenomenon observed in MALDI-MS is the generation of predominantly singly charged ions compared to electrospray ionisation where multiply charged ions are commonly observed. In MALDI-MS there is a slight shift towards multiply charged states for high mass analytes and with certain matrices like  $\alpha$ CHCA. This may not be a true representation of the sample because these large species can have a high kinetic energy and enhanced detection efficiency (Karas *et al.*, 2000).

An important consideration in the generation of ions within MALDI-MS is the initial starting conditions of the analytes within the matrix either as a surface preparation or as a solid solution. One paper (Karas *et al.*, 2000) has suggested possible matrix – analyte conditions within the matrix – analyte preparation which could be associated with possible ions.

$[\infty T/M_n]$

For neutral analyte in a pure uncontaminated matrix.

$[\infty T/M_n/Cat^+/B^-]$

or

$[\infty T/M_n/Me^{2+}/2B^-]$

Neutral analyte with salt contaminated matrix

$[\infty T/(M_n + xH^{x+})_n/nx B^-]$

Precharged poly-protonated analyte in matrix

$[\infty T/(M_n - xH^{x-})_n/nx Cat^+]$

Or

$[\infty T/(M_n - xH^{x-})_n/nx/2 Me^{2+}]$

Precharged poly-deprotonated analyte in matrix

$\infty T$  = Excess matrix

$M$  = Analyte

$Cat^+$  = Cation eg.  $Na^+$ ,  $K^+$  etc

$Me^{2+}$  = Doubly charged cation eg.  $Zn^{2+}$

$H$  = Proton

$B^-$  = Anion eg.  $Cl^-$

These are some of the possible matrix-analyte conditions present in the MALDI preparations. It has also been shown (Krüger *et al.*, 2001) that the

inclusion of dyes into MALDI matrix crystals did not change the charge state of the analytes supporting the theory of the incorporation of charged analytes within matrix. This report demonstrated that a small amount of the solvent is incorporated within the matrix-analyte co-crystal formation allowing the generalisation that the analytes within a matrix are in the same charge state as the analytes within the solvent. The incorporation of solvent within the matrix could also be important with charge separation by ion solvation thus reducing the possibility of ion neutralisation. Also the evaporation of this solvent from within the matrix-analyte co-crystals could explain the degradation of MALDI signal over periods of time after preparation.

The ion clusters formed during the desorption/ablation event can be highly charged species when they are formed. However, some of these clusters can rapidly evaporate in a short period of time after ablation due to the loss of neutral molecules and as a result of the formation of neutrals from reaction products within the gas plume. Some clusters can form singly charged clusters due to neutralisation in the gas plume by matrix ion interactions and trapped electrons which form during the matrix photo ionisation process, (Karas *et al.*, 2000). It has been shown that only a few nm's of the matrix lose electrons resulting in low numbers of electrons in the gas plume. In the remaining material the electrons are captured by the matrix to form matrix anions (Knochenmuss 2006).

Within the ionisation process matrix is a competitor for charge and if the functional group of the analytes is for example a carboxylic acid and a carboxylic acid matrix was used then the charge transfer would favour matrix

ion formation because of its excess. Thus reducing the signal intensity for the analyte of interest. The matrix also benefits ion formation by providing collisional energy within the gas plume. These collisions help reduce the coulomb attractions between ion pairs and without the additional collisions due to the matrix some of these ion pairs would recombine resulting in the neutralisation of these ions and hence the loss of these ion signals.

Chemical noise is present in nearly all MALDI spectra except in some situations when the analyte concentration is high and the laser fluence is low. This effect could be caused by depleting matrix ions in the gas phase by deprotonation. The same effect is true for competing analytes, where different analytes can suppress the signal from other analytes or matrix in the positive ion mode. This is the case if one or more of the analytes are strongly basic. Almost all other spectra contain chemical noise this is often composed of charged clusters with a high matrix content (Krutchinsky *et al.*, 2002).

In the preceding section, the proposed method of cluster formation and ionisation was discussed. However, another concept of ion formation is photoexcitation and energy pooling. This involves the photoexcitation of neighbouring molecules to an excited state, if the two neighbouring molecules have significant interactions due to wavefunction overlap, the energy could be redistributed between the molecules.

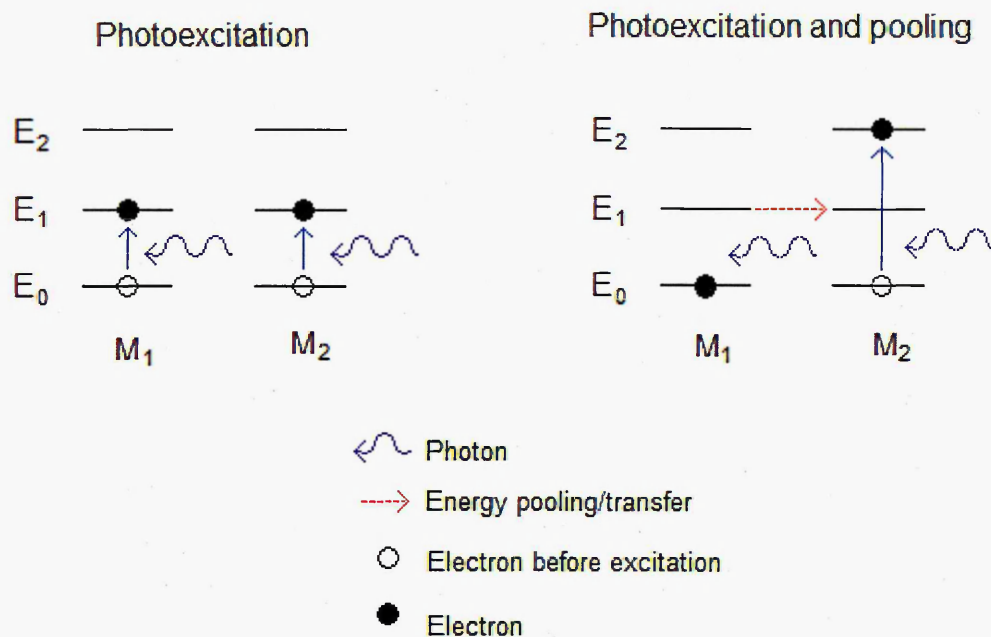


Figure 1.25 Schematic representation of photoexcitation and energy pooling.

By this energy pooling effect energy can also be mobile across the matrix with energy hopping. These events are treated as pseudo-particles called “excitons”. The time per hop of an exciton is  $\sim 50$  psec this allows ample time for energy redistribution within the 0.5-1.5 nsec excited state lifetime within MALDI (Knockenmuss 2006). Analytes with a lower excited states than the matrix can act to reduce the efficiency of MALDI.

Energy pooling and cluster generation are thought to be the two primary ionisation mechanisms in MALDI but there are several other mechanisms thought to contribute to MALDI imaging. These include direct multi-photon ionisation of matrix or matrix-analyte complexes, excited state proton transfer (Breuker *et al.*, 2003), polar fluid model, pneumatic assistance, and electron transfer and cationisation (Knockenmuss 2006).

During the secondary reaction processes in the gas phase collisions of analytes with matrix ions and neutrals and matrix-matrix collisions result in the formation of many of the commonly observed ions eg.  $M^+$ ,  $MH^+$ ,  $MNa^+$ ,  $A^+$ ,  $AH^+$ ,  $ANa^+$  etc.

## **1.8 Scope of this thesis.**

There are two areas of small molecule MALDI-imaging that are covered within this thesis, these are lipid imaging and small molecule xenobiotic imaging.

### **1.8.1 Imaging lipids**

Lipids can perform both structural and functional roles within the body and are known to be important mediators of cell signalling, acting as second messengers in cellular events such as cell growth, cellular proliferation and cell death. Alterations in lipid metabolism are associated with many disorders and disease states throughout the body. Therefore the study of lipid distribution and abundance is an important area of research (Woods and Jackson 2006, Jackson *et al.*, 2007, Adibhatia *et al.*, 2006, Jackson *et al.*, 2005, Fahy *et al.*, 2005). One of the most lipid rich organs is the brain. In the brain lipids account for approximately 50% dry weight, deregulation in lipid metabolism in the brain is commonly associated with many brain disorders and diseases including, bi-polar disorders, schizophrenia, Alzheimer's, Parkinson's and Niemann-Pick diseases (Adibhatia *et al.*, 2006).



Woods and Jackson (Woods and Jackson 2006) demonstrated how the relative abundance of lipids within different areas of the brain can change. They demonstrated that PC 32:0 has a different distribution between the cerebellar cortex and cerebellar peduncle, and that different classes of lipids can be observed using positive and negative ion mode MALDI. Within this work DHA was used as the matrix. This work follows on from earlier studies (Jackson *et al.*, 2005a) in which they showed the relative abundance of various different lipid species in white and grey brain matter. Stubiger and Belgacem (Stubiger and Belgacem 2007), demonstrated the use of a novel matrix for lipid analysis using MALDI-MS. Within this work 2,4,6-Trihydroxyacetophenone (THAP) was used, and it was shown that this matrix was very good for lipid profiling. They also demonstrated that the THAP tolerates high salt concentration and shows excellent cationisation properties. This is beneficial because the addition of salt has been shown to reduce the spectral complexity in complicated mixtures of lipids. MALDI-ion mobility-TOFMS imaging of lipids has been reported (Jackson *et al.*, 2007). It was shown that lipids, peptides and matrix related ions tend to form individual trend lines when plotted as mobility drift time against  $m/z$ . DHB clusters have a shorter drift time followed by peptides and finally lipids. In this study it was shown that peptides were consistently around 12% slower in drift time, than isobaric lipids. This technology is highly beneficial in imaging applications because it allows for the separation of isobaric ions resulting in image generation of an ion of interest without interference from isobaric matrix ions.

A high proportion of the published lipid analysis work involving MALDI, lipid species are reported using simple nomenclature i.e. PC 32:0 or PC 36:2. This nomenclature gives the basic information about the lipid species. PC 36:2 states that this is a phosphatidylcholine lipid with fatty acids totalling 36 carbons and 2 double bonds. There are several possible lipid species which could equal PC 36:2 including PC 18:0/18:2 or PC 18:1/18:1. Using MALDI these can sometimes be difficult to tell apart due to limited MS and MS/MS information in positive ion mode for the M+H ions. It has been shown (Jackson *et al.*, 2005b) that the addition of alkali metals to the matrix can aid in the fragmentation and formation of informative ion species within MALDI MS/MS analysis. The doping of the matrices is commonly performed using Na, K or Li as alkali metals to aid in the formation and fragmentation of these adducts (Jackson *et al.*, 2005b). An alternative method is the use of enzymes. Phospholipase A2 (PLA2) is an enzyme that selectively cleaves the fatty acid at the Sn2 position of glycerophospholipid prior to mass analysis, this allows the identification of the fatty acid chains by their mass differences and the location of each chain (Fuchs & Schiller 2008).

### **1.8.2 Imaging Xenobiotic compounds**

A major area for the application of MALDI-MS imaging is imaging xenobiotics, drugs and metabolites. It has been shown (Prideaux *et al.*, 2006) that indirect MALDI imaging of xenobiotic compounds in skin can be achieved by blotting the tissue onto solvent soaked cellulose membrane, followed by spray coating the membrane with matrix instead of using tissue sections. This work concluded that the use of solvents in the blotting method can increase analyte

extraction by up to 80 fold, however, this technique can lead to analyte redistribution.

In other reports, the distribution of clozapine in rat brain tissue has been reported (Hsieh *et al* 2007). The autoradiographic images and the MALDI-MS/MS images were in almost complete agreement demonstrating the huge potential for this technique for drug and metabolite studies. However, drug distribution studies by MALDI-MSI are in an early stage and the continual advancement of instrumentation, matrices and methodologies will continue to increase the sensitivity and specificity of this technique.

## **1.9 Aims of this project.**

The aims of this PhD Project can be summarised as follows.

1. To assess the use of MALDI imaging for the identification and spatial distribution analysis of endogenous small molecules, including the use of statistical analysis to identify differences within histologically different tissues. Demonstrate the benefit of PCA statistical analysis for the reduction in the complexity of the data obtained within MALDI imaging, allowing the rapid identification of possible ions of interest.
2. To investigate the use of MALDI imaging for the direct analysis of xenobiotics within tissue sections. Further expand MALDI imaging into whole body tissue section analysis and combine new advances in MALDI MSI with the incorporation of a further separation step of ion

mobility. Using this technique to demonstrate the potential for this technology to improve the drug discovery process by eliminating the need for the synthesis of expensive radiolabelled compounds for distribution analysis and also reduce the number of animals required in this process.

## 1.10 References

Adibhatia R.M; Hatcher J.F; Dempsey R.J. The AAPS Journal 2006, 8 (2) Article 36.

Allwood D. A; Dreyfus R. W; Perera I. K; Dyer P. E. **1996**, Rapid Commun. Mass Spectrom. 10, 1575-1578.

Ashburn T.T; Thor K.B. **2004**, Nature Reviews, Drug Discovery. 3, 673 – 683.

Baldwin M. A; Medzihradzky K. F; Lock C. M; Fisher B; Settineri T. A; Burlingame A. L. **2001**, Anal. Chem. 73, 1707-1720.

Baluya D. L; Garrett T. J; Yost R. A; **2007**, Anal. Chem. 79, 17, 6862-6867.

Batoy S. M. A. B; Akhmetova E; Miladinovic S; Smeal J; Wilkins C. L. **2008**, Applied Spectroscopy Reviews. 43, 485-550.

Beaudry F; Ferland C.E; Vachon P. **2009**, Biomedical Chromatography, 23, 9, 940-950.

Beavis R. C; Chait B. T; Fales H. M. **1989a**, Rapid Comm. Mass Spectrom. 3, 12, 432-435.

Beavis R. C; Chait B. T; Standing K. G.. **1989b**, Rapid Comm. Mass Spectrom. 3, 12, 436-439.

Benazouz M; Hakim B; Deburn J.L; Strivay D; Weber G. **1999**, Rapid Commun. Mass Spectrom. 13, 23, 2302-2304.

Bereman M.S; Lyndon M.M; Dixon R.B; Muddiman D.C. **2008**, Rapid Commun. Mass Spectrom. 22, 10, 1563-1566.

Berkenkamp S; Menzel C; Karas M; Hillenkamp F. **1997**, Rapid Commun. Mass Spectrom. 11, 26.

Breuker K; Knochenmuss R; Zhang J; Stortelder A; Zenobi R. **2003**, Int. J. Mass Spectrom. 226, 211-222.

Calvano C. D; Carulli S; Palmisano F. **2009**, Rapid Commun. Mass Spectrom. 23, 1659-1668.

Caprioli R.M; Farmer T.B; Gile J. **1997**, Analytical Chemistry. 69,4751-4760.

Castner D. G. **2003**, Nature. 422, 129-130.

Cha S; Yeung E. S. **2007**, Anal. Chem. 79, 2373-2385.

Chan K; Lanthier P; Liu X; Sandhu J.K; Stanimirovic D; Li J. **2009**, Analytica Chmica Acta. 639, 57-61.

Chaurand P; Norris J.L; Cornett S; Mobley J.A; Caprioli R.M. **2006**, Journal of proteome research. 5, 11, 2889-2900.

Chaurand P; Schwartz S.A; Caprioli R.M. **2004**, Journal of proteome research. 3, 2, 245-252.

Chaurand P; Schwartz S.A; Reyzer M.L; Caprioli R.M. **2005**, Toxicologic Pathology, 33: 92-101

Coe R.A.J. **2000**, Regul. Toxicol. Pharmacol. 31, S1-S3.

Cooper L; Rennie E.E; Shpinkova L.G; Holland D.M.P; Shaw D.S. **2002**, Int. J. Mass Spectrom. 220, 3, 359-374.

Demirev P; Westman A; Reimann C.T; Hakansson P; Barofsky D; Sundqvist B.U.R; Cheng Y.D; Seibt W; Siegbahn K. **2005**, Rapid Communications in Mass Spectrometry 6, 187-191.

Dreisewerd K. **2003**, Chem. Rev. 103, 395-425.

Eijkel G. B; Kaletas B. K; Van Der Wiel I. M; Kros J. M; Luidert T. M; Heeren R. M. A. **2009**, Surf. Interface Anal. 41, 675-685.

Fahy E; Subramaniam S; Brown H.A; Glass C.K; Merrill A.H Jr; Murphy R.C; Raetz C.R.H; Russell D.W; Seyama Y; Shaw W; Shimizu T; Spener F; Meer G; VanNieuwenhze M.S; White S.H; Witztum J.L; Dennis E.A. **2005**, Journal of Lipid Research. 46, 839-862.

Falkner J. A; Kachman M; Veine D. M; Walker A; Strahler J.R; Andrews P.C. **2007**, J Am Soc Mass Spectrom. 188, 5, 850-855.

Franzen J. **1997**, Int. J. mass Spectrom. Ion Process. 164, 19-34.

Fuchs B; Schiller J. **2008**, Eur. J. Lipid Sci. Technol. 111, 1, 83-98.

Gaskell S.J. **1997**, J. Mass Spectrom. 32, 677-688.

Giles K; Pringle S. D; Worthington K. R; Little D; Wildgoose J. L; Bateman R. H. **2004**, Rapid Commun. Mass Spectrom. 18, 2401-2414.

Glückmann M; Pfenninger A; Krüger R; Thierolf M; Karas M; Horneffer V; Hillenkamp F; Strupat K. **2001**, Int. J. Mass Spectrom. 210/211, 121-132.

Guo Z; He L. **2007**, Anal. Bioanal. Chem. 387, 1939-1944.

Gyemant G; Toth A; Bajza I; Kandra L; Liptak A. **2001**, Carbohydrate research, 334, 4 315-322.

Hankin J.A; Barkley R.M; Murphy R.C. **2007**, J Am Soc Mass Spectrom, 18, 1646-1652.

Heeren R. M. A; Kukrer-Kaletas B; Taban I. M; MacAleese L; McDonnell L. A. **2008**, Applied Surface Science, 255, 1289-1297.

Hinshelwood J; Spencer D. I. R; Edwards Y. J. K; Perkins S.J. **1999**, J. Mol. Bio. 294, 2, 587-599.

Hsieh Y; Casale R; Fukuda E; Chen J; Knemeyer I; Wingate J; Morrison R; Korfmacher W. **2006**, Rapid Commun. Mass Spectrom. 20, 965-972.

Hsieh Y; Chen J; Korfmacher W.A. **2007**, Journal of Pharmacological and Toxicological Methods, 55, 2, 193-200.

Huang F; Fan X; Murry K.K. **2008**, Int. J. Mass Spectrom. 274, 21-24.

Irungu J; Go E. P; Zhang Y; Dalpathado D.S; Liao H-X; Haynes B.F; Desaire H. **2008**, J Am Soc Mass Spectrom. 19, 8, 1209-1220.

Jaskolla T. W; Karas M; Roth U; Steinert K; Menzel C; Reihs K. **2009**, J. Am. Soc. Mass Spectrom. 20, 1104-1114.

Jackson S. N; Ugarov M; Egan T; Post J.D; Langlais D; Schultz J.A; Woods A.S. **2007**, J. Mass Spectrom. 42, 1093-1098

Jackson S. N; Wang HY.J; Woods S. A. **2005a**, Anal. Chem. 77, 4523-4527.

Jackson S. N; Wang H-Y. J; Woods S. A. **2005b**, J. Am. Soc. Mass Spectrom. 16, 2052-2056.

Jaskolla T; Fuchs B; Karas M; Schiller J. **2009**, J. Am. Soc. Mass Spectrom. 20, 867-874.

Kanu A.B; Dwivedi P; Tam M; Matz L; Hill Jr.H.H. **2008**, J. Mass Spectrom. 43, 1-22.

Karas M; Bachmann D; Hillenkamp F. **1985**, Anal. Chem. 57, 2935-2939.

Karas M; Bahr U; Fournier I; Glückmann M; Pfennenger A. **2003** Int. J. Mass Spectrom. 226, 239-248.

Karas M; Glückmann M; Schäfer **2000**, J Mass Spectrom, 35, 1-12

Kertesz V; Van Berkel G. J; Vavrek M; Koeplinger K. A; Schneider B. B; Covey T. R. **2008**, Anal. Chem. 80, 5168-5177.

Kim J-S; Kim J-I; Kim H-J. **2005**, Anal. Chem. 77, 7483-7488.

Klerk L. A; Altelaar A.F.M; Froesch M; McDonnell L.A; Heeren R. M. A. **2009**, Int. J. Mass Spectrom. 285, 19-25.

Knochenmuss R. **2006**, Analyst 131, 966-986

Kolakowski B. M; Mester Z. **2007**, Analyst, 132, 842-864.

Krutchinsky A. N; Chait B. T. **2002**, J. Am. Soc. Mass Spectrom. 13, 2, 129-134.

Kukrer-Kaletas B; Van Der Wiel I. M; Stauber J; Dekker L. J; Guzel C; Kros J. M; Luidert T. M; Heeren R. M. A. **2009**, Proteomics, 9, 2622-2633.

Laugesen S; Roepstorff P. **2003**, J. Am. Soc. Mass Spectrom. 14, 992-1002.

Lindsay M.A. **2003**, Nature Reviews Drug Discovery, 2, 831-838.

Luxembourg S. L; Mize T. H; McDonnell L. A; Heeren R. M. A. **2004**, Anal. Chem. 76, 5339-5344.

Maas J; Binder R; Steinke W. **2000**, Regul. Toxicol. Pharmacol. 31, S15-S21.



Monroe E. B; Annangudi S. P; Hatcher N. G; Gutstein H. B; Rubakhin S. S; Sweedler J. V. **2008**, Proteomics 8, 18, 3746-3754.

Morris H. R; Paxton T; Panico M; McDowell R; Dell A. **1997**, J. Protein Chem. 16, 5, 469-479.

Ng R. **2004**, Drugs From Discovery to Approval. John Wiley and Sons Inc

Oakes K; Hart P. J; Cole L; Trim P. J; Djidja M-C; Anderson D. M; Francese S; Clench M. R. **2009**, International Mass Spectrometry Conference, Bremen, PMM:251

Oppenheimer S. R; Claude E, Bahrainwala T. **2009**, Waters Application Note, 720003216en.

Overberg A; Karas M; Bahr U; Kaufmann R; Hillenkamp F. **1990**, Rapid Commun. Mass Spectrom, 4, 293-296.

Overberg A; Karas M; Hillenkamp F. **1991**, Rapid Commun. Mass Spectrom, 5, 128-131.

Postle A.D; Wilton D.C; Hunt A.N; Attard G.S. **2007**, Progress in Lipid Research. 46, 200-224.

Potchoiba M. J; Nocerini M. R. **2004**, Drug Metabolism and Desorption, 32, 10, 1190-1198.

Potchoiba M. J; West M; Nocerini M. R. **1997**, Drug Metabolism and Desorption, 26, 3, 272-277.

Prideaux B; Atkinson S.J; Carolan V.A; Morton J; Clench M.R. **2007**, Int. J. Mass Spectrom. 260,243-251.

Pringle S. D; Giles K; Wildgoose J. L; Williams J. P; Slade S. E; Thalassinou K; Bateman R. H; Bowers M. T; Scrivens J. H. **2007**, Int. J. Mass Spectrom. 261, 1, 1-12.

Reyzer M.L; Caprioli R.M. **2005**, Journal of Proteome Research, 4, 1138-1142.

Ricaurte G. A; DeLanney L. E; Irwin I; Langston J. W; **1988**, Brain Res. 446, 1, 165-168.

Ross S.K; Bell A.J. **2002**, Int. J. Mass Spectrom. 218, L1-L6.

Sams-Dodd F. **2005**, Drug Discovery Today. 10, 2, 139-147.

Schnoll-Bitai I; Ullmer R; Hrebicek T; Rizzi A; Lacik I. **2008**, Rapid Commun. Mass Spectrom. 22, 2961-2970.

Schwartz S.A; Reyzer M.L; Caprioli R.M. **2003**, J. Mass Spectrom. 38, 699-708.

Simmons D. A. **2008**, ABI Technical Note, improved MALDI-MS imaging performance using continuous laser rastering.

Smirnov I. P; Zhu X; Taylor T; Huang Y; Ross P; Papayanopoulos I. A; Martin S. A; Pappin D. J. **2004**, Anal. Chem. 76, 2958-2965.

Snovida S. I; Rak-Banville J.M; Perreault H. **2008**, J. Am. Soc. Mass Spectrom. 19, 1138-1146.

Solon E. G; Kraus L. **2002**, Journal of Pharmacological and Toxicological Methods. 46, 73-81.

Solon E. G; Lee F. **2002**, Journal of Pharmacological and Toxicological Methods. 46, 83-91.

Stoekli M; Knochenmuss R; McCombie G; Mueller D; Rohner T; Staab D; Wiederhold KH. **2006**, Methods in Enzymeology 412, 94-106.

Stoekli M; Staab D; Staufenbiel M; Wiederhold KH; Signor L. **2002**, Analytical Biochemistry 311, 33-39.

Strupat K; Karas M; Hillenkamp F. **1991**, Int. J. Mass Spectrom. Ion Process. 111, 89-102.

Stübiger G; Belgacem O. **2007**, Anal. Chem 79, 3206-3213

Sugiura Y; Shimma S; Setou M. **2006**, J Mass Spectrom. Soc. Jpn. 54, 2, 45-48.

Sugiura Y; Setou M. **2009**, J. Neuroimmune Pharmacol. In Press, DOI 10.1007/s11481-009-9162-6

Su A-K; Lin C-H. **2006**, *Talanta*, 68, 673-678.

Takats Z; Wiseman J. M; Cooks R.G. **2005**, *J. Mass Spectrom.* 40, 1261-1275.

Takats Z; Wiseman J. M; Gologan B; Cooks R.G. **2004**, *Science*. 306, 471-473.

Tanaka K. **1988**, *Rapid Communications in Mass Spectrometry*. 2,151-153.

Tang K; Taranenko N. I; Allman S. L; Chang L. Y; Chen C. H; Lubman D. M. **1994**, *Rapid Comm. Mass Spectrom.* 8, 9, 727-730.

Tojo K; Ishigaki N; Kadoya A; Watanabe K; Ido Y. **2008**, *Advanced Solid-State Photonics*, Poster Presentation, WE35.

Trim P.J; Henson C.M; Avery J.L; McEwen A; Snel M.F; Claude E; Marshall P.S; West A; Princivalle A.P; Clench M.R. **2008**, *Anal. Chem.* 80, 8628-8634.

Ulberg S. **1954**, *Acta Radiol. Suppl.* 118, 1-110.

Wang H.Y.J; Jackson S.N; McEuen J; Woods A.S. **2005**, *Anal. Chem.* 77, 6682-6686.

Wiseman J. M; Ifa D. R; Song Q; Cooks R. G. **2006**, *Angew. Chem. Int. Ed.* 45, 7188-7192.

Wolstenholme R; Bradshaw R; Clench M. R; Francese S. **2009**, *Rapid Commun. Mass Spectrom.* 23, 3031-3039.

Woods A.S; Jackson S.N. **2006**, *The AAPS Journal* 8, (2), 44, 391-395

Wu K. J; Steding A; Becker C. H. **1992**, *Rapid Comm. Mass Spectrom.* 7, 2, 142-146.

[www.chm.bris.ac.uk](http://www.chm.bris.ac.uk)

[www.sunchrom.de/pdf/SunChrom%20SunCollect\\_english.pdf](http://www.sunchrom.de/pdf/SunChrom%20SunCollect_english.pdf)

[www.bdal.com/uploads/media/ImagePrep-2008-eBook.pdf](http://www.bdal.com/uploads/media/ImagePrep-2008-eBook.pdf)

www.labcyte.com/portrait®\_630\_spotter/default.92.html

www.shimadzu-biotech.net/pages/products/2/chip.php

www.waters.com

Zheng L; McQuaw C. M; Baker M. J; Lockyer N. P; Vickerman J. C; Ewing A. G; Winograd N. **2008**, Applied Surface Science. 255, 1190-1192.

Zhang Z; Zhu M; Tang W. **2009**, Current Pharmaceutical Design, 15, 2220-2235.

## CHAPTER 2

---

**MALDI-MS Imaging of Lipids in Rat  
Brain Tissue with Integrated  
Unsupervised and “Supervised”  
Multivariate Statistical Analysis.**

# MALDI-MS Imaging of Lipids in Rat Brain Tissue with Integrated Unsupervised and “Supervised” Multivariate Statistical Analysis.

## 2.1 Introduction

### 2.1.1 Lipids

Lipids can perform both structural and functional roles within the body and are known to be important mediators of cell signalling, acting as second messengers in cellular events such as cell growth, cellular proliferation and cell death. An alteration in lipid metabolism is a factor associated with many disorders and disease states throughout the body, therefore the study of lipid distribution and abundance is an important area of research. Adibhatla *et al.*, 2006 have presented work on the role of lipids and Lipidomics in brain injury and disease. Lipid analysis can experimentally observe ~100 molecular species within a given class of glycerophospholipids from crude tissue extracts. There are estimated 300 – 400 distinct species of sphingolipids within human tissue. Mammalian cells may contain ~1000 – 2000 lipid species overall.

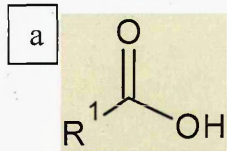
The main topic covered by Adibhatla *et al.*, 2006 involves an overview of the roll of lipids in cerebral ischemia (stroke). They describe the significant loss of phosphatidylcholine (PC) in the brain of stroke model animals. In brain tissue, PC synthesis is predominantly via the cytidine-5'-diphosphocholine pathway. Inhibition of this pathway by the inactivation of cytidyltransferase causes cell

death. Lipid peroxidation has been shown to occur early in the pathogenesis of Alzheimer's disease. By products of lipid peroxidation include acrolein which is a very strong electrophile, which reacts with DNA bases. The resulting changes to the DNA bases can result in mutagenesis and carcinogenesis.

Jackson *et al.*, 2007 published work using ion mobility MALDI for the detection and separation of lipids in brain tissue, using this technique they were able to separate the ions associated with lipids from similar or isobaric ions associated with peptides and DHB matrix related ions, they have also demonstrated the use of gold nanoparticles as a possible matrix for the detection and imaging of cerebroside. One of the most lipid rich organs is the brain, lipids account for approximately 50% dry weight of the brain, deregulation in lipid metabolism in the brain is commonly associated with many brain disorders and diseases including, bi-polar disorders, schizophrenia and Alzheimer's, Parkinson's and Niemann-Pick diseases (Adibhatla *et al.*, 2006).

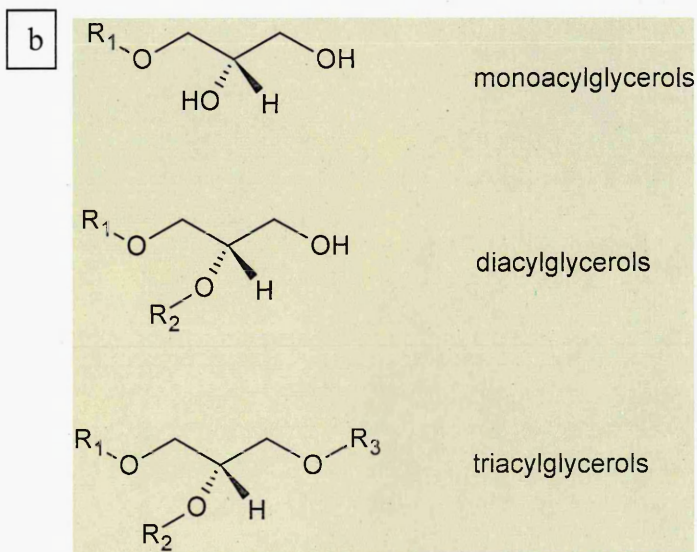
Fahy *et al.*, 2005 have presented a comprehensive classification system and nomenclature for lipids. They define lipids as *"hydrophobic or amphipathic small molecules that may originate entirely or in part by carbanion-based condensations of thioesters and/or by carbocation-based condensations of isoprene units."* using this system of classification most lipids can be sub-classified into 8 categories, fatty acyls, glycerolipids, glycerophospholipids, sphingolipids, sterol lipids, prenol lipids, saccharolipids and polyketides.

## Fatty Acyls



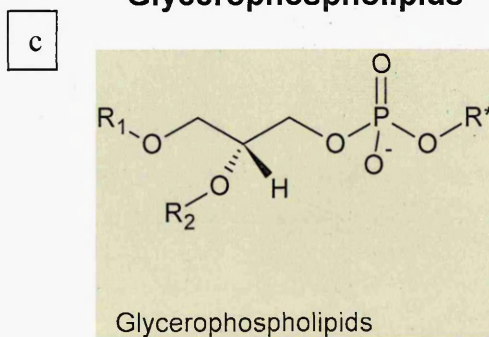
R<sup>1</sup> = carbonyl chain

## Glycerolipids



R<sup>1</sup>, R<sup>2</sup> and R<sup>3</sup> = acyl chains

## Glycerophospholipids

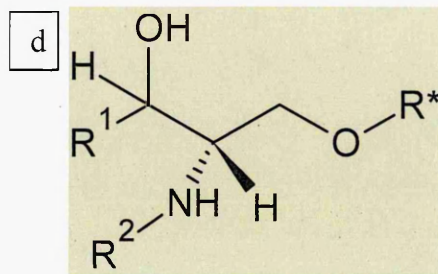


R<sup>1</sup>, R<sup>2</sup> = acyl chains

R\* = Sub class



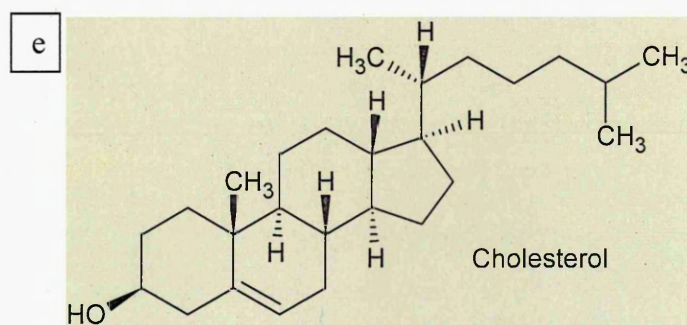
## Spingolipids



$R^1, R^2$  = carbonyl chains

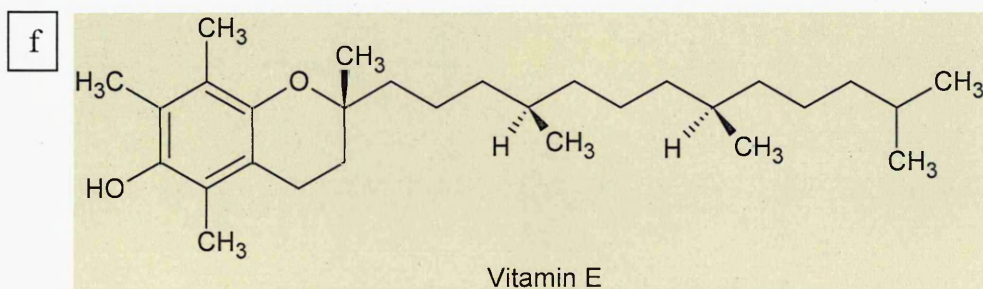
$R^*$  = group denoting sub group

## Sterol lipids



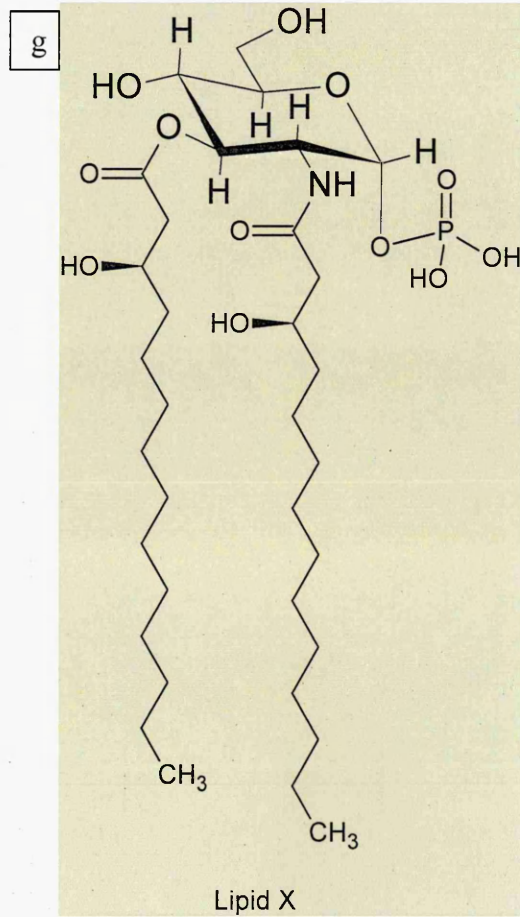
Cholesterol is an example of a sterol lipid

## Prenol lipids



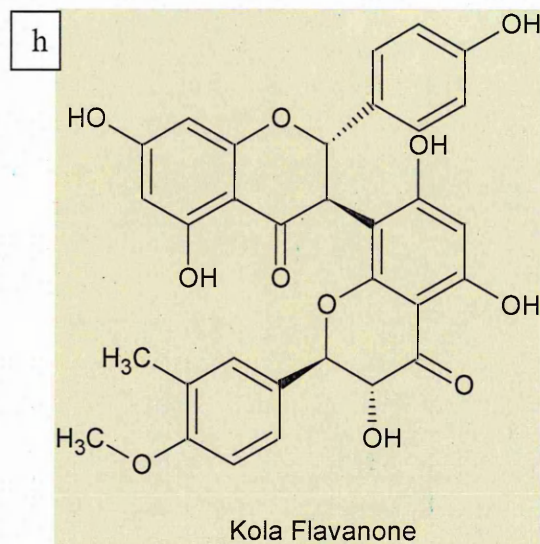
Vitamin E is an example of a prenil lipid

## Saccharolipids



Lipid X is an example of a prenyl lipid

## Polyketides

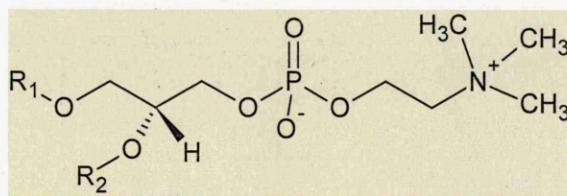


Kola flavanone is an example of a polyketides

Figure 2.1 Generic structures of several lipid species. a) Fatty acids, b) Glycerolipids, c) Glycerophospholipids, d) Shingolipids, e) Sterols, f) Prenols, g) Saccharolipids, h) polyketides.

Within each of these categories there are several classes and subclasses of molecules. The main class of lipids studied in this work are phosphatidylcholines which are a subclass of the glycerophospholipids category.

## Phosphatidylcholine



Phosphatidylcholine is a class of glycerophospholipids.

Figure 2.2 Phosphatidylcholine structure.

### 2.1.2 MALDI Statistical Analysis

In the work reported here the use of principal component analysis (PCA) to aid the interpretation of MALDI-MSI data, using as a model system lipid variations within brain tissue has been investigated. To date MALDI-MS image analysis has been largely concerned with mapping the distribution of known analytes in tissues. An important step in the progression of its application is the determination of unknown variants for metabolite and protein profiling in both clinical and disease studies. PCA is a statistical approach that can be used as a means of determining latent variables in multivariate data sets. Van den Berg *et al.*, 2006 have presented work on the comparison of data pre-treatment of a metabolomic data set prior to PCA. Shown in table 2.1 are some of the possible pre-treatments used for multi dimensional complex data sets, including MALDI-MS imaging data (Van den Berg *et al.*, 2006).

Class	Method	Formula	Unit	Goal	Advantages	Disadvantages
I	Centering	$\tilde{x}_{ij} = x_{ij} - \bar{x}_i$	0	Focus on the differences and not the similarities in the data	Remove the offset from the data	When data is heteroscedastic, the effect of this pretreatment method is not always sufficient
II	Autoscaling	$\tilde{x}_{ij} = \frac{x_{ij} - \bar{x}_i}{s_i}$	(-)	Compare metabolites based on correlations	All metabolites become equally important	Inflation of the measurement errors
	Range scaling	$\tilde{x}_{ij} = \frac{x_{ij} - \bar{x}_i}{(x_{i_{\max}} - x_{i_{\min}})}$	(-)	Compare metabolites relative to the biological response range	All metabolites become equally important. Scaling is related to biology	Inflation of the measurement errors and sensitive to outliers
	Pareto scaling	$\tilde{x}_{ij} = \frac{x_{ij} - \bar{x}_i}{\sqrt{s_i}}$	0	Reduce the relative importance of large values, but keep data structure partially intact	Stays closer to the original measurement than autoscaling	Sensitive to large fold changes
	Vast scaling	$\tilde{x}_{ij} = \frac{(x_{ij} - \bar{x}_i)}{s_i} \cdot \frac{\bar{x}_i}{s_i}$	(-)	Focus on the metabolites that show small fluctuations	Aims for robustness, can use prior group knowledge	Not suited for large induced variation without group structure
	Level scaling	$\tilde{x}_{ij} = \frac{x_{ij} - \bar{x}_i}{\bar{x}_i}$	(-)	Focus on relative response	Suited for identification of e.g. biomarkers	Inflation of the measurement errors
III	Log transformation	$\tilde{x}_{ij} = 10 \log(x_{ij})$ $\tilde{x}_{ij} = \tilde{x}_{ij} - \bar{\tilde{x}}_i$	Log 0	Correct for heteroscedasticity, pseudo scaling. Make multiplicative models additive	Reduce heteroscedasticity, multiplicative effects become additive	Difficulties with values with large relative standard deviation and zeros
	Power transformation	$\tilde{x}_{ij} = \sqrt{(x_{ij})}$ $\tilde{x}_{ij} = \tilde{x}_{ij} - \bar{\tilde{x}}_i$	10	Correct for heteroscedasticity, pseudo scaling	Reduce heteroscedasticity, no problems with small values	Choice for square root is arbitrary.

Table 2.1 List of statistical processing methods used within MALDI-MS imaging data processing with advantages and disadvantages. (reproduced from Van den berg et al., 2006)

Van den berg et al., 2006 have found that for their application autoscaling and range scaling seem to perform better than other methods based on biological expectations from the experiment. However they found that pareto scaling remained closer to the original measurement than autoscaling and that the data does not then become dimensionless.

Skrobot et al., 2007 presented work using PCA and LDA (Linear Discriminant Analysis) to identify the presence of four different contaminant solvents in gasoline. Due to the complex nature of the gasoline mass spectrometry data,

there was a need for data pre-treatment to reduce the dimensionality of the data set before LDA. The authors used Fisher weights and PCA to reduce the complexity of the data before LDA. Govorukhina *et al.*, 2006 have demonstrated the use of CODA (component detection algorithm) for data pre-treatment of an LC-MS data set obtained from a human serum sample. The data set was then analysed using PCA. This allowed the separation of cytochrome C spiked and non spiked samples. The use of PCA for the analysis of MALDI-MSI data has been reported previously by McCombie *et al.*, 2005. In this work the coefficients of principal components were plotted as images in order to identify regions of tissue that were different. In our own groups previous work applying PCA to MALDI-MSI data issues arising from inhomogeneous matrix coverage and salt concentration in tissue were discussed and possible solutions suggested (Prideaux *et al.*, 2007).

### 2.1.3 Brain Tissue Analysis

Figure 2.3 shows a schematic image of the brain indicating the regions selected for PCA comparison. These regions were identified from the histological section (not shown) using The Rat Brain in stereotaxic coordinates (Paxinos *et al.*, 1998). One of the objectives of this work was to see if mass spectrometry could differentiate between white and grey matter. Brain grey matter is composed of cells called neurons specialised in transmitting information. Brain white matter is composed of Glial cells, astrocytes and oligodendrocytes. Astrocyte have been demonstrated to participate in "neurotransmission", oligodendrocytes facilitate electrical signalling because of their myeline sheaths which are mainly composed of

lipids. These myelin sheaths aggregate together and are responsible for the pale colour typical of the white matter.

In figure 2.3 certain regions of the brain are identified and colour coded, the cerebral cortex (yellow) is involved with cognitive function e.g sensory and motor. The corpus callosum (red) represents the white matter of the cerebral cortex and is made of oligodendrocytes and connects the cerebral cortex to the rest of the brain. The hippocampal formation (purple) is implicated in processing and storage of memory. The thalamus (blue) acts like an essential link between the sensory inputs and the grey matter in the cerebral cortex. The grey cerebellar cortex (grey) is predominantly involved in movement coordination and partially in cognition. The white cerebellar cortex (green) is the white matter in the cerebellum and connects the cerebellum to the brainstem and thalamus.

The aim of the work presented in this chapter of this thesis is to use PCA in conjunction with histology to differentiate regions of tissue (in this case regions of the brain), using both unsupervised and "supervised" PCA.



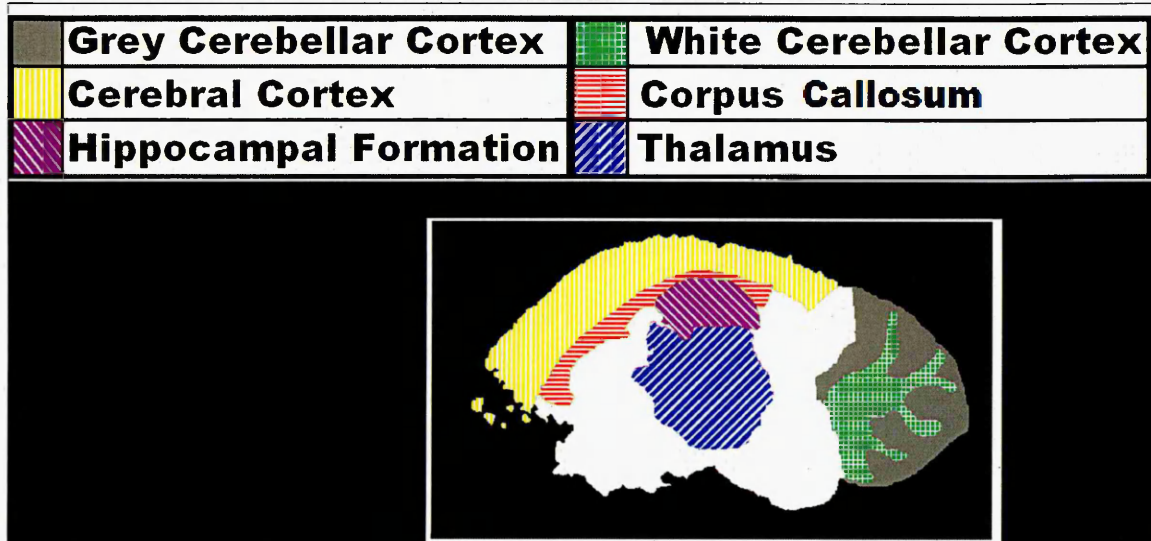


Figure 2.3 Schematic diagram of the brain regions selected for the PCA. The 6 highlighted regions of the brain displayed illustrate where each of the 10 MALDI mass spectra were acquired for subsequent multivariate analysis.

## 2.2 Experimental

### 2.2.1 Preparation of Tissue Sections for MALDI-MS Analysis

Male Wistar rats were sacrificed by schedule one method according to Home Office (UK) regulations. The rats were then decapitated and the connective tissue was cut between the skin and the top of the skull. The skin and connective tissue were peeled back to reveal the top of the skull and forceps were slid into the base of the skull through the hole at which the spinal cord exits the skull. The forceps were kept in contact with the interior surface of the skull at all times resulting in the brain carefully being moved away from the skull, the back of the skull was then broken out away from the brain tissue 3-4mm at a time until the back of the skull had been removed. The forceps were then slid inside the skull just to the left of the centre line, ensuring that



contact with the interior of the skull was maintained resulting in the brain tissue remaining undamaged. The left part of the skull was then broken away from the brain revealing the cerebral cortex of the left hemisphere, the same procedure was then repeated for the right side of the skull revealing the entire brain, a small round ended spatula was then slid under the brain and gently moved backwards and forwards to sever the nerves and blood vessels including the optic nerves, until the brain was freed, the brain was then removed from the skull and immediately snap frozen for 15 seconds in liquid nitrogen cooled isopentane, the frozen tissue was then stored at  $-80^{\circ}\text{C}$  until required.

When required the tissue was mounted onto a 2.5mm thick cork disc in the desired orientation and held in place with a minimal amount of optimum cutting temperature (OCT) embedding medium, ensuring that no OCT embedding medium was near the region to be sectioned figure 2.4. This has been shown by Schwartz et al., 2003 to markedly reduce the spectral quality in MALDI MS, because OCT contains a polymer which ionises very well within MALDI MS and hence reduces the information that can be obtained (Figure 2.5). Tissue sections ( $12\mu\text{m}$ ) were cut using a Leica CM1510 cryostat (Leica Microsystems, Wetzlar, Germany) set at  $-12^{\circ}\text{C}$ , each section was thaw mounted onto cleaned aluminium plates.



Figure 2.4 Image of a rat brain mounted on cork using OCT.

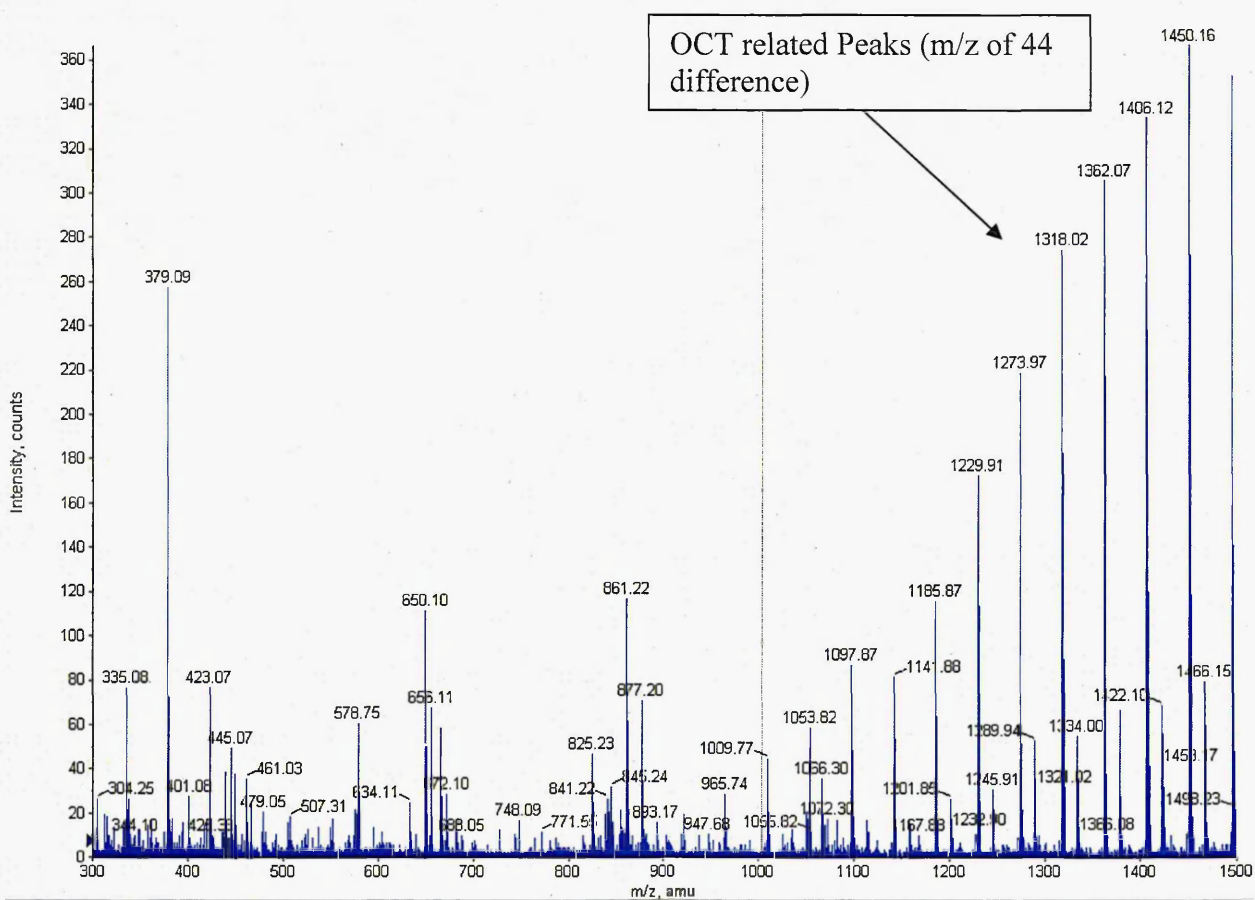


Figure 2.5 Spectra obtained from OCT contaminated sample, OCT related peaks appear as a polymer with peaks at regular m/z 44 intervals.

### **2.2.2 Sample Preparation**

The tissue sections were washed in graded ethanol solutions at 50%, 70%, 90% and 100% (ethanol/water) for a period of 30 seconds at each grade and briefly air dried between washes in order to remove excess salts from the tissue prior to matrix application. After washing, the tissue was air dried for 20mins and then spray coated with 10ml of 25mgml<sup>-1</sup>  $\alpha$ -CHCA in ethanol with 0.1% TFA. Spray coating was performed using a gravity fed pneumatic air spray gun, Iwata studio series compressor fitted with an Iwata Eclipse gravity feed airgun (Iwata-Media Inc., Portland, OR, USA) set at 40psi. The samples were spray coated at a distance of 25cm, for 20 series of 2 passes of the air brush, with 30 second intervals, this was carried out to obtain an even matrix coating whilst avoiding sample over wetting which would result in analyte migration.

The aluminium sample plates were cut to size and mounted onto an Opti-Tof<sup>®</sup> LC MALDI target plate (Applied Biosystems/MDS Sciex, Concord, Ontario, Canada) using double sided carbon conductive tape.

### **2.2.3 Mass Spectrometric Analysis**

The samples were analysed in positive ion mode using an Applied Biosystems/MDS Sciex hybrid quadrupole time-of-flight instrument (Q-Star Pulsar-i) fitted with an orthogonal MALDI ion source, using the oMALDI server 5.0 software. A 355nm frequency tripled 1kHz Nd:YAG laser which has an elliptical laser spot of approximately 150 x 100  $\mu$ m was used at an energy of 40% (4.0 $\mu$ J) and a repetition rate of 1kHz. The laser was fired at the sample with 150  $\mu$ m spatial resolution, with the laser firing for approximately 3

seconds per spot. The “dynamic pixel” feature of the software that moves the laser within the defined pixel dimensions during acquisition was on (Simmons 2008). A further comparison of the data obtained from white and grey matter has been made using unwashed brain tissue which has been analysed using a 5KHz Nd:YVO<sub>4</sub> laser. This data was compared to show the differences between white and grey matter without, washing the tissue prior to matrix application. Within this comparison the matrix has been printed using a Portrait multi reagent spotter (LabCyte Inc, CA).

#### **2.2.4 Principal component analysis**

Principal component analysis (PCA) was carried out using the MarkerView™ statistical analysis package (Applied Biosystems/MDS Sciex, Concord, Ontario, Canada). Ten Spectra were randomly selected from each of the 6 distinct brain regions identified in figure 2.3, i.e the cerebral cortex (yellow), corpus callosum (red), hippocampal formation (purple), thalamus region (blue), grey cerebella cortex (grey) and white cerebella cortex (green). The spectra were imported into the MarkerView™ software with a mass tolerance of 0.1 amu (i.e. the bin size the data was grouped into), and a minimum signal count of 4.0 which removed background noise. The data was normalised against m/z 190 the protonated molecule of the matrix and then m/z 184 the Phosphatidylcholine head group. In order to reduce the number of ions shown in the loadings plots that were not related to the lipid mass region all peaks below m/z 500 were excluded from the analysis. PCA was carried out using Pareto scaling. Pareto scaling uses the square root of the standard deviation as a scaling factor to reduce the dominance of large scale intensity changes in the matrix and other high abundance ions (Van den Berg *et al.*,

2006). These may mask the variation in lower abundance ions during PCA. The overall outcome of PCA is greatly affected by the masking of the underlying relevant information by ions relating to matrix coating and other endogenous molecules. Since these molecules were not of interest within the context of this work the data pre-treatment described above was used. PC1 versus PC2 was chosen for display since these components resulted in the highest overall degree of separation of the spectra within the PCA scores plots.

Within this work both unsupervised and “supervised” PCA was carried out and compared. With unsupervised PCA each spectra is classed as an individual so the principal components are selected which account for the greatest separation of each of the individual spectra. In “supervised” PCA each spectra is assigned manually to a specified group, the software then selects the principal components which account for the greatest variation between each of the groups. (Van den Berg *et al.*, 2006). A possible better description of this mode of operation of the software is PCA-DA (discriminate analysis). On the version of the software used within this work “supervised” PCA was used however this terminology has been changed in later versions of the software to PCA-DA.

In the header for each of the scores and loadings plots (figures 2.6a-2.6d) the principal components that have been plotted are shown with the percentage variance (Van den Berg *et al.*, 2006), or the percentage of the variance accounted for from each of the principal components shown in brackets. Also shown is the type of scaling used (Pareto) and if “use groups” shows that the

corresponding scores or loadings plot was taken from a “supervised” PCA data set.

### **2.2.5 Image Processing**

The imaging data sets were then converted into analyze 7.5 file format using oMALDI server 5.0 software

All images were processed using 'BioMap' ion imaging software (<http://www.maldi-msi.org>) resulting in the production of a 2D ion density map. Images were normalised against the matrix ion at m/z 190 and the phosphatidylcholine head group m/z 184.

### **2.2.6 Profile Data acquisition.**

Following the acquisition of the Nd:YVO<sub>4</sub> laser (Described in chapter 6) some of these experiments were repeated. MALDI-MS mass spectra were acquired as profiles and are shown in figures 2.11, 2.12, 2.13 and 2.14 demonstrating the increased amount of information that can now be obtained from tissue samples. The brain tissue sections were obtained in the same manner as mentioned above but were not washed in ethanol prior to matrix application. Matrix application was performed using a Portrait multi reagent spotter (LabCyte Inc. CA) to print the matrix on the tissue. This data has been included into this chapter to demonstrate the advances in the methodology and technology that has enabled the improvement in quantity and quality of data obtainable from MALDI-MS experiments within recent years.

## **2.3 Results and Discussions**

### **2.3.1 PCA Analysis**

Principal component analysis has been used here to attempt to identify hidden variables between spectra taken from the regions of brain tissue. Figures 2.6a and 2.6c shows the scores plot for unsupervised and "supervised" PCA respectively, each shows some differentiation between sample groups taken from each of the brain regions. Brain regions more associated with white matter are shown predominantly on the left side of the scores plot in both the unsupervised and the "supervised" PCA, and regions more associated with grey matter are shown predominately on the right side. It was found upon interpretation of the loadings plot for unsupervised and "supervised" PCA shown in figure 2.6 b and d respectively, the variance between spectra taken from these two groups of tissue regions is predominantly accounted for by two main lipid associated ions at  $m/z$  734.45 PC 32:0  $[M+H]^+$  and  $m/z$  788.48 PC 36:1  $[M+H]^+$ . The 2D ion density maps produced from the Biomap software (<http://www.maldi-msi.org>) are shown in figures 2.7a and 2.7b for the two ions of interest  $m/z$  734.45 and  $m/z$  788.48 respectively. Ion  $m/z$  734.45, shown in figure 2.6a has a positive PC1 loading correlating with the positive PC1 scores of the grey matter associated brain region spectra, the image clearly shows elevated levels of this ion in the brain grey matter. Ion  $m/z$  788.48, shown in figure 2.7b, has a negative PC1 loading correlating with the negative PC1 scores of the white matter associated groups of spectra, the image clearly shows that this ion is elevated in brain regions associated with white matter.

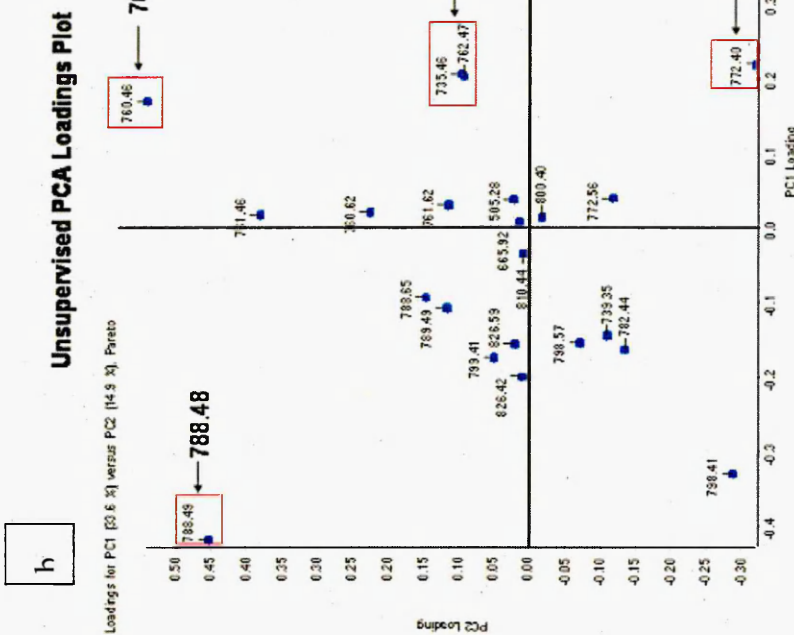
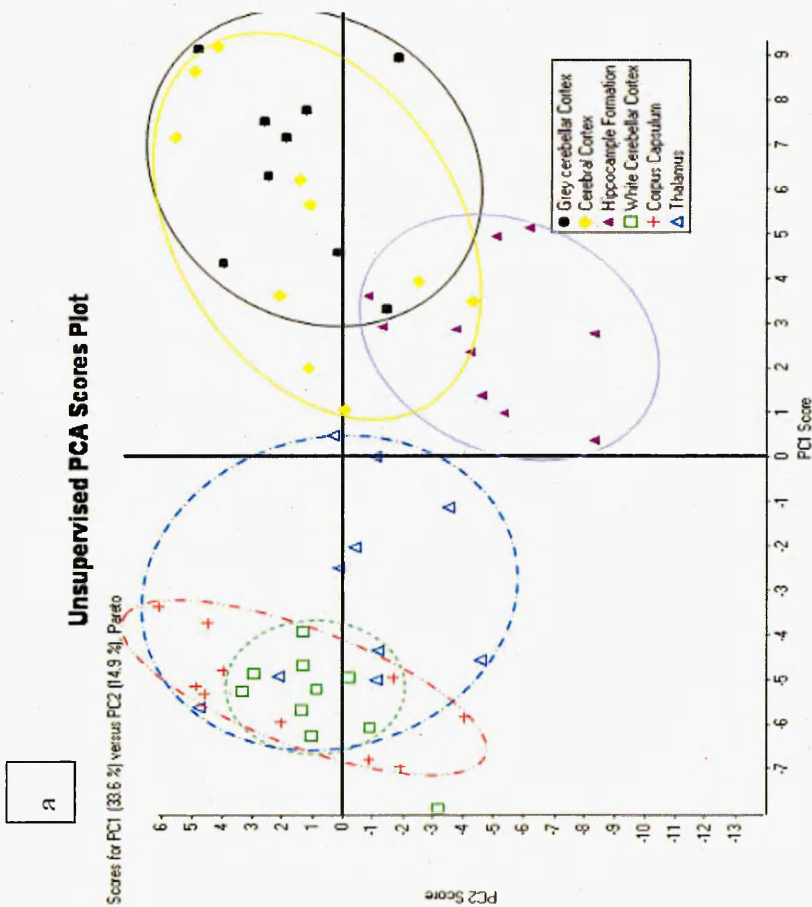


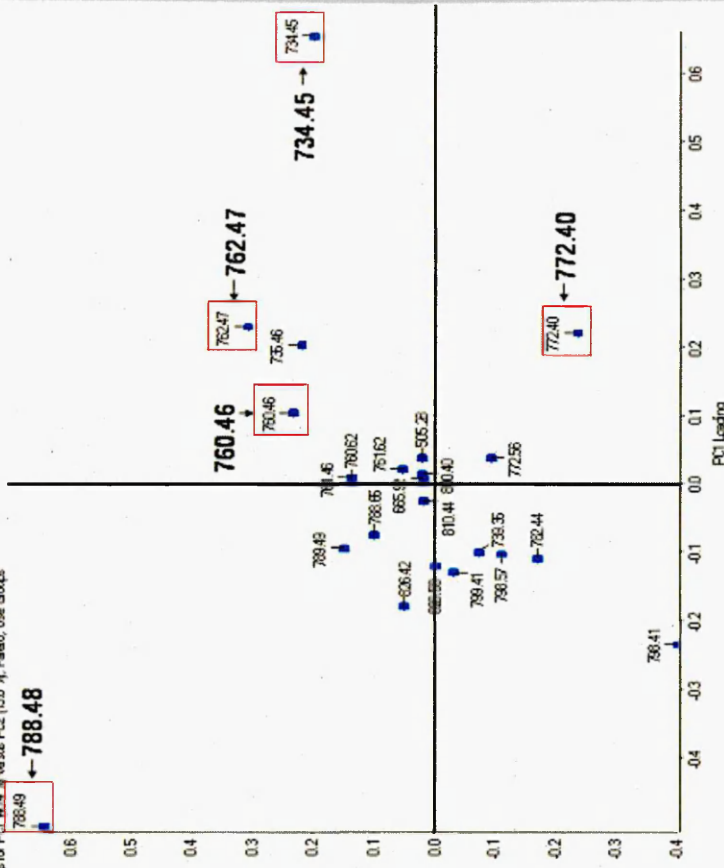
Figure 2.6 a Unsupervised scores plot generated from the PCA, scores plot of PC1 versus PC2 using pareto scaling with the points from each of the six regions of the brain encircled as a visual aid no statistical significance should be drawn from these visual aids. b) Unsupervised loadings plot generated from the PCA, loadings plot of PC1 versus PC2 using pareto scaling, showing possible ions of interest including the ions predominantly responsible for the separation of white and grey matter brain regions m/z 788.48 and m/z 734.45 respectively shown in red and showing the ion of interest m/z 762.47.



d

### Supervised PCA Loadings Plot

Loadings for PC1 (85.4 %) versus PC2 (15.0 %). Pareto, Use Groups



c

### Supervised PCA Scores Plot

Scores for PC1 (85.4 %) versus PC2 (15.0 %). Pareto, Use Groups

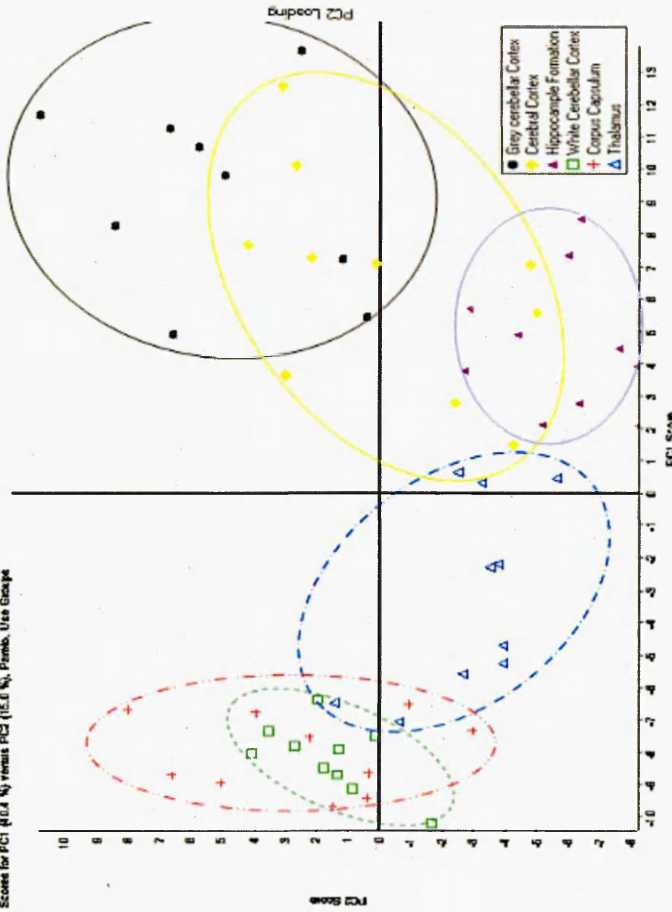


Figure 2.6 c “supervised” scores plot generated from the PCA, scores plot of PC1 versus PC2 using pareto scaling with the points from each of the six regions of the brain encircled as a visual aid no statistical significance should be drawn from these visual aids. d) “supervised” loadings plot generated from the PCA, loadings plot of PC1 versus PC2 using pareto scaling, showing possible ions of interest including the ions predominantly responsible for the separation of white and grey matter brain regions m/z 788.48 and m/z 734.45 respectively shown boxed in red and showing the ion of interest m/z 762.47 shown to have a positive PC1 and a Positive PC2 which corresponds to the grey cerebellar cortex region in the scores plot, and m/z 772.46 which has a positive PC1 and a negative PC2 which relates to the Hippocampal formation in the scores plot.

### 2.3.2 Image Analysis

The ion image of  $m/z$  762.47 shown in figure 2.7d illustrates the potential advantage of “supervised” PCA over unsupervised PCA in this application. Using unsupervised PCA, the grey cerebellar cortex and cerebral cortex groups are not clearly distinguished from each other, in the corresponding loadings plot it appears that the  $m/z$  762.47 ion may be equally associated with both regions. Using “supervised” PCA, the grey cerebellar cortex and the cerebral cortex are more clearly distinguished and the  $m/z$  762.47 ion displays correlation with the positioning of the grey cerebellar cortex group in the scores plot. On imaging the  $m/z$  762.47 ion, shown in figure 2.7d, it appears the assumptions derived from the “supervised” PCA are more beneficial than those derived from the unsupervised PCA as the  $m/z$  762.47 ion is shown to be more elevated in the grey cerebellar cortex region of the brain.

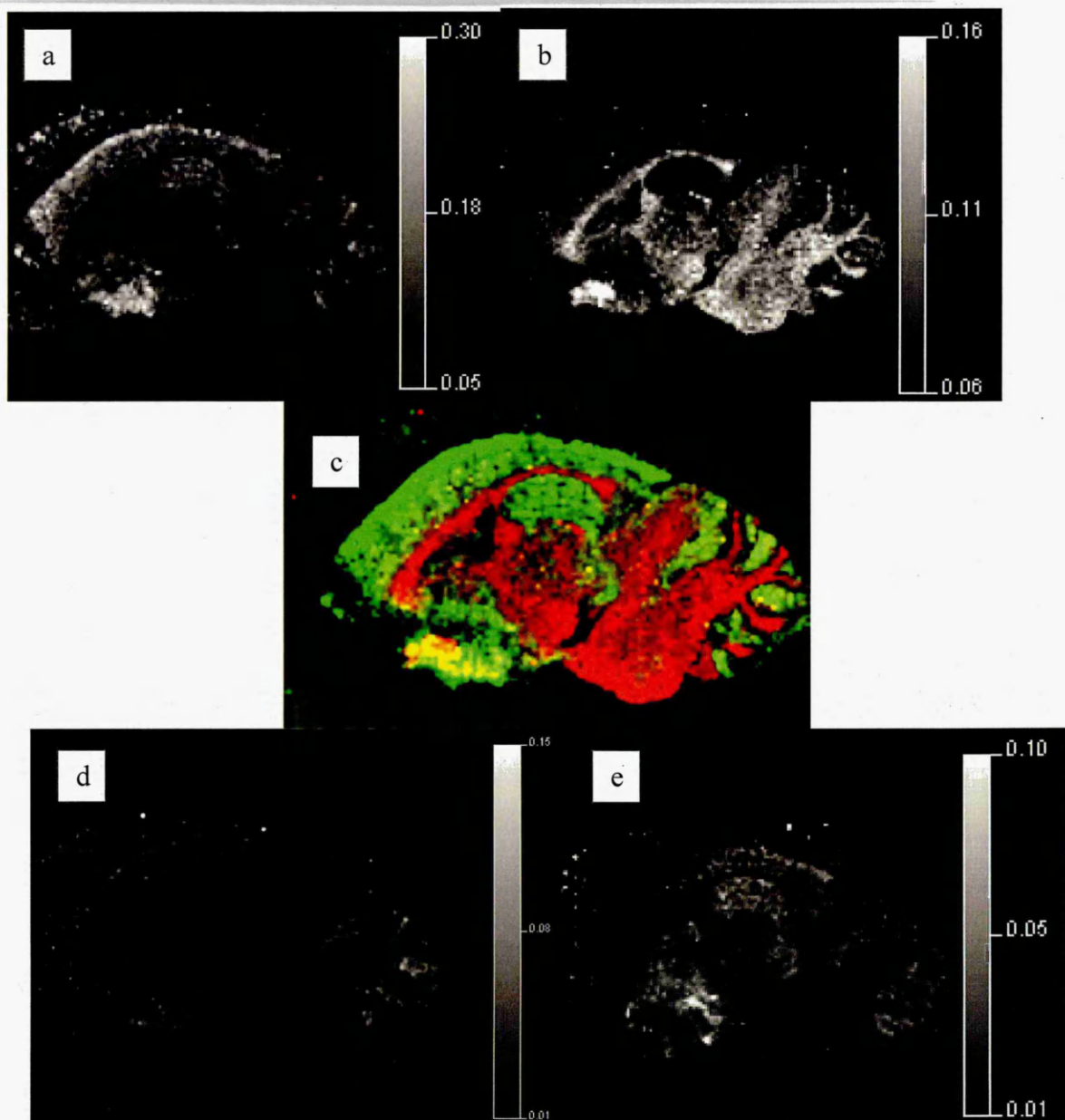


Figure 2.7 a) 2D ion density map of  $m/z$  734.45 which has a highly positive PC1 loading and has been shown to be associated predominantly with regions of grey matter within the brain. b) 2D ion density map of  $m/z$  788.48 which has a highly negative PC1 loading and has been shown to be associated predominantly with regions of white matter within the brain. c) 2D ion density map overlay of  $m/z$  734.45 (GREEN) which has a highly positive PC1 loading overlaid with 2D ion density map produced from imaging ion  $m/z$  788.48 (RED). Complimentary images can be seen areas shown in yellow are areas associated to both white and grey matter. d) 2D ion density map of ion  $m/z$  762.47 which has a positive PC1 loading and a positive PC2 loading and is shown to be elevated in the region of the brain relating to the grey cerebellar cortex. e) 2D ion density map of  $m/z$  772.40 which has a positive PC1 loading and a negative PC2 loading and is shown to be elevated within the grey cerebellar cortex, a section of the cerebral cortex, partially in the thalamus and especially in the hippocampal formation. The area with the highest intensity includes the striatum, ventral pallidum and other ventral nuclei that have not been included in the PCA analysis within this work.

Other possible ions of interest show from the PCA analysis include  $m/z$  772.40. The image of this possible ion of interest is shown in figure 2.7e, the image of  $m/z$  772.40 shows a slightly elevated abundance of this molecule within the grey cerebellar cortex, cerebral cortex and especially in the hippocampal formation, tentative assignment of this ion shows it to be PC 32:0  $[M+K]^+$  this distribution is possibly from the washing process, showing that the removal of surface salts was not uniformly achieved, however, this distribution pattern has been seen in subsequent experiments, also the image of the potassium adduct of the matrix ion does not show this distribution which may be expected if this was a result of inadequate washing.

### 2.3.3 Lipid Analysis

Tentative assignment of the lipid identifications has been performed based on their masses and according to previously published data (Jackson *et al.*, 2005). Figure 2.8 shows a representative mass spectrum with the phospholipid region enlarged and inset. PC 32:0  $[M+H]^+$  at  $m/z$  734.45, PC 34:1  $[M+H]^+$  at  $m/z$  760.46, PC 34:0  $[M+H]^+$  at  $m/z$  762.47, PC 32:0  $[M+K]^+$   $m/z$  772.40 and PC 36:1  $[M+H]^+$  at  $m/z$  788.48 have been identified, Table 1 shows a comparison of the calculated mass and the experimentally observed mass for each of the lipids.

Total mass spectra with inset enlarged and labelled lipid region

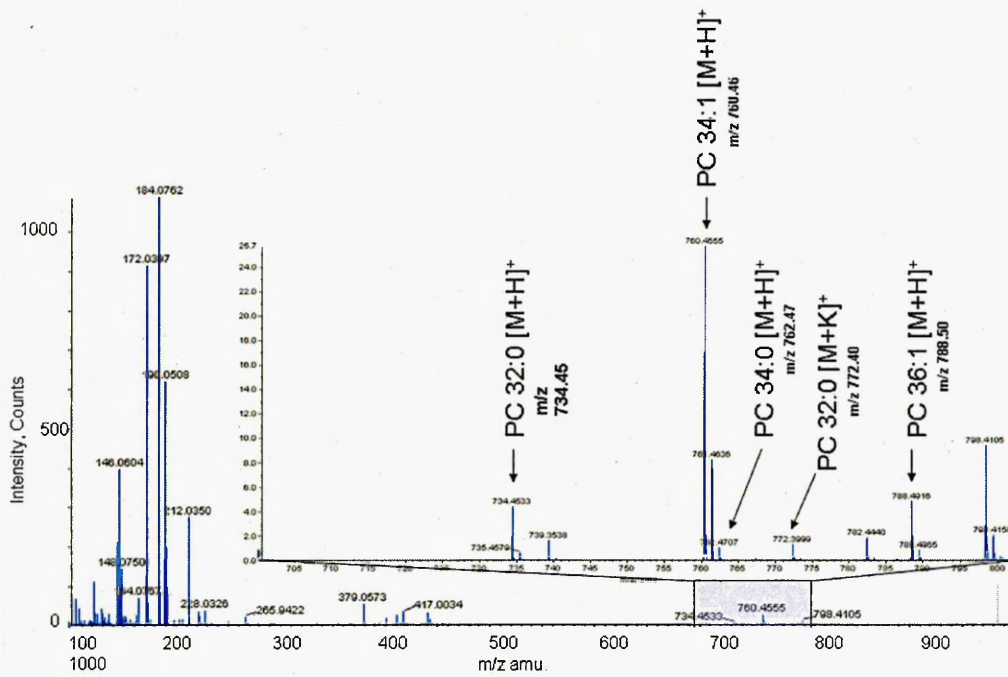


Figure 2.8 Total mass spectra obtained with the phospholipid region enlarged and inset, shown with the tentative phospholipid assignments according published phospholipid data (Jackson et al., 2005) Peaks have been assigned to the following phosphatidylcholines, PC 32:0 [M+H]<sup>+</sup> at m/z 734.45, PC 34:1 [M+H]<sup>+</sup> at m/z 760.46, PC 34:0 [M+H]<sup>+</sup> at m/z 762.47, PC 32:0 [M+K]<sup>+</sup> at m/z 772.40 and PC 36:1 [M+H]<sup>+</sup> at m/z 788.48.

Lipid	Formula	Calculated mass	Observed mass
PC 32:0 [M+H] <sup>+</sup>	C <sub>40</sub> H <sub>81</sub> NO <sub>8</sub> P	734.57	734.45
PC 32:0 [M+K] <sup>+</sup>	C <sub>40</sub> H <sub>80</sub> NO <sub>8</sub> PK	772.53	772.40
PC 34:0 [M+H] <sup>+</sup>	C <sub>42</sub> H <sub>85</sub> NO <sub>8</sub> P	762.60	762.47
PC 34:1 [M+H] <sup>+</sup>	C <sub>42</sub> H <sub>83</sub> NO <sub>8</sub> P	760.59	760.46
PC 36:1 [M+H] <sup>+</sup>	C <sub>44</sub> H <sub>87</sub> NO <sub>8</sub> P	788.62	788.48

Table 2.2 Comparison of the observed lipid masses and the calculated mass.

Figure 2.9 and figure 2.10 show two randomly selected mass spectra taken from two distinct areas of the brain, figure 2.9 is taken from the cerebral cortex

(grey matter) and figure 2.10 is taken from the corpus callosum (white matter) from these spectra it can be clearly seen the difference in abundance of  $m/z$  734.45 and  $m/z$  788.48, this is in agreement with Woods and Jackson 2006, showing that PC 32:0 abundance is primarily responsible for the identification of grey matter, and PC 36:1 abundance is greatly increased in brain regions associated with white matter, within this work it has been further shown that brain regions can be further subdivided using MALDI MSI and observing changes in lipid abundance, as shown in figure 2.7d of  $m/z$  762.47 which shows higher abundance within the grey cerebeller cortex.

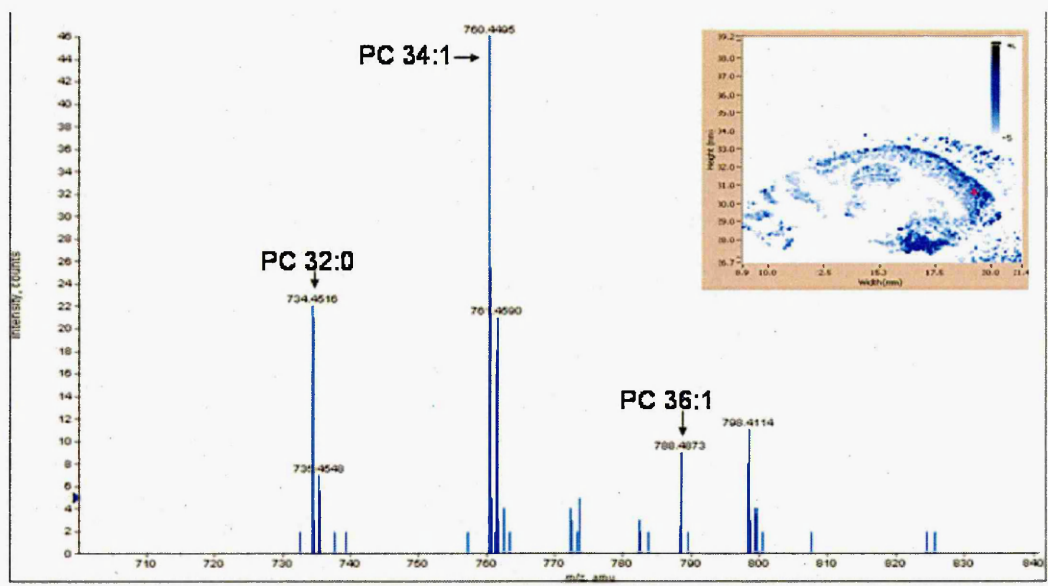


Figure 2.9 Single spectra showing the lipid region with spectral location inset, taken from the cerebral cortex (grey matter) tentative lipid assignments are given for the prominent lipids.



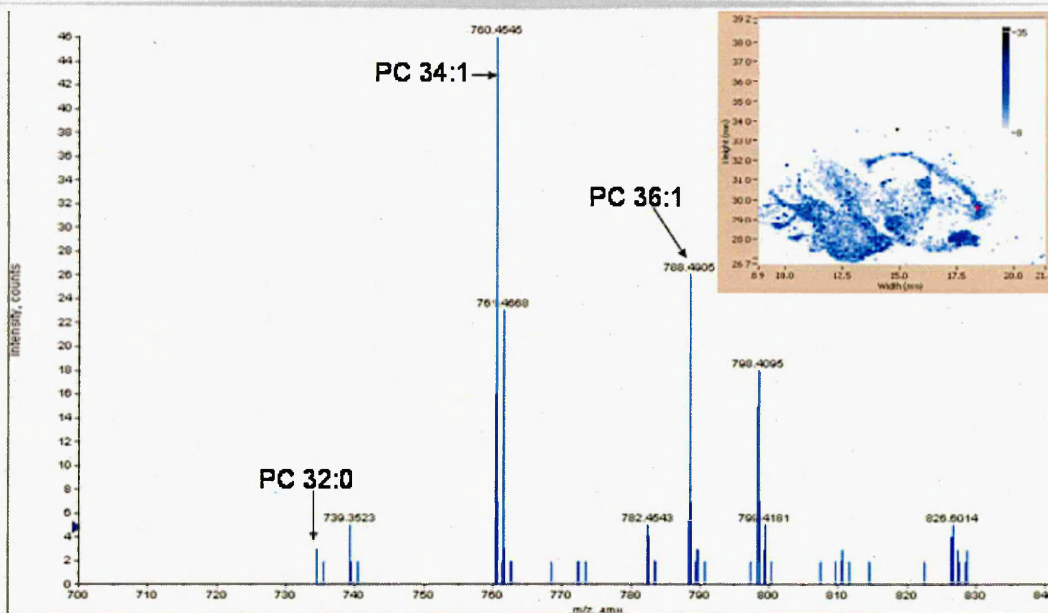


Figure 2.10 Single spectra showing the lipid region with spectral location inset, taken from the corpus callosum (white matter) tentative lipid assignments are given for the prominent lipids.

From the data obtained in this work, it appears that “supervised” PCA has advantages over unsupervised PCA for the interpretation of MALDI-MS image data in some instances. Using unsupervised PCA the samples are separated by principal components, treating each sample individually. In “supervised” PCA, samples are grouped prior to PCA. This leads to a more effective separation of the groups from each other.

Specific rat brain regions were identified from sections using the histological data. Analysis of 10 selected spectra acquired from each of the regions using “supervised” PCA has been shown to separate the regions into distinct groups in the scores plot in contrast to unsupervised analysis. The PCA scores plots of PC1 versus PC2 for both the unsupervised and “supervised” analysis show that it is possible to partially separate white and grey matter; white matter regions have a predominantly negative PC1 score and grey matter has a

predominantly positive PC1. This indicates that ions with a negative PC1 loading will be associated more with the white matter regions of the brain. This is shown in figure 2.7b the image of PC 36:1 m/z 788.48; in contrast figure 2.7a shows the image of the PC1 positive ion m/z 734.45 relating to PC 32:0 which is more associated with grey matter.

The data sets sampled from the thalamus region of the brain have a negative PC1 score, indicating that the thalamus is comprised of white matter. This is not entirely the case since the thalamus is known to be comprised of both white and grey matter regions. The profiles obtained from 10 locations within the thalamus may have been randomly taken from areas of the thalamus associated more with white matter and may not show a true representation of this region.

It is possible to identify ions of interest from the loadings plot which are likely to be more prominent in the different regions of grey matter especially the grey cerebellar cortex from the hippocampal formation, due to the grey cerebellar cortex having a positive PC2 and the hippocampal formation having a negative PC2 score, this is only possible in the "supervised" PCA data set because with unsupervised PCA the two regions overlap. Ions with a positive PC1 and a positive PC2 loading are more likely to be higher in the grey cerebellar cortex. Figure 2.7d shows the respective image of the ion m/z 762.47 which represents lipid PC 34:0, showing that this lipid is elevated within this region of the brain. From the PCA, using this data set and PC1 versus PC2, it is not possible to distinguish different regions of the white matter.



### 2.3.4 Profile Data Analysis

The methodology and technology within this field is rapidly improving. Shown in figure 2.11 is an example of the data obtainable from a brain tissue section using some of the latest matrix application technologies (Portrait multi reagent spotter from LabCyte Inc. CA)

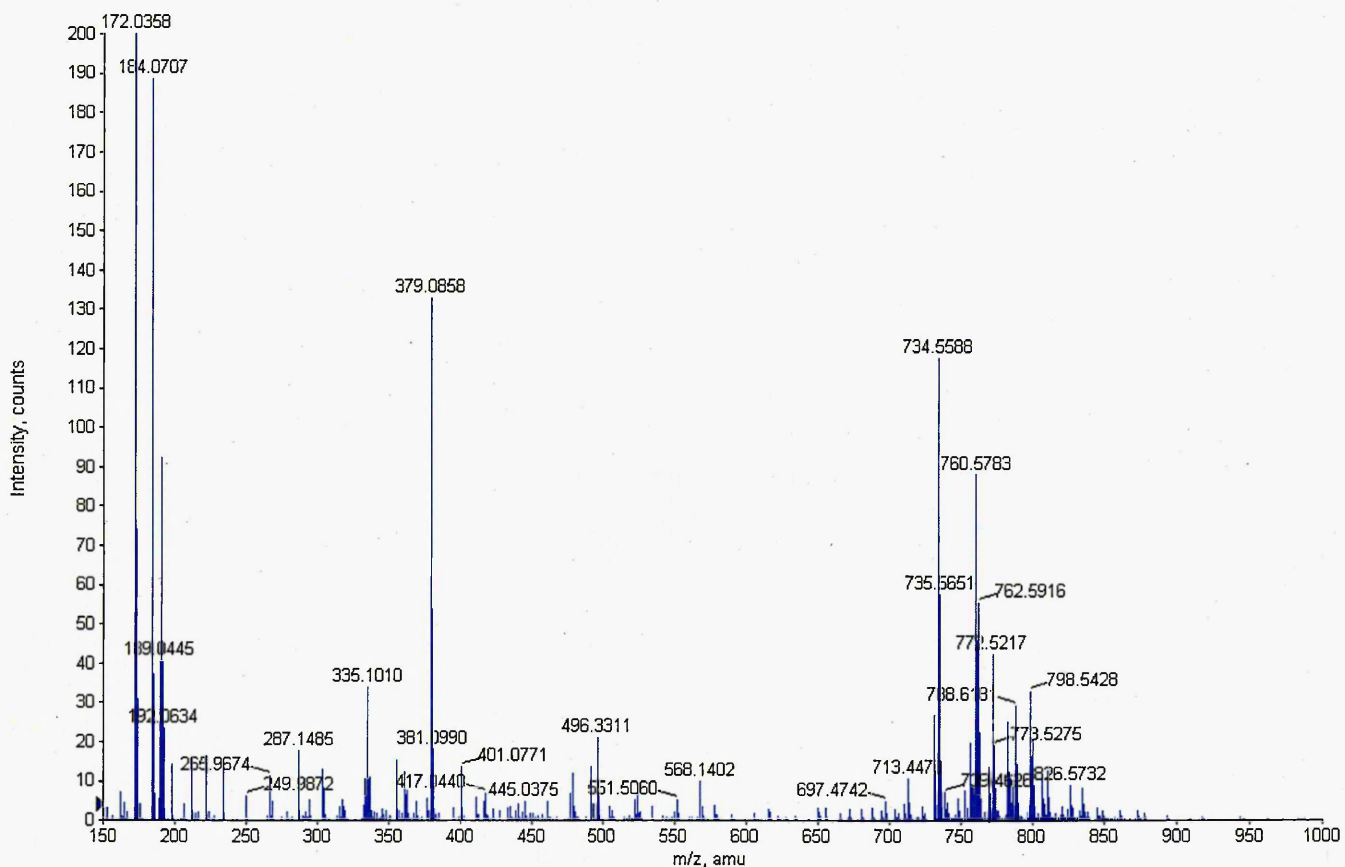


Figure 2.11 Combined Profile obtained from areas of white and grey cerebellar cortex, using the Portrait multi reagent spotter for matrix printing. The array of data within the lipid rich region of the spectra can be seen.

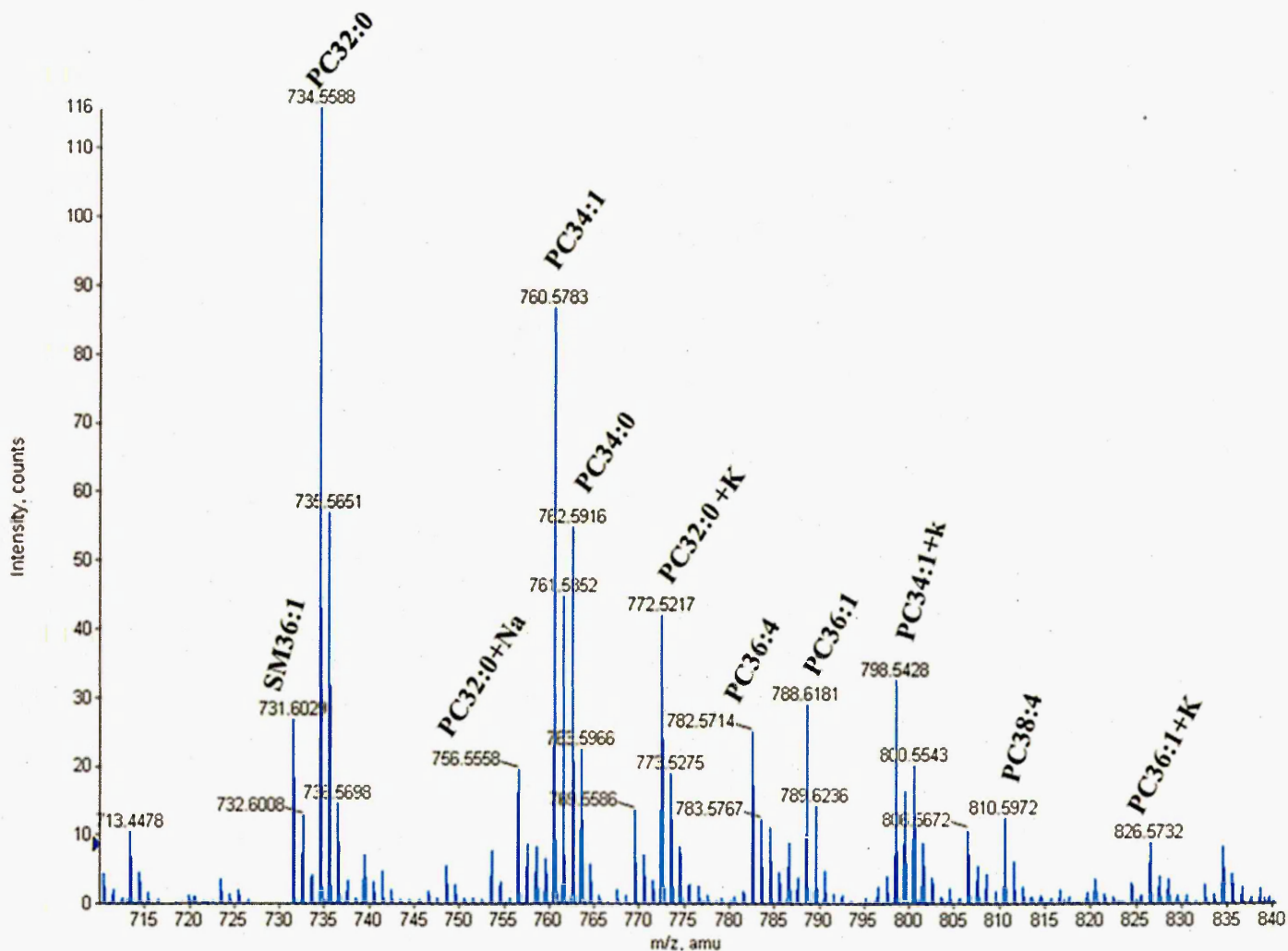


Figure 2.12 Enhanced view of the lipid region within figure 2.11. Several lipid species have been tentatively identified based on their mass.

Table 2.3 below contains the mass data shown in figure 2.12 and a comparison of the theoretical and measured mass is made and the PPM mass error is shown.

Calculated Mono-isotopic m/z	Observed m/z	PPM error (2dp)	Possible Lipid species	Ion Species
731.6067	731.6029	-5.19	SM 36:1	[M+H] <sup>+</sup>
734.5622	734.5588	-4.63	PC 32:0	[M+H] <sup>+</sup>
756.5519	756.5558	5.15	PC 32:0	[M+Na] <sup>+</sup>
760.5856	760.5783	-9.60	PC 34:1	[M+H] <sup>+</sup>
762.5935	762.5916	-2.49	PC 34:0	[M+H] <sup>+</sup>
772.5259	772.5217	-5.44	PC 32:0	[M+K] <sup>+</sup>
782.5700	782.5714	1.79	PC 36:4	[M+H] <sup>+</sup>
788.6169	788.6181	1.52	PC 36:1	[M+H] <sup>+</sup>
798.5415	798.5428	1.63	PC 34:1	[M+K] <sup>+</sup>
810.6013	810.5972	-5.06	PC 38:4	[M+H] <sup>+</sup>
826.5728	826.5732	0.48	PC 36:1	[M+K] <sup>+</sup>

*Table 2.3 Comparison of the theoretical and measured mass taken from the spectra shown in figure 2.12. Identified are the possible Lipids species and the PPM mass error. All the PPM mass errors are below 10PPM.*

PC 32:0

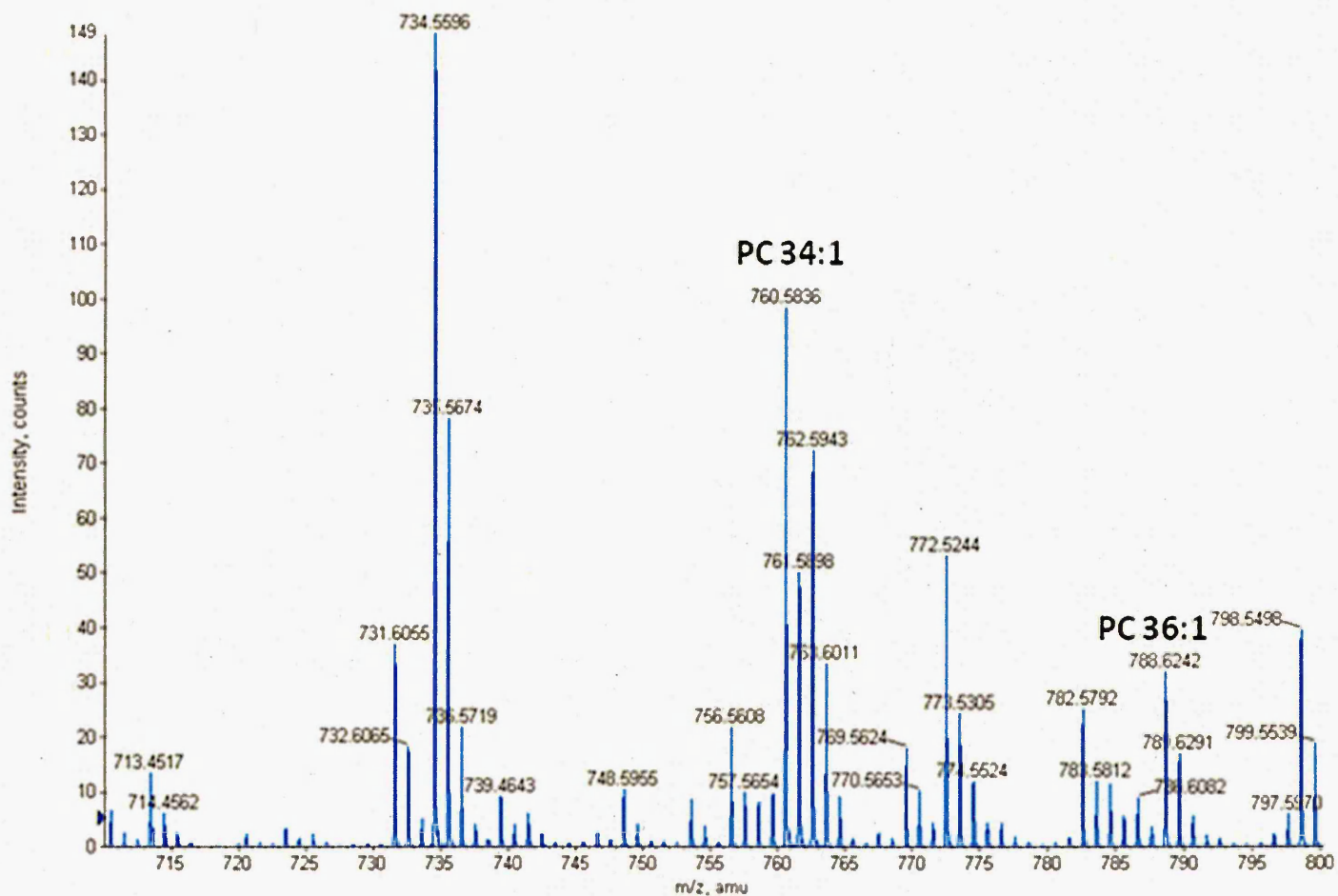


Figure 2.13 MALDI spectra obtained from a grey matter brain tissue using the Portrait multi reagent spotter for matrix printing.

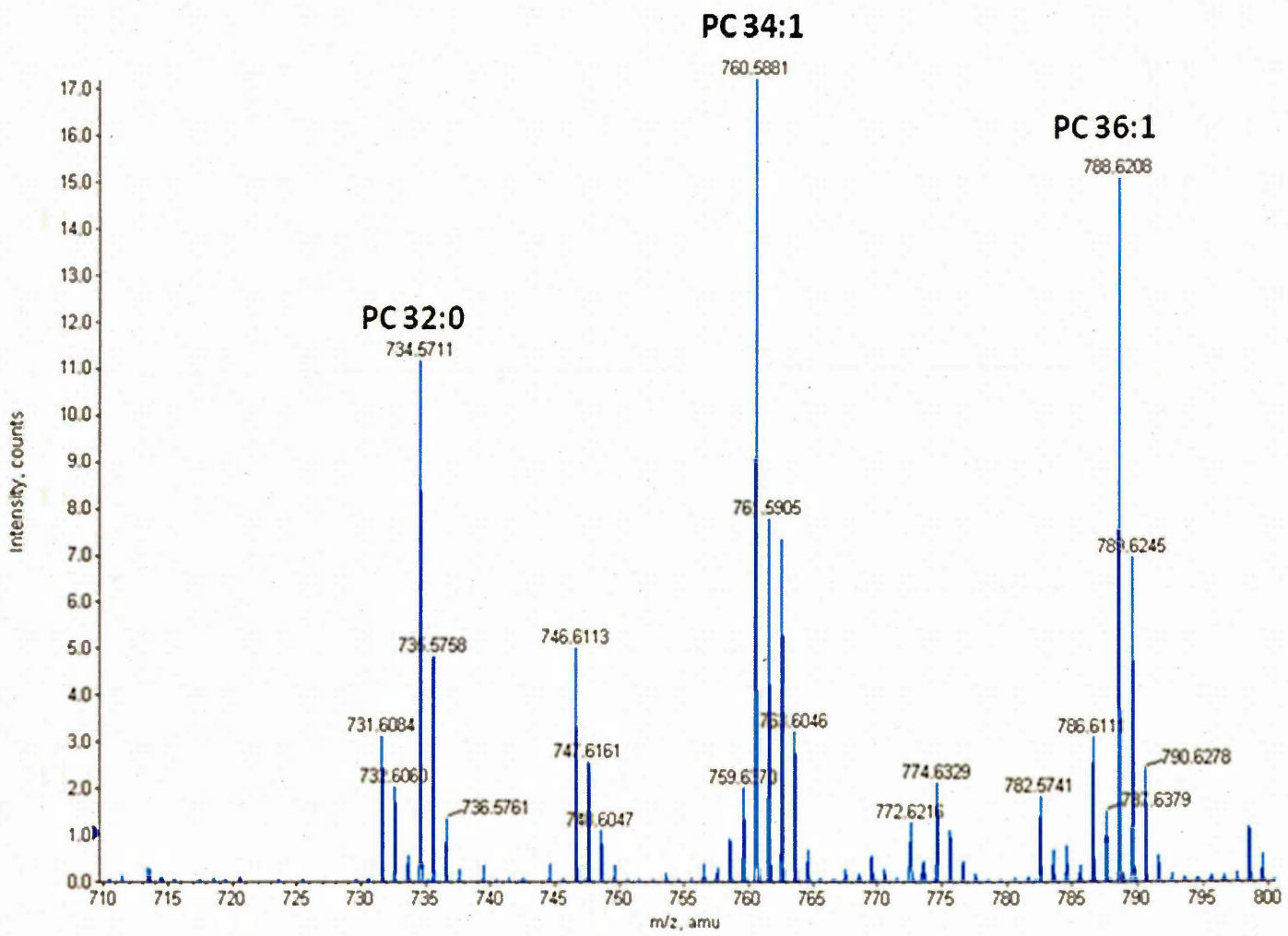


Figure 2.14 MALDI spectra obtained from white matter brain tissue using the Portrait multi reagent spotter for matrix printing.

The mass spectra shown in figures 2.13 and 2.14 are in agreement with the previous work showing a marked difference in the relative abundance of PC 32:0 and PC 36:1 between the white and grey matter brain tissue this is in agreement with Woods and Jackson 2006, showing that PC 32:0 abundance is increased in regions of grey matter, and PC 36:1 abundance is increased in brain regions associated with white matter.

## 2.4 Conclusions

Whilst unsupervised PCA is useful when analysing samples of unknown origin, where some information on the grouping of samples, based on histology is known, "supervised" PCA i.e. PCA-DA may be advantageous.

Shown is a reliable method for the determination of ions of interest associated with distinct tissue regions. This technique could be further utilised for the identification of possible biomarkers of disease from known diseased and control populations of samples. Also for the determination of tumour markers within tissues, for imaging of tumour progression and detection of the chemical tumour margin.

Also shown in this chapter is an indication of the level of improvement within the technology and with sample preparation and data acquisition techniques. This shows how MALDI-MS methodologies have advanced within the last three years during which this PhD project was completed.

## 2.5 References

Adibhatla R.M.; Hatcher J.F; Dempsey R.J. **2006**, *The AAPS Journal*, 8 (2) Article 36.

Fahy E; Subramaniam S; Brown H.A; Glass C.K; Merrill A.H Jr; Murphy R.C; Raetz C.R.H; Russell D.W; Seyama Y; Shaw W; Shimizu T; Spener F; Meer G; VanNieuwenhze M.S; White S.H; Witztum J.L; Dennis E.A. **2005**, *Journal of Lipid Research*. 46, 839-862.

Govorukhina N.I; Reijmers T.H; Nyangoma S.O; van der Zee A.G.J; Jansen R.C; Bischoff R. **2006**, *Journal of chromatography A*. 1120, 142-150

Jackson S.N; Ugarov M; Egan T; Post J.D; Langlais D; Schultz J.A; Woods A.S. **2007**, *Journal of Mass Spectrometry*. 42, 1093-1098.

Jackson S.N; Wang HY.J; Woods S.A. **2005**, *Analytical Chemistry*, 77, 4523-4527.

McCombie G; Staab D; Stoeckli M; Knochenmuss R. **2005**, *Analytical Chemistry*, 77, 6118-6124.

Paxinos G; Watson C. **1998**, *The Rat Brain in Stereotaxic Coordinates*, 4th Edition, Academic Press.

Prideaux B; Atkinson S.J; Carolan V.A; Morton J; Clench M.R. **2007**, *International Journal of Mass Spectrometry* 260, 243-251.

Schwartz S.A; Reyzer M.L; Caprioli R.M. **2003**, *Journal of mass spectrometry*, 38: 699-708.

Skrobot V.L; Castro E.V.R; Pereira R.C.C; Pasa V.M.D; Fortes I.C.P. **2007**, *Energy and Fuels* 21, 3394-3400.

Simmons D. A. **2008**, ABI Technical Note, improved MALDI-MS imaging performance using continuous laser rastering.

Van den Berg R.A; Hoefsloot H.C.J; Westerhuis J.A; Smilde A.K; van der Werf M.J. **2006**, *BMC Genomics* 7:142.

Woods A.S; Jackson S.N. **2006**, *The AAPS Journal*, 8 (2) Article 44.

[www.maldi-msi.org](http://www.maldi-msi.org)

## CHAPTER 3

---

**Matrix Assisted Laser Desorption  
Ionisation – Ion Mobility Separation  
– Mass Spectrometry Imaging of  
Small Molecules.**

**A New Dimension in MALDI  
Imaging.**



## **Matrix Assisted Laser Desorption Ionisation – Ion Mobility Separation – Mass Spectrometry Imaging of Small Molecules.**

### **3.1 Introduction**

#### ***3.1.1 A New Dimension in MALDI Imaging.***

In this chapter examples of the benefits of MALDI- ion mobility separation – mass spectrometry imaging (MALDI-IMS-MSI) of small molecules compared to conventional MALDI-MS imaging. Described are several examples of the benefits arising from the additional separation step obtained by MALDI-IMS-MSI. Several analytes have been chosen to demonstrate this.

#### ***3.1.2 Introduction into MALDI Imaging of small molecules.***

Biological MALDI MSI of small molecules is a rapidly developing field. Within the field of biological MALDI MSI of small molecules there are several areas, often the two most widely studied are perhaps lipidomics and xenobiotic imaging

##### ***3.1.2.1 Lipidomics.***

Lipidomics is the study of lipids within biological systems. Lipids are a large class of bio-molecules with several classes and sub classes. They play essential structural and functional roles. This includes for example the role of phospholipids as key constituents of biological membranes (Fuchs & Schiller

2008). Fatty acid oxidation is essential for the generation of energy, Lysophosphatidylcholines have been shown to be important biomarkers of diseases like atherosclerosis and rheumatoid arthritis (Matsumoto *et al.*, 2007 and Fuchs *et al.*, 2005). Sphingolipids have been shown to have important roles within cellular processes including apoptosis, cellular growth and proliferation and drug resistance (Fuchs *et al.*, 2007, Ogretmen 2006 and Modrak *et al.*, 2006).

The field of lipidomics has grown considerably in the last few years. The first "Lipidomics" paper was published by Han *et al.*; 2003, within The Journal of Lipid Research. This was not the first paper published on lipids, but it was the first paper to use the term "Lipidomics". In this work the authors demonstrate the detection of multiple lipid species from an extract of mouse myocardial tissue. They also present a review of the analysis of lipidomes from biological samples using ElectroSpray Ionisation - Mass Spectrometry (ESI-MS).

### **3.1.2.2 *Xenobiotic imaging.***

A second important area of interest within small molecule imaging is the study of xenobiotics; primarily drugs and their metabolites. The use of MALDI-MSI imaging within this area has grown considerably and it has been used for the study of xenobiotics within excised tissue sections and whole body analysis (Reyzer *et al.*, 2003, Stoeckli *et al* 2007). This application of MALDI-MSI to xenobiotics has allowed the study of drugs and their metabolites simultaneously and also the possibility to study the biological effect of these substances within whole body sections. This ability to image multiple analytes

simultaneously with limited sample preparation is the key to the success of MALDI Imaging within this field. MALDI-MSI can aid in the drug development process to provide evidence of specific drug and metabolite localisation within tissues, and aid in the determination of drug efficacy and toxicity (Khatib-Shahidi *et al.*, 2006).

The first work presenting the detection of xenobiotics directly from biological tissue sections using MALDI was presented by Troendle *et al.*, 1999. Within this work they demonstrate the detection of the anticancer drug paclitaxel from rat liver tissue sections, showing the detection and ms/ms identification of the paclitaxel  $[M+K]^+$  ion at  $m/z$  892. Also demonstrated was the detection of paclitaxel  $[M+H]^+$  and  $[M+Na]^+$  within ovarian tumour xenograph sections and the confirmation by ms/ms from a known standard.

The first xenobiotic MALDI-MSI experiments were published by Reyzer *et al.*, 2003. Reyzer *et al.*, 2003 presented work showing the distribution of SCH226374 within mouse tumour sections. The sections were coated in SA and the detection and imaging of SCH226374 was achieved by single reaction monitoring (SRM). SRM involved the monitoring of the transition of  $m/z$  695 – 228. Reyzer *et al.*, also presented an image of an undisclosed compound A within a coronal rat brain section.

This technology has been used for whole body MALDI-MSI as reported by Stoeckli *et al.*, 2007. This group presented work on the distribution of a compound within a whole body rat section. They mapped the distribution of

the compound and its metabolites and compared these data to the results of a whole body autoradiography study carried out using a C<sup>14</sup> labelled compound.

Conventional xenobiotic distribution studies utilise whole body autoradiography (WBA). This technique can take several days to complete depending on the isotope used. WBA is relatively expensive compared to MALDI, due to the need to develop radio labelled drug compounds whilst maintaining the drug efficacy. There is also a need for special control measures for the handling of radioactive material. Another disadvantage is the inability to determine the molecular species (whole drug or metabolite) because only the distribution of the isotope is imaged.

### **3.1.2.3 MALDI-Ion mobility-MS**

Ion mobility mass spectrometry has been shown to be beneficial for the analysis of lipids. Jackson *et al.*, 2005 have presented work on the analysis of phospholipids in rat brain using conventional MALDI-TOFMS and MALDI-Ion Mobility – TOF-MS. Within this work they concentrated on phospholipids because they are a major component in brain tissue, and altered levels of phospholipids within tissues have been associated with many disease states.

Jackson *et al.*, 2005 used a prototype MALDI-IM-TOFMS instrument which included a 15cm drift cell at 1600V and containing helium at a pressure of 5torr. The resultant mass spectra acquired with this instrument obtained from the rat brain showed that PC32:0, PC34:1 and SM 18:0 ions were the most dominant. This is expected because PC's and SM's (sphingomyelin's)

account for more than 50% of the membrane phospholipids in eukaryotic cells.

Jackson *et al.*, demonstrated that structurally different biomolecular ions form distinct familial trend lines with a 2D plot of drift time against  $m/z$  (as shown in figure 3.1). Within these trend lines there are a few percent of variation in drift time between some familial ions. They found that lipid trend lines are generally about 12% slower in drift time than isobaric peptides. They have shown drift time separated familial trend lines corresponding to lipids, peptides, aromatics and oligonucleotides. This ability to separate ions based on their class prior to mass analysis aids in the identification of analytes within the low mass window. Specifically the ability to separate isobaric ions prior to mass analysis. Jackson and colleagues demonstrated this with the separation of a CHL isotope ion from an isobaric peptide.

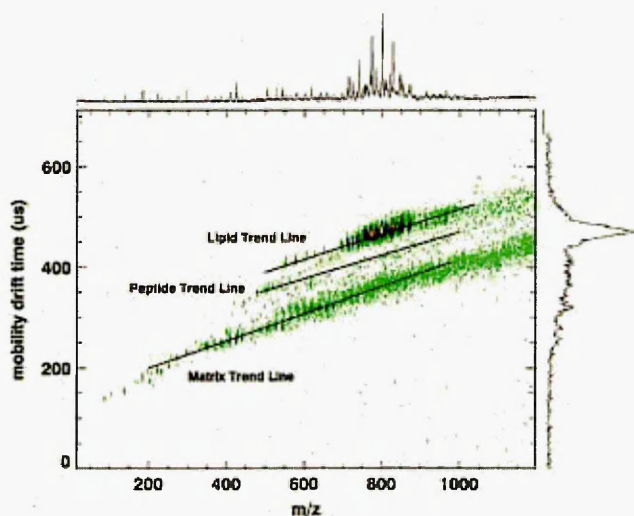


Figure 3.1 2D MALDI-ion mobility-TOFMS plot showing the familial trend lines associated with ion molecule class taken from Jackson *et al.*, 2007.

This work has been further expanded into an imaging technology by the same group (Jackson *et al.*, 2007). The use of a MALDI-ion mobility-TOFMS imaging instrument was reported. This comprised a periodic focusing MALDI-IM-TOFMS instrument with a 15cm ion mobility drift cell operating at 3.5 torr He pressure and 1700V. Using this instrument the ion mobility drift time took several milliseconds, while the TOF flight times took tens of microseconds. This time differential allows good integration of ion mobility into a TOF mass spectrometer, because several TOF analysis can be performed per mobility separation cycle. Within this work the distribution of lipids within coronal brain sections are reported after ion mobility separation. The distribution of PC 34:1 [M+K]<sup>+</sup> is reported. This is the most abundant lipid in rat brain tissue. Also shown are the distributions of PC 36:1 [M+K]<sup>+</sup> and PC 38:6 [M+K]<sup>+</sup>. Not shown are the same ion images without the ion mobility separation. This prevents a comparison of the mobility separated data from the conventional data. Therefore the true benefit of the ion mobility separation can not be assessed. Within this study the authors also demonstrate the use of gold nanoparticles as a MALDI matrix for the analysis of cerebroside in rat brain tissue. One of the issues with the use of MALDI-IMS-MS imaging is discussed i.e. the size of the data files obtained. Since such an image contains several mass spectra at different ion mobility drift times, this adds another dimension of data to already large data files obtained via conventional MALDI-MS imaging. The authors excluded all ions outside of the mobility and mass region of interest, thus limiting their data size.

### 3.1.3 MALDI Synapt HDMS system

The work presented here was conducted on a Synapt HDMS system (Water Corporation, Manchester, UK). This system is a quadrupole ion mobility separation time of flight mass spectrometer (Q-IMS-TOF-MS). A detailed description of this instrument can be found in the introduction to this thesis and has been given by Giles *et al.*, 2004.

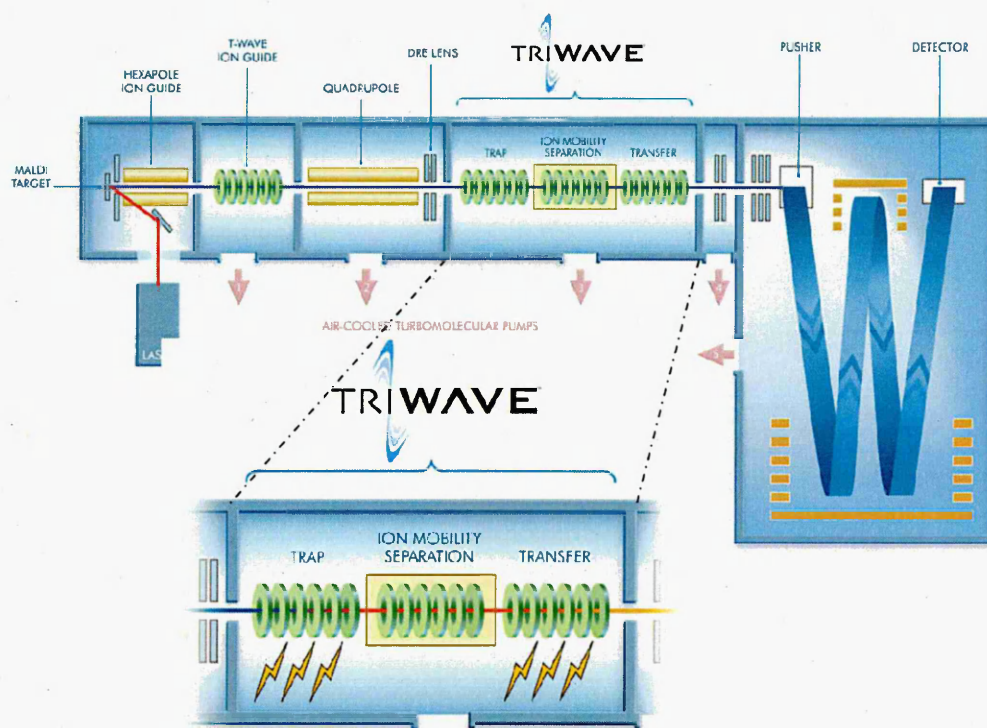


Figure 3.2 Schematic of the instrument configuration of the MALDI Synapt HDMS system (Water Corporation, Manchester, UK)

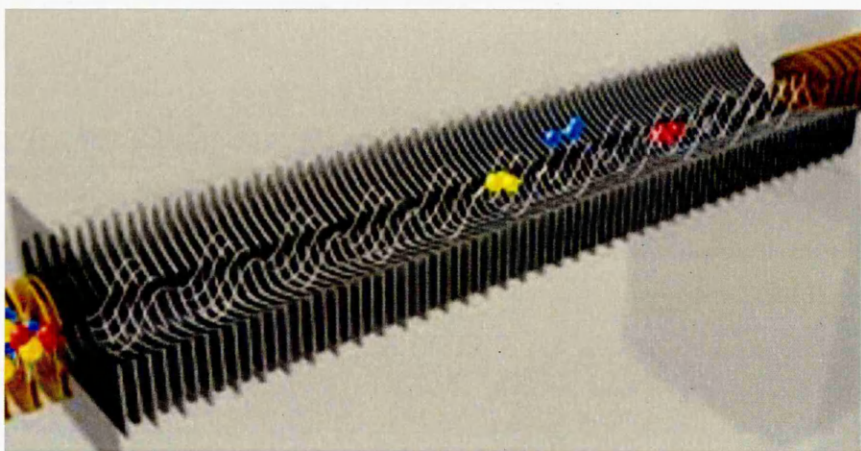


Figure 3.3 schematic of the inside of the ion mobility cell within the Synapt HDMS instrument (Water Corporation, Manchester, UK), shown are ions “surfing” the travelling wave along the stacked ring ion guides. ([www.youtube.com](http://www.youtube.com))

Figure 3.2 shows a schematic of the Synapt HDMS system (Waters Corporation, Manchester, UK) with inset a zoomed view of the schematic of the Tri-Wave region of the instrument containing the ion mobility cell. Indicated on the schematic are the regions where ms/ms fragmentation can be achieved. If ion fragmentation is performed in the Trap region of the instrument then the resultant fragment ions can be separated within the IMS cell, alternatively fragmentation can be performed in the Transfer region of the instrument. In this case all the fragment ions maintain the same drift time as the precursor ions because these ions have already been separated within the ion mobility cell. There is a third option and that is to effectively remove the ion mobility separation step from the system, if this is done the Tri-Wave region of the instrument acts as a series of ion guides transferring the ions to the TOF analyser.



## **3.2 Experimental methods.**

All animal studies were subject to ethical approval and all the animal use and handling in this work abides by UK Home Office Regulations and Guidelines.

### ***3.2.1 Organ Sample Preparation***

Organs were harvested and snap frozen by submersion in liquid nitrogen cooled isopentane for 30 seconds, once snap frozen the tissues were stored in a -80°C freezer until required. When required the tissues were removed from the freezer and placed in a CM1510 cryostat (Leica Microsystems, Wetzlar, Germany) set at -18°C and allowed to acclimatise for 30 minutes. Tissues were mounted onto cork discs in the desired orientation and fixed in place using the minimal amount of OCT, ensuring that no OCT embedding medium was near the area to be sampled. Sections (12µm) were cut and thaw mounted onto cleaned aluminium plates.

### ***3.2.2 Large Tissue Section Preparation.***

The euthanised animal was placed in a metal restraint this ensured the nose, spine and the base of the tail were aligned. This restraint was then frozen in a hexane/Cardice bath for 40mins. The animal was then placed into a frozen frame and surrounded with Carboxymethyl cellulose (CMC) and lowered back into the Hexane/Cardice bath for a further 20mins resulting in a solid block for sectioning.

Sections (30µm) were obtained using a Leica CM3050 cryostat (Leica Microsystems, Wetzlar, Germany) and placed onto cleaned aluminum plates

using the Macro-tape-transfer system (Instrumedics Inc, St Louis, MO), this involves coating the cleaned aluminum plates with a thin adhesive coating and allowed to dry. A 30 $\mu$ m whole body section was cut and adhered to an adhesive transfer tape, the section was then laid on the pre-coated aluminum plate. The sample was then covered and subjected to a UV light which causes the adhesive coating on the aluminum plate to polymerise bonding the section to the aluminum plate, the tape was then removed, leaving the section adhered to the aluminum plate, which was cut to size and spray coated with matrix.

### **3.2.3 Matrix Application.**

Tissue sections were cut to size and spray coated with 5mgml<sup>-1</sup>  $\alpha$ CHCA in 50:50:0.1 ethanol:water:TFA (v:v:v) for positive ion mode and for negative ion mode the sections were spray coated with 5mgml<sup>-1</sup>  $\alpha$ CHCA in 50:50 ethanol:water (v:v), both matrices were spray coated using a SunCollect automatic sprayer (SunChrom, Friedrichsdorf, Germany) by spraying an initial seeding layer at 1 $\mu$ l min<sup>-1</sup> followed by an additional layer sprayed at 2.5 $\mu$ l min<sup>-1</sup> and a further 3 layers at 5 $\mu$ l min<sup>-1</sup> until a uniform matrix layer was achieved without sample overwetting. Matrix coated tissue sections were then mounted onto Waters MALDI imaging targets (Waters Corporation, Manchester, UK) using double sided tape.

### **3.2.4 Mass Spectrometric Imaging.**

Sections were optically scanned using a CanoScan 4400F flatbed scanner (Canon, Reigate, UK) the digital image of the tissue section was imported into

MALDI Image Pattern Creator (Waters Corporation, Manchester, UK) In this software, the instrument was taught the dimensions of the image by locating the four corners of the image plate, this allowed the creation of the image area around the sample. The pattern was then uploaded into MassLynx (Waters Corporation, Manchester, UK) and the parameters of the image experiment were created. The instrument was operated in positive ion V-mode using a frequency tripled Nd:YAG (355nm) laser firing at a repetition rate of 200Hz. Prior to imaging analysis, the mass spectrometer was calibrated using a mixture of poly ethylene glycol (PEG) standards (Sigma-Aldrich, Gillingham, UK) with average molecular weights of 400 and 600, providing coverage of the m/z range studied. Image resolution was set to 150 $\mu$ m in both x and y directions, and the mass range was set to m/z 100-1500, to ensure a wide coverage of possible ions of interest.

### ***3.2.6 Ion Mobility Data Analysis.***

Ion mobility data analysis was performed using MassLynx 4.1 and DriftScope 2.1 software (Waters Corporation, Manchester, UK). DriftScope allows the visualisation of the imaging or profiling data by showing it as a colour map of drift time against m/z and the relative intensity as a colour change. This allows identification of ions of interest and the ability to show if there are any interfering isobaric ions which can be separated by their respective drift times. Isobaric ions which do show mobility separation can be selectively imaged by extracting the drift time information and converting the file to an Analyse 7.5 file format using MALDI image Converter software (Waters Corporation, Manchester, UK). MS/MS ion mobility separation data analysis was

performed by extracting the drift time information, and using MassLynx to show the MS/MS spectra for individual drift times allowing easier identification of ions by removing isobaric interferences.

### 3.2.7 Image visualisation

All images were processed using 'BioMap' ion imaging software (<http://www.maldi-msi.org>) resulting in the production of a 2D ion density map.

### 3.2.8 Mass Resolution

The mass spectral resolution required to separate two ions at a similar mass-to-charge can be calculated using the following equation. This has been performed for some of the ions which have been imaged.

$$\text{Mass Resolution required} = \frac{m/z \text{ of lowest ion}}{\text{mass difference between the two ions}}$$

This is conventionally written as:

$$R = \frac{m}{\Delta m}$$

Equation 3.1 Mass resolution ( $R$ ) required to separate two overlapping ions, the lowest ion  $m/z$  ( $m$ ) and with a mass difference ( $\Delta m$ ).

### 3.3 Results

#### 3.3.1 Lipid analysis

Lipid analysis provides a good platform to demonstrate some of the advantages of MALDI-IMS-MSI. Figure 3.4 shows a driftscope plot between  $m/z$ 700-750 from an image of a tumour xenograph imaged *in situ* in the dorsal flank of a whole body mouse section. At least 3 trends can be selected. Figure 3.5 shows the mass spectra of each of the trend lines highlighted in Figure 3.4. The ions associated with the shortest drift time consist primarily of chemical noise. The second trend line contains primarily phosphatidylinositols (PI) species and the final trend line contains primarily phosphatidylcholine (PC) and phosphatidylethanolamine (PE) lipids. This ability to separate ions based on their relative cross sectional area is a huge benefit for small molecule imaging applications.

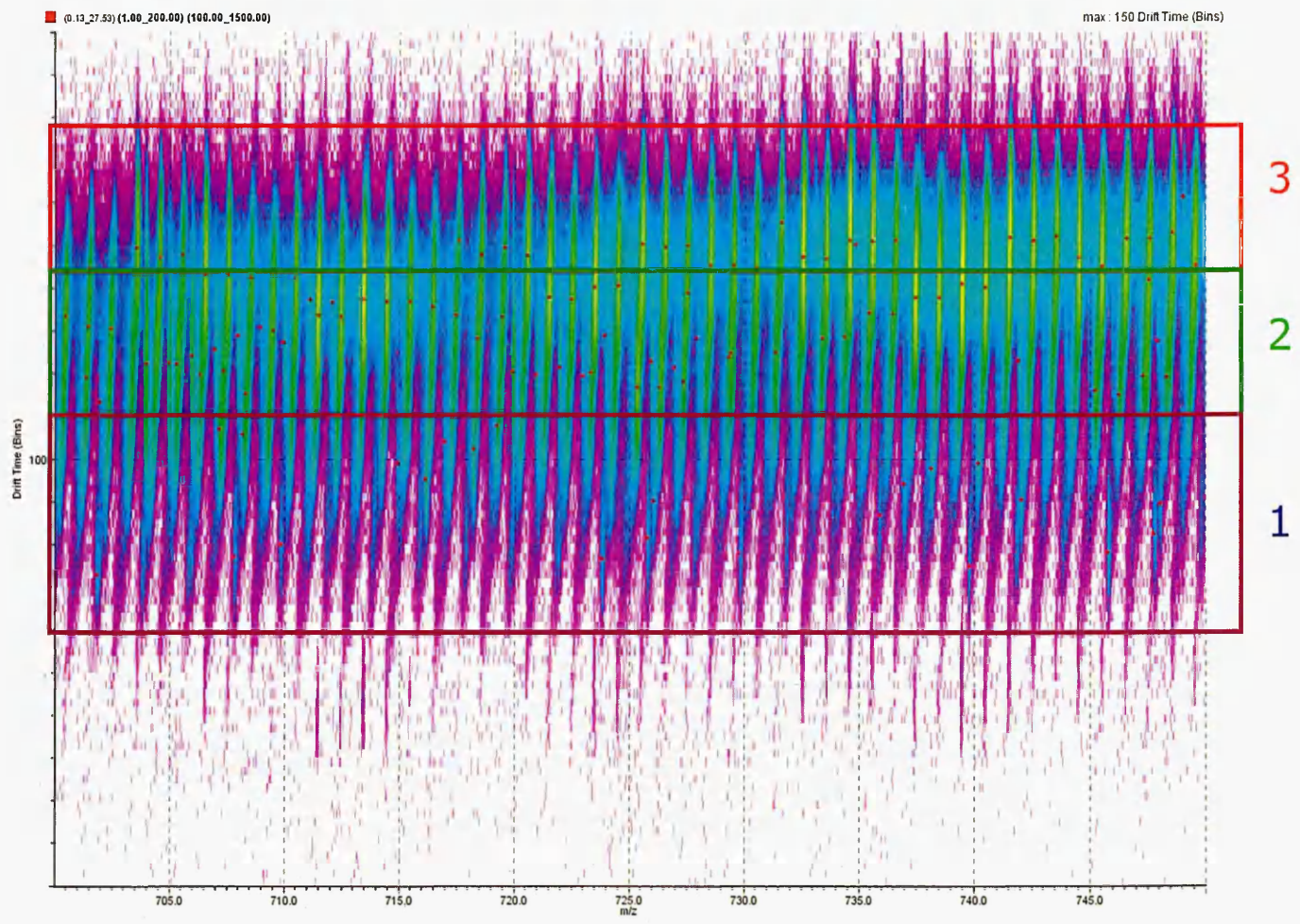


Figure 3.4 Driftscope plot of  $m/z$ 700 – 750 indicating the possible separation of lipid classes and chemical noise and matrix ions.



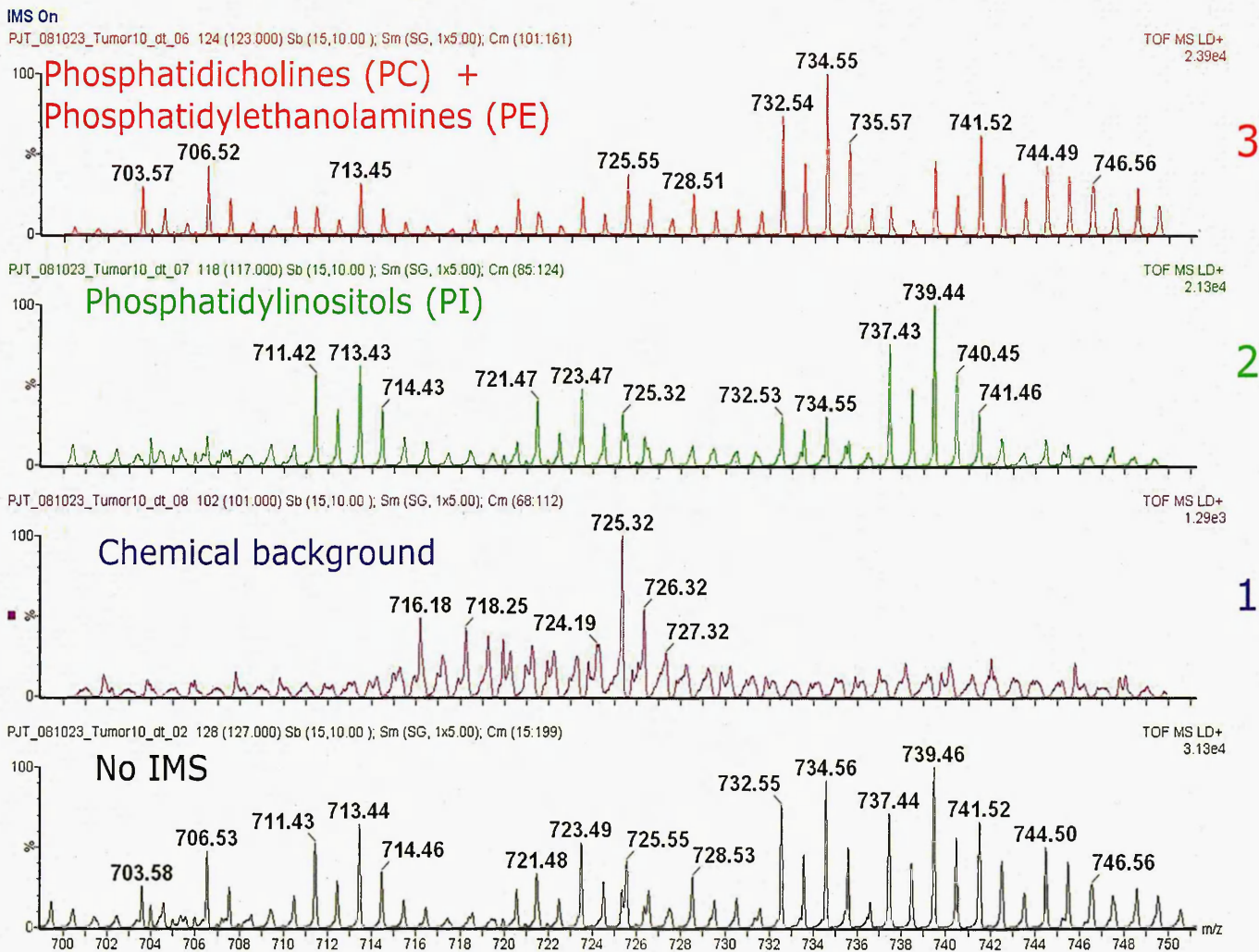


Figure 3.5 Mass spectra obtained from each of the 3 regions highlighted in figure 3.4 and a total mass spectra of the same region without IMS.

Assignment of the predominant lipid class within each of the IMS mass spectra shown in figure 3.5 is based on the mass-to-charge of some of the ions present. This possibility of separating lipid classes using ion mobility could improve the detection of certain lipids by positive ion MALDI-MS. Due to their excellent desorption/ionisation efficiency PC lipids dominate positive ion MALDI-MS mass spectra. This can cause some of the other ions to be masked. By using ion mobility the PC lipids can be separated from the rest of

the mass spectra allowing easier detection and visualisation of some of the lower abundance lipids.

### **3.3.2 Removal of matrix interference.**

One of the major issue in small molecule imaging using conventional MALDI-MSI is interference caused by matrix related ions within the low mass region. This is especially true when  $\alpha$ CHCA is used as the matrix, because there are several matrix clusters in the low mass region with associated sodiated and potassiated adducts. This advantage of MALDI-IMS-MSI can be seen in the mass spectra presented in Figure 3.6a Two ions of similar mass-to-charge can be observed. One is a  $^{13}\text{C}$  isotope of a possible matrix related ion at  $m/z$  401.072. This ion is interfering with the imaging of a potentially important ion of interest at  $m/z$  402.012 associated with rat kidney. Figure 3.6b & c also shows the biomap images for each ion.



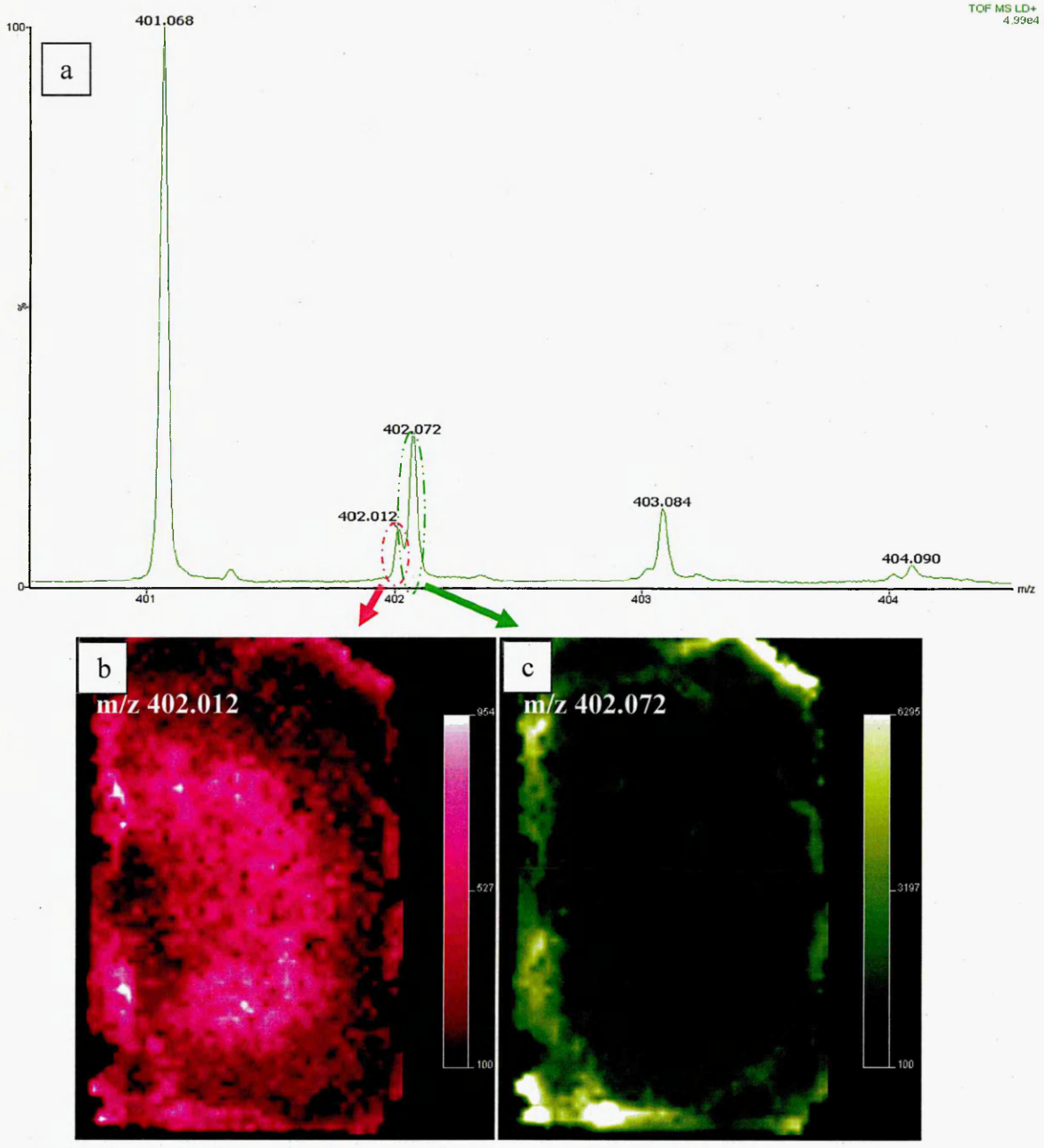


Figure 3.6 a) MALDI mass spectrum of rat kidney in the region  $m/z$  400 – 405, showing two overlapping peaks selected for imaging. b) 2D ion plot of ion  $m/z$  402.012 showing primary distribution of this ion within the kidney, and some surrounding signal. c) 2D ion plot of ion  $m/z$  402.072 showing its spatial distribution primarily in the surrounding matrix, and not in the kidney tissue.

The 2D ion plots shown in Figure 3.6 clearly show that the two ions have different distributions with conventional MALDI-MSI, Figure 3.6b shows the distribution of  $m/z$  402.012 that would be produced. One issue with the imaging mass resolution is due to Biomap binning the data into 0.2Da mass bins this markedly reduces the effective mass resolution of the image. This distribution is not the correct distribution for the ion  $m/z$  402.012 it is a combination image from  $m/z$  402.012 and interference from  $m/z$  402.072 due to the overlapping nature of the peaks within the mass spectra. Separation of these ions within this imaging experiment would be difficult.

The mass resolution required to separate these two ions can be calculated using equation 3.1.

$$R = \frac{m}{\Delta m}$$
$$R = \frac{402.012}{(402.072 - 402.012)}$$
$$R = \frac{402.012}{0.06}$$
$$R = 6700 \text{ to } 0 \text{ dp}$$

From this calculation the mass resolution required to separate these two different ions using conventional mass spectrometry requires an instrument with a mass resolution above ~6700. The Q-Star Pulsar-*i* has a specified mass resolution of ~10,000 at FWHM (Full Width at Half Maximum) at  $m/z$  850 (Baldwin *et al.*, 2001) and therefore should be able to separate these two ions. The Synapt HDMS also has a specified mass resolution of ~10,000 at FWHM at  $m/z$  1172 (Bagal *et al.*, 2008) and therefore should be able to separate these two ions based solely on their mass. The FWHM resolution at

m/z 401.068 is 7864 showing that these peaks should be resolved, but they are only partially resolved.

This can be overcome with the inclusion of ion mobility. Each of these two ions have a different drift time within the T-wave ion mobility cell of the Synapt (Water corporation, Manchester, UK).

The Driftscope plot for these ions is shown in figure 3.7a each ion has been encircled and the respective mobilagram which is a plot of drift time against intensity, is shown in figure 3.7b the differences in the two ions mobility can clearly be seen by the two peaks.

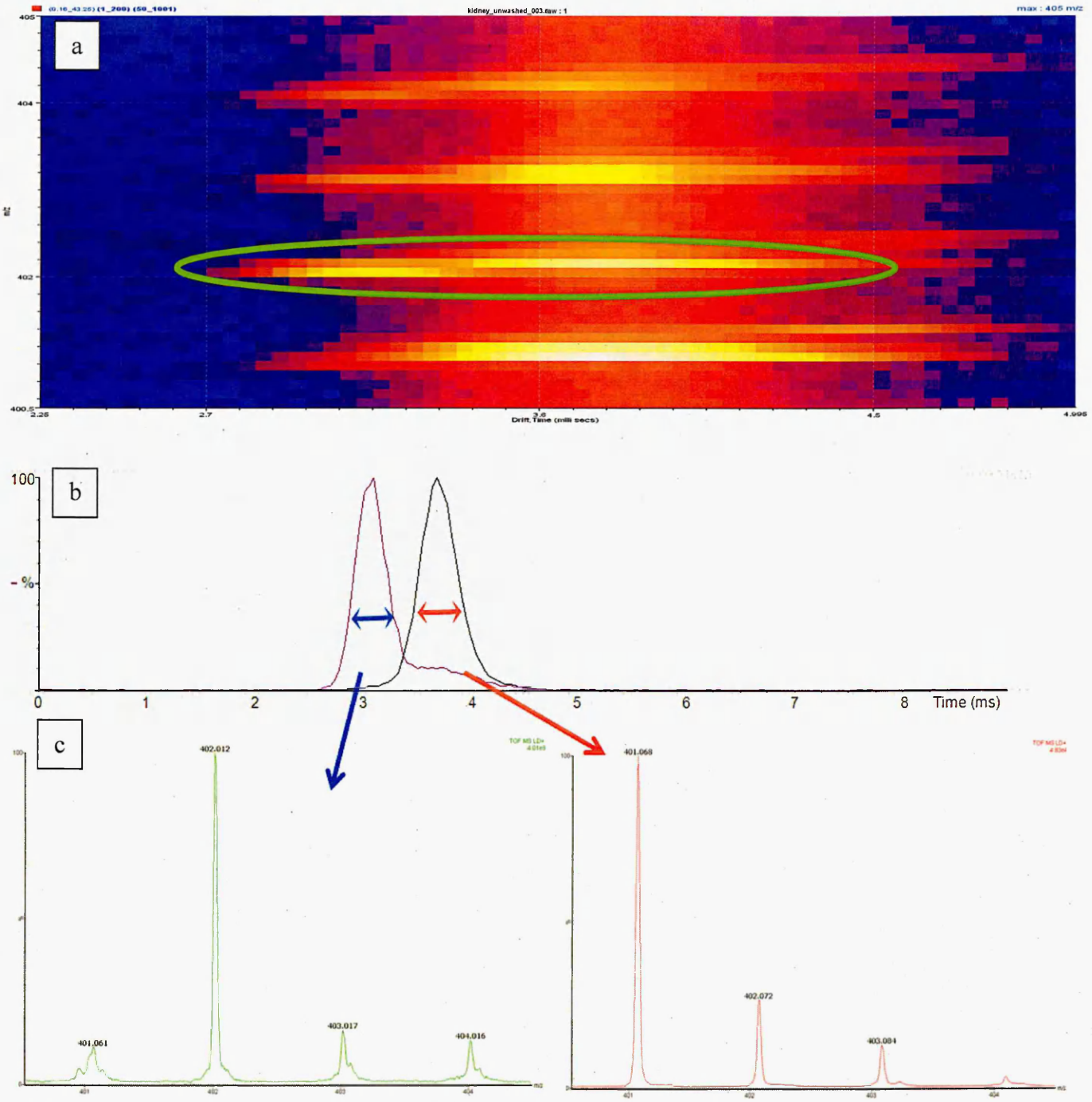


Figure 3.7 a) drift scope plot with the highlighted region of interest. b) Mobilogram of the two ions encircled in (a). c) mass spectra extracted from the Mobilogram showing the different ions associated with the differences in drift time.

With IMS separation

No IMS separation

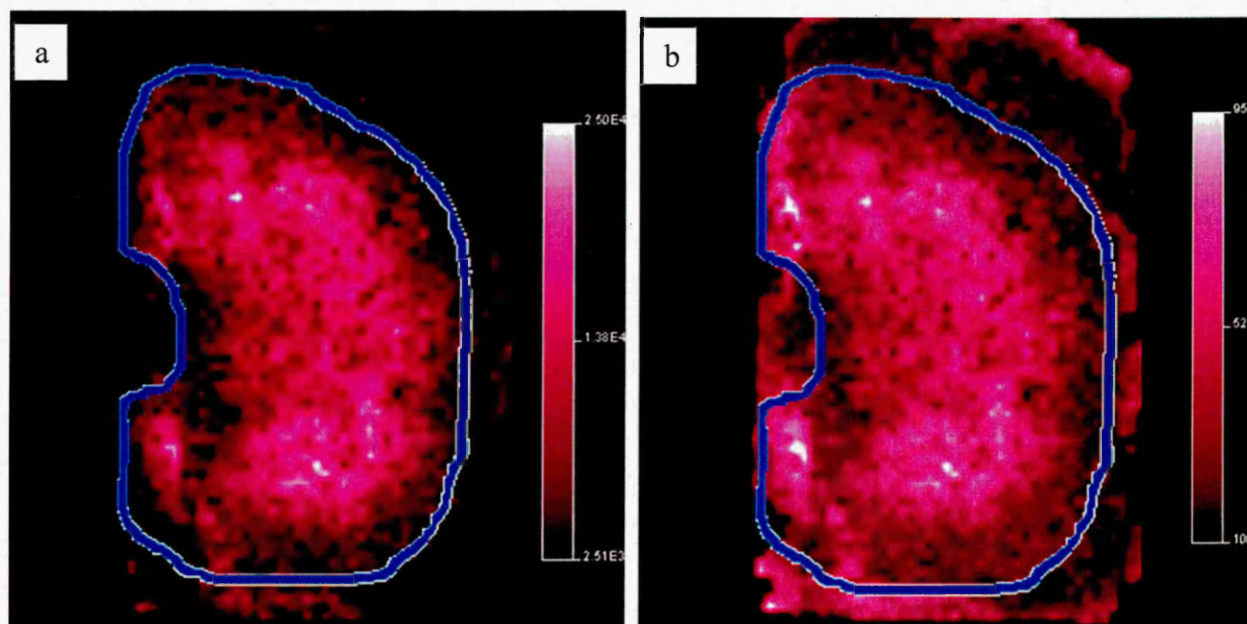


Figure 3.8 a) MALDI-MS image of  $m/z$  402.01 in a rat kidney section obtained a) with ion mobility separation on, b) without ion mobility separation. The ion mobility separation has removed the interference surrounding the kidney caused by unresolved chemical noise. Blue line indicating tissue margin, (Signal outside margin primarily due to chemical noise)

Figure 3.8 demonstrates the advantage of MALDI-IMS-MSI when analysing small molecules. The ion mobility has been shown to separate a matrix related ion from an endogenous species. This separation allows a more representative image of the distribution of the desired ion to be obtained.

### 3.3.3 Separation of ions of interest.

Shown above is an example of the ability to separate matrix related ions from endogenous species. This is not the only type of interference found within MALDI MSI. Another common problem is the interference of two or more potentially relevant endogenous ions. Providing the ions which are observed



have a difference in their respective average collisional cross sectional area then they normally can be separated using ion mobility.

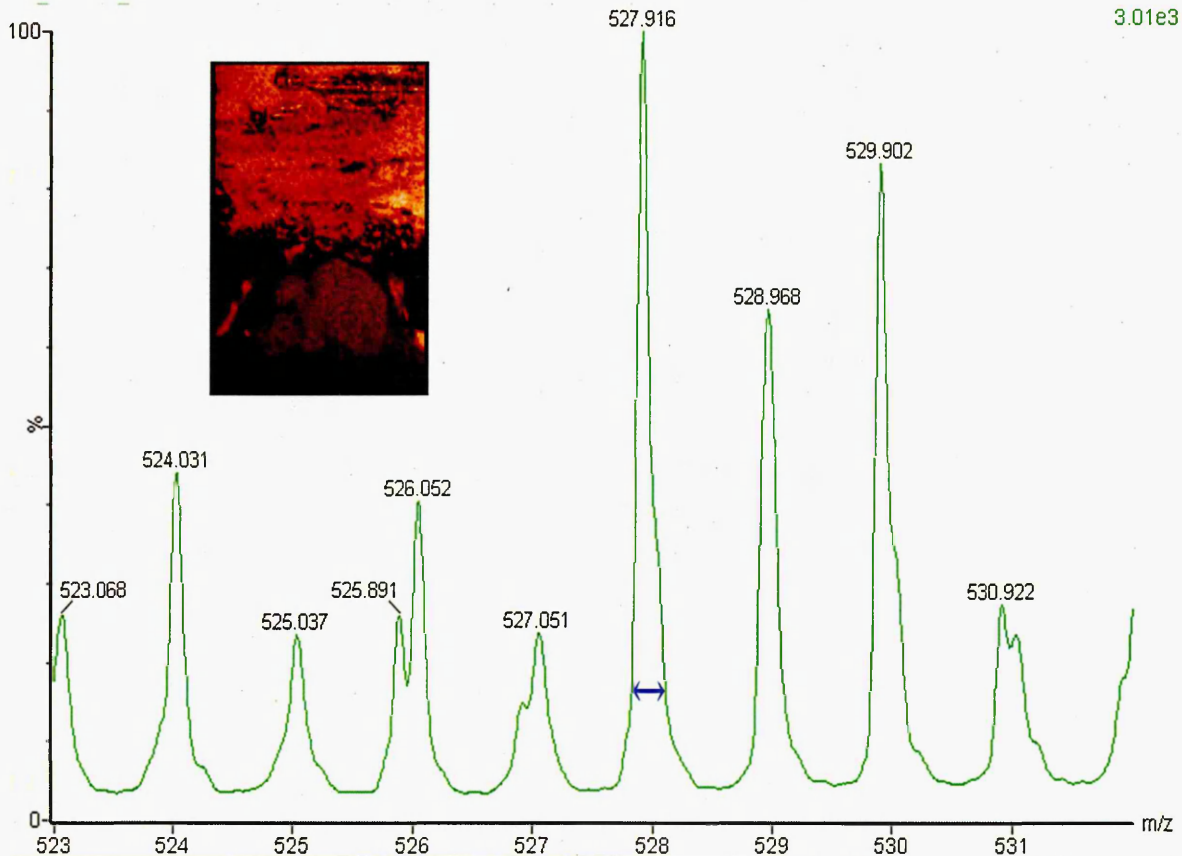


Figure 3.9 Partial MALDI mass spectrum obtained from a tissue section containing a DU145 tumour xenograph, highlighted is a peak at  $m/z$  527.916 with a shoulder of a second peak. Inset is the 2D ion plot of peak  $m/z$  527.916.

From the mass spectrum shown in figure 3.9 a peak at  $m/z$  527.916 can be seen with the shoulder of a second peak at  $m/z$  528.035 masked by the dominant peak. If this peak at  $m/z$  527.916 is imaged with a mass window of 0.2Da without the use of ion mobility the 2D ion map that is produced shows a relatively uniform distribution of this ion within the tissue section with a lower relative abundance within the tumour xenograph.

The same region of the mass spectra can be viewed using Driftscope 2.1, this allows the visualisation of the ion mobility separation. Figure 3.10 shows the Driftscope plot, encircled is the area of the driftscope plot containing the ion at  $m/z$  527.916 and the ion at  $m/z$  528.035. The two ions can be clearly seen within this region and that each has a slightly different drift time. The ions are separated based on their drift time even though they are not mass spectrally resolved.

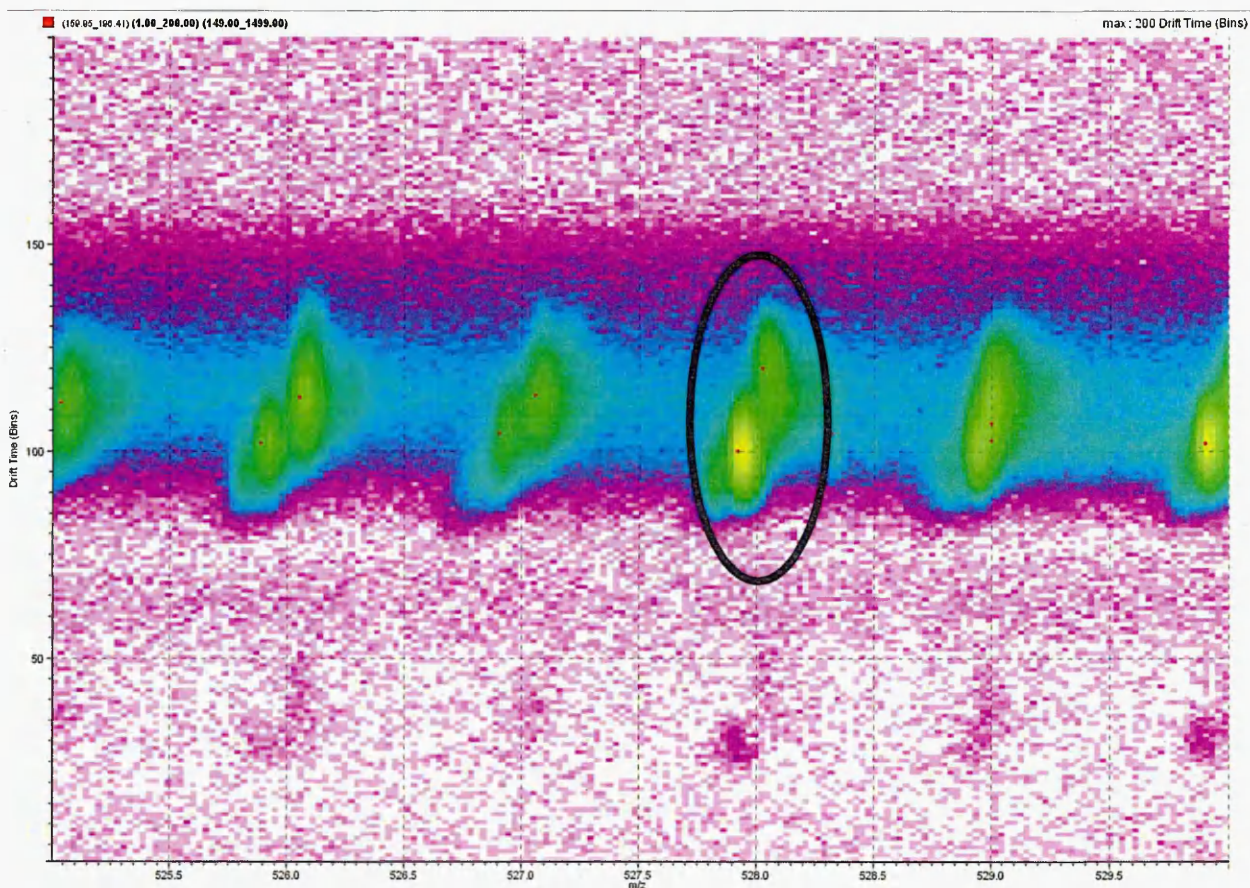


Figure 3.10 Driftscope plot of the same mass region as shown in figure 3.9, encircled is the ions that account for the peak at  $m/z$  527.916 there are at least 2 ions which are accounting for this peak.

The Mobilogram plot of the drift time for the two ions at  $m/z$  527.916 and  $m/z$  528.035 are shown in figure 3.11. Two different drift times can be seen for these ions, however base line separation does not occur. The drift time associated spectra are shown in figure 3.12 (a and b)

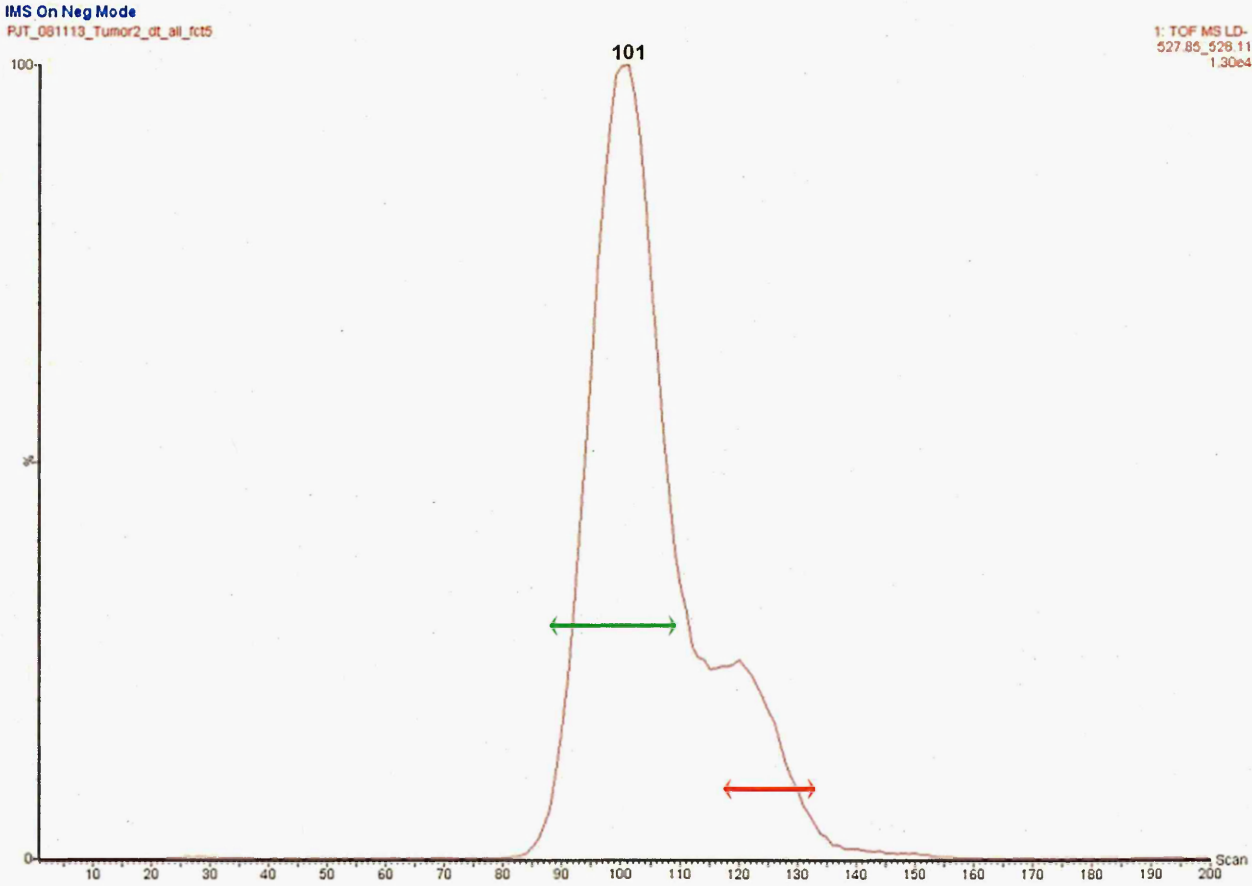


Figure 3.11 Mobilogram from the peak at  $m/z$  527.9, this shows two different drift times associated with this mass range.



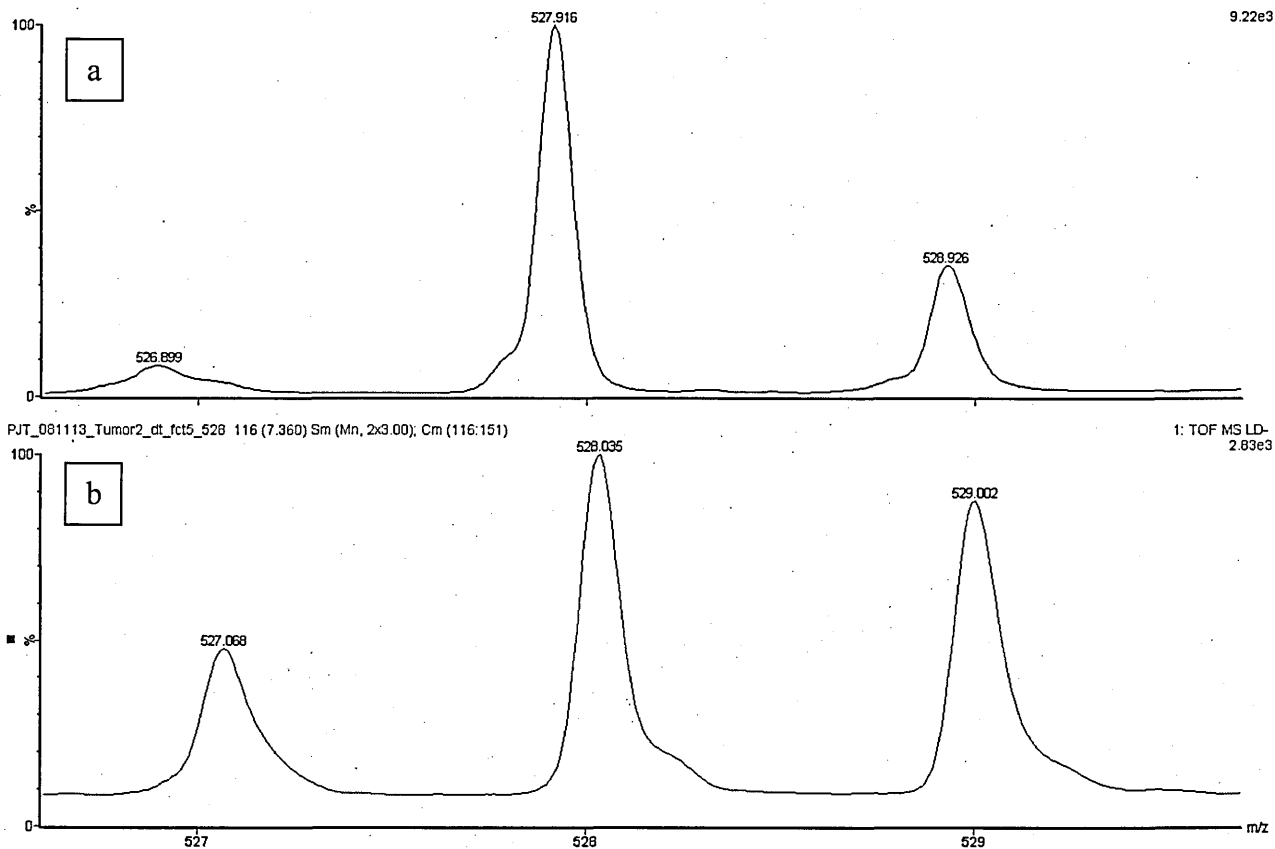


Figure 3.12a) MALDI mass spectra obtained after ion mobility separation showing the ions accounting for the faster drift time. b) Mass spectra accounting for the peak with the slower drift time shown in figure 3.11

The resolution required to resolve these peaks can be calculated using equation 3.1.

$$R = \frac{m}{\Delta m}$$

$$R = \frac{527.916}{(528.035 - 527.916)}$$

$$R = \frac{527.916}{0.119}$$

$$R = 4436 \text{ to } 0 \text{ dp.}$$

From this calculation the mass resolution required to separate these two different ions using conventional mass spectrometry requires an instrument with a mass resolution above  $\sim 4436$ . As mentioned above the Q-Star Pulsar-*i* has a specified mass resolution of  $\sim 10,000$  at FWHM at  $m/z$  850 (Baldwin *et al.*, 2001) and therefore should be able to separate these two ions. The Synapt HDMS also has a specified mass resolution of  $\sim 10,000$  at FWHM at  $m/z$  1172 (Bagal *et al.*, 2008) and therefore should be able to separate these two ions based solely on their mass.

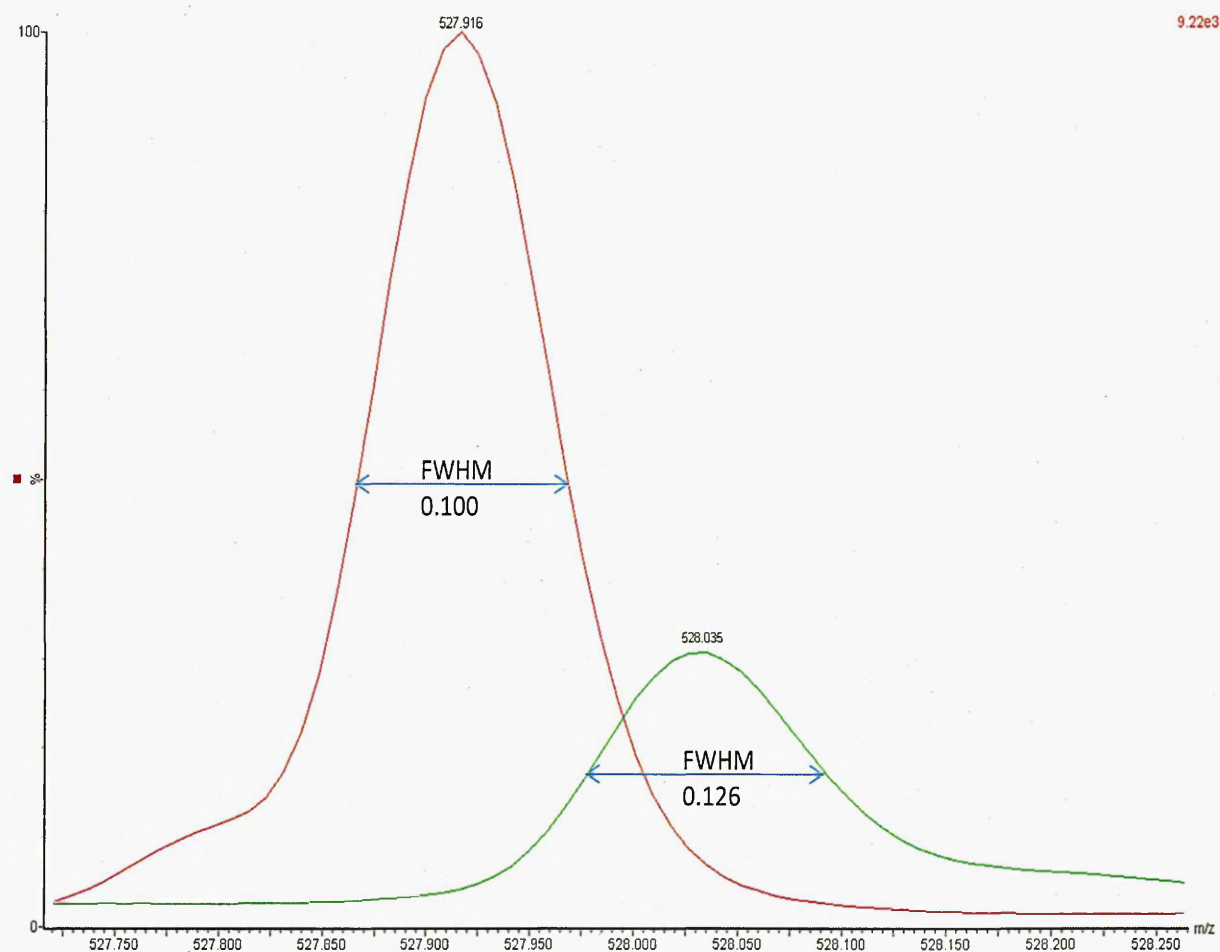


Figure 3.13 Mass spectra of the overlapping ions at  $m/z$  527.916 and 528.035 after ion mobility separation showing the measurements at FWHM.

From the ion mobility separated spectra the resolution obtainable at  $m/z$  527.916 is 5279.16 at FWHM showing that these two peaks can be separated. The separation of these peaks can be seen in figure 3.13. These peaks are not base line resolved but there is a clear valley between the two peaks. The smaller peak at  $m/z$  528.035 has a resolution of  $\sim 4190$  (FWHM) which is less than the required resolution to separated these two peaks at half maximum, hence the over lapping nature of these peaks.

Figure 3.12 shows the mass spectra selected from the drift times determined in figure 3.11. The mass spectra now show that there is definitely two peaks present, one at  $m/z$  527.916 and the other peak which was accounting for the shoulder of the previous peak at  $m/z$  528.035. Because the two ions have been separated their drift times were used to extract the data for the images. Figure 3.14a shows the 2D ion plot which is created from the ion mobility separated data for the ion at  $m/z$  527.916 it can now be seen that the area in the top right hand side of the image is now missing. This image is the opposite of the image created by imaging the ion mobility separated ion at  $m/z$  528.035 where this ion is localised solely within the bone tissue of the mouse section.

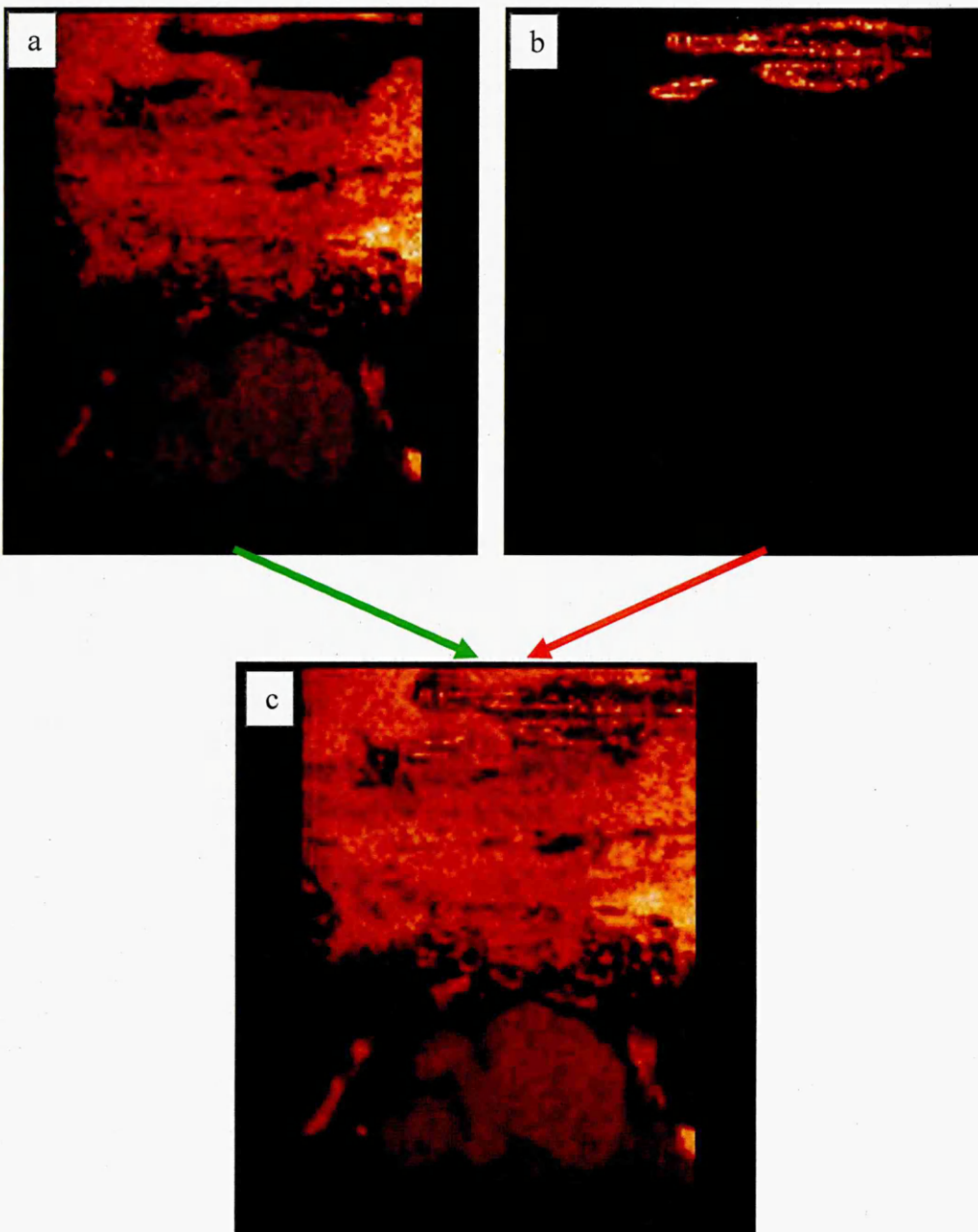


Figure 3.14a) 2D ion plot of the ion mobility separated ion at  $m/z$  527.916. b) 2D ion plot of the ion mobility separated ion at  $m/z$  528.035 each of these two ions have very different distributions within the tissue. c) 2D ion plot of  $m/z$  527.8 - 528.0 without ion mobility separation.

### **3.3.4 Separation of endogenous and xenobiotic species.**

The separation of endogenous/matrix ions from ions relating to xenobiotics is possibly one of the most important areas for the application of MALDI-IMS-MSI. This topic will be discussed in detail in chapters 4 and 5 of this thesis.

## **3.4 Conclusion**

In this work, some of the benefits of MALDI-IMS-MSI have been demonstrated compared to conventional MALDI-MSI, using a MALDI Synapt HDMS system (Water Corporation, Manchester, UK). Separation of lipid classes based on their mobility has been shown which can simplify spectra from complex samples, by the removal of ion classes not required in the analysis. Also shown is the use of MALDI-IMS-MSI for the removal of interfering ions from imaging results thus increasing the confidence in the spatial distribution observed for ions of interest within MALDI imaging experiments. Demonstrated is the removal of matrix related ions affecting imaging of endogenous ions allowing the removal of the matrix ring of interference surrounding tissue sections and other matrix interferences. The benefit of the additional separation step obtained by ion mobility has been shown to be highly effective in separating endogenous ions of interest with different average collisional cross sectional areas which could have completely different distribution which when using conventional MALDI-MSI could be missed and the distribution differences could be overlooked.

MALDI-IMS-MSI allows for increased confidence of the images acquired and allows for a true representation of ion distribution within tissue sections.

The resolution of the Synapt HDMS (Waters Corporation, Manchester) is reported as being 10,000 at  $m/z$  1172 FWHM (Bagal *et al.*, 2008), within the work reported here the best calculated resolution was 7864 at  $m/z$  401.068. The reduction in the mass resolution obtainable from MALDI-MSI of tissue frequently observed. This is possibly due to the complexity of the signals observed from on tissue MALDI, resulting in overlapping peaks. The work reported here was also based on summed spectra from an image which causes slight broadening of the peaks due to slight statistical mass variation hence increasing the full width at half maximum and reducing the calculated resolution. Also compression of the data within Biomap software may be an issue.

It is accepted that these ions could be imaged on conventional MALDI-MSI platforms using  $ms/ms$  techniques however the ion mobility allows this separation without  $ms/ms$ . This could allow the imaging of multiple ions of interest with similar specificity as  $ms/ms$  techniques without the compromises in the number of analytes that can be imaged within a single imaging experiment.

### 3.5 References

- Bagal D; Zhang H; Schnier P. D. **2008**, *Anal. Chem.* 80, 2408-2418.
- Baldwin M. A; Medzihradzky K. F; Lock C. M; Fisher B; Settineri T. A; Burlingame A. L. **2001**, *Anal. Chem.* 73, 1707-1720.
- Fuchs B; Schiller J. **2008**, *Eur. J. Lipid Sci. Technol.* 111, 1, 83-98.
- Fuchs B; Schiller J; Cross M.A. **2007**, *Chem. Phys. Lipids.* 150, 229-238.
- Fuchs B; Schiller J; Wagner U; Hantzschel H; Arnold K. **2005**, *Clin. Biochem.*, 38, 925-933.
- Giles K; Pringle S.D; Worthington K.R; Little D; Wildgoose J.L; Bateman R.H. **2004**, *Rapid Commun. Mass Spectrom.* 18, 2401-2414.
- Jackson S.N; Ugarov M; Egan T; Post J.D; Langlais D; Schultz J.A; Woods A.S. **2007**, *J. Mass Spectrom.* 42, 1093-1098.
- Jackson S.N; Wang H-Y.J; Woods A.S. **2005**, *J. Am. Soc. Mass Spectrom.* 16, 133-138.
- Khatib-Shahidi S; Andersson M; Herman J.L; Gillespie T.A; Caprioli R.M. **2006**, *Anal. Chem.* 78, 6448-6456.
- Matsumoto T; Kobayashi T; Kamata K. **2007**, *Curr. Med. Chem.* 14, 3209-3220.
- Modrak D.E; Gold D.V; Goldenberg D.M. **2006**, *Mol. Cancer Ther.* 5 (2), 200-208.
- Ogretmen B. **2006**, *FEBS Letters*, 580, 5467-5476.
- Reyzer M.L; Hsieh Y; Ng K; Korfmacher W.A; Caprioli R.M. **2003**, *J. Mass Spectrom.* 38, 1081-1092.
- Stoekli M; Staab D; Schweitzer A. **2007**, *Int. J. Mass Spectrom.* 260, 2/3, 195-202.
- Troendle F.J; Reddick C.D; Yost R.A. **1999**, *J. Am. Soc. Mass Spectrom.* 10, 1315-1321.

## CHAPTER 4

---

### **Matrix Assisted Laser Desorption Ionisation - Ion Mobility Separation - Mass Spectrometry Imaging of Vinblastine in Whole Body Tissue Sections**



## **Matrix Assisted Laser Desorption Ionisation - Ion Mobility Separation - Mass Spectrometry Imaging of Vinblastine in Whole Body Tissue Sections.**

### **4.1 Introduction**

#### **4.1.1 MALDI-MSI**

Since the development of MALDI imaging it has been used for the study of the distribution of a variety of biomolecules. In addition to imaging, statistical packages have been used to assist in the identification of tissue markers. McCombie et al., 2005 presented work using clustering and multivariate analysis for the improved imaging of rat brain sections. Van de Plas et al., 2007 showed the use of PCA statistical analysis to aid tissue morphology assessment using MALDI imaging. Within this work each principle component of a data set obtained from a rat spinal cord was imaged showing some of the morphological features. Prideaux et al., 2007 presented work using PCA to distinguish between control and hydrocortisone dosed porcine skin, identifying ions associated with each of the two groups. Within chapter 2 of this thesis the possibility of using PCA to identify possible ions of interest from a MALDI imaging data set obtained from a rat brain sagittal section has been shown, using PCA ions associated with white or grey matter were identified, as well as ions predominantly associated with distinct brain regions. Such packages can be used to overlay drug distribution patterns and to clearly identify the localisation of a drug or metabolite within a tissue section.

#### 4.1.2 Xenobiotic MALDI-imaging

The first demonstration of the use of MALDI to directly study pharmaceutical compounds in animal tissue was published by Troendle *et al.*, 1999. In this work, the matrix was applied to the tissue surface by pipetting and electrospraying followed by analysis using MALDI quadrupole ion trap mass spectrometry. The technique was employed to detect the anti-cancer drug paclitaxel in a human ovarian tumour and the anti-psychotic drug spiperone in spiked sections of rat liver tissue.

Caprioli's group have worked on studies of drug distribution in collaboration with Schering-Plough. They have reported a study of the distribution of anti-tumour drugs in mouse tumour tissue and rat brain (Reyzner *et al.*, 2003). In these experiments, the matrix was applied to intact tissue by either spotting small volumes of the matrix in selected areas, or by coating the entire surface by pneumatic spraying. MALDI images were created by using the tandem mass spectrometric technique of selected reaction monitoring (SRM) to specifically monitor the drug under study. Such an approach minimises the potential for ions arising from either endogenous compounds or the MALDI matrix to interfere with the analyte signals. The brain has in fact been the most common target for MALDI-MSI studies of drug distribution, Hsieh *et al.*, 2006 & Hsieh *et al.*, 2007, have reported the detection and imaging of clozapine in rat brain tissue by an SRM approach and Wang *et al.*, 2005 have reported the localisation and analysis of chlorisondamine and cocaine in rat

brain following either intracranial or intraperitoneal injection, although imaging was not attempted in this work.

Rohner *et al.*, 2005 reviewed MALDI imaging and described imaging work being carried out at Novartis. In this article they demonstrated for the first time the use of MALDI-MSI to study drug distribution in a whole body mouse section. In a more recent report this group describe some of the practical aspects of obtaining MALDI-MSI data for drug and metabolite distributions in whole body sections and report on some of the limitations of the technique (Stoeckli *et al.*, 2007). This pioneering work was extended by Khatib-Shahidi *et al.*, 2006 who combined this approach with their own work on protein imaging to produce whole body images showing the location of drug, drug metabolites and endogenous markers for various organs of the body. The exciting possibility of imaging markers of efficacy along with the analytes to provide *in-vivo* pharmacodynamic data is discussed in their article. Atkinson *et al.*, 2007 showed in a study of the distribution of the bioreductive anti-cancer drug AQ4N in H460 lung tumour xenografts, that not only could the pro-drug and its active form be imaged in one experiment, but that imaging the distribution of ATP co-localised the active reduced form of the drug to regions of hypoxia.

Another application of MALDI-MSI in drug and xenobiotic distribution has been the study of trans-dermal absorption (Bunch *et al.*, 2004). Here it was demonstrated that the absorption of the anti-fungal agent ketoconazole into skin could be examined by MALDI-MSI by the use of an indirect tissue blotting

approach. This work has been subsequently extended to show that the absorption of a wide range of xenobiotics into skin can be studied, but the sample preparation technique required *i.e.* direct or indirect imaging, and the choice of substrate for indirect imaging, is hugely influenced by the analyte (Prideaux *et al.*, 2007). In the same paper this group have also described some preliminary data from a combined solvent assisted transfer/derivatisation approach to sample preparation that may be useful for particularly intractable analytes.

During early stage drug development, drug and metabolite distribution studies are carried out in animal tissues using a range of techniques including Whole Body Autoradiography (WBA), this technique images the spatial distribution of a radiolabelled isotope within whole body sections. Whilst widely employed WBA has a number of limitations, firstly it requires the expensive synthesis of radiolabelled drugs (Ulberg *et al.*, 1954). WBA does not distinguish between a parent drug and its metabolites as it only images the radiolabel, which in some cases may be one of the drug metabolites and not the whole drug, thus providing misleading results. Further analysis is usually required to obtain additional information on the chemical species *i.e.* whether it is the parent drug or a metabolite that is present. This invariably involves the homogenisation of tissues for subsequent HPLC-MS analysis, however, in this process spatial specificity is lost.

Recent improvements in MALDI-MS imaging have shown the possibility of imaging drug and metabolite distribution in tissue with previously unobtainable

spatial resolution and analyte specificity. Several groups have presented data on xenobiotic distribution within whole body sections since the first report by Rohner *et al.*, 2005 and they showed the distribution of an administered drug within the central nervous system of a whole body section of a mouse. This work has been extended by several groups, including Stoeckli *et al.*, 2007 who demonstrate a method for sectioning whole body sections and collecting them on adhesive tape, sections were freeze-dried before mounting them on to MALDI target plates using double sided tape. Spray coating with matrix was finally followed by gold sputter coating. Their findings showed good correlation between the WBA and MALDI MSI data after an intra-tracheal administration of 0.5mg/kg of an undisclosed compound. The distribution of the parent drug and metabolite could be seen in the MSI data after oral dose but the WBA could not discriminate. Khatib-Sahahidi *et al.*, 2006 presented whole body imaging of proteins within rat sections, to discriminate between different tissue regions and to identify protein signals related to mouse glioma tumour and healthy mouse tissue. This work also demonstrated the ability of whole body imaging to show the distribution of olanzapine and two of its metabolites, at different time points, showing the distribution differences between each metabolite and the whole drug.

#### **4.1.3 MALDI-IMS-MS**

One recent advance in MALDI MSI instrumentation is the addition of a further dimension of separation, namely ion mobility separation (IMS). IMS separates ions on the basis of not only charge and mass but also by the ions collisional cross sectional area, thus allowing the possible separation of

isobaric ions (Jackson *et al.*, 2007). MALDI-Ion Mobility Separation-MS imaging has the ability to improve the imaging of some drugs and metabolites by separating xenobiotic related ions from endogenous or matrix related isobaric ions, thus improving the confidence in the image interpretation. Ion mobility separation within MS/MS experiments allows a range of precursor ions to be admitted into the ion mobility cell to undergo ion mobility separation, which can then be followed by dissociation within the transfer region, resulting in the product ions all having the same drift time as their respective precursor ion. This allows multiple MS/MS data to be acquired within a single experiment or laser shot. In this work we have studied the distribution of vinblastine ( $C_{46}H_{58}N_4O_9$ ) in rat whole body tissue sections, using a commercial quadrupole time of flight instrument incorporating ion mobility separation in order to compare MALDI-MS, MS/MS, IMS-MS and MALDI-IMS-MS/MS. A comparison of the various MALDI imaging modalities with whole body autoradiography employing tritiated ( $^3H$ ) vinblastine has also been conducted.

#### 4.1.4 Synapt HDMS

A full description of the MALDI Synapt HDMS™ (Waters Corporation, Milford, USA) instrument is given elsewhere (Pringle *et al.*, 2006 and within Chapters 1 & 3 of this Thesis), but a brief description will be given here. This instrument has a quadrupole orthogonal acceleration time-of-flight geometry and is equipped with an ion mobility separation device located between the quadrupole and the time-of-flight analyser. The ion mobility separator used consists of three consecutive travelling wave ion guide (TWIG) regions

(Figure 4.1). Giles *et al.*, 2004 give a detailed description of travelling wave ion guides. Ion mobility separation is performed in the middle travelling wave ion guide device. The first travelling wave ion guide is used to store ions when an ion mobility separation is performed and gate ions into the ion mobility separation TWIG when required. This maximises the duty cycle of the ion mobility separation. This region is referred to as the trap T-wave. The final travelling wave device is used to transfer ions from the ion mobility separator to the time-of-flight mass analyser and is referred to as the transfer T-wave. Collision induced dissociation can be achieved in either or both the trap or transfer T-wave. The middle TWIG is where the ion mobility separation occurs. This is achieved using travelling low voltage waves which transverse the TWIG in the presence of a low pressure inert gas.

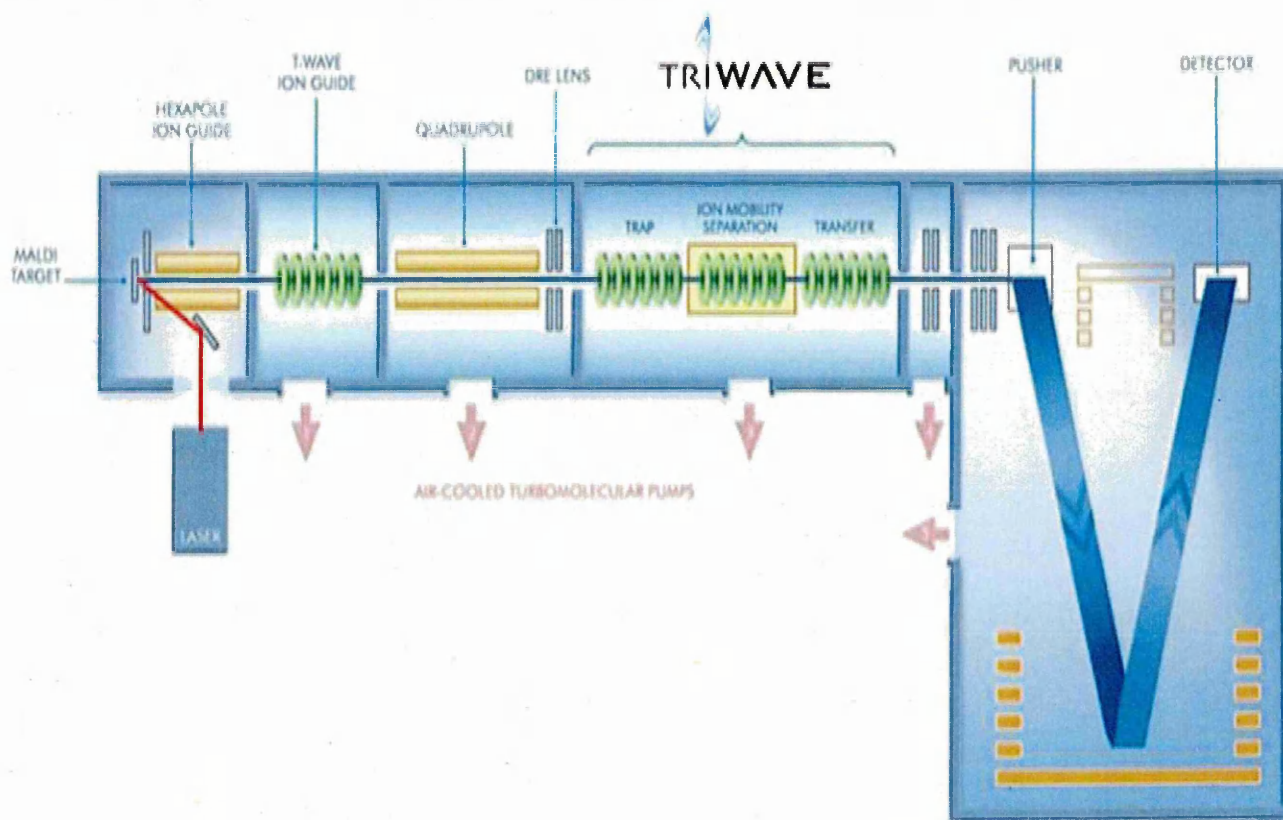


Figure 4.1 Schematic of the MALDI HDMS SYNAPT system, this instrument has a quadrupole orthogonal acceleration time-of-flight geometry and is equipped with an ion mobility separation device located between the quadrupole and the time-of-flight analyser. The ion mobility separator used consists of three consecutive travelling wave regions: The Trap T-Wave, Ion Mobility separation T-Wave and the transfer T-wave. Collision induced dissociation can be achieved in either or both the trap or transfer T-wave. (Waters, Manchester, UK)

The instrument used for the study reported here was equipped with an interchangeable MALDI source, which can be replaced with atmospheric pressure ionisation sources, such as electrospray ionisation, atmospheric pressure chemical ionisation *etc.* Matrix assisted laser desorption/ionisation was performed in an intermediate pressure environment ( $9 \times 10^{-2}$  mbar) using a frequency tripled Nd:YAG laser (355 nm). Imaging data was obtained by



moving the tissue sections in a raster pattern on an x/y-stage relative to the laser position, which remained fixed.

#### 4.1.5 Vinblastine

Vinblastine ( $C_{46}H_{58}N_4O_9$ ) is a chemical analogue of vincristine ( $C_{46}H_{56}N_4O_{10}$ ) (Figure 4.2) and was first isolated from the Madagascar periwinkle plant. Both Vinca alkaloids vinblastine and vincristine act by binding to tubulin and inhibit microtubule assembly thus arresting cell growth during metaphase (Zhigaltsev *et al.*, 2005). Tellingen *et al.*, 1993 have also shown vinblastine by HPLC-MS to be extensively distributed within the body, and retained within several body tissues including the GI tract where it has been detected 72 hours after administration of a 6mg/kg I.V. dose. The retention of vinblastine and its major metabolite desacetylvinblastine within certain tissue type is thought to be the reason behind vinblastine's efficacy against certain tumour types derived from malignant transformations of these tissue types (GE Healthcare UK Limited, 2006).

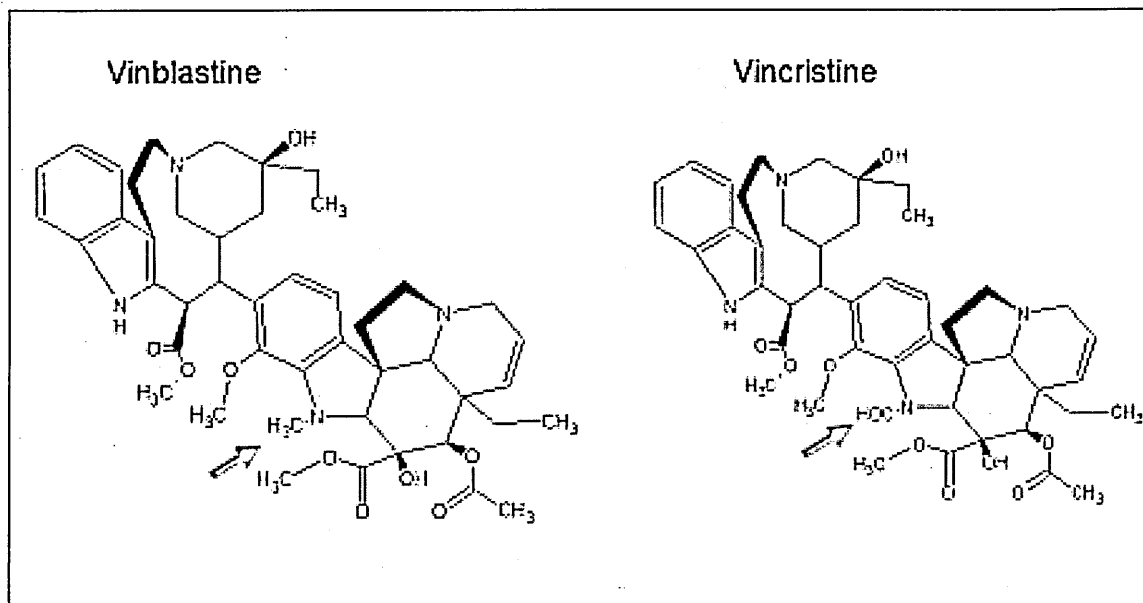


Figure 4.2 Structures of Vinblastine ( $C_{46}H_{58}N_4O_9$ , mono isotopic mass 810.420) and vincristine ( $C_{46}H_{56}N_4O_{10}$  mono isotopic mass 824.400) structures. These compounds are chemical analogues of each other with a difference on one group between a  $CH_3$  and  $COH$ . Indicated is the difference between the two molecules.

The overall aims of this work were to image the distribution of vinblastine within rat whole body sections 1 hour post dose, to show the initial distribution of vinblastine, and to show the spatial distribution of the drug within the tissues. Also a comparison of WBA with MALDI imaging for direct drug distribution analysis within rat whole body sections was made along with an investigation of any advantages arising from combining ion mobility separation with MALDI MSI for imaging xenobiotic distributions within tissues.

## 4.2 Experimental

All animal studies were conducted in accordance with UK Home Office Regulations and Guidelines.

### 4.2.1 Preparation of Tissue Sections

#### 4.2.1.1 Sample Preparation for non radiolabelled vinblastine.

The dose formulation was 5.974mg of the Vinblastine sulfate salt in 1ml of saline, purity was checked by HPLC using a Gemini 5µm column (C18, 250,4.6cm) with mobile phases 25mM ammonium acetate in water and 25mM ammonium acetate in methanol.

In this cold dose experiment two Sprague-Dawley (CrI: CD®BR – Albino) rats (265g and 251g) were injected intravenously with 6mg/kg Vinblastine and euthanised 1 hour post dose.

#### 4.2.1.2 Sample Preparation for radiolabelled <sup>3</sup>H vinblastine.

Tritiated Vinblastine was purchased from GE Healthcare (Buckinghamshire UK) as a solution in methanol and was stored at -20°C until required, radio chemical purity was 98.4% and the specific activity was 333MBq/mg (9.01mCi/mg) (Tellingan *et al.*, 1993), the dose formulation was made by adding 0.0055µg of the radiolabelled vinblastine to 12.04mg of the non radiolabelled vinblastine, and dissolving this in 2ml saline, resulting in a final concentration of ~6.02mg/ml.

Two Sprague-Dawley (CrI: CD®BR – Albino) rats (351g and 387g) were injected intravenously with 6mg/kg  $^3\text{H}$ -Vinblastine and euthanised 1 hour post dose.

#### **4.2.1.3 Sample Oxidation.**

The brain, liver, kidney and the plasma were harvested from two animals 1 and 4 hours following the administration of the  $^3\text{H}$  Vinblastine. These organs were then homogenised using a bench top homogeniser. After homogenisation 163.9mg brain homogenate, 197.2mg kidney homogenate, 207.2mg liver homogenate and 503.1mg of plasma were each placed into ashless combustion cones (Perkin-Elmer), each cone was then combusted using a 307 Packard Oxidise (Perkin Elmer Life Sciences), the sample remaining after combustion was mixed with 10ml Monophase Solution and 5ml water to produce a scintillation cocktail. The radioactivity within each cocktail was then counted using a Tri-carb 2300TR liquid scintillation counter (Perkin Elmer Life Sciences) giving a result in dpm for each sample, this was then converted to  $\mu\text{g}$  equiv/g using the known specific activity.

#### **4.2.1.4 Sample Preparation.**

Each euthanised animal was placed in a metal restraint this ensured the nose, spine and the base of the tail were aligned, this restraint was then frozen in hexane/Cardice bath for 40 mins. The animal was then placed into a frozen frame and surrounded with Carboxymethyl cellulose (CMC) and lowered back into the Hexane/Cardice bath for a further 20 mins resulting in a solid block for sectioning.

Sections (30 $\mu$ m) were obtained using a Leica CM3050 cryostat (Leica Microsystems, Wetzlar, Germany). Sections were taken at a set level through the sample to show the kidney, liver, heart (Figure 4.3).

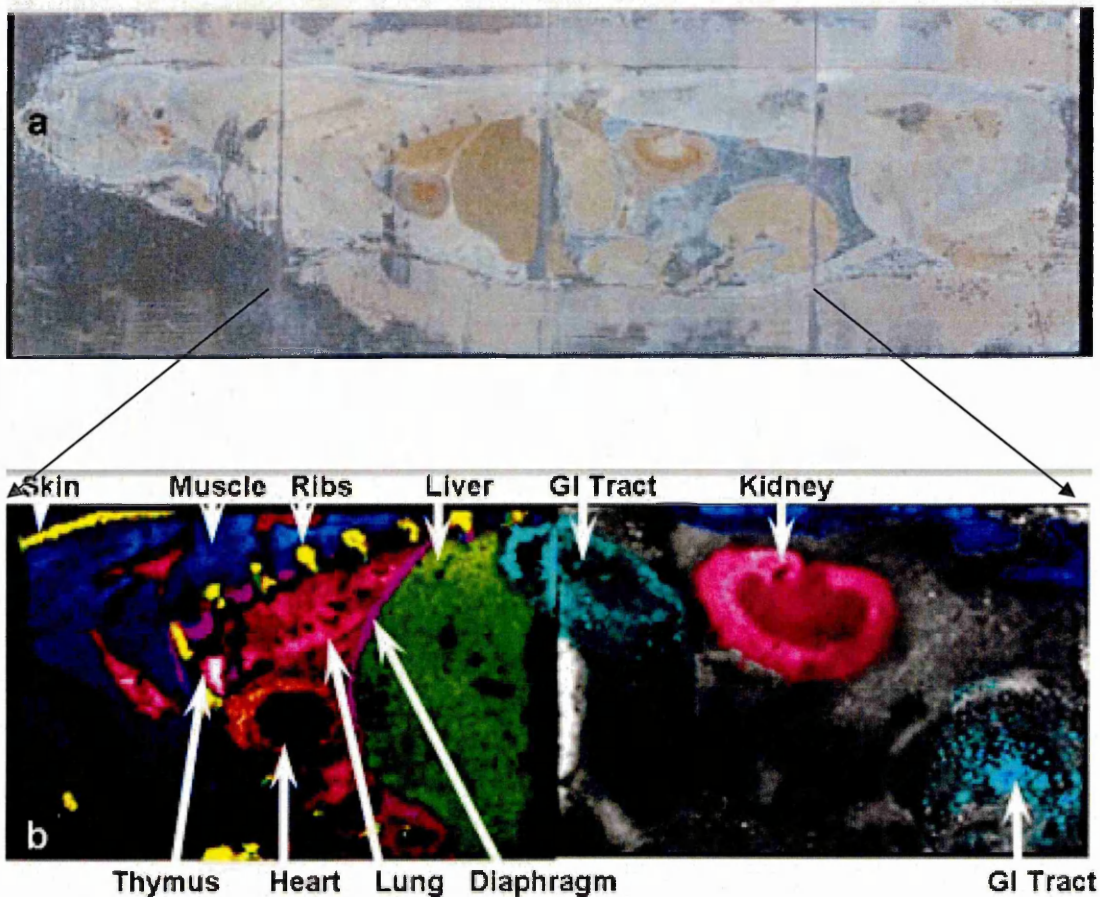


Figure 4.3 a) Optical image of the whole body section used for the MALDI imaging experiments, showing the anatomical features and their relative locations within the section before matrix coating. b) MALDI-MSI image of the same tissue section, highlighting the anatomical features by imaging the distribution of specific ions, the varying colour is only an aid to visual identification and not intended to show relative ion intensity.

#### **4.2.1.5 MALDI Imaging section handling.**

The whole body sections were transferred to clean aluminium foil plates using a Macro-Tape-Transfer-System® (Instrumedics Inc. St. Louis, MO) and freeze dried for 45 mins and then stored at -80°C until imaged.

Tissue sections were thawed and spray coated with 50ml of 25mg.ml<sup>-1</sup>  $\alpha$ -CHCA in 70:30 (v/v) ethanol:water (0.1% TFA), matrix was applied to the sections using a gravity fed pneumatic air spray gun, Iwata studio series compressor fitted with an Iwata Eclipse gravity feed airgun (Iwata-Media Inc., Portland, OR, USA) set to 40psi. Samples were sprayed from a distance of 25cm. 20 series of 2 passes of the airbrush at 45 second intervals to avoid sample wetting.

#### **4.2.1.6 Mass Spectrometric Analysis.**

The whole body sections were optically scanned for future reference and the sample plates were cut to 44mm x 40mm in order to fit onto the MALDI Imaging Target plates (Waters Corporation, Milford, USA) the aluminium sample plates were then stuck to the target plates using double sided tape.

In order to set the tissue area to be analysed a digital image of the tissue, on the MALDI sample support, was generated using a CanoScan 4400F flatbed scanner (Canon, Reigate, UK). The digital image produced was imported into MALDI Imaging Pattern Creator (Waters Corporation, Milford, USA). In this software, the instrument was taught the dimensions of the image by locating the four corners of the image plate, this allowed the creation of the image area

around the sample. The pattern was then uploaded into MassLynx (Waters Corporation, Milford, USA) and the parameters of the image experiment were created. The instrument was operated in positive ion V-mode prior to imaging analysis, the mass spectrometer was calibrated using a mixture of poly(ethylene glycol) standards (Sigma-Aldrich, Gillingham, UK) with average molecular weights of 400 and 600, providing coverage of the  $m/z$  range studied. The spacing between points on the raster was 300  $\mu\text{m}$  in both  $x$  and  $y$  direction. Imaging data were obtained by moving the tissue sections in a raster pattern on an  $x/y$ -stage relative to the laser position, which remained fixed. At each position, data were acquired for 400 laser shots (2 s).

All measurements including the calibration were performed with ion mobility separation activated.

The mass spectrometer was set up as follows: precursor ion selection was performed with the quadrupole, the precursor ion window was set between  $m/z$  785 and 835. This wide selection window was chosen to allow the transmission of the protonated molecule of vinblastine parent drug ( $m/z$  811) and endogenous lipids of interest simultaneously. Selected ions were then first separated using ion mobility and then collision induced dissociation occurred in the transfer T-wave. Collision induced dissociation occurred after the precursor ions were separated by ion mobility meaning that fragment ions retained the same ion drift time as their associated precursor ions. Therefore, it is possible to assign fragment ions to their precursor ions, because they have the same drift time (Figure 4.4).

The ion mobility related data analysis was accomplished using "DriftScope" software (Waters Corporation, Milford, USA). This enables specific drift time and  $m/z$  regions to be extracted, the resultant data sets were then converted into Analyze 7.5 file format using MALDI Imaging converter software (Waters Corporation, Milford, USA). Image visualisation was performed using BioMap 3.7.5.5 (Novartis, Basel, CH) (<http://www.maldi-msi.org>).



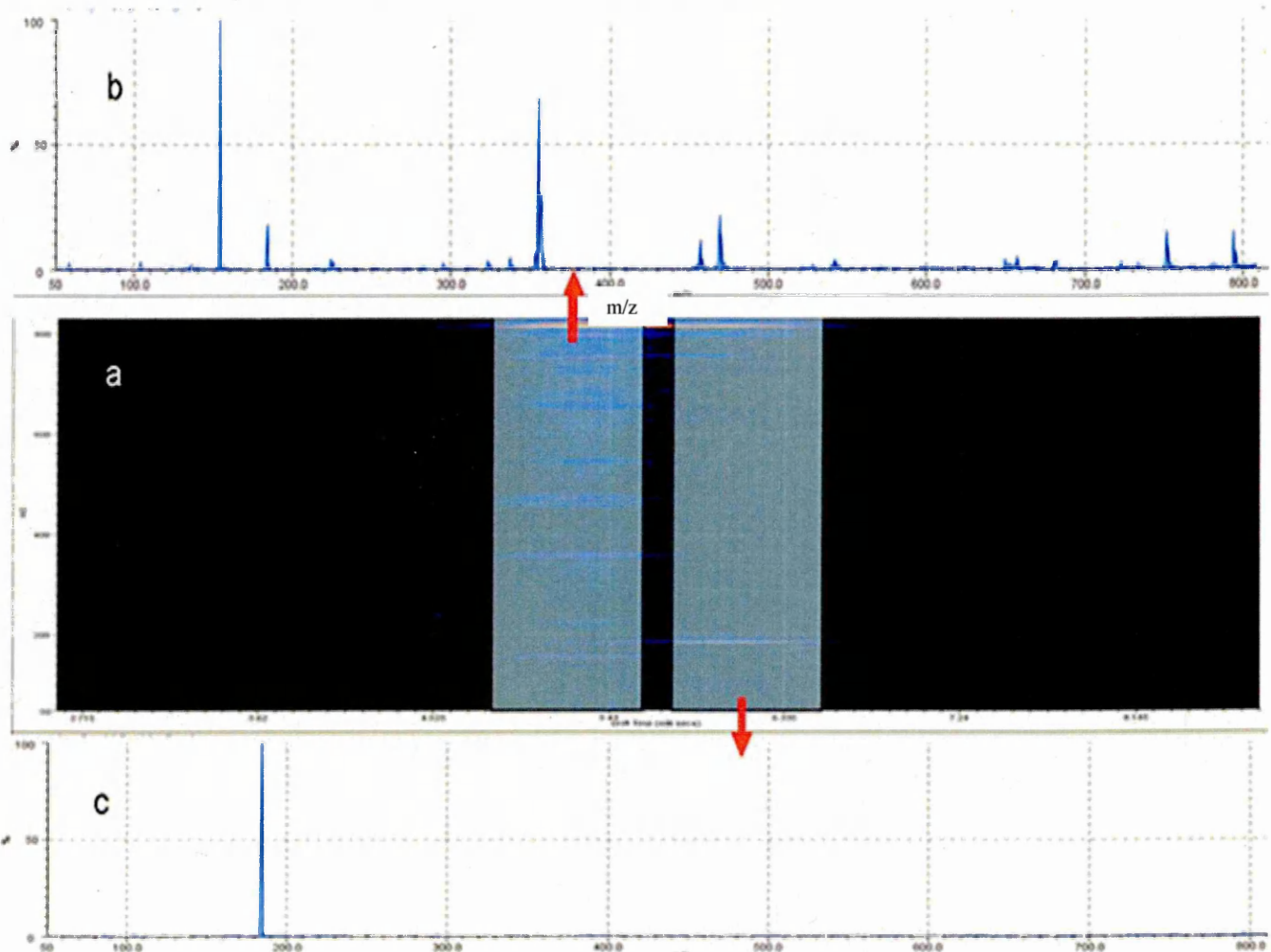


Figure 4.4 a) MALDI-IMS-MS/MS transfer  $m/z$  ionation pattern of vinblastine spot on tissue, viewed within "DriftScope" showing the separation of vinblastine from endogenous lipid  $m/z$  811. Two distinct product ion patterns are seen with different drift times, vinblastine has a shorter drift time (4.8-5.6ms) compared to that of the endogenous lipid (5.8-6.5ms). b) Product ion mass spectrum arising from the drift time of 4.8-5.6ms, from the known dissociation pattern of vinblastine it can be seen that this drift time relates to vinblastine. c) Product ion mass spectrum arising from the longer drift time 5.8-6.5ms, this clearly is derived from an endogenous PC lipid as indicated by the intense and characteristic product ion at  $m/z$  184 corresponding to the PC head group ( $H_2PO_4CH_2CH_2N(CH_3)_3^+$ ).

Product ions selected for imaging were chosen by the known dissociation of vinblastine under CID this is shown in figure 4.5 (Favretto *et al.*, 1998). The product ions were then analysed in the orthogonal TOF.

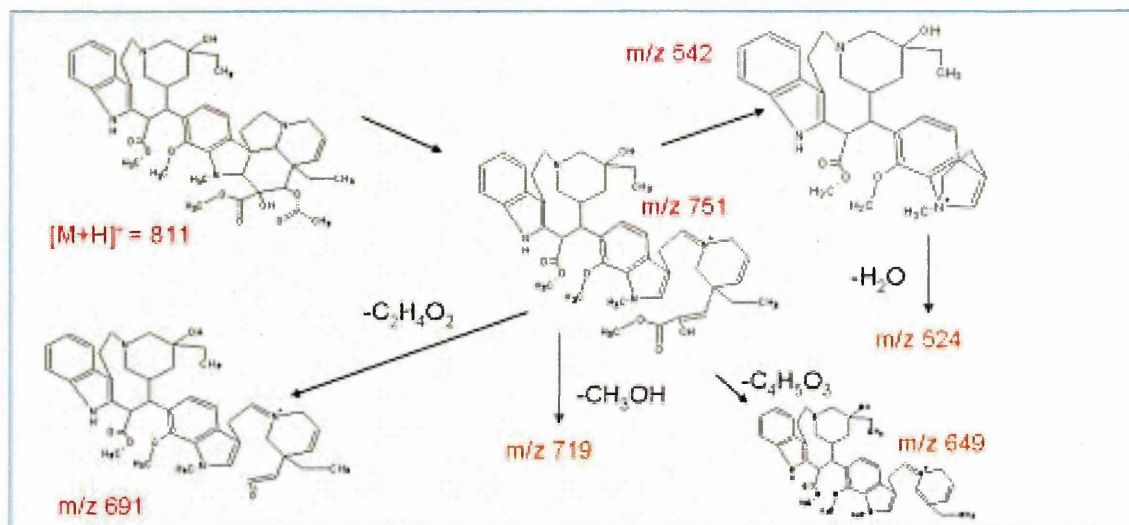


Figure 4.5 Chemical structure of vinblastine and the main dissociation pathways leading to the formation of the observed product ions in the MS/MS spectrum. (Favretto *et al.*, 1998)

#### 4.2.1.7 Quantitative Whole Body Autoradiography (QWBA) tissue handling, Imaging and quantitation.

Sections for QWBA were obtained according to the methodology previously described under "sample preparation" within this section, but in this case the sections were placed onto tape strips and freeze-dried for 45 mins. A section from a CMC block containing blood spots spiked with known concentrations of tritiated vinblastine was treated in the same way. After freeze drying, the tissue section and the standards were placed directly onto an imaging plate with no protective film, due to the short emission length of tritium. The image

plates with the sections were then left for a two week exposure time in a lead box. After the two week incubation the plates were imaged using the Fuji BAS 1500 bio-image analyser (Raytek, Sheffield, UK). The electronic images were analysed using a validated PC-based image analysis package SeeScan Densitometry software (LabLogic, Sheffield). The set of [<sup>3</sup>H]-labelled blood standards were used to construct a calibration curve over a range of radioactivity concentrations.

The lower limit of quantification for the QWBA was defined as the lowest quantifiable standard (12.0 nCi/g). Individual tissue concentrations of radioactivity were expressed in nCi/g and converted to µg equivalents drug/g (µg equiv/g) using the calculated specific activity of test material in the dose formulation. This gave a lower limit of quantification of 12.20 µg equiv/g.

#### **4.2.1.8 Tissue spiking.**

In order to obtain the best results from the tissue imaging experiments using ion mobility separation, the mobility drift time of the whole drug needed to be established, this was achieved by spotting 2µl of 0.5mg/ml vinblastine onto an unwashed 12µm kidney tissue section, which was then spray coated in matrix to simulate the actual experiment. A spot profile was then obtained and the drug drift time established from the "Driftscope" plot.

## 4.3 Results and Discussion

### 4.3.1 MALDI-MS

The positive ion MALDI mass spectrum of vinblastine spotted on tissue showed that the protonated molecule of vinblastine had a  $m/z$  811.4 this is within a signal rich region of the mass spectrum (Figure 4.6). This region included ions from alkali metal adducts and singly charged species of several lipids, as well as ions from other molecules such as matrix related ions. Thus, there was considerable interference from endogenous ions when vinblastine was imaged using MALDI-MS imaging as shown in figure 4.7a. To increase the specificity of a MALDI imaging experiment, MS/MS data is often obtained and converted to an image. The 2D ion density maps for vinblastine ( $m/z$  811.4) and its product ions shown in figure 4.7 illustrate the distribution of the vinblastine within the tissue sections. The majority of product ion intensity distributions were in good agreement with each other, showing the higher distribution of vinblastine to be within the liver, renal cortex and tissue surrounding the GI tract, with the exception of the distribution of the precursor ion at  $m/z$  811.4 (Figure 4.7a) and the transition of  $m/z$  811 - 751 (Figure 4.7c) which showed a slightly different distribution. This difference was most prominent within the kidney, the distribution of the precursor ion and the product ion  $m/z$  751 showed a relatively high signal intensity within the renal pelvis, but the other 7 known product ions did not show this distribution, it is therefore proposed that this observed signal intensity was due to an isobaric interference.

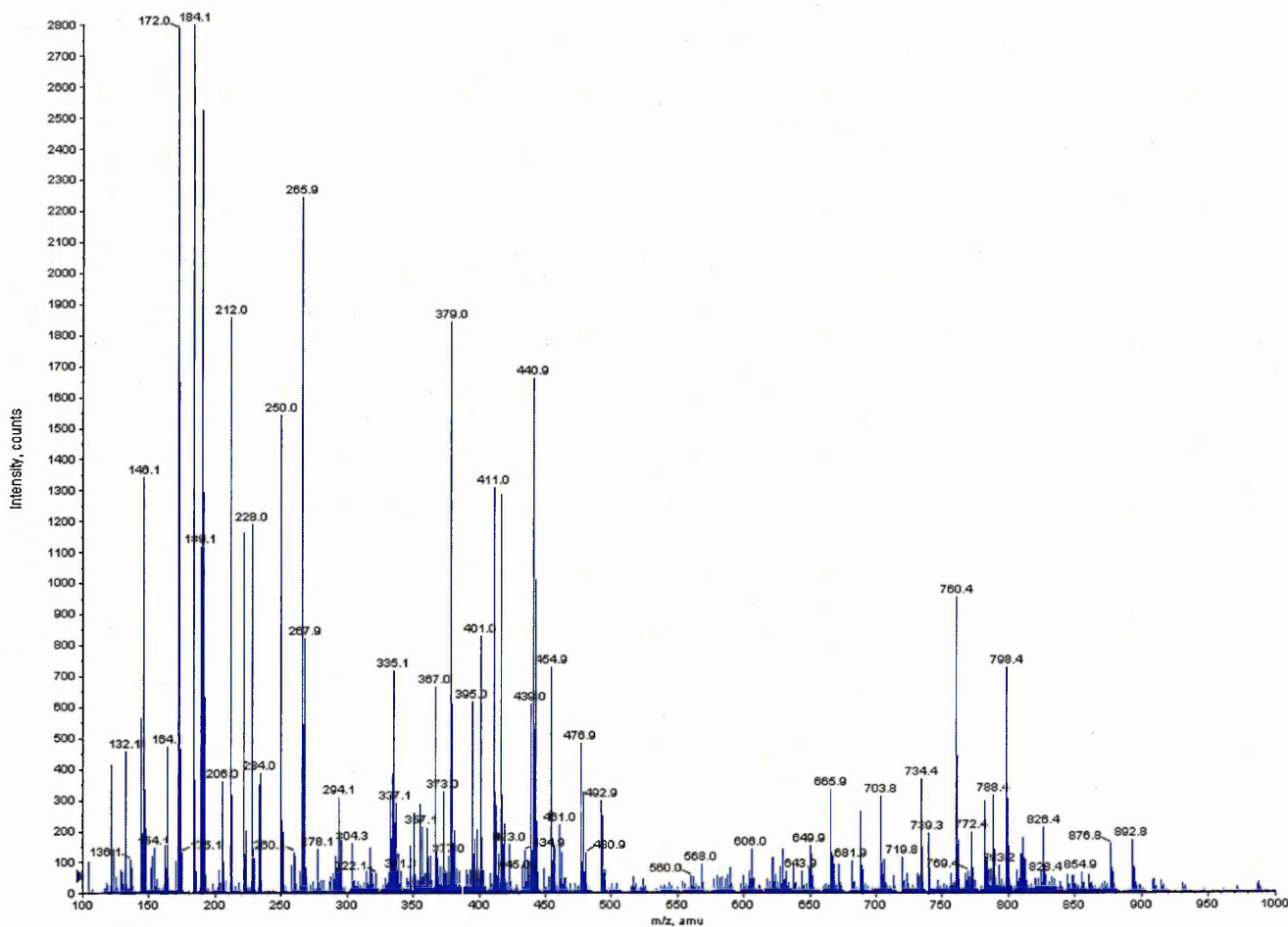


Figure 4.6 Total MALDI-MS mass spectrum of vinblastine spotted on tissue, showing the complexity of signals around the mass of vinblastine  $m/z$  811.4. This region includes ions from alkali metal adducts and singly charged species of several lipids, as well as ions from other species such as matrix related ions.



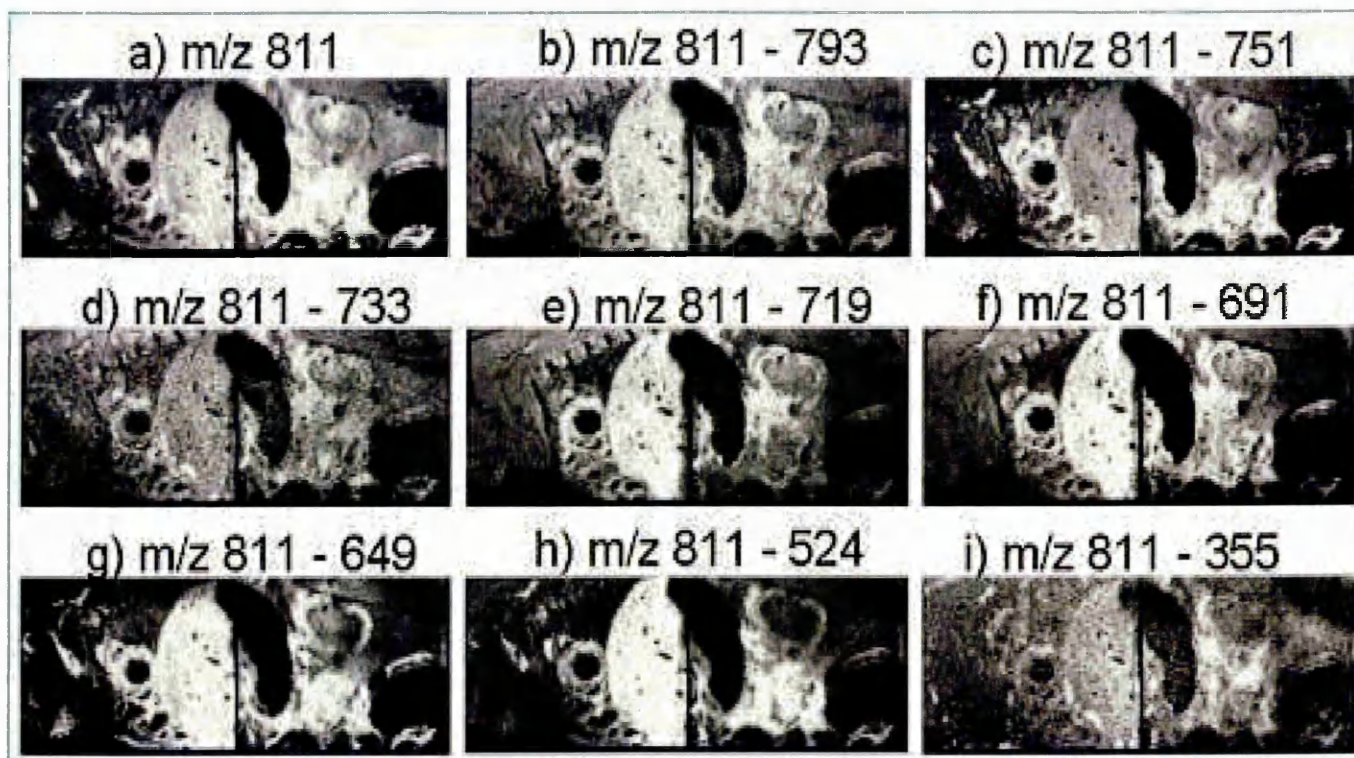


Figure 4.7 MALDI-MS/MS Images from the thoracic and abdominal cavities showing the distribution of the precursor and product ions of vinblastine. a)  $m/z$  811.4, b)  $m/z$  811-793, c)  $m/z$  811-751, d)  $m/z$  811-733, e)  $m/z$  811-719, f)  $m/z$  811-691, g)  $m/z$  811-649, h)  $m/z$  811-524, i)  $m/z$  811-355. (For organ identification see Figure 4.3b)

Ion mobility adds an additional separation step within the MALDI imaging experiment. To establish the ion mobility drift time associated with vinblastine, a spiked tissue section was analysed using IMS-MS/MS. The resulting "DriftScope" plot showed the separation of more than one ion at  $m/z$  811 (Figure 4.8). Since the dissociation occurs within the transfer region of the instrument all the product ions share the same drift time as their respective precursor ions. If the product ion spectrum from the ion which has the shorter drift time of (4.8-5.6ms) is selected the product ion spectrum matches that of vinblastine (Figure 4.4b). The product ion spectrum which shows the longer drift time of (5.8-6.5ms) shows a strong peak at  $m/z$  184

(H<sub>2</sub>PO<sub>4</sub>CH<sub>2</sub>CH<sub>2</sub>N(CH<sub>3</sub>)<sub>3</sub>)<sup>+</sup> (Figure 4.4c), indicating that the product ion originates from an endogenous phosphatidylcholine type lipid species.

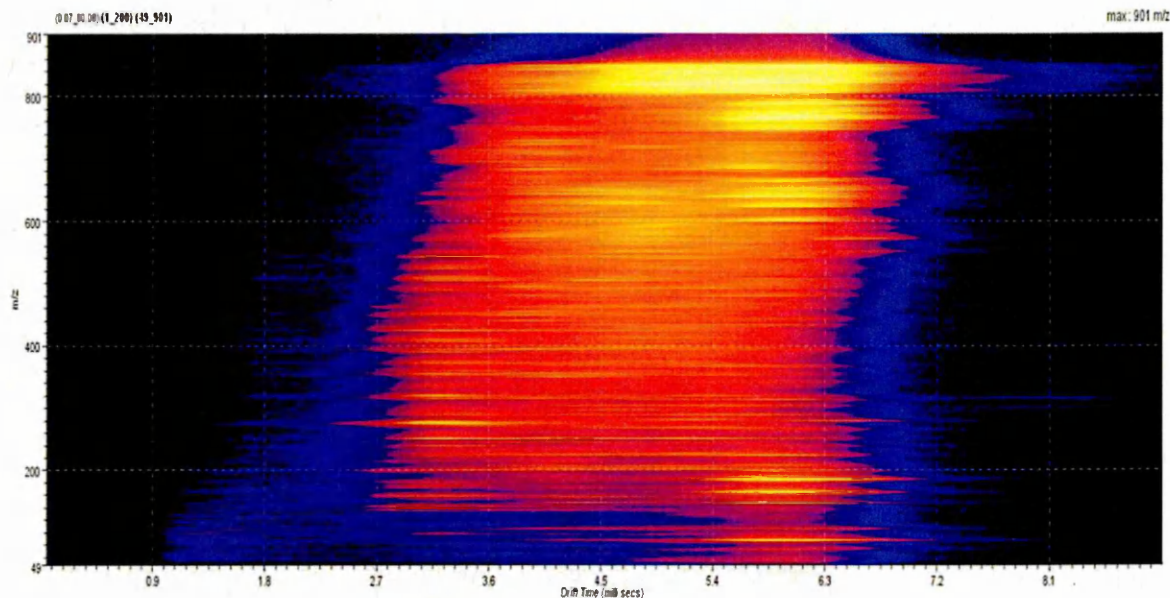


Figure 4.8 "DriftScope" plot of the data obtained from the vinblastine dosed whole body MALDI-IMS-MS/MS image, showing the complexity of signals within the data set, numerous ions can be seen with various drift times. Ion intensity is shown as a colour gradient. Precursor ions have been mobility separated and the fragment ions can be seen vertically aligned.

The same experimental parameters were used within the spot analysis and the image acquisition, which allows the application of the drift time separation to be used to process the MALDI IMS-MS/MS image data. The "DriftScope" plot for the MALDI-IMS-MS/MS whole body imaging experiment showed a complexity of signals (Figure 4.8), within the whole body section data set. Figure 4.9 shows a comparison of the MALDI-MS/MS image and the MALDI-IMS-MS/MS image obtained by extracting only those ions which have a drift time of 4.8-5.6ms, *i.e.* the same data set with and without ion mobility



separation. The removal of the interfering signal within the renal pelvis by incorporating IMS increases the specificity of the IMS MS and MS/MS images.

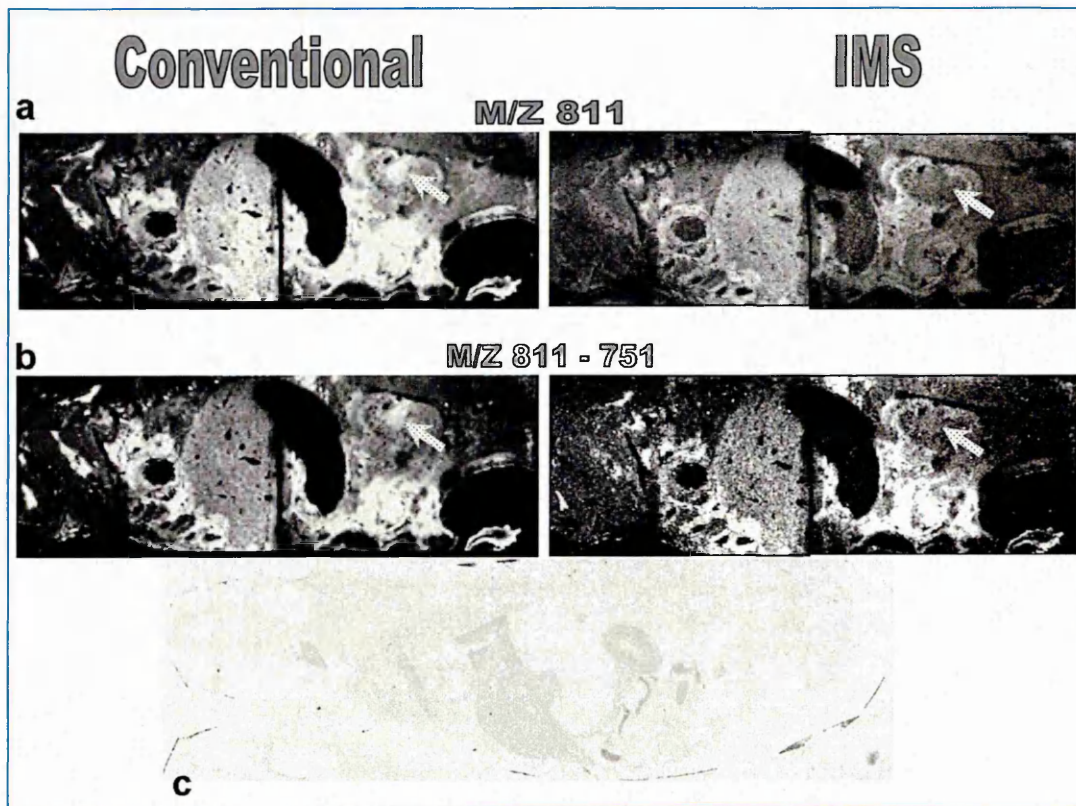


Figure 4.9 Comparison of  $m/z$  811 and  $m/z$  811-751 using MALDI-IMS-MS/MS and conventional MALDI-MS/MS clearly demonstrates the advantages of ion mobility separation within MALDI xenobiotic imaging. Indicated is the main difference with the distribution of the ion of interest within the renal pelvis, c) shows the whole body autoradiography plot of an corresponding section from a tritiated vinblastine dose, it can be seen that there is almost no signal in the renal pelvis, confirming the results of the MALDI-IMS-MS/MS.

### 4.3.2 Whole body autoradiography

$^3\text{H}$  distribution shown in the sample oxidation data could represent the whole drug or any of the metabolites which contain the radiolabel. The concentrations of the radiolabel in the liver ( $22.70 \mu\text{g equiv/g}$ ) and in the



kidney (30.15  $\mu\text{g equiv/g}$ ) were highest at 1 hour post dose (Table 4.1), the MALDI image shows the largest relative concentration in the liver with less in the kidney (Figure 4.9). The reason for the discrepancy between the sample oxidation data and the MALDI Imaging data, is most likely due to the species specificity obtained using MALDI imaging.

<b>6mg/kg IV tritiated vinblastine</b>		
<b>Sample</b>	<b><u>1 hour post dose</u></b> ( $\mu\text{g equiv/g}$ )	<b><u>4 hour post dose</u></b> ( $\mu\text{g equiv/g}$ )
<b>Plasma</b>	<b>0.53</b>	<b>0.27</b>
<b>Brain</b>	<b>0.23</b>	<b>0.34</b>
<b>Kidney</b>	<b>30.15</b>	<b>12.86</b>
<b>Liver</b>	<b>22.70</b>	<b>13.28</b>

*Table 4.1 The sample oxidation data following administration of  $^3\text{H}$  radiolabelled Vinblastine. Concentrations of radioactivity are greatest in all tissues and plasma except in the brain at 1 hour post dose. Highest concentrations of radioactivity were measured in the kidney at 30.2 $\mu\text{g equiv/g}$  1 hour post dose. The concentration within the brain and the plasma are in the same order of magnitude at 1 and 4 hours post dose.*

Using MALDI-IMS-MSI only the distribution of the parent drug has been imaged whereas in the sample oxidation data only the radioactivity has been measured and not solely the parent drug. The sample oxidation data shows a very small amount of radioactivity in the brain, this correlates to the MALDI image shown in figure 4.10, where vinblastine has been imaged using MALDI-

MS/MS on a 12 $\mu$ m brain section from a dosed animal and vinblastine is only distributed in the ventricle and not within other brain regions.

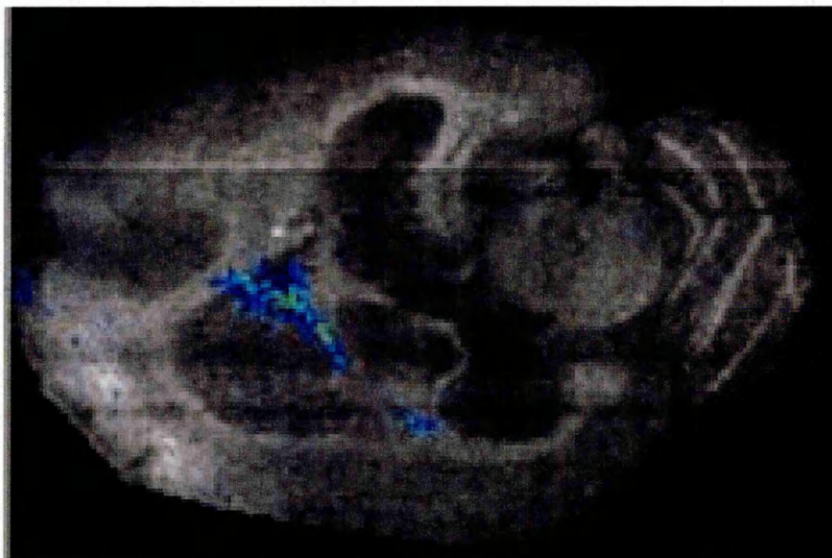


*Figure 4.10 MALDI-MSI image of an axial brain section of a rat after 6mgkg<sup>-1</sup> IV dose of vinblastine, imaged is the distribution of the product ion of vinblastine at m/z 355, overlaid onto a background of an endogenous lipid, showing that vinblastine is only present in the ventricle.*

Within this work Quantitative WBA (QWBA) was carried out using tritiated vinblastine sulphate, there are some issues with the use of tritium as a radio labelled molecule that need to be accounted for, the main problem with using tritium in QWBA studies is the loss of the radioactivity through freeze-drying, this occurs through the formation of <sup>3</sup>H<sub>2</sub>O within the sample and then the loss of this <sup>3</sup>H<sub>2</sub>O during the freeze-drying process, to assess the extent of this a test sample was freeze-dried. This showed limited loss of radioactivity, and any loss of radioactivity during freeze-drying was accounted for by the inclusion of the known standards.

The QWBA data was quantified using SeeScan Densitometry software (LabLogic, Sheffield). The measured photostimulated luminescence (PSL) is converted to nCi/g within the software. A calibration graph was constructed from the PLS values of the known samples within the software. Table 4.2 shows the measured radioactivity in nCi/g of numerous tissues measured from the QWBA sections shown in figure 4.11, also shown is the calculated  $\mu\text{g}$  equiv/g of vinblastine and its metabolites. Table 4.2 shows that the areas with the highest concentration of radioactivity include the small intestine mucosa and contents, which is also in agreement with the 2D ion plots for both MALDI-MS/MS, MALDI-IMS-MS and MS/MS (Figure 4.9). One anomaly that arose was that the QWBA data gave a high concentration of radioactivity within the lung tissue but signal intensity for the MALDI imaging data for vinblastine within the lung tissue was relatively low. This may be due to a tissue suppression effect. This has been previously reported by Stoeckli *et al.*, 2007, or due to the chemical specificity of the MALDI technique and that the radioactive signal is not from the parent drug but a metabolite, however this is likely to only have a small effect because vinblastine is known to be present within the lungs after 4 hours as reported by Tellingan *et al.*, 1993.

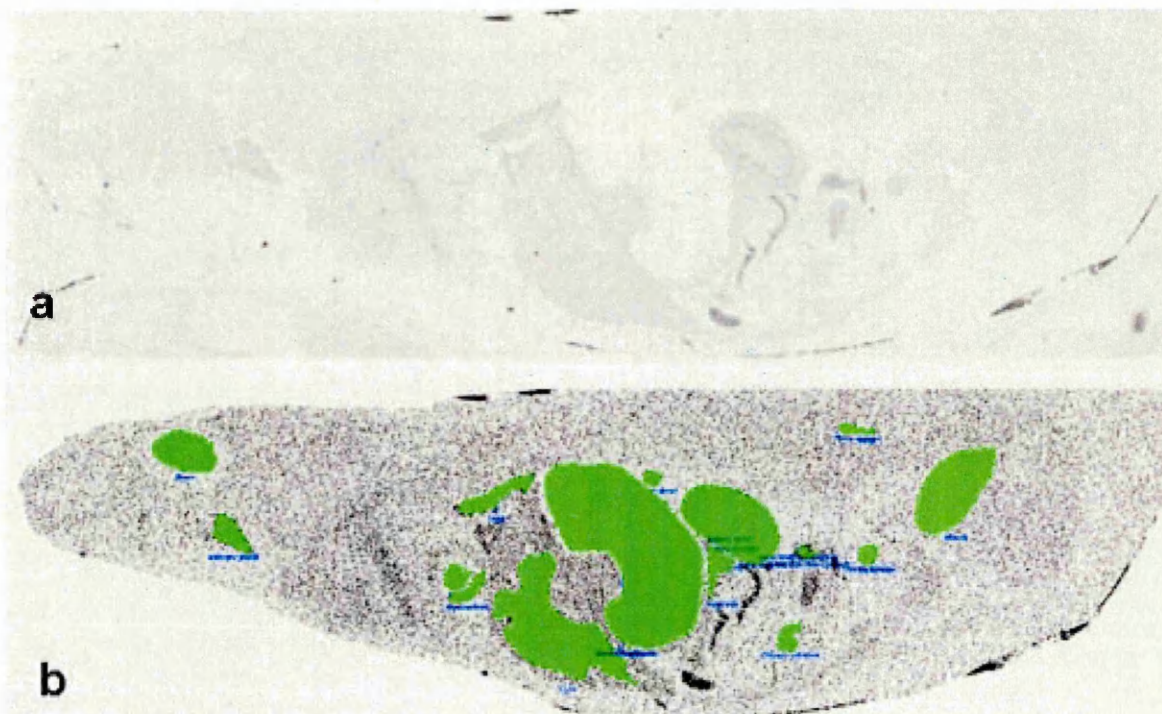


Figure 4.11 a) Whole body autoradiograph showing the distribution of  $^3\text{H}$  in a 1 hour post dose Rat dosed with 6mg/kg IV  $^3\text{H}$  Vinblastine. b) shows the areas selected for analysis and quantification using the "SeeScan" software.

Tissue	Rat 33M	Rat 33M
	1 hour (nCi/g)	1 hour ( $\mu\text{g}$ equiv/g)
Adrenal gland	24.8	25.1
Blood	2.08	BLQ
Bone	0.0	BLQ
Bone marrow	15.1	15.3
Caecum contents	15.9	16.1
Kidney	43.0	43.5
Kidney cortex	33.9	34.3
Kidney medulla	60.1	60.8
Kidney pelvis	14	14.2
Liver	31.1	31.5
Lung	59.8	60.5
Muscle	8.5	BLQ
Myocardium	19.8	20.0
Pancreas	28.1	28.4
Prostate	1.5	BLQ
Salivary gland	47.9	48.5
Small intestine contents	135.0	136.6
Small intestine mucosa	58.3	59.0
Stomach contents	0	BLQ
Stomach mucosa	21.0	21.3
Urinary bladder	41.1	41.6

Table 4.2 Tissue concentrations of radioactivity calculated from the WBA image using "SeeScan" software from the known standards and the calculated  $\mu\text{g}$  equiv/g of the drug or metabolite. (BLQ - Below Limit of Quantification).

Confirmation of the vinblastine distribution in whole body sections was carried out by QWBA. As already discussed this technique does not have the chemical specificity that MALDI has, however, it does retain the spatial

information for the distribution of the tritium radiolabel ( $^3\text{H}$ ). Figure 4.9 shows the QWBA image, when this image is compared to the MALDI images (figure 4.7 and 4.9) good spatial agreement is observed. The distribution of the radiolabel within the kidney shows a high intensity within the renal cortex ( $34.3 \mu\text{g equiv/g}$ ) and a much lower signal within the renal pelvis ( $14.2 \mu\text{g equiv/g}$ ), this is in agreement with the product ions within the MALDI-MS/MS data set excluding  $m/z$  811 and  $m/z$  811 - 751. In the kidney the QWBA data shows an area, which is a broken ring of higher intensity (figure 4.12d), corresponding to the position of the medulla. Comparison of the QWBA and MALDI images with the original tissue sections shown in figure 4.12, show that the area with the QWBA signal and the MALDI imaging signal may in fact be the area of tissue between the renal cortex and the medulla. This area contains a number of lymphatic ducts. As previously reported by Tellingan *et al.*, 1993 vinblastine is retained within the lymphatic tissue for extended periods of time, and this is a possible explanation for the high concentration of vinblastine observed in the QWBA and the MALDI images in this region. The agreement between the QWBA, MALDI-IMS-MS and MS/MS data show the added specificity and confidence that can be obtained with the addition of ion mobility separation to MALDI imaging experiments.



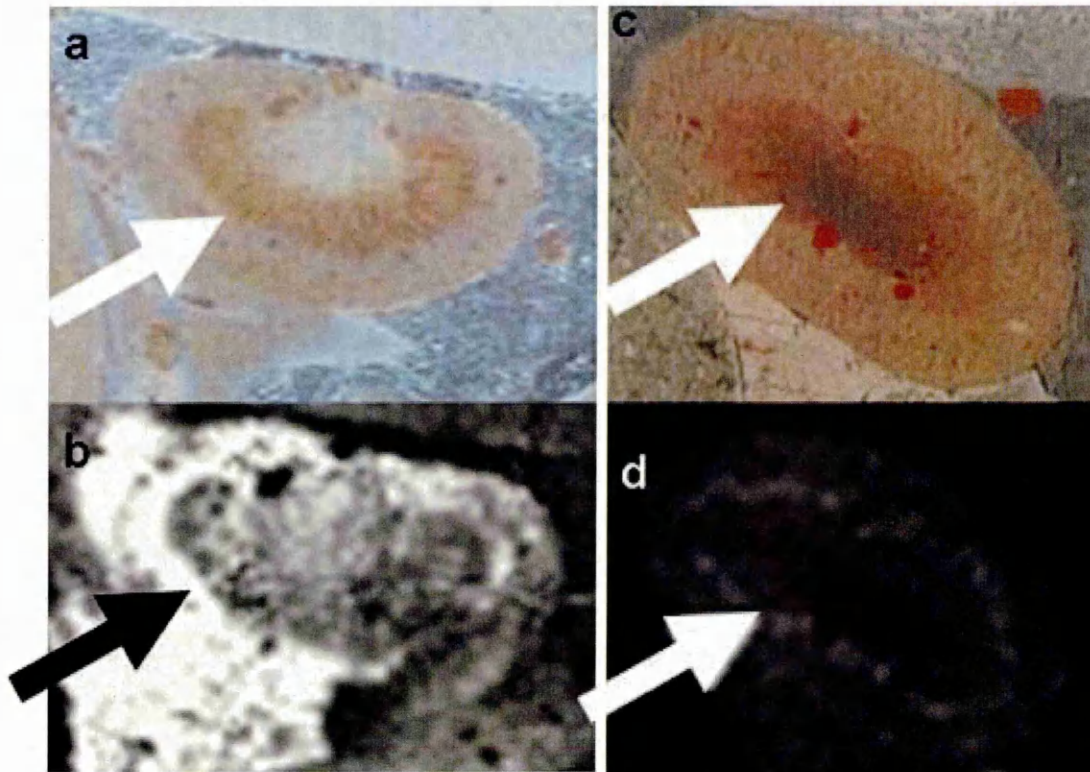


Figure 4.12 Enhanced images of the kidney from the whole body sections, before and after imaging. a) an optical image of the kidney from the whole body section dosed at  $6\text{mgKg}^{-1}$  IV vinblastine before matrix application. b) the same tissue section as shown in 4.12a but imaged by MALDI-IMS-MS showing the distribution of vinblastine within the kidney, with the highest intensity (white) showing a broken ring of intensity between the cortex and medulla. c) optical image of the kidney within the whole body section dosed with  $^3\text{H}$  Vinblastine. d) Whole Body auto radiography of the tissue section shown in 4.12c, indicated is the broken ring of slightly higher intensity (white) between the cortex and medulla is indicated.

#### 4.4 Conclusions.

Shown here is a method for the direct analysis of vinblastine within a rat whole body section. The combination of MALDI-IMS-MSI with MS-MS has been shown to improve the selectivity of MALDI-MSI experiments over and above that normally obtainable with MALDI-MSI.

MALDI-IMS-MS imaging of vinblastine within rat whole body sections has been shown to correlate with the spatial distribution of  $^3\text{H}$  vinblastine in QWBA experiments and to show the analyte specificity comparable to that of earlier HPLC-MS experiments.

Ion mobility separation has been shown to separate isobaric interferences from MALDI imaging data obtained from highly complex biological samples as shown here from whole body tissue sections from dosed animals, increasing the confidence in the resulting image.

Image acquisition was achieved within a relatively short time period, without the need for radio labelled compounds, further development of this technique and integration within the pharmaceutical industry could dramatically reduce the cost of drug development by removing the need to synthesise radiolabelled drug candidates and the health and safety issues arising from handling radioactive material. This technique could also ultimately reduce the number of animal experiments required during early phase drug development. With further advances in MALDI-MSI instrumentation and methodology the potential for single experiments that show the spatial distribution of drug



candidates and their metabolites along with indications of local and systemic biological effects with high analyte specificity may be realised.

Vinblastine distribution shown within this work correlates with previously published studies of the distribution of vinblastine (Tellingén *et al.*, 1993). These studies were carried out using tissue homogenates and HPLC-MS combined with QWBA. MALDI imaging of vinblastine specifically shows the spatial distribution of vinblastine.

## 4.5 References

Atkinson S.J; Loadman P.M; Sutton C; Patterson L.H and Clench M.R. **2007**, *Rapid Commun. Mass Spectrom.* 21, 1271-1276.

Bunch J; Clench M.R and Richards D.S. **2004**, *Rapid Commun. Mass Spectrom.* 18, 351-360.

Favretto D; Piovan A; Cappelletti E.M. **1998**, *Rapid Commun. Mass Spectrom.* 12, 982-984.

GE Healthcare UK Limited, **2006**. Safety Data Sheet, SDS036/v06, January 2006.

Giles K; Pringle S.D; Worthington K.R; Little D; Wildgoose J.L; Bateman R.H. **2004**, *Rapid Commun. Mass Spectrom.* 18, 2401-2414.

Hsieh Y; Chen J; and Krofmacher W.A. **2007**, *J. Pharm. Tox. Meth.* 55, 193-200.

Hsiesh Y; Casale R; Fukuda E; Chen J; Knemyer I; Wingate J; Morrison R. and Korfmacher W. **2006**, *Rapid Commun. Mass Spectrom.* 20, 965-972.

<http://www.maldi-msi.org>

Jackson S.N; Ugarov M; Egan T; Post J.D; Langlais D; Schultz J.A; Woods A.S. **2007**, *J. Mass Spectrom.* 42, 1093-1098.

Khatib-Shahidi S; Andersson M; Herman J.L; Gillespie T.A; Caprioli R.M. **2006**, *Anal. Chem.* 78, 6448-6456.

McCombie G; Staab D; Stoeckli M; Knochenmuss R. **2005**, *Analytical Chemistry*, 77, 6118-6124.

Prideaux B; Atkinson S.J; Carolan V.A; Morton J; Clench M.R. **2007**, *Int. J. Mass Spectrom.* 260, 243-251.

Pringle S.D; Giles K; Wildgoose J.L; Williams J.P; Slade S.E; Thalassinos K; Bateman R.H; Bowers M.T; Scrivens J.H. **2006**, *Int. J. Mass Spectrom* 261, 1-12.

Reyzner M.L; Hsieh Y; Ng K; Korfmacher W.A and Caprioloi R.M. **2003**, *J. Mass Spectrom.* 38, 1081-1092.

Rohner T.C; Staab D; Stoeckli M. **2005**, *Mech. Ageing and Dev.* 126, 177-185.

Stoeckli M; Staab D; Schweitzer A. **2007**, *Int. J. Mass Spectrom.* 260, 195-202.

Tellingen O.V; Beijnen J.H; Nooijen W.J; Bult A. **1993**, *Cancer Chemoth. Pharm.* 32, 286-292.

Trim P.J; Atkinson S.J; Princivalle A.P; Marshall P.S; West A; Clench M.R. **2008**, *Rapid Comm. Mass Spectrom.* 22, 1503-1509.

Troendle; F. J; Reddick; C. D; and Yost R. A. **1999**, *J. Am. Soc. Mass Spectrom.* 10, 1315-1321.

Ulberg S. **1954**, *Acta Radiol. Suppl.* 118, 1-110.

Van de Plas R; Ojeda F; Dewil M; Van Den Bosch L; De Moor B; Waelkens E. **2007**, *Pacific Symposium on Biocomputing* 12, 458-469.

Wang H-Y. J; Jackson S.H; McEuen J and Woods A.S. **2005**, *Anal Chem* 77, 6682-6686.

Zhigaltsev I.V; Maurer N; Akhong Q.F; Leone R; Leng E; Wang J; Semple S.C; Cullis P.R. **2005**, *J. Control. Release*, 104, 103-111.

## CHAPTER 5

---

**Lipid Distribution within HCT116  
Tumours, Tumour Margin and  
Surrounding Tissue, and the Effects  
of a Chemotherapeutic drugs.**

Chapter 5

## **Lipid Distribution within HCT 116, Tumour Margin and Surrounding Tissue, and the Effects of a Chemotherapeutic drug administration on Lipids.**

### **5.1 Introduction.**

There has been extensive research into identifying possible cancer markers using MALDI-MSI primarily focussing on proteins and peptides (Burnum *et al.*, 2008). Schwamborn *et al.*, 2007 presented work on the identification of prostate carcinoma by MALDI-MSI. They have identified two ions predominantly associated with non cancerous glands at 2753 and 6704Da and two ions that are predominantly associated with cancerous glands at 4964 and 5002Da, using Support Vector Machine (SVM) algorithm generated by ClinProTools Software (Bruker Daltonics, Germany). They were also able to discriminate between cancerous and non-cancerous tissue sections resulting in an overall cross validation of 88%, with a sensitivity of 85.21% and a selectivity of 90.74%. The algorithm used was based on a set of 22 peaks (because these were identified as being the most prominent peaks accountable for the highest percentage of variation between the two groups) from which the four accounting for the greatest variation between cancerous and non-cancerous regions are those mentioned above.

#### **5.1.1 Role of lipids in cellular processes within cancer**

Lipids have been shown to have major roles within cellular processes, and to include both structural and functional roles. They are known to be important

mediators of cell signalling. Lipids act as second messengers in cellular events such as cell growth, cellular proliferation, cell death and apoptosis.

The field of lipidomics has grown rapidly in recent years, however, there is still some catching up to be done for it to be at the same level of research as there is in proteomics.

There have been several studies published looking at the role of lipids within cellular systems. Fuchs *et al.*, 2007 have reported changes in the glycerophospholipid composition of hematopoietic progenitor cells due to apoptosis using  $^{31}\text{P}$  NMR and MALDI. Apoptosis causes glycerophospholipid composition of the outer surface of the cell membrane to change, there is a loss of membrane asymmetry due to negatively charged phosphatidylserine transfer from the inner to the outer membrane layer. They also show a decrease in diacyl-phosphatidylcholine and phosphatidylethanolamine and an increase in ether-linked glycerophosphocholines and ether-linked glycerophosphoethanolamines in apoptotic cell membranes. The MALDI-MS experiments within this work were carried out using cellular lipid extracts. Analysis was carried out using a Bruker AutoFlex system (Bruker Daltonics, Germany) fitted with an  $\text{N}_2$  laser. As a matrix the authors used para-nitroaniline, because phosphatidylethanolamine is detectable as a negative ion and this removes the high intensity phosphatidylcholine peaks observed in positive ion MALDI.

Due to their role in cellular processes lipids have been investigated as possible targets for cancer therapeutics, this has been reviewed by Ogretmen

2006 and Modrak *et al.*, 2006. These reviews concentrate on the role of sphingolipids in pathogenesis and as possible targets for cancer therapeutics. Sphingolipids are a large group of lipids which include several subgroups derived from an aliphatic amino alcohol called sphingosine (figure 5.1). One of the main subgroups that have undergone investigation is ceramides and their synthesis and metabolism. Ceramides have a sphingosine backbone and a fatty acid chain which can be of various lengths. Within nature these fatty acid chains generally contain an even number of carbons, commonly either C12, C14, C16, C18, C22, C24 and C26 (Ogretmen 2006). The use of odd chain lengths can be useful for quantitation using HPLC or similar because synthetically made odd number carbon chain lengths can be incorporated into analytical samples, as internal standards.

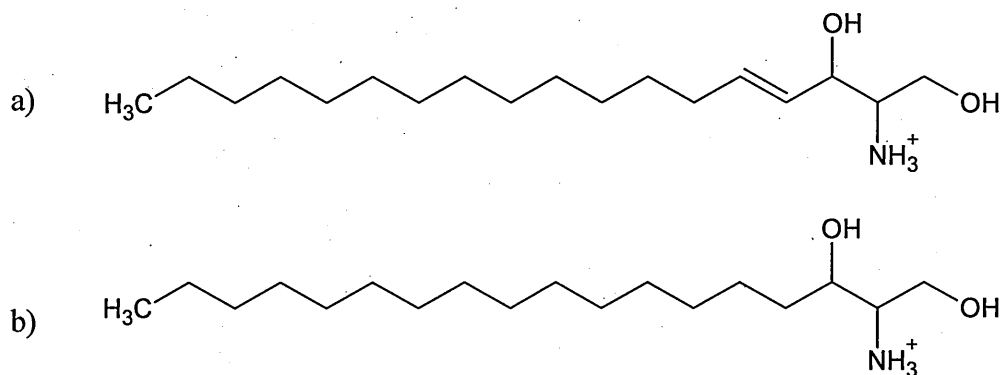


Figure 5.1 schematic structure of a) sphingosine, b) sphinganine

Apoptosis has two pathways, termed receptor mediated and non-receptor mediated. Both pathways use ceramides as an intracellular, pro-apoptotic signalling molecule.

Ceramides have a role in the induction of apoptotic cell death and are produced by cancer cells prior to apoptosis due to exposure to chemotherapeutics or radiotherapy. Within this process ceramides act as an intracellular second messenger which activates certain enzymes which lead to apoptosis (Modrak *et al.*, 2006). The ceramides that increase due to cellular stress causing agonists are long chain ceramides. These are synthesised via the activation of the *de novo* synthesis pathway and/or via the hydrolysis of sphingomyelin by sphingomyelinases (Ogretmen 2006). Figure 5.2 shows the biosynthetic pathway of certain sphingolipids.

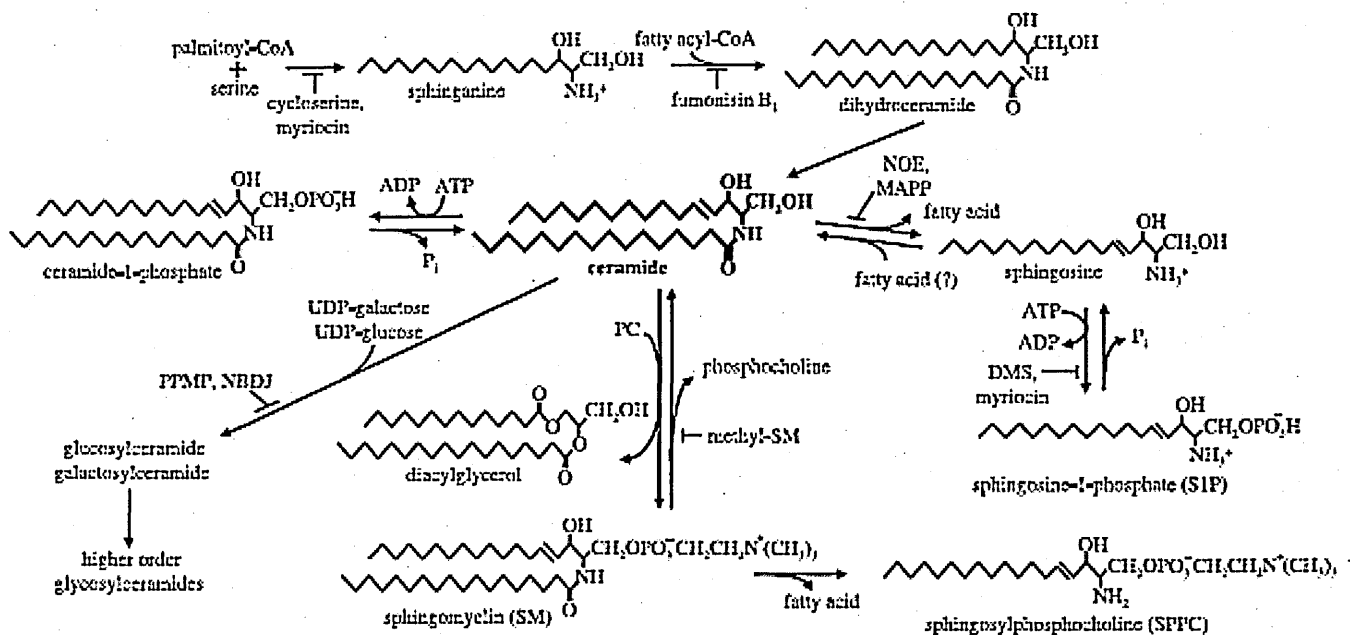


Figure 5.2 The biosynthetic pathway of certain sphingolipids (Modrak *et al.*, 2006)

The role of ceramides in apoptosis may be due to their possible self assembly into channels resulting in the outer membrane of mitochondria becoming permeable to small proteins, thus releasing intramembrane space proteins inducing apoptosis (Stiban *et al.*, 2006).



Ceramide is pro-apoptotic however dihydroceramide has been shown by Stiban *et al.*, 2006 to act as an apoptotic inhibitor. Dihydroceramide only differs from ceramide by one bond. Dihydroceramide lacks a critical *trans* double bond at the 4, 5 position (Figure 5.1a&b). Stiban *et al.*, 2006 propose that the ratio between ceramide and dihydroceramide may be important in apoptosis. In this work they found that the addition of dihydroceramide markedly reduced the permeability of the mitochondrial outer membrane by ceramide. They have shown that dihydroceramide is not able to disassemble the ceramide channel once it was formed. However, dihydroceramide does inhibit the formation of ceramide channels. These data indicate that dihydroceramide has an effect on the formation of the ceramide channels, but does not actively disassemble them.

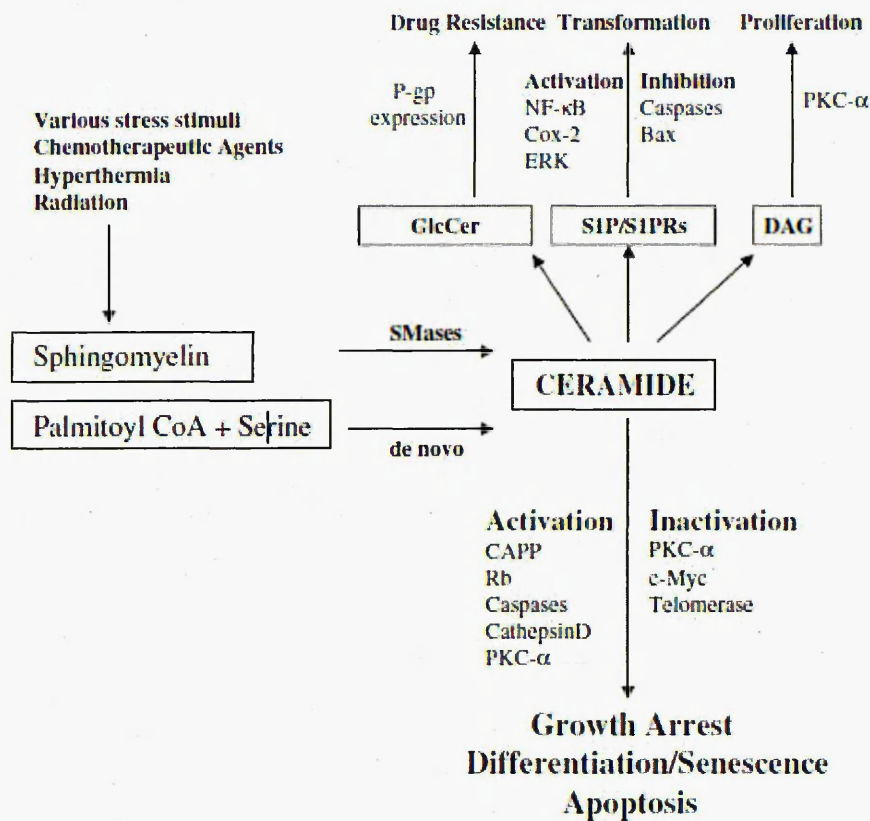


Figure 5.3 Some of the roles of sphingolipids within cancer growth regulation and therapy (Ogretmen 2006).

A brief overview of the role of ceramides within the regulation of cellular processes and drug resistances is shown in Figure 5.3 (Ogretmen 2006). As well as having apoptotic effects ceramides can also undergo synthesis and breakdown into other molecules. Sphingosine-1-Phosphate (S1P) can be produced by the hydrolysis of ceramide by ceramidases into sphingosine, followed by the conversion of sphingosine into S1P by sphingosine kinase. S1P is considered to be a pro-survival lipid and is involved in cancer proliferation, inflammation, vasculargenesis, malignant transformation and resistance to apoptotic cell death (Ogretmen 2006).

### 5.1.2 Tumour Xenograft methodology

The cell lines used within this work to form the tumour xenografts were from the HCT 116 cell line. Brattain *et al.*, 1981 have shown the methodology for obtaining and establishing the HCT 116 cell line (as well as HCT 116a and HCT 116b). The HCT 116 cell line is derived from a human colonic carcinoma removed from surgery (Brattain *et al.*, 1981). The tissue was minced into 1-2mm<sup>3</sup> pieces. The small tissue pieces were then washed several times in a culture medium. The tissue pieces were then disaggregated with 0.25% Trypsin. The cells obtained from this process were more than 90% viable cells. Primary cultures from these cells were found to have 3 morphological variants HCT 116, HCT 116a and HCT 116b. These morphological variants were separated by sedimentation and centrifugation.

The methodology used within this work separated the cells using centrifugation in a linear gradient of percoll in tissue culture medium. HCT 116 cells were found in the density range of 1.037 – 1.080 g/ml. The density range of HCT 116a and HCT 116b was 1.026 – 1.068 and 1.044 – 1.092 g/ml respectively. Due to the overlapping nature of each of the cell types the gradient between 1.050 – 1.074 g/ml was selected, plated and grown in cell culture to form the initial culture of predominantly HCT 116 cells. Several sub cultures were made from this original culture and grown until only the HCT 116 cells were observed by phase contrast microscopy (Figure 5.4). HCT 116 cells formed tumours in ~50% of animals given an inoculation of  $5 \times 10^6$  cells, with an average latency of 16 days to form a tumour of at least 1cm in diameter.

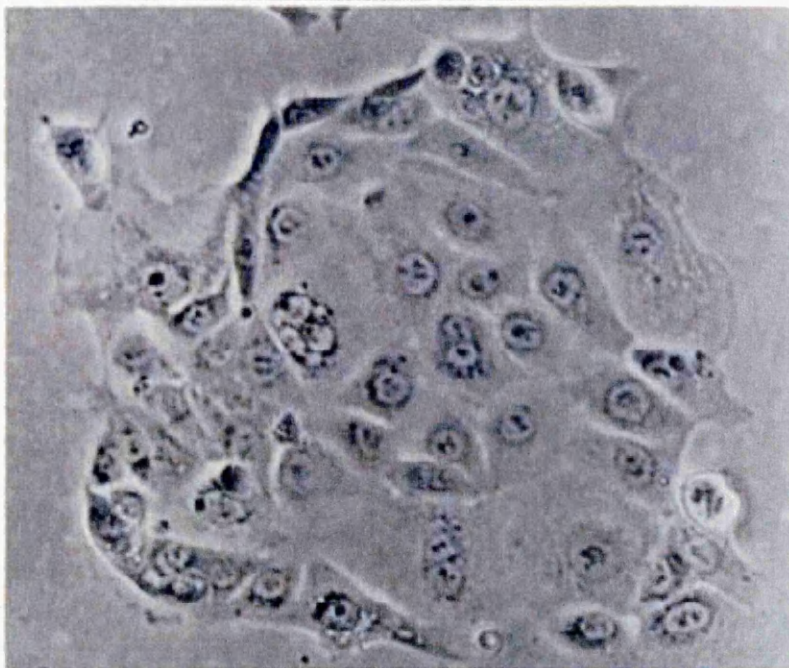


Figure 5.4 100x magnification of HCT 116 cells in culture (Brattain *et al.*, 1981)

### 5.1.3 Vinblastine

Vinblastine is a chemotherapeutic compound that inhibits microtubule assembly during metaphase (Zhigaltsev *et al.*, 2005) preventing cellular replication and hence tumour growth. Vinblastine is a chemical analogue of vincristine which was first isolated from the Madagascar periwinkle plant.

Vinblastine has been shown by Caron & Herwood 2007 to inhibit palmitoylation of tubulin *in vivo* in CEM cells and vinblastine caused microtubules to disassemble and result in the cells becoming apoptotic. Vinblastine treatment was shown to decrease palmitoylation of tubulin, and caused apoptosis in approximately 30% of cells after a 15min incubation with vinblastine at a clinically relevant concentration. This adds evidence that vinblastine does not only affect mitotic cells, since only 3.5% of these cells were mitotic. The authors propose that the apoptotic response to vinblastine is caused by either the lack of microtubules, or a change in the relative orientation of microtubules in the plasma membrane. This in turn disrupts the

organisation of protein complexes in the cell surface membrane, which initiates the apoptotic process. This is due to the effect of vinblastine on microtubule assembly and palmitoylation of tubulin.

The structure of vinblastine is shown in figure 5.5. Shown in figure 5.6 is the structure of desacetylvinblastine which is the major metabolite of vinblastine.

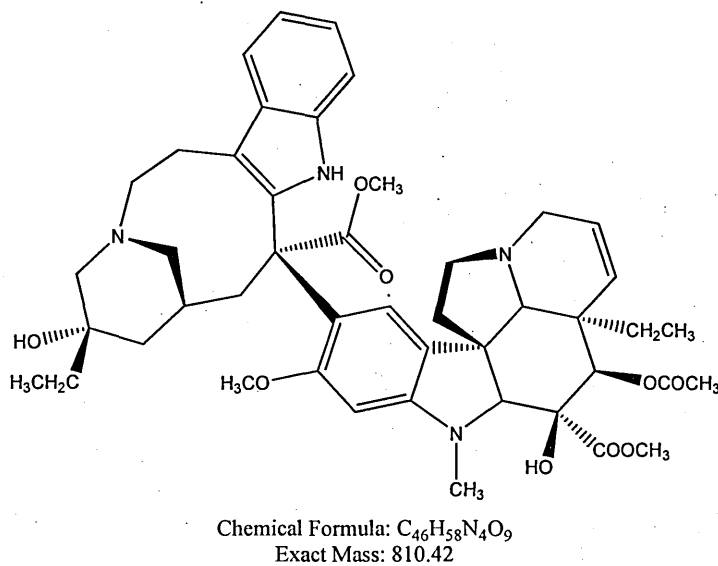


Figure 5.5 Structure of vinblastine

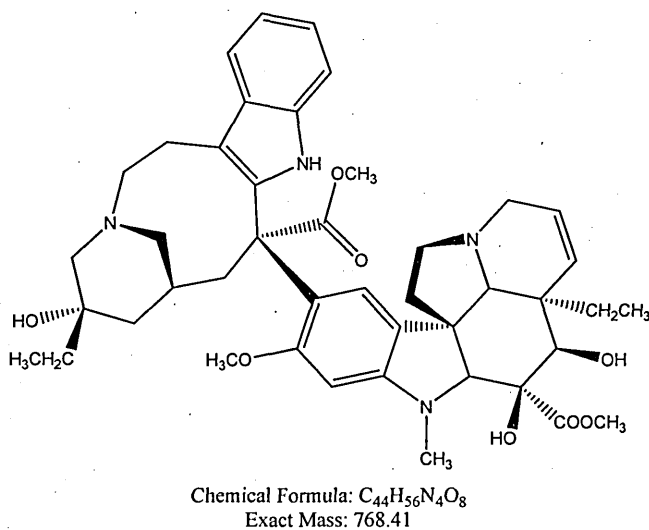


Figure 5.6 Structure of desacetylvinblastine the major metabolite of vinblastine.

When vinblastine is analysed there always appears to be an associated ion at  $m/z$  809.4 as shown in figure 5.7. The proposed structure for this ion is shown in figure 5.8.

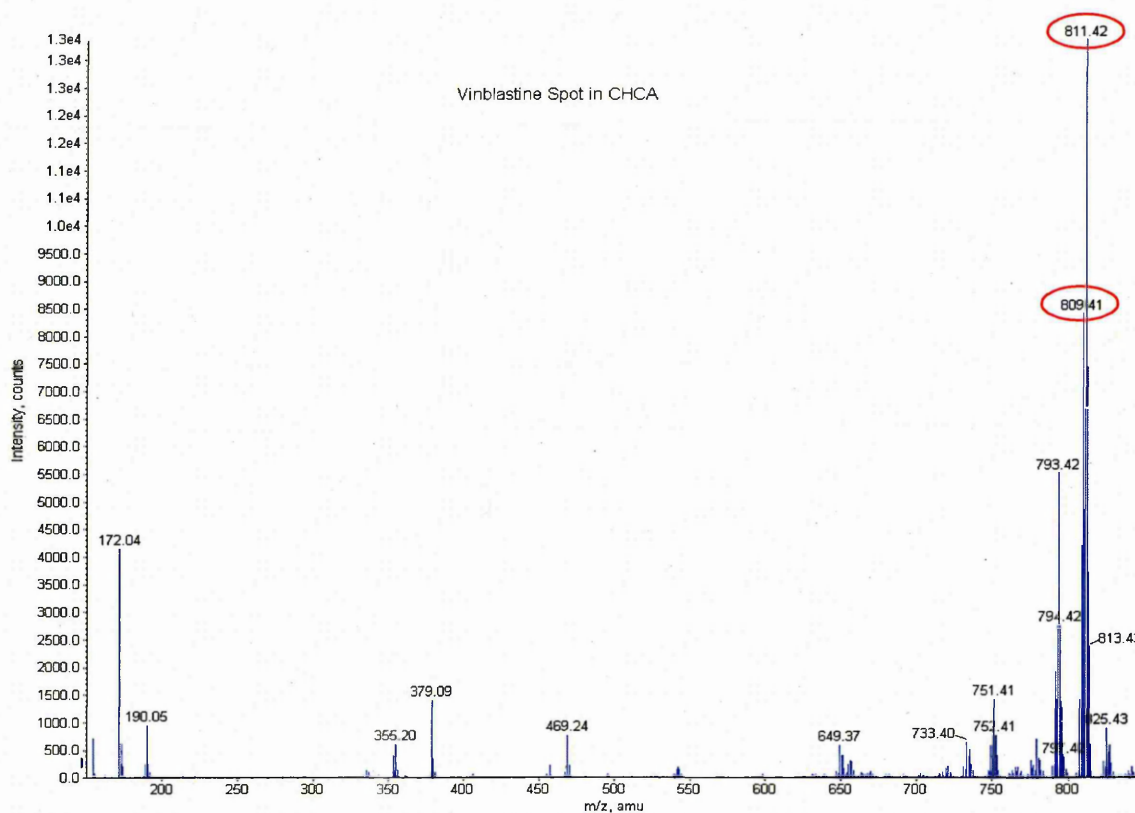


Figure 5.7 MALDI MS profile of vinblastine showing the  $[M+H]^+$  peak at  $m/z$  811.4 and the associated peak at  $m/z$  809.4.

From the ion a proposed structure for the ion  $m/z$  809.4 is given in figure 5.8 this possible structure based on the mass and the proposed structure being the least energetic option.

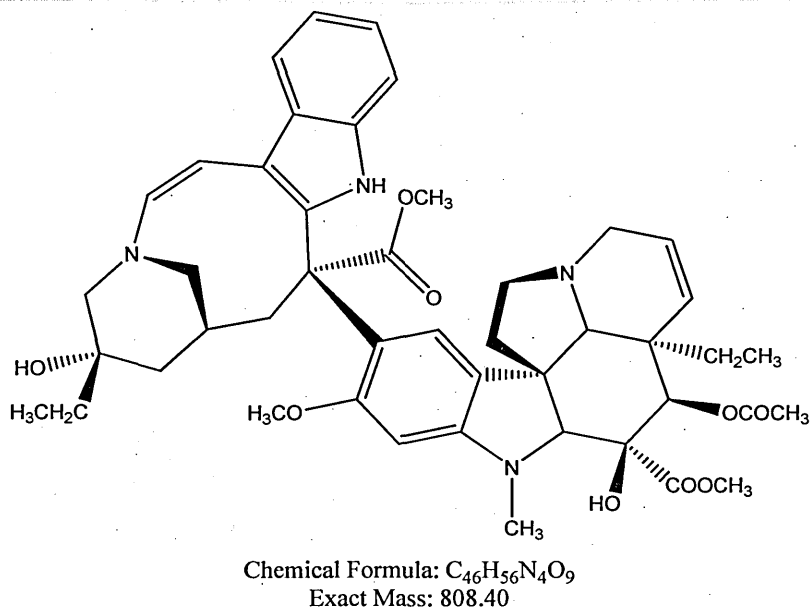


Figure 5.8 Proposed structure for the ion observed at  $m/z$  809.4. Highlighted in red is the bond believed to have changed from the original vinblastine structure.

#### 5.1.4 Principle Component Analysis (PCA) in MALDI

PCA analysis is beneficial for processing MALDI imaging data. Within this work the PCA analysis was performed to try and identify possible markers for each of the tissue regions, we have previously discussed this method (Chapter 2 of this thesis). Other research groups have used PCA in a slightly different way Van de Plas *et al.*, 2007 used PCA as a multivariate pre analysis tool to identify ions that are spatially related to form images of several ions based on their PCA loadings. This method can be useful as an initial step to determine differences within the tissue section.

Within this work positive ion MALDI was used for the detection and spatial distribution studies of phosphatidylcholine and sphingomyelin lipids.

## 5.2 Methodology

All animal studies were subject to ethical approval and all the animal use and handling in this work abides by UK Home Office Regulations and Guidelines.

### 5.2.1 Sample Preparation HCT 116

HCT 116 cells were sourced from the National Cancer Institute, Tumour Repository (Maryland, USA). The cells were grown at 37°C in a high humidified atmosphere of 5% CO<sub>2</sub> : 95% air, in a growth medium of PAA Gold: 1640 RPMI (PAA Laboratories GmbH, Pasching, Austria) with 2mM L-Glutamine and 5% Foetal Bovine Serum (FBS). Prior to inoculation the HCT 116 cells were prepared as a single cell suspension. The adherent cells were removed from the flask by the addition of trypsin/EDTA. The cells were re-suspended in incubation media containing plasma to deactivate the trypsin. This was followed by centrifugation to pellet the cells which were re-suspended in plasma-free media at a density of  $1 \times 10^8$  cells ml<sup>-1</sup>.

HsdHan<sup>TM</sup>: RNU-Foxn1 - Rowett nude rats (Harlan UK Ltd, Oxon, UK) received a single subcutaneous injection of the HCT 116 cell suspension (300 µl containing  $15 \times 10^6$  cells) on the right dorsal flank. Following inoculation, rats were monitored regularly and bodyweight, general observations and tumour dimensions were recorded up to three times a week. Digital callipers were used in the measurement of the tumours, and the following algorithm used to determine tumour volume:



$$\text{Tumour volume (mm}^3\text{)} = \frac{(\text{Length (mm)} \times \text{width(mm)}^2)}{2}$$

*Equation 5.1 Determination of tumour volume (private communication with Quotient Bioresearch Ltd).*

Once tumours had reached the target volume of around 1000 mm<sup>3</sup>, each animal was selected as either, Control, 2Hr post dose and 6 Hr post dose. The control received no injection and the 2Hr and 6Hr animals were both dosed intravenously with 6mg/kg Vinblastine and euthanised 2 and 6 hours post dose respectively.

### **5.2.2 Xenograft sectioning**

After the animal was euthanised the tumour xenografts were excised and snap frozen in a hexane cardice bath, once frozen the xenografts were stored in a -80°C Freezer until sectioned.

When required the tissues were removed from the freezer and placed in a CM1510 cryostat (Leica Microsystems, Wetzlar, Germany) set at -18°C and allowed to acclimatise for 30 minutes. Tissues were mounted onto cork discs in the desired orientation and fixed in place using OCT. Sections (12µm) were cut and thaw mounted onto glass microscope slides, and stored at -80°C until required.

### **5.2.3 Matrix Coating**

When required the sections were removed from the freezer and allowed to warm to room temperature before opening, to prevent condensation on the sample. The samples were then spray coated with 5mgml<sup>-1</sup> αCHCA in 50:50:0.1 ethanol:water:TFA (v:v:v) using an ImagePrep station (Bruker

Daltonics, Germany). This covered the tissue section with a fine matrix coating allowing time between matrix coats for co-crystallisation to occur between analytes and the matrix.

#### **5.2.4 QStar Pulsar-i Image accusation**

The glass slides were cut to size and mounted using double sided tape onto a recessed Opti-Tof<sup>®</sup> LC MALDI target plate holder (Applied Biosystems/MDS Sciex, Concord, Ontario, Canada). The recessed target holder enables the sample level to be maintained when using glass slides. This is essential because variation in the sample height alters the laser focus and the position that the laser fires.

The samples were analysed in positive ion mode using an Applied Biosystems/MDS Sciex hybrid quadrupole time-of-flight instrument (Q-Star Pulsar-i) fitted with an orthogonal MALDI ion source, using the oMALDI server 5.1 software. A 355nm frequency tripled 1-20KHz Nd:YVO<sub>4</sub> laser (Elforlight Ltd, Daventry, Northants, UK). The laser was set to a repetition rate of 5KHz. The laser was fired at the sample with 150 µm spatial resolution, with the laser firing for approximately 3 seconds per spot.

#### **5.2.5 Synapt Image accusation**

In order to set the tissue area to be analysed a digital image of the tissue, on the MALDI sample support, was generated using a CanoScan 4400F flatbed scanner (Canon, Reigate, UK). The digital image produced was imported into MALDI Imaging Pattern Creator (Waters Corporation, Milford, USA). In this software, the instrument was taught the dimensions of the image by locating

the four corners of the image plate. This allowed the creation of the image area around the sample. The pattern was then uploaded into MassLynx (Waters Corporation, Milford, USA) and the parameters of the image experiment were created. The instrument was operated in positive ion V-mode prior to imaging analysis, the mass spectrometer was calibrated using a mixture of poly(ethylene glycol) standards (Sigma-Aldrich, Gillingham, UK) with average molecular weights of 400 and 600, providing coverage of the  $m/z$  range studied. The spacing between points on the raster was 200  $\mu\text{m}$  in both x and y direction. Imaging data were obtained by moving the tissue sections in a raster pattern on an x/y-stage relative to the laser position, which remained fixed. At each position, data were acquired for 400 laser shots (2 s) using a 200Hz Nd:YAG laser.

All measurements including the calibration were performed with ion mobility separation activated.

### **5.2.6 PCA-DA Data Processing.**

Principal components analysis - Discriminate Analysis (PCA-DA) was carried out using the MarkerView™ statistical analysis package (Applied Biosystems/MDS Sciex, Concord, Ontario, Canada). Ten Spectra were randomly selected from each of the 6 tissue regions, viable tumour, necrotic centre and connective tissue from both the vinblastine dosed and the non dosed sections. The spectra were imported into the MarkerView™ software with a mass tolerance of 0.5 amu (i.e. the bin size the data was grouped into), and a minimum signal count of 4.0 which removed background noise. The data was normalised against  $m/z$  379 the protonated dimer of the matrix. The

Trim P.J. Chapter 5

matrix associated ions were then excluded from the analysis along with isotopic peaks using a function of the software. PCA-DA was carried out using Pareto scaling. Pareto scaling uses the square root of the standard deviation as a scaling factor to reduce the dominance of large scale intensity changes in high abundance ions (Van den Berg *et al.*, 2006). These may mask the variation in lower abundance ions during PCA-DA. The overall outcome of PCA-DA is greatly affected by the masking of the underlying relevant information by high intensity ions. D1 versus D2 was chosen for display since these components resulted in the highest overall degree of separation of the spectra within the PCA-DA scores plots 22.9% and 21.9% respectively.

In the header for each of the scores and loadings plots (Figure 5.10 & 5.11) the discriminate components that have been plotted are shown with the percentage variance (Van den Berg *et al.*, 2006), or the percentage of the variance accounted for from each of the discriminate components shown in brackets. Also shown is the type of scaling used which was Pareto (DA).

### **5.2.7 Image processing**

The imaging data sets obtained using the Q-Star Pulsar-*i* were converted into Analyze 7.5 file format using oMALDI server 5.1 software.

The ion mobility related data analysis obtained on a Synapt HDMS system was accomplished using "DriftScope" software (Waters Corporation, Milford, USA). This enables specific drift time and *m/z* regions to be extracted, the resultant data sets were then converted into Analyze 7.5 file format using MALDI Imaging converter software (Waters Corporation, Milford, USA).

All Image visualisation and processing was carried out using BioMap 3.7.5.5 ion imaging software (Novartis, Basel, CH) (<http://www.maldi-msi.org>) resulting in the production of a 2D ion density map. Images were normalised against the matrix ion at  $m/z$  190.

### **5.2.8 Histological staining.**

The tissue sections were retained after imaging for Haematoxylin and Eosin staining. This allows for a comparison between the MALDI imaging data and the histology.

After imaging, the tissue sections were washed at a 45° angle using 5ml of 100% ethanol, this step completely removed the matrix which was left on the tissue. The tissue sections were then rehydrated using a series of graded alcohols. Each section was submerged in 100% ethanol for 3 minutes, followed by a further 3 minutes in 95% and 70% ethanol. The rehydrated tissue section were then repeatedly dipped into deionised water for 2 minutes until the ethanol had been removed. The initial stain of Haematoxylin was then applied by submerging the section into filtered haematoxylin for 1 minute. Haematoxylin stains basophilic structures within the cells predominantly the nuclei with a blue-purple colour. The tissue sections were then gently washed under running tap water for 3-5 minute until the water ran clear. The effects of the haematoxylin can be lightened using a 1-3 second dip in acid alcohol if required but this was not needed in this experiment. The tissue sections were washed in 70% ethanol followed by 95% ethanol for 3 minutes each prior to counterstaining for 20 seconds in 5% eosin in ethanol. Eosin stains eosinophilic structures pink. After counterstaining tissues sections were again washed in 95% ethanol twice, followed by 2 washes in 100% ethanol each for

3 minutes. In order to dehydrate the section. Dehydrated sections were then placed in xylene for at least 10 minutes until cover slipped.

### 5.2.9 PPM mass error calculations

The PPM (Parts Per Million) mass error was calculated for each of the possible lipid species observed. The calculations were carried out using the equation shown in equation 5.2. Using data that had been recalibrated to the matrix ions.

$$PPM\ Error = \left( \frac{Measured\ Mass - Theoretical\ Mass}{Measured\ Mass} \right) \times 1000000$$

*Equation 5.2 PPM mass error calculation.*

## 5.3 Results and discussion.

To enable comparison between the mass spectrometric data and the actual tissue sections H&E staining was carried out on the same sections after mass spectrometric analysis. The sections are shown in figure 5.9 with inset an image obtained at 40x magnification to demonstrate the tissue regions.

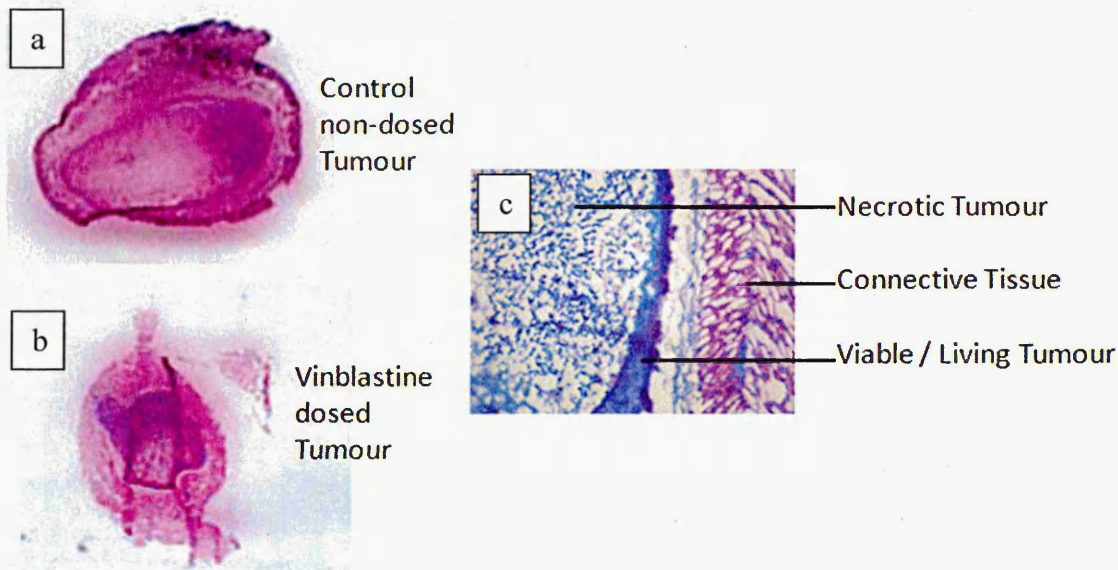


Figure 5.9 a) H&E stained section of the Control, non-dosed tumour section after MALDI imaging. b) H&E stained section of the dosed tumour xenograft after MALDI imaging, c) A magnified image of the control tissue section showing the 3 distinctively different tissue regions.

The use of PCA has been shown to be beneficial for interrogating MALDI imaging data (McCombie *et al.*, 2005. Prideaux *et al.*, 2007) shown in figure 5.10 and 5.11 are the scores and loadings plots respectively.

PCA DA is shown in figure 5.10 to nearly separate all six groups of 10 randomly selected spectra from the viable tumour, necrotic centre and connective tissue from both the dosed and non-dosed tumour sections. There is some overlap between the connective tissue and some of the viable tumour spectra from the control non-dosed tissue section.

The Scores plot (figure 5.10) shows that one of the 6hr post dose MS spectra from the viable tumour (VT0) appears to be associated with the connective tissue MS spectra. This is probably due to the viable tumour being a thin ring

of cells. This MS spectrum could have been taken from the connective tissue region and not the viable tumour, or possibly a combination of ions from both tissue regions due to the image resolution being at  $150\mu\text{m}$ . PCA-DA allows incorrectly identified MS spectra to be discriminated.





Principal Component	Variance (%)	Total Variance (%)
PC1	22.87	22.87
PC2	21.94	44.80
PC3	21.23	66.03
PC4	19.99	86.02
PC5	13.98	100.00

Table 5.1 The percentage variance and total variance accounted for by each principle component selected by the PCA DA software.

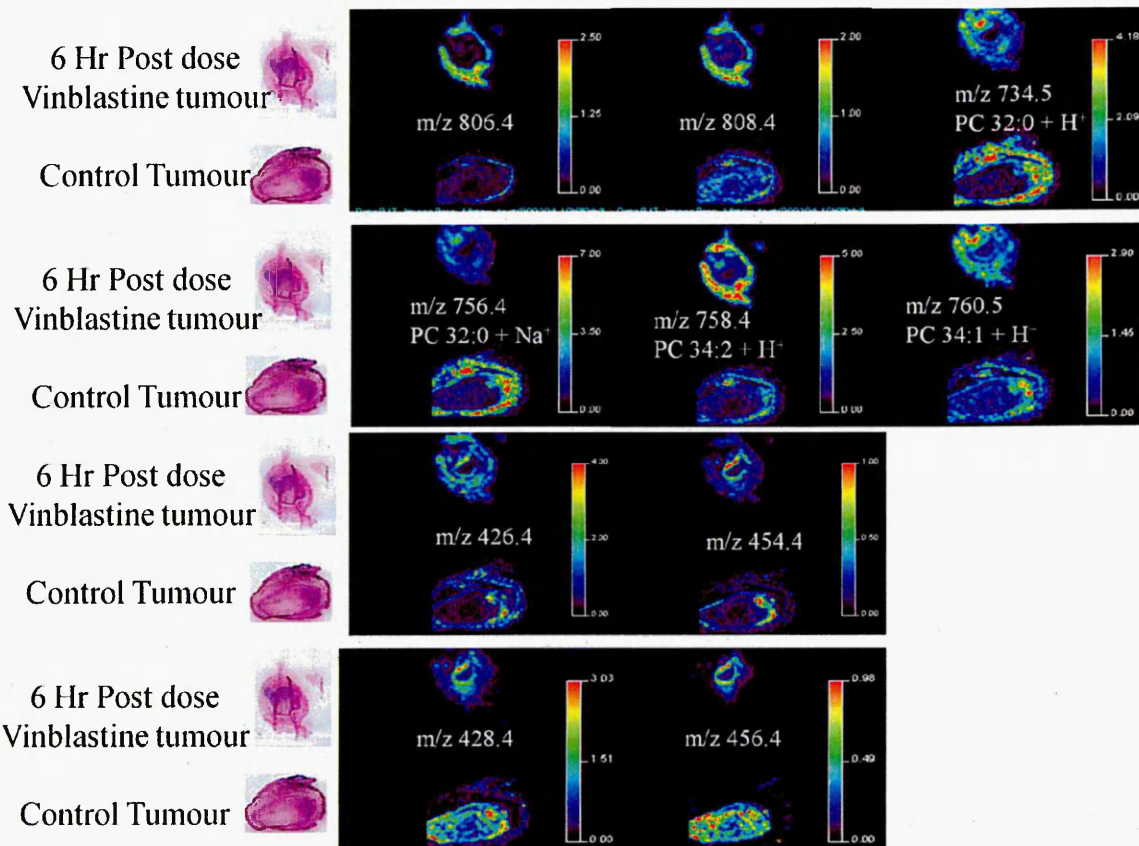


Figure 5.11 2D ion plots showing the distribution of some of the ions of interest within the tissue sections selected from the loadings plot, with the corresponding H&E stained tissue section. Identifications have been made based on MS/MS data analysis.

Possible ions of interest accounting for the separation of the different tissue regions can be seen in the loadings plot figure 5.10b. Images generated from some of these possible ions of interest are shown in figure 5.11.

MS/MS spectra were obtained and have been used to confirm the identity of some of these ions accounting for the major differences between the tissue types. Figures 5.12, 5.13, 5.14 and 5.15 show the interpreted MS/MS spectra used to identify  $m/z$  756.4 one of the ions of interest.

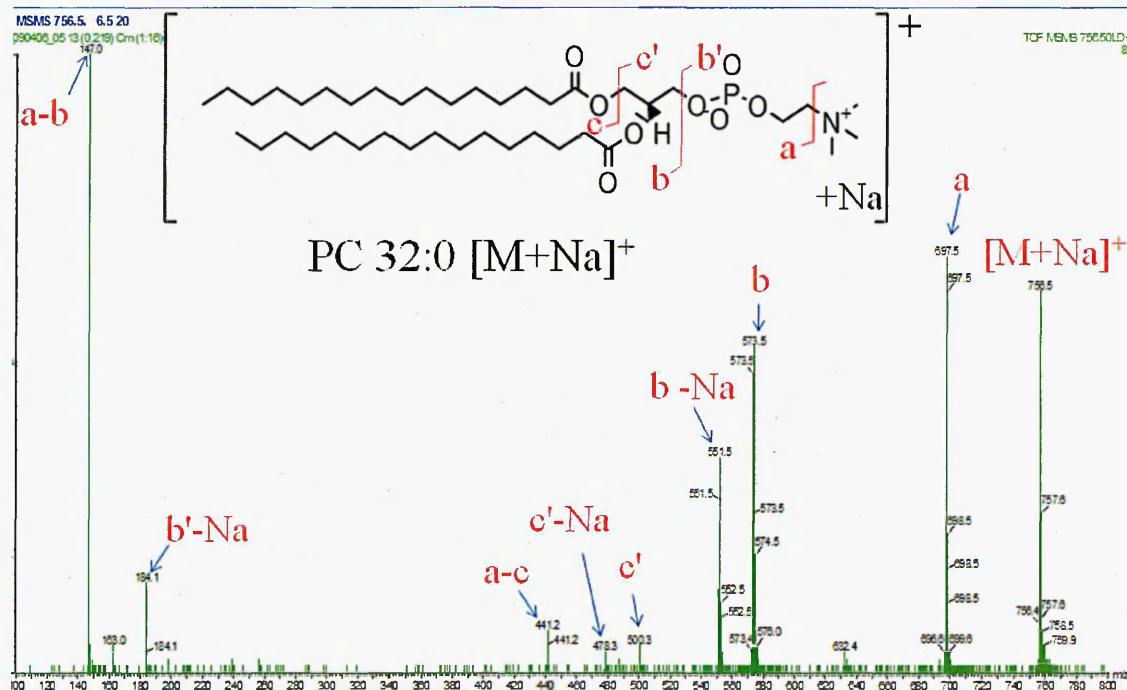


Figure 5.12 Product ion mass spectrum for  $m/z$  756 and the interpretation identifying this ion as PC 32:0 [M+Na]<sup>+</sup>

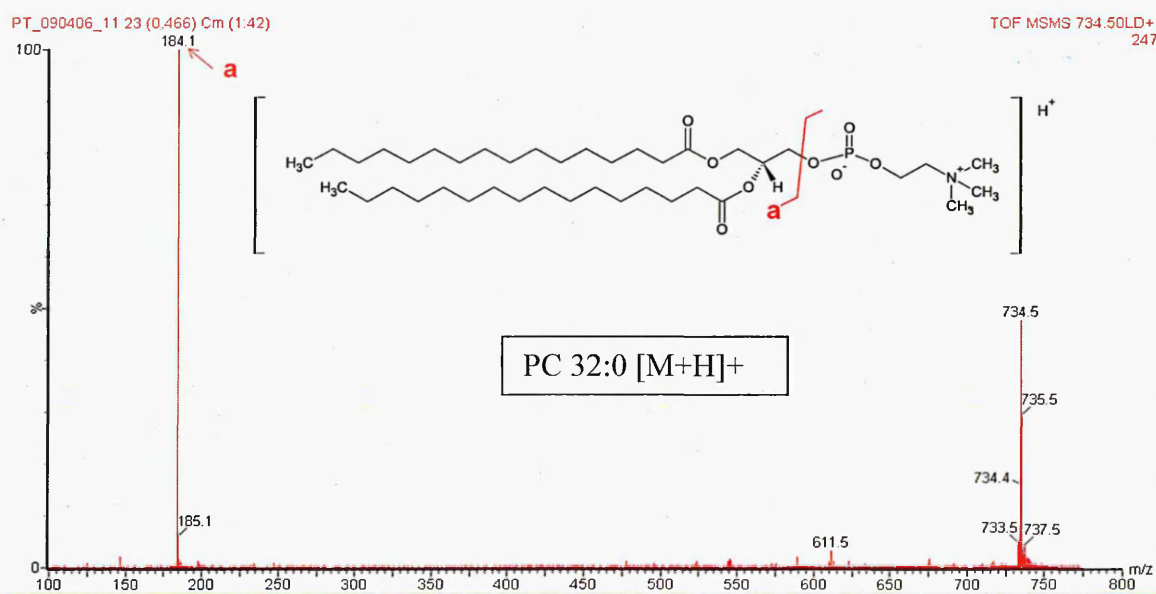


Figure 5.13 Product ion mass spectrum for  $m/z$  734 and the interpretation identifying this ion as PC 32:0 [M+H]<sup>+</sup>. Fatty acid chains shown is only one option for this configuration, based on the mass.

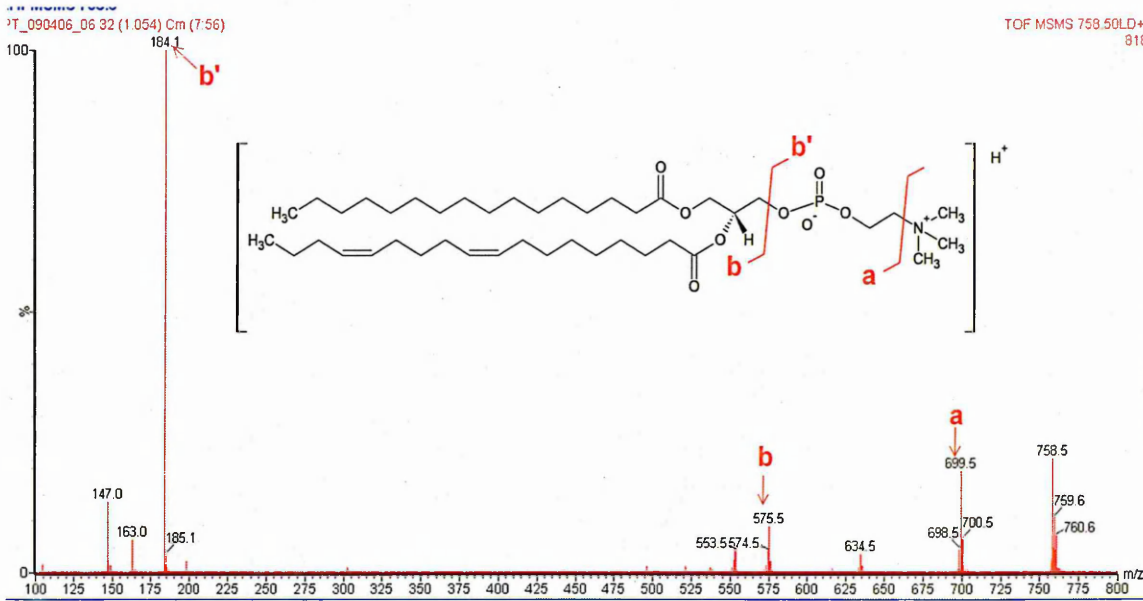


Figure 5.14 Product ion mass spectrum for  $m/z$  758 and the interpretation identifying this ion as PC 34:2  $[M+H]^+$ : Note the fatty acid chains shown are only one option for this configuration, based on the mass.

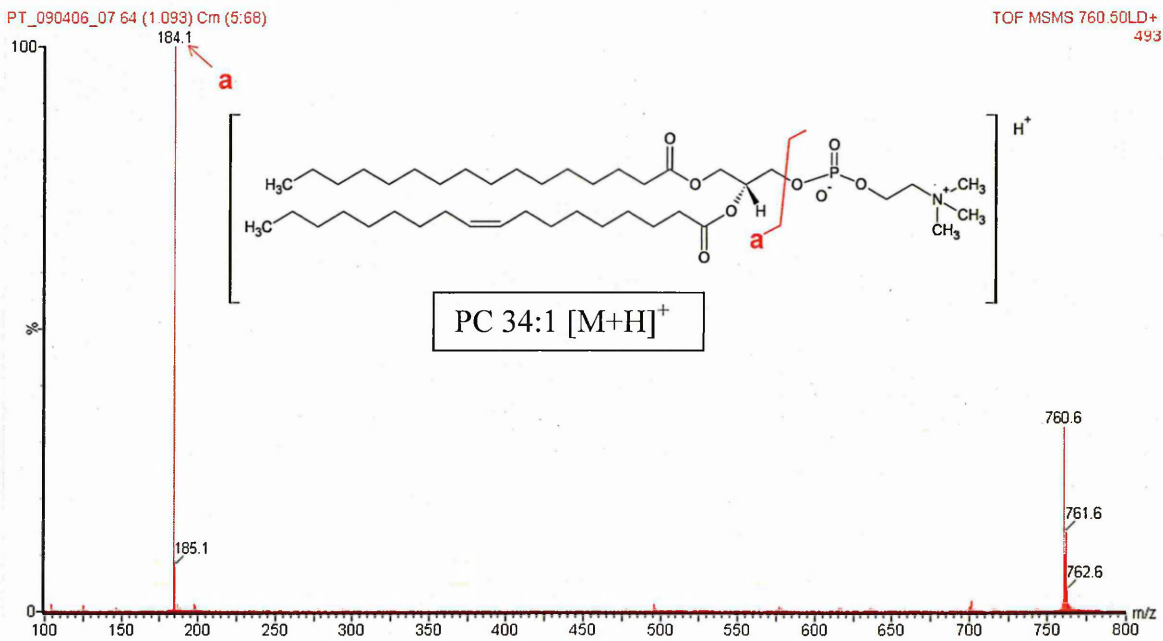


Figure 5.15 Product ion mass spectrum for  $m/z$  760 and the interpretation identifying this ion as PC 34:1  $[M+H]^+$  Fatty acid chains shown is only one option for this configuration, based on the mass.

Another method of data processing that was used within this work was the interpretation of the results by directed image processing. This involves looking for the distribution of some possible ions of interest from the calculated  $m/z$  values for a set of lipid species. Table 5.2 shows a list of lipid species calculated  $m/z$  values and the observed values of the ions near those masses, and their possible assignments to lipid species, also shown in table 5.2 is the relative intensity of the ions simply depicted for rapid comparison between the tissue sections and the corresponding tissue regions. Very low to no signal observed this related to a signal count between 0 - 0.01au and is shown by a (-), low relative abundance this related to a signal count between 0.01 - 0.1au and is shown by (+), followed by (++) which denotes medium relative abundance this related to a signal count between 0.1 - 0.5au, and a relatively high abundance which related to a signal count between 0.5 - 1au is shown by (+++) and a very high abundance (>1au) is denoted by (++++) . This table is just as a visual comparison for a range of lipids throughout each tissue region, and the relative abundances are from visual comparison, all data used in the compilation of this table is from data normalised against the matrix ion  $m/z$  190.



Calculated m/z	Observed m/z	PPM Error (2dp)	Possible species	Ion Species	Viable Tumour		Connective Tissue		Necrotic Centre	
					Non-Dosed	Dosed	Non-Dosed	Dosed	Non-Dosed	Dosed
300.2903	300.2918	5.00	Sphingosine	[M+H] <sup>+</sup>	-	-	-	-	+	-
302.3059	302.2632	-141.27	Sphinganine	[M+H] <sup>+</sup>	-	+	-	-	-	-
322.2722	322.2875	47.47	Sphingosine	[M+Na] <sup>+</sup>	-	-	-	-	-	-
324.2878	324.3017	42.86	Sphinganine	[M+Na] <sup>+</sup>	-	-	-	-	-	-
338.2461	338.2596	39.91	Sphingosine	[M+K] <sup>+</sup>	-	+	-	+	-	-
340.2618	340.3061	130.18	Sphinganine	[M+K] <sup>+</sup>	++	++	-	+	-	-
369.3521	369.3501	-5.41	Cholesterol	[M-H <sub>2</sub> O+H] <sup>+</sup>	+++	+++	-	++	-	-
465.3457	465.3513	12.03	SPPC	[M+H] <sup>+</sup>	+	+	-	+	-	-
482.3611	482.3855	50.58	C-16Lyso-PAF	[M+H] <sup>+</sup>	+	++	-	-	-	-
487.3277	487.2911	-75.11	SPPC	[M+Na] <sup>+</sup>	-	-	+	-	-	-
503.3016	503.3213	39.14	SPPC	[M+K] <sup>+</sup>	-	-	+	++	-	-
510.3924	510.3803	-23.71	C-18Lyso-PAF	[M+H] <sup>+</sup>	+	++	++	++	-	-
524.3716	524.3872	29.75	C16 - PAF	[M+H] <sup>+</sup>	+	+	+++	++	-	-
552.4029	552.4127	17.74	C18 - PAF	[M+H] <sup>+</sup>	++	++	++	++	-	-

Table 5.2 List of possible Sphingolipid species and whether they were detected within different tissue regions of the dosed and non dosed tissue sections. An arbitrary visual scale was used with the following indications of relative abundance, Very low to no signal observed is shown by a (-), low relative abundance is shown by (+), followed by (++) which denotes medium relative abundance, and a relatively high abundance is shown by (+++) and a very high abundance is denoted by (+++). This table is just as a visual comparison for a range of lipids throughout each tissue region. All data used in the compilation of this table is from data normalised against the matrix ion m/z 190. (Possible lipid species not confirmed by MS/MS) SPPC = sphingosylphosphorylcholine, PAF = Platelet activating factor, LPC = Lyso phosphatidylcholine. PPM mass errors have been calculated and displayed, Red- >20ppm, Yellow - 10-20ppm, Green - <10ppm.

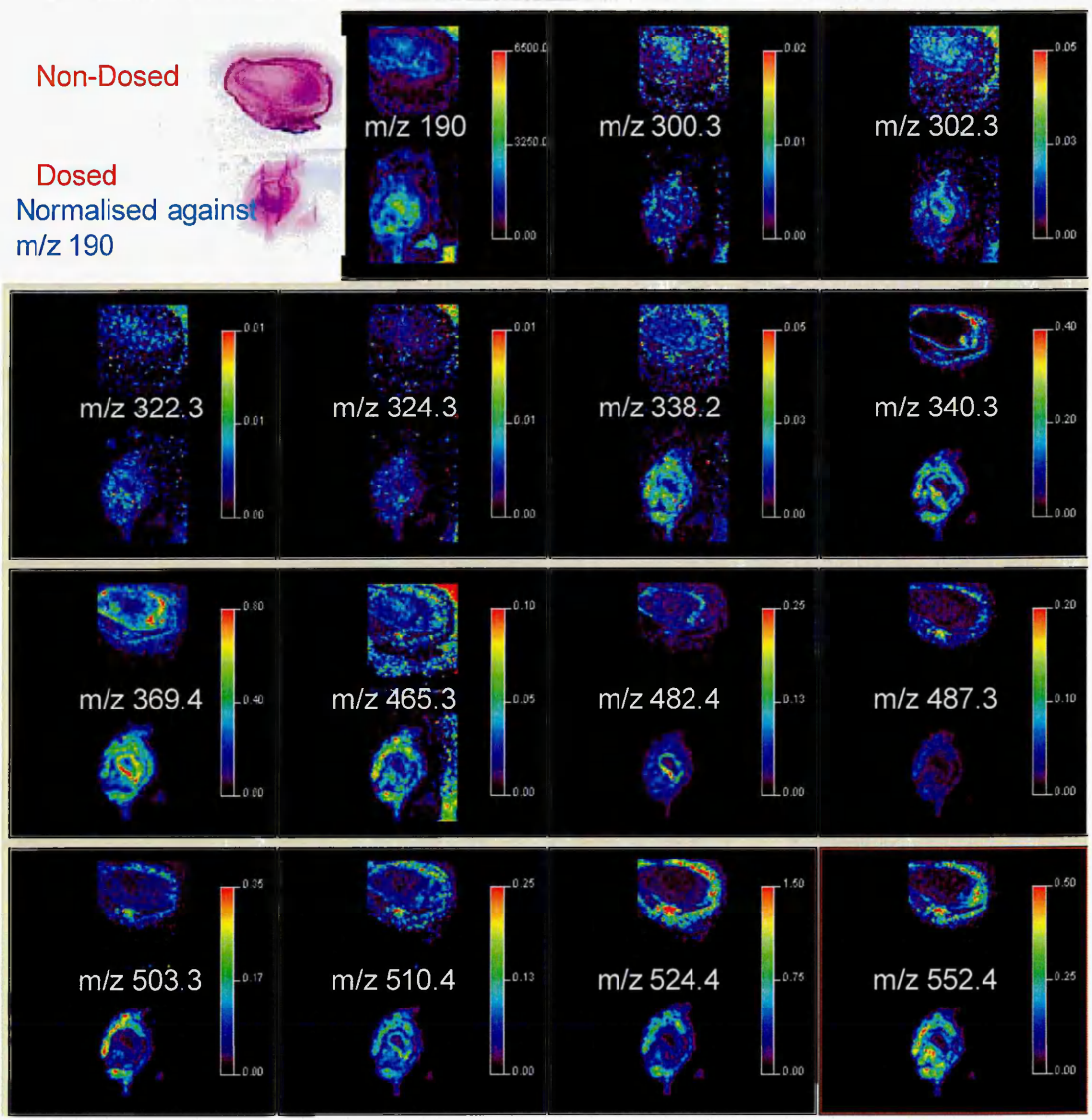


Figure 5.16 2D ion plots of the m/z values listed in Table 5.2

Calculated Mono-isotopic m/z	Observed m/z	PPM error (2dp)	Possible species	Ion Species	Viable Tumour		Connective Tissue		Necrotic Centre	
					Non-Dosed	Dosed	Non-Dosed	Dosed	Non-Dosed	Dosed
647.5128	647.4541	-90.66	SM (18:1/12:0)	[M+H] <sup>+</sup>	-	-	-	+	-	-
669.4947	669.4840	-15.98	SM (18:1/12:0)	[M+Na] <sup>+</sup>	+	+	+	+	+	-
675.5441	675.5155	-42.34	SM (18:1/14:0)	[M+H] <sup>+</sup>	+	+	-	-	-	-
677.5598	677.5285	-46.20	SM (18:0/14:0)	[M+H] <sup>+</sup>	-	-	-	-	+	-
685.4687	685.4669	-2.63	SM (18:1/12:0)	[M+K] <sup>+</sup>	++	++	-	+	-	-
697.5260	697.4719	-77.57	SM (18:1/14:0)	[M+Na] <sup>+</sup>	+++	++	+	+	-	-
699.9918	699.9654	-37.72	SM (18:0/14:0)	[M+Na] <sup>+</sup>	+	+	+	+	+	-
703.5754	703.5685	-9.81	SM (18:1/16:0)	[M+H] <sup>+</sup>	++	++	++	+	-	-
705.5911	705.5783	-18.14	SM (18:0/16:0)	[M+H] <sup>+</sup>	+++	+++	-	+	+	-
713.5000	713.4486	-72.04	SM (18:1/14:0)	[M+K] <sup>+</sup>	++	++	++	+	-	-
715.5156	715.4669	-68.07	SM (18:0/14:0)	[M+K] <sup>+</sup>	+	+	-	+	-	-
725.5573	725.5453	-16.54	SM (18:1/16:0)	[M+Na] <sup>+</sup>	++++	+	++	+	+	-
727.5730	727.5575	-21.30	SM (18:0/16:0)	[M+Na] <sup>+</sup>	+++	++	-	-	+++	-
729.5811	729.4713	-148.48	SM (18:1/18:1)	[M+H] <sup>+</sup>	++	++	-	+	-	-
731.6067	731.6037	-4.10	SM (18:0/18:1)	[M+H] <sup>+</sup>	-	-	+	++	-	-
731.6067	731.6037	-4.10	SM (18:1/18:0)	[M+H] <sup>+</sup>	-	-	+	++	-	-
733.6224	733.5644	-79.07	SM (18:0/18:0)	[M+H] <sup>+</sup>	+++	+++	-	++	-	-
741.5313	741.5270	-5.80	SM (18:1/16:0)	[M+K] <sup>+</sup>	++	+	++	+	-	-
743.5469	743.5436	-4.44	SM (18:0/16:0)	[M+K] <sup>+</sup>	+	+	+	+	++	-
751.5730	751.5418	-41.51	SM (18:1/18:1)	[M+Na] <sup>+</sup>	+	+	+	+	+	-
753.5886	753.5886	0.00	SM (18:0/18:1)	[M+Na] <sup>+</sup>	-	-	+	++	-	-
753.5886	753.5886	0.00	SM (18:1/18:0)	[M+Na] <sup>+</sup>	-	-	+	++	-	-
755.6043	755.5615	-56.65	SM (18:0/18:0)	[M+Na] <sup>+</sup>	+++	++	-	+	+	-
759.6380	759.5751	-82.81	SM (18:1/20:0)	[M+H] <sup>+</sup>	-	-	+	+++	-	-
761.6537	761.5886	-85.48	SM (18:0/20:0)	[M+H] <sup>+</sup>	+++	+++	+	+++	-	-
767.5469	767.5297	-22.41	SM (18:1/18:1)	[M+K] <sup>+</sup>	+	+	+	+	+	+
769.5626	769.5670	5.72	SM (18:0/18:1)	[M+K] <sup>+</sup>	-	+	-	++	+	-
769.5626	769.5670	5.72	SM (18:1/18:0)	[M+K] <sup>+</sup>	-	+	-	++	+	-
772.5861	772.5321	-69.90	SM (18:0/18:0)	[M+K] <sup>+</sup>	+++	+	+++	+	-	-
781.6199	781.5742	-58.47	SM (18:1/20:0)	[M+Na] <sup>+</sup>	+	+	+	+++	+	--
783.6356	783.5804	-70.45	SM (18:0/20:0)	[M+Na] <sup>+</sup>	++	+	-	++	+	-
787.6693	787.6232	-58.53	SM (18:1/22:0)	[M+H] <sup>+</sup>	+	+	+	++	-	-
789.6850	789.6367	-61.17	SM (18:0/22:0)	[M+H] <sup>+</sup>	+	++	+	+	+	-
797.5939	797.5631	-38.62	SM (18:1/20:0)	[M+K] <sup>+</sup>	-	-	+	++	-	-
799.6095	799.5593	-62.78	SM (18:0/20:0)	[M+K] <sup>+</sup>	++	++	+	+	+	-



809.6512	809.6204	-38.04	SM (18:1/22:0)	[M+Na] <sup>+</sup>	+	+	++	++	+	-
812.6747	812.6281	-57.34	SM (18:0/22:0)	[M+Na] <sup>+</sup>	+	+	+	+	++	-
813.6771	813.6827	6.88	SM (18:1/24:1)	[M+H] <sup>+</sup>	-	+	+	+	+	-
815.7006	815.7040	4.17	SM (18:0/24:1)	[M+H] <sup>+</sup>	+	++	+	+	+	-
815.7006	815.7040	4.17	SM (18:1/24:0)	[M+H] <sup>+</sup>	+	++	+	+	+	-
817.7163	817.7100	-7.70	SM (18:0/24:0)	[M+H] <sup>+</sup>	++	++	-	-	++	-
825.6252	825.6110	-17.20	SM (18:1/22:0)	[M+K] <sup>+</sup>	+	+	+	+	+	+
827.6408	827.6186	-26.82	SM (18:0/22:0)	[M+K] <sup>+</sup>	+	++	+	+	++	-
831.7319	831.7100	-26.33	SM (18:0/25:0)	[M+H] <sup>+</sup>	+	+	+	++	-	-
835.6669	835.6707	4.55	SM (18:1/24:1)	[M+Na] <sup>+</sup>	+	+	++	+	+	-
837.6825	837.6866	4.89	SM (18:0/24:1)	[M+Na] <sup>+</sup>	+	+	++	+	++	-
837.6825	837.6886	7.28	SM (18:1/24:0)	[M+Na] <sup>+</sup>	+	+	++	+	++	-
839.6982	839.6952	-3.57	SM (18:0/24:0)	[M+Na] <sup>+</sup>	-	+	-	-	++	-
841.7163	841.6880	-33.62	SM (18:1/26:1)	[M+H] <sup>+</sup>	-	+	-	-	++	-
843.7319	843.6853	-55.23	SM (18:0/26:1)	[M+H] <sup>+</sup>	+	+	+	+	+	-
843.7319	843.6853	-55.23	SM (18:1/26:0)	[M+H] <sup>+</sup>	+	+	+	+	+	-
845.7397	845.6969	-50.61	SM (18:0/26:0)	[M+H] <sup>+</sup>	+	+	+	++	+	-
851.6408	851.6581	20.31	SM (18:1/24:1)	[M+K] <sup>+</sup>	-	-	-	++	-	-
853.6565	853.6782	25.42	SM (18:0/24:1)	[M+K] <sup>+</sup>	+	+	++	+	+	-
853.6565	853.6782	25.42	SM (18:1/24:0)	[M+K] <sup>+</sup>	+	+	++	+	+	-
853.7138	<b>853.6782</b>	-41.70	SM (18:0/25:0)	[M+Na] <sup>+</sup>	+	+	++	+	+	-
855.6721	855.6956	27.46	SM (18:0/24:0)	[M+K] <sup>+</sup>	+	+	+	+	++	-
863.6982	863.6933	-5.67	SM (18:1/26:1)	[M+Na] <sup>+</sup>	++	+	+	+	+	-
865.7138	865.6999	-16.06	SM (18:0/26:1)	[M+Na] <sup>+</sup>	+	+	+	-	+	-
865.7138	865.6999	-16.06	SM (18:1/26:0)	[M+Na] <sup>+</sup>	+	+	+	-	+	-
867.7295	867.6948	-39.99	SM (18:0/26:0)	[M+Na] <sup>+</sup>	+	+	+	+	++	-
870.3960	870.5500	176.90	SM (18:0/25:0)	[M+K] <sup>+</sup>	+	+	-	++	+	-
879.6721	879.7280	63.54	SM (18:1/26:1)	[M+K] <sup>+</sup>	+	+	+	+	++	-
881.6878	881.7506	71.22	SM (18:0/26:1)	[M+K] <sup>+</sup>	+	+	+	+	+	-
881.6878	881.6878	0.00	SM (18:1/26:0)	[M+K] <sup>+</sup>	+	+	+	+	+	-
883.7034	883.7420	43.68	SM (18:0/26:0)	[M+K] <sup>+</sup>	+	+	-	+	+	-

Table 5.3 List of possible Sphingomyelin (SM) species and whether they were detected within different tissue regions of the dosed and non dosed tissue sections. An arbitrary visual scale was used with the following indications of relative abundance, Very low to no signal observed is shown by a (-), low relative abundance is shown by (+), followed by (++) which denotes medium relative abundance, and a relatively high abundance is shown by (+++) and a very high abundance is denoted by (++++). This table is just as a visual comparison for a range of lipids throughout each tissue region. All data used in the compilation of this table is from data normalised against the matrix ion  $m/z$  190. PPM mass errors have been calculated and displayed, Red - >20ppm, Yellow - 10-20ppm, Green - <10ppm.

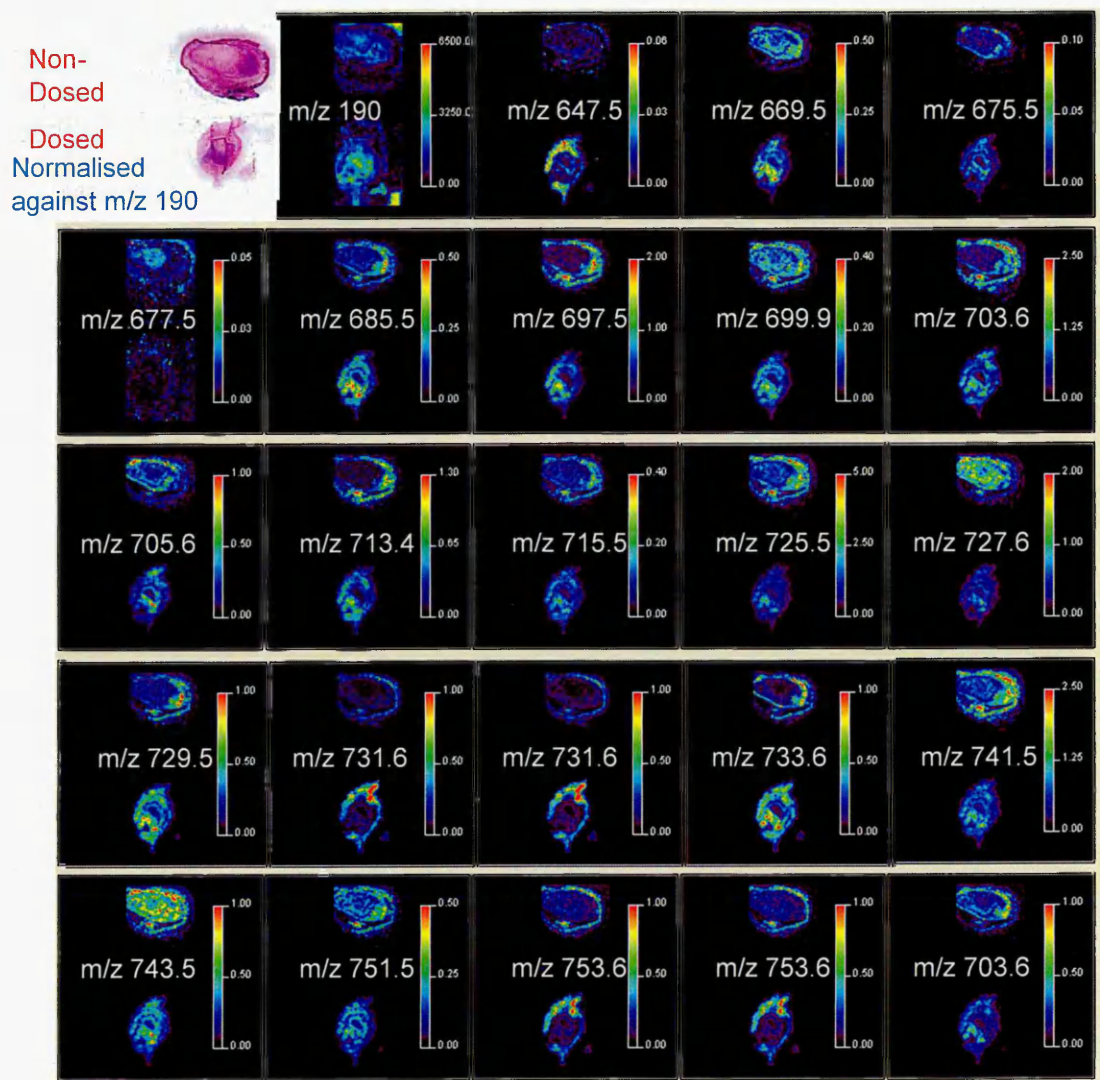


Figure 5.17 2D ion plots of the m/z values listed in Table 5.3

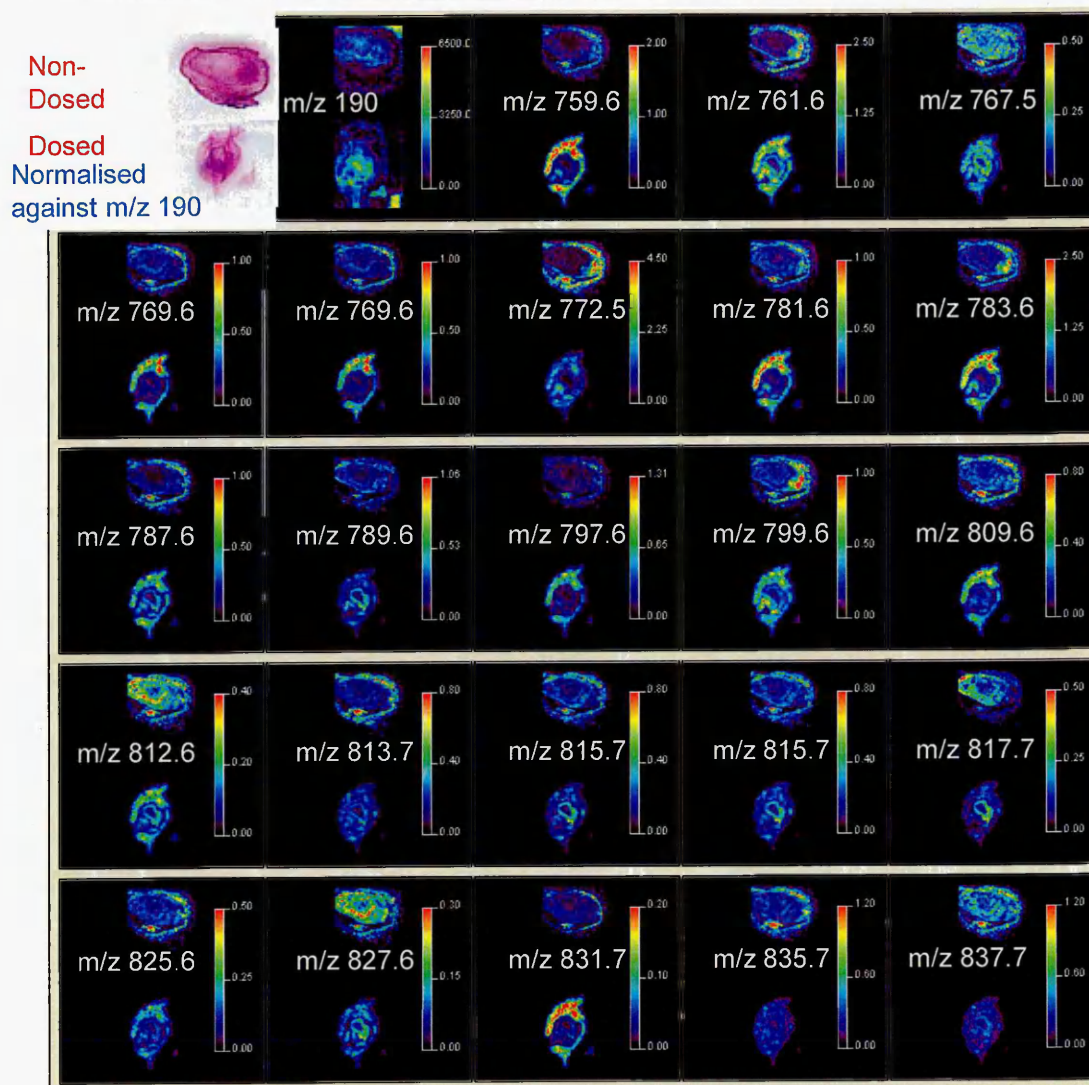


Figure 5.18 2D ion plots of the  $m/z$  values listed in Table 5.3



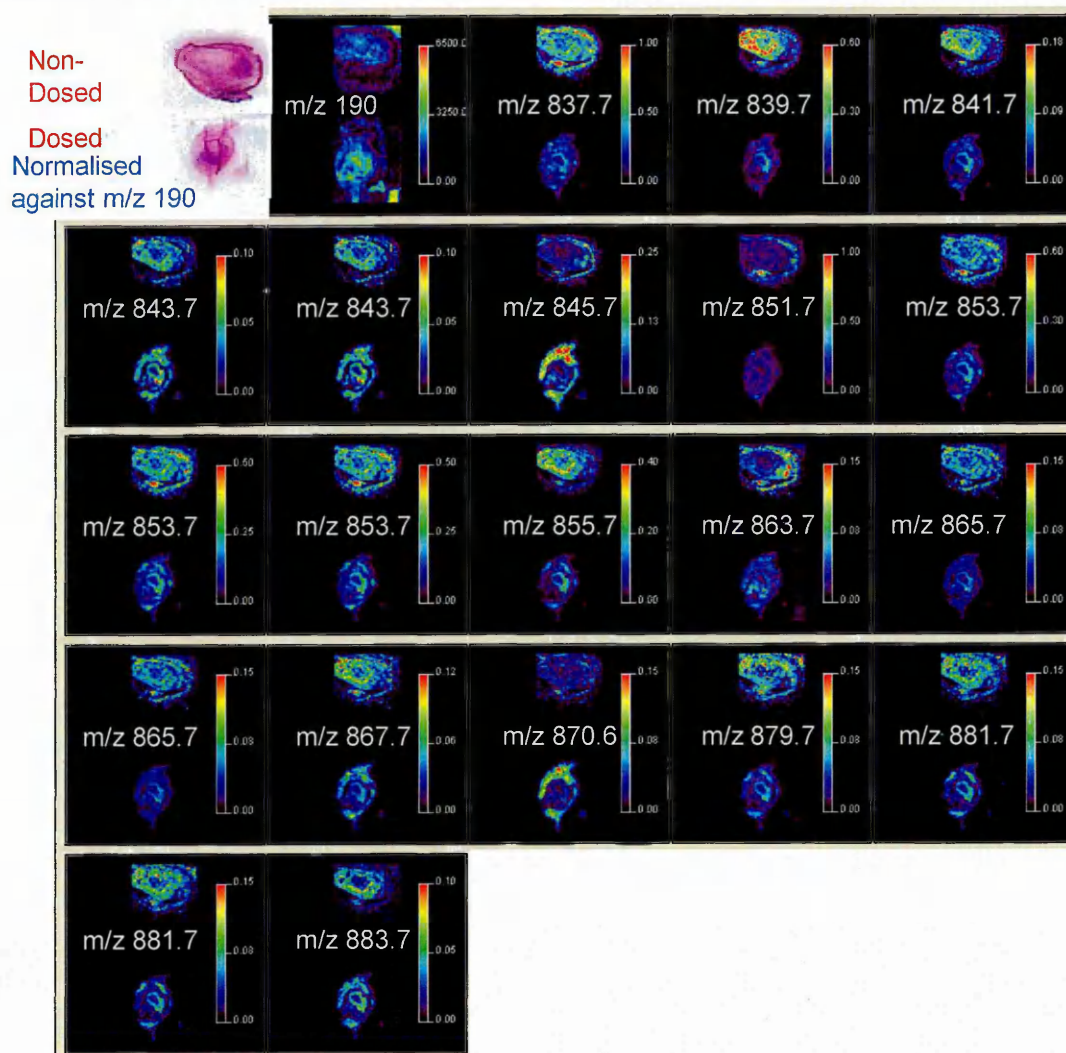


Figure 5.19 2D ion plots of the  $m/z$  values listed in Table 5.3

There are several differences in the distribution within the tissues of some of the possible sphingolipids. There are several ions predominantly associated with the viable tumour region of each section. There are also possibly more interestingly ions which only appear or are present in higher relative abundance within the dosed or non dosed tumours. Several ions are present in the necrotic centre of the control tumour which do not appear to be present in the necrotic centre of the vinblastine dosed tumour including  $m/z$  727.6, 839.6 and 841.6. This is possibly due to the control tumour xenograph being much larger than the dosed xenograph with a large necrotic centre compared

to the necrotic centre of the dosed tumour. The size difference in the tumours is not a result of the dosing regime but due to the initial rate of tumour growth prior to dosing.

Calculated m/z	Observed m/z	Error PPM	Possible species	Ion Species	Viable Tumour		Connective Tissue		Necrotic Centre	
					Non-Dosed	Dosed	Non-Dosed	Dosed	Non-Dosed	Dosed
718.5309	718.5674	50.80	PC 31:1	[M+H] <sup>+</sup>	++	++	-	+	-	-
732.5543	732.5576	4.50	PC 32:1	[M+H] <sup>+</sup>	++	++	-	++	-	-
734.5622	734.5647	3.40	PC 32:0	[M+H] <sup>+</sup>	++	++	+++	++	-	-
756.5519	756.5512	-0.93	PC 32:0	[M+Na] <sup>+</sup>	++	+	+++	+	-	-
758.5700	758.5692	-1.05	PC 34:2	[M+H] <sup>+</sup>	+	+	+	+++	-	-
760.5856	760.5836	-2.63	PC 34:1	[M+H] <sup>+</sup>	++	++	+	++	-	-
762.5935	762.5961	3.41	PC 34:0	[M+H] <sup>+</sup>	+	+	+	+	-	-
772.5259	772.5321	8.03	PC 32:0	[M+K] <sup>+</sup>	++	+	++	+	-	-
782.5676	782.5739	8.05	PC 34:1	[M+Na] <sup>+</sup>	++	+	+	++	-	-
782.5700	782.5739	4.98	PC 36:4	[M+H] <sup>+</sup>	++	+	+	++	-	-
784.5856	784.5862	0.76	PC 36:3	[M+H] <sup>+</sup>	+	+	++	++	+	-
786.6013	786.6065	6.61	PC 36:2	[M+H] <sup>+</sup>	+	+	+	++	-	-
788.6169	788.6248	10.02	PC 36:1	[M+H] <sup>+</sup>	+	++	+	+	-	-
798.5415	798.5534	14.90	PC 34:1	[M+K] <sup>+</sup>	++	+	+	+	-	-
806.5700	806.5820	14.88	PC 38:6	[M+H] <sup>+</sup>	-	-	-	++	-	-
810.6013	810.6122	13.45	PC 38:4	[M+H] <sup>+</sup>	+	+	+	+	-	-
812.6169	812.6281	13.78	PC 38:3	[M+H] <sup>+</sup>	+	+	+	+	+	-
820.5856	820.5454	-48.99	PC 39:6	[M+H] <sup>+</sup>	-	-	-	++	-	-
826.5728	826.6110	46.21	PC 36:1	[M+K] <sup>+</sup>	+	+	+	+	+	-
834.6013	834.6229	25.88	PC 40:6	[M+H] <sup>+</sup>	-	-	+	+	-	-

Table 5.4 List of possible PC lipid species and whether they were detected within different tissue regions of the dosed and non dosed tissue sections. An arbitrary visual scale was used with the following indications of relative abundance, (<0.1au) very low to no signal observed (-), (0.1-1au) low relative abundance (+), (1-5au) medium relative abundance (++), (>5au) relatively high abundance (+++). This table is just as a visual comparison for a range of lipids throughout each tissue region. All data used in the compilation of this table is from data normalised against the matrix ion m/z 190. (possible lipid species not confirmed by MS/MS). PPM mass errors have been calculated and displayed, Red- >20ppm, Yellow - 10-20ppm, Green - <10ppm.

PPM mass error has been calculated, and has been shown within the tables 5.2, 5.3 and 5.4. Some of the high PPM errors are due to unresolved peak overlapping, or peak masking due to higher abundance peaks masking the signal of lower abundance peaks. Another possibility is due to the observed peak relating to an ion other than the possible lipid suggested.

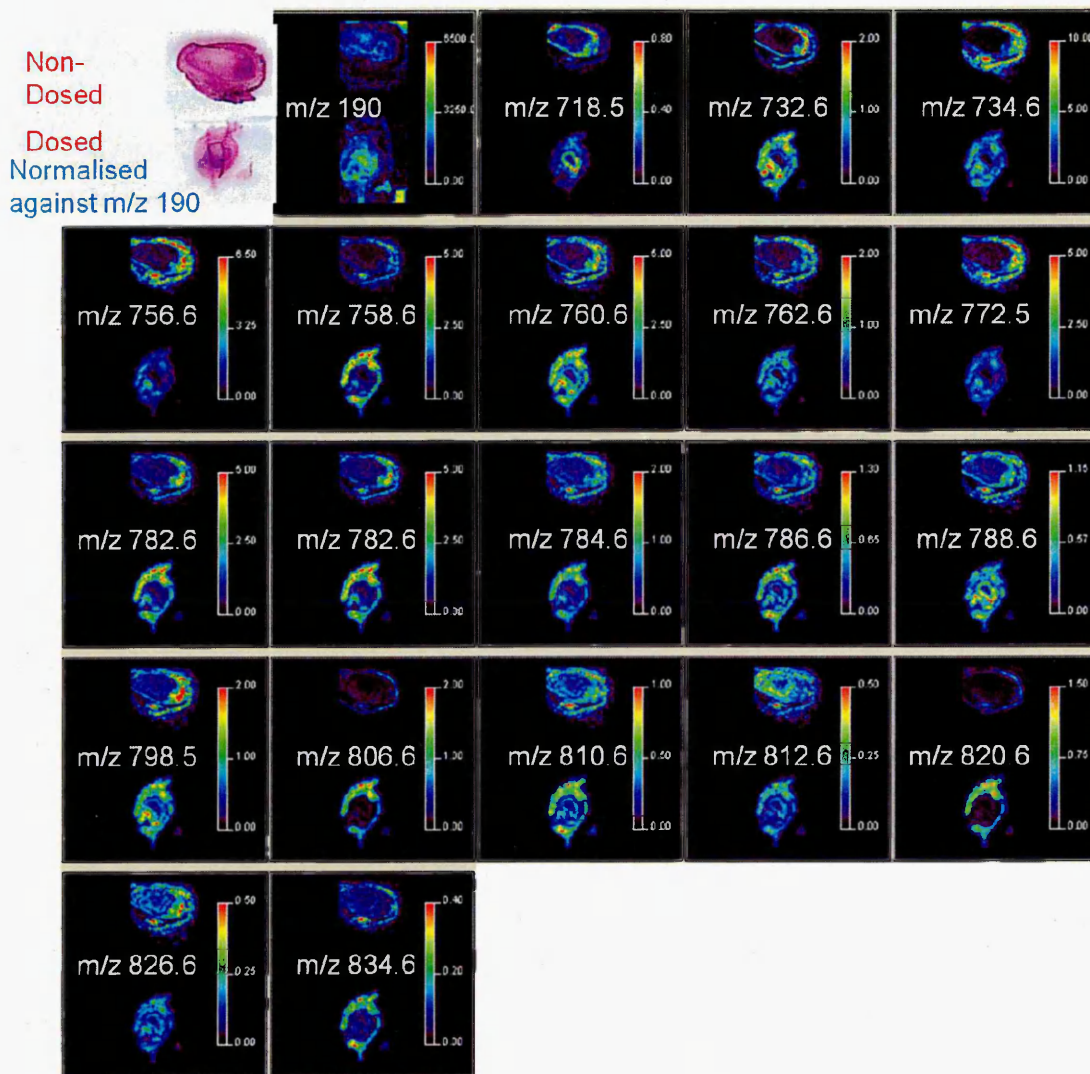


Figure 5.20 2D ion plots of possible phosphatidylcholine (PC) lipids species listed in Table 5.4



A different scale was needed to tabulate the results of the PC lipids because of their high abundance and the ease with which this class of lipids is observed with positive ion MALDI-MS.

There are in fact thousands of possible ions of interest arising from endogenous compounds that can be detected from a single experiment. This is far too many to complete conventional MS/MS analysis and subsequent identification on within this work. However in the preceding sections an attempt has been made to identify some of the important lipid species present.

The determination of the distribution of vinblastine within whole body tissue sections is reported in chapter 4 of this thesis. It has been shown that for a true image of the distribution of vinblastine in tissue sections ion mobility is beneficial. For this reason sections were analysed on a Synapt HDMS system (Waters Corporation, Manchester. UK). The total drift time plot is shown in figure 5.21 for an area of the 6Hr post dose tissue section. Only a part of the tissue section is depicted within the driftscope plot due to the file size. The image data has been divided up into "functions" each function contains up to 2GB of information. The file size needs to be divided up into files each less than 2GB in size due to the file size constraints within Microsoft Windows (Microsoft Corporation. USA) ([www.microsoft.com](http://www.microsoft.com)). This is the reason the data is assigned functions.

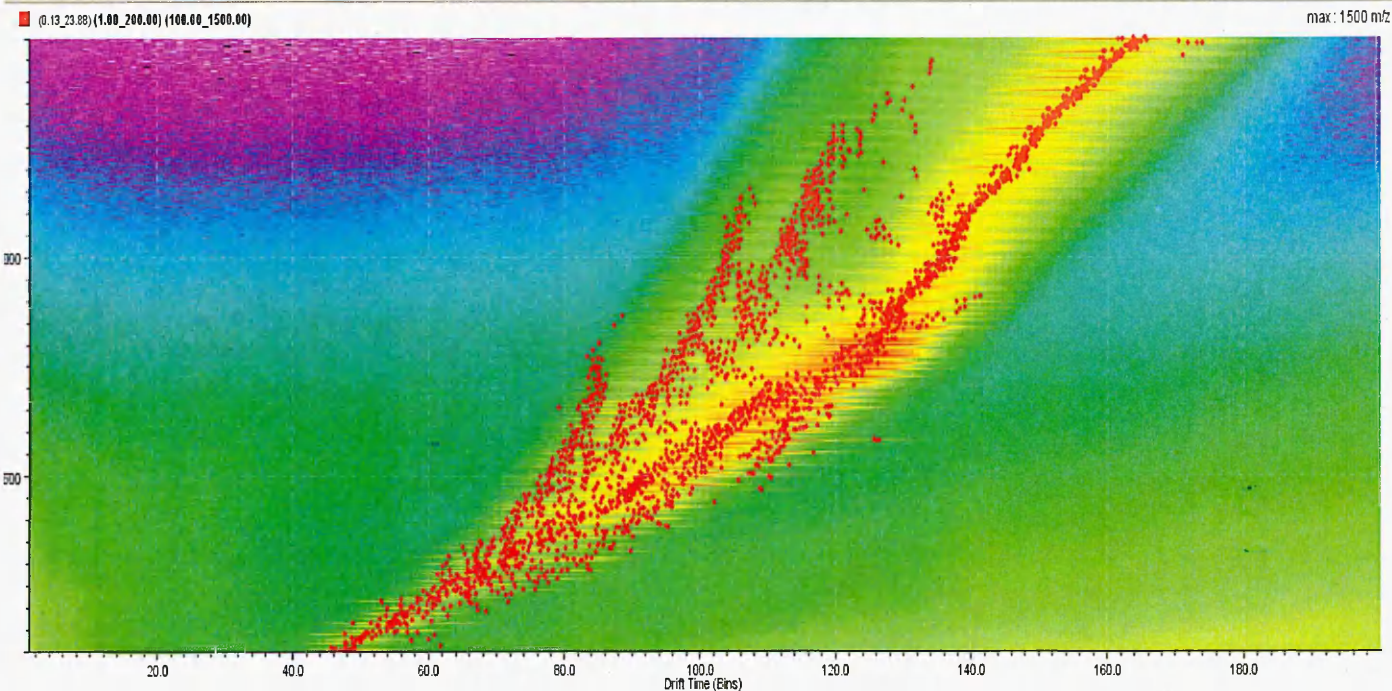


Figure 5.21 DriftScope plot from the imaging data acquired from a portion of a 6Hr post dose tumour tissue section. Familial trend lines can be seen.

Within the driftscope plot the intensity maxima form intense trend lines (red dots). These are familial trend lines each associated with a distinct group of species related ions. To image the distribution of vinblastine the ion mobility data must be retained as well as the retention time data or pixel location information. In order to retain both parts of information the data needs to be extracted from the driftscope plot which shows the drift time but not the spatial information into a chromatogram which contains the spatial location information for each pixel prior to constructing an image. This is achieved by selecting the ions of interest within driftscope as indicated by the circles in Figure 5.22a this  $m/z$  and drift time combination is then extracted for each function within the image data file. The extracted file contains the retention time chromatogram for the individual mobility separated ion. This information



can then be converted into a Biomap file so an image can be obtained (Figure 5.22c & 5.22e).

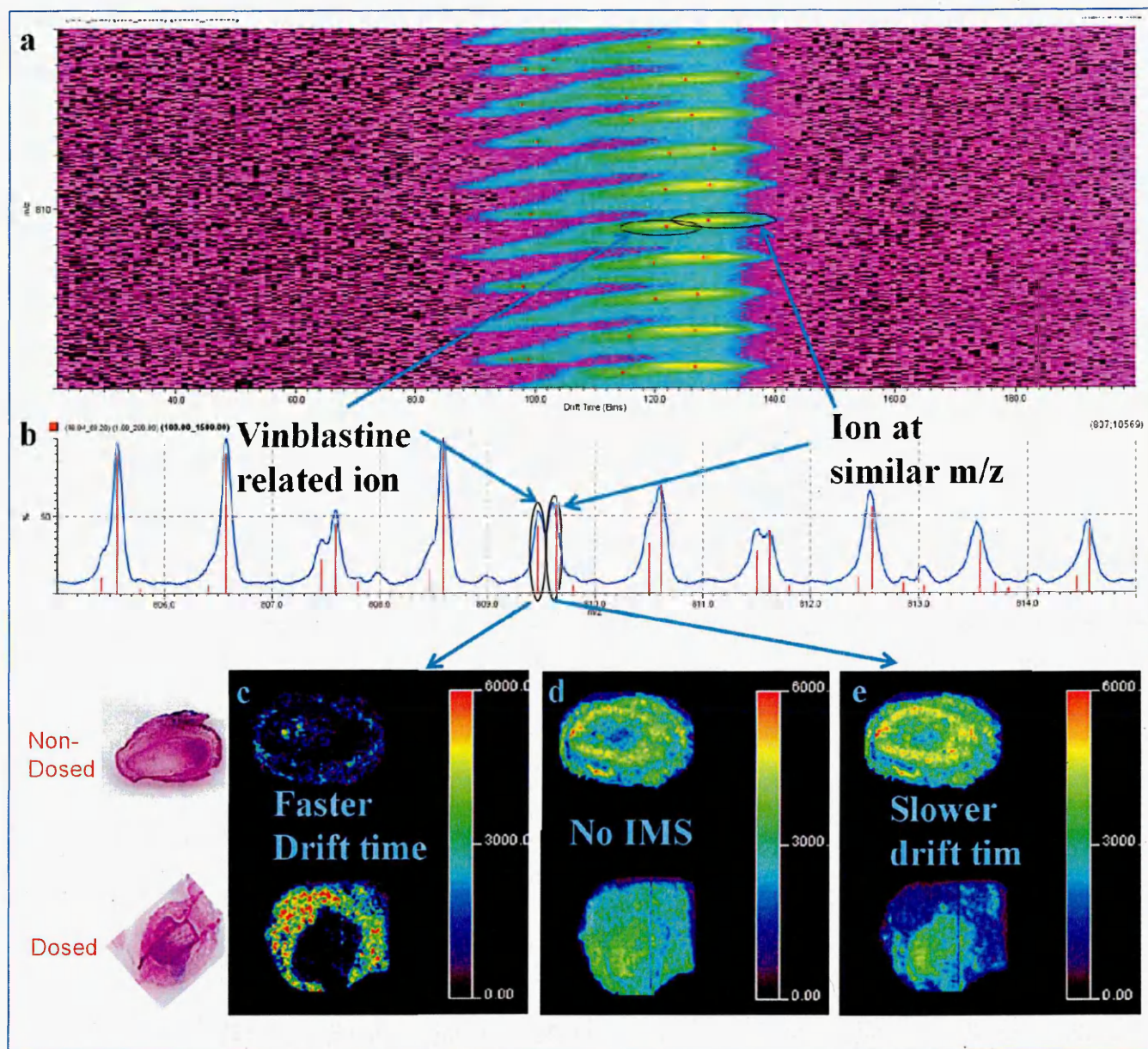


Figure 5.22 a) DriftScope plot of the region in which Vinblastine ions can be seen, encircled is an ion associated with vinblastine at  $m/z$  809.4 and also encircled is the interfering ion. b) Mass spectrum showing the overlapping peaks of interest. c) Ion mobility separated 2D ion plot of the vinblastine associated ion  $m/z$  809.4. d) Biomap image created without ion mobility separation, clearly showing the effect of ion masking due to interference. e) Biomap image of the interfering ion after ion mobility separation.

It can be clearly seen in Figure 5.22c, d & e that in order to obtain a true distribution of the vinblastine associated ion at  $m/z$  809.4 ion mobility separation is required. Using conventional MALDI MS imaging the image depicted in Figure 5.22d is obtained. It would appear from this image that only the distribution of the interference which has been imaged and it would be concluded on that there is no vinblastine related ion within the dosed tissue section. If the ion mobility separated image is obtained (Figure 5.22c) then the only ion present is in the dosed tissue section in the connective tissue region. This shows the benefit of the ion mobility separation within this application. The most likely reason that the vinblastine related ion is only distributed within the connective tissue is due to the limited penetration of the drug into the viable tumour due to the poor vasculature of the viable tumour hence the drug is not present in the main bulk of the tumour at the same level as the connective tissue.

#### **5.4 Conclusion.**

Shown here is a method for the analysis of lipids within dosed and control HCT 116 tumour xenographs. Data interpretation has been carried out using PCA-DA as a method for identifying ions of interest within the tissue sections. A manual directed imaging approach has also been carried out, by calculating the  $m/z$  of known lipids followed by the image acquisition of these masses.

Several possible ions of interest have been imaged and statistical identification of ions of interest associated with distinct tissue regions have been achieved using PCA-DA.

MALDI-IMS-MSI has been shown to improve the specificity of MALDI-MSI experiments over and above that normally obtainable with MALDI-MSI. Showing the true distribution of a vinblastine associated ion at  $m/z$  809.4, which was not observed using conventional MALDI MSI.

## 5.5 References.

Brattain M.G; Fine W.D; Khaled M; Thompson J; Brattain D.E. **1981**, *Cancer Research*. 41, 1751-1756.

Burnum K. E; Frappier S. L; Caprioli R. M. **2008**, *Annual Review of Analytical Chemistry*. 1, 689-705.

Caron J.M; Herwood M. **2007**, *Chemotherapy*, 53, 51-58.

Fuchs B; Schiller J; Cross M.A. **2007**, *Chem. Phys. Lipids*. 150, 229-238.

McCombie G; Staab D; Stoeckli M; Knochenmuss R. **2005**, *Analytical Chemistry*, 77, 6118-6124.

Modrak D.E; Gold D.V; Goldenberg D.M. **2006**, *Mol. Cancer Ther.* 5 (2), 200-208.

Ogretmen B. **2006**, *FEBS Letters*, 580, 5467-5476.

Prideaux B; Atkinson S.J; Carolan V.A; Morton J; Clench M.R. **2007**, *International Journal of Mass Spectrometry* 260, 243-251.

Trim P.J; Henson C.M; Avery J.L; McEwen A; Snel M.F; Claude E; Marshall P.S; West A; Princivalle A.P; Clench M.R. **2008**, *Analytical Chemistry*. 80, 8628-8634.

Schwamborn K; Krieg R.C; Reska M; Jakse G; Knuechel R; Wellmann A. **2007**, *Int. J. Mol. Med.* 20, 155-159.

Stiban J; Fistere D; Colombini M. **2006**, *Apoptosis* 11 (5), 773-780.

Van de Plas R; Ojeda F; Dewil M; Van Den Bosch L; De Moor B; Waelkens E. **2007**, *Pacific symposium on biocomputing* 12, 458-469.

Van den Berg R.A; Hoefsloot H.C.J; Westerhuis J.A; Smilde A.K; van der Werf M.J. **2006**, *BMC Genomics* 7:142.

[www.microsoft.com](http://www.microsoft.com)

## CHAPTER 6

---

**High Repetition Solid State Laser  
and Raster Imaging for High  
Throughput, High Resolution  
MALDI-Imaging.**

## High Repetition Solid State Laser and Raster Imaging for High Throughput, High Resolution MALDI-Imaging.

### 6.1 Introduction

#### 6.1.1 *How lasers work*

Laser is an acronym for Light Amplification by Stimulated Emission of Radiation. Lasers rely on the absorption and emission of energy at particular energy levels. In order to understand how lasers work it is necessary to understand atoms, molecules and their electron configuration. An atom is composed of a nucleus containing protons and neutrons, which are orbited by electrons in distinct orbital's. Each orbital can only accommodate a set number of electrons. The innermost orbital can accommodate up to 2 electrons, the second orbital can accommodate up to 8 electrons, and each further orbital can accommodate increasing numbers of electrons. These orbital's are subdivided into smaller orbital's containing up to two electrons each occupying a different area within the space around the nucleus. Electron orbital's increase in energy the further away they are from the nucleus of the atom. If all the electrons are in their lowest possible orbital energy combination this is called the ground state for that atom. There is a defined way in which electron orbital's fill based on their energy levels. The energy between two levels is constant. For an electron to change its electron configuration it needs to gain or lose a specific amount of energy dependant on the configuration it



changes between. There also needs to be space for the electrons to move into. Electrons do not therefore continuously absorb energy but it is quantised energy absorption and emission resulting in a change in the electron configuration.

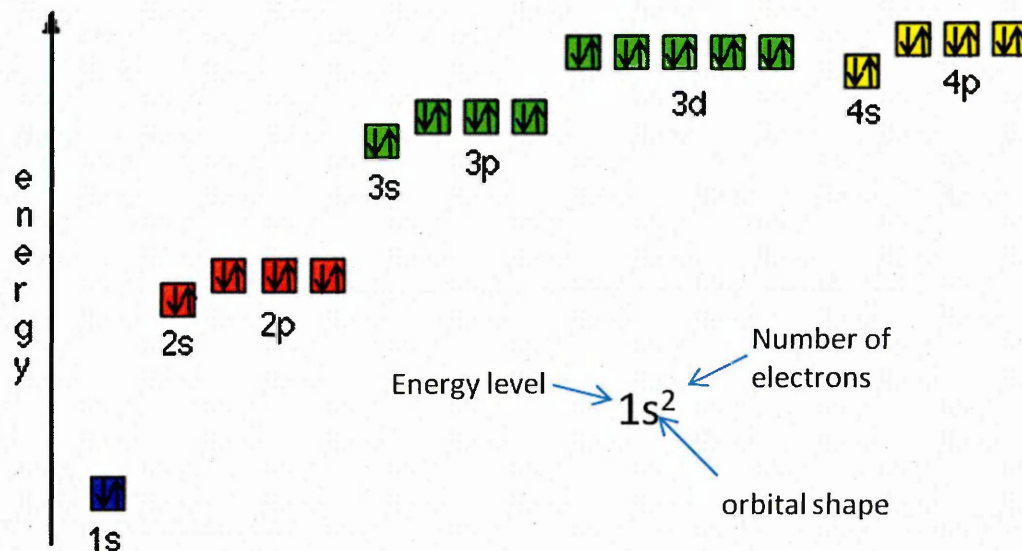
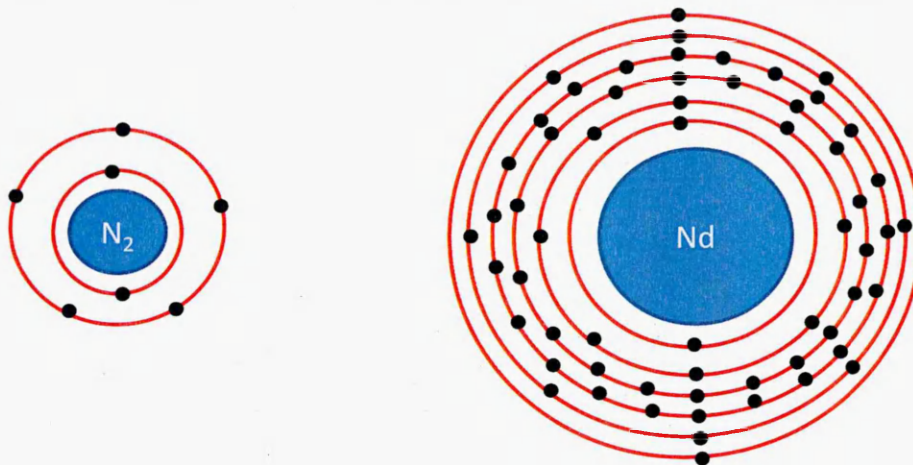


Figure 6.1 Electron configuration with respect to energy levels, this configuration would be written as  $1s^2, 2s^2p^6, 3s^2p^6d^{10}, 4s^2p^6$ .

The Diagram shown in figure 6.1 shows the electron rings represented as boxes. Each box represents an electron orbital which can contain a pair of electrons which is indicated using up and down arrows (representing that the electrons may not be identical). The letters s, p and d represent the orbital's shape



Nitrogen electron configuration  
 $1s^2, 2s^2p^3$

Neodymium electron configuration  
 $1s^2, 2s^2p^6, 3s^2p^6d^{10}, 4s^2p^6d^{10}f^4, 5s^2p^6, 6s^2$

Figure 6.2 A graphical shell model representation of the electron rings within nitrogen and neodymium. Each shell represents an energy level

Electrons can undergo a transition from one orbital or energy level to another higher level or lower level depending on whether energy is absorbed or emitted. Energy can be absorbed from collisions with other molecules, atoms or electrons or from the absorption of a photon that matches the energy quanta required to excite an electron from one energy level to another, this is shown by equation 6.1.

$$h\nu = E_2 - E_1$$

Equation 6.1 Relationship between frequency and energy levels, where  $h$  is Planck's constant,  $\nu$  is the Frequency of the photon,  $E_2$  is the 2<sup>nd</sup> energy level (Excited state) energy and  $E_1$  is the ground state (original state) energy.



The same energy photon is emitted when the electron returns to  $E_1$  from  $E_2$  the wave length of this photon ( $\lambda$ ) can be calculated by equation 6.2, this only occurs when only two energy levels are involved.

$$\lambda = \frac{hc}{E_2 - E_1}$$

*Equation 6.2 Calculating the wavelength ( $\lambda$ ) of an emitted photon due to decay from  $E_2$  to  $E_1$ .*

Simulated emission / decay can occur when a neighbouring atom emits a photon of frequency  $\nu$ , when this occurs a pair of new photons identical to the absorbed one in phase, frequency and direction are emitted unlike spontaneous emission which emits a photon with no phase or directional relationship. The phenomenon of simulated emission / decay is the principle of how lasers work.

Electrons are not restricted to a single increase or decrease in energy levels, most lasers rely on many energy levels, each molecule has characteristic energy levels and decay rates. Shown in figure 6.3 and 6.4 are the energy levels within the  $N_2$  molecule, and Nd from the Nd:YAG laser two of the most common lasers used within MALDI.

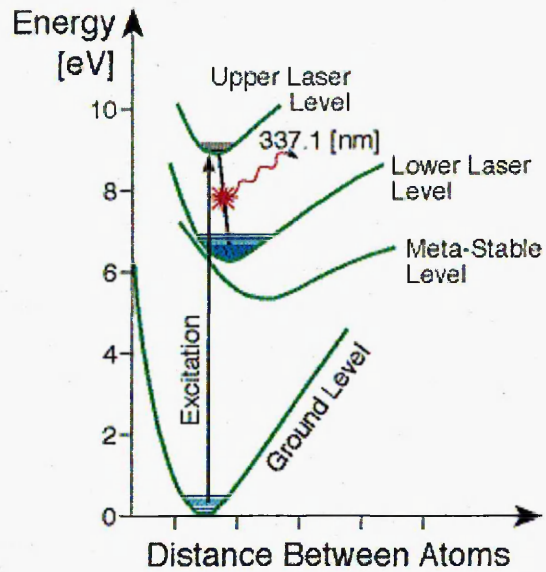


Figure 6.3 The energy levels within a  $N_2$  molecule responsible for the generation of a photon at 337nm. (<http://www.fineartradiography.com/hobbies/lasers/nitrogen/>)

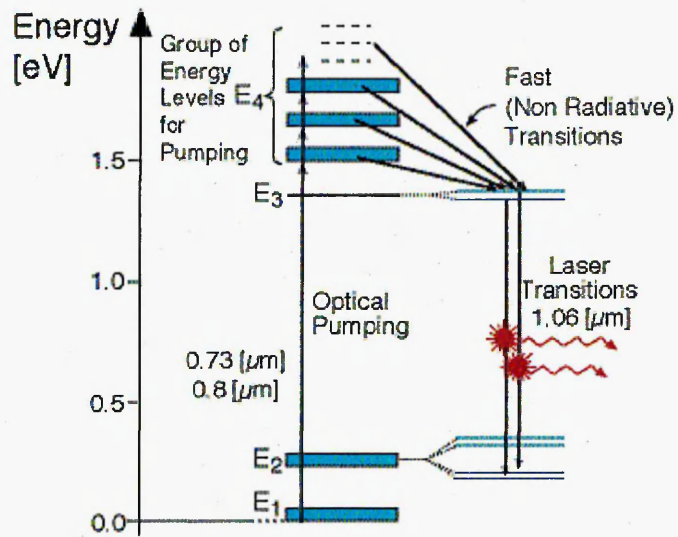


Figure 6.4 The energy levels within a Nd atom responsible for the generation of a photon at 1064nm. (<http://stwww.weizmann.ac.il/Lasers/laserweb/Ch-6/C6s2t2p2.htm>) (Pumped at 0.808 $\mu$ m)

$N_2$  lasers are based on the energy levels shown in figure 6.3. A pulse of high voltage is used to excite the electrons from the ground state to the upper laser level. This excites a large number of electrons to an excited state, and is rapidly followed by stimulated emission of a photon at 337.1nm. The initial energy level drop between the upper laser level and the lower laser level occurs very rapidly, followed by a slower decay down to the meta-stable level, after which it decays even more slowly back to the ground state.

Nd:YAG lasers are based on the energy levels of neodymium. This is doped into yttrium aluminium garnet ( $Y_3Al_5O_{12}$ ), usually at approximately 1%. At this concentration some of the neodymium can replace the yttrium within the crystal lattice. Traditional Nd:YAG lasers used to be pumped or excited by the use of flash lamps (Holle *et al.*, 2006) but modern Nd:YAG lasers are diode pumped. These are smaller and cheaper than previous flash lamp pumped lasers. Such laser diodes are similar to light emitting diodes, and emit light (which for this application is around 808nm) when an electrical current is passed through them. This results in the excitation of the neodymium to the excited state (E4), and then by non radiative decay they drop to a lower energy level (E3) which is shortly followed by simulated emission at 1064nm wavelength. This is then commonly tripled for MALDI to form a laser at 355nm. This wavelength tripling is achieved by a two stage process, initially by second harmonic generation by the combination of two photons into a single frequency doubled, half wavelength photon, by passing the initial laser light photon at 1064nm through a LBO crystal (Lithium TriBorate) in

a type I process (type I, the two input photons enter the crystal vertically polarised, the resulting photon exits the crystal in an orthogonal (Horizontal) polarisation). The second stage is by sum frequency generation where two simultaneous input frequencies, one photon at 1064nm and the second frequency doubled photon at 532nm from the second harmonic generation, are mixed in a second LBO crystal, in a type II process (Type II, The two input photons are orthogonally polarised and the output photon is polarised parallel to the IR input photon). This generates an output frequency photon at 355nm.

The Nd:YVO<sub>4</sub> laser works in the same way as the Nd:YAG laser since the active ion is still neodymium. The difference in the gain material, this results in a laser capable of much higher repetition rates than the Nd:YAG. This is due to the upper state lifetime of the gain materials. This upper state lifetime is the time taken by an excited electron to decay to the lower energy state, this is a measure of the ability of the material to store energy. The low repetition rate of the N<sub>2</sub> laser is not due to the upper state lifetime of the gain material but most likely due to the degradation of the gas at higher frequencies. If a laser is pulsed faster than the upper state lifetime the laser output pulse energy reduces. This is hence a limiting factor for repetition rates for MALDI lasers. Vanadate has a shorter upper state lifetime than YAG and hence it is used for very high repetition lasers.

### 6.1.2 Lasers in use for MALDI

Several laser types have been used in MALDI MS for the Laser desorption/ionisation process. MALDI was first reported using a frequency quadrupled Nd:YAG laser at 266nm (Karas *et al.*, 1985) however most older commercial instruments use N<sub>2</sub> lasers at 337nm. This is most likely due to N<sub>2</sub> lasers being smaller and cheaper than other lasers available at the time like the flash-lamp pumped lasers. N<sub>2</sub> lasers although cheap have some significant limitations, the repetition rate for N<sub>2</sub> lasers that are commercially available is limited to about 50Hz (Holle *et al.*, 2006) and they have an average life span of  $2 \times 10^7$  shots. A typical imaging experiment of a sagittal rat brain section approximately 10mm x 20mm area, imaged at a resolution of 150 $\mu$ m x 150 $\mu$ m results in approximately 8911 (67x133) spots per image. Commonly each spot has an acquisition time of 3 seconds. Using a 50Hz N<sub>2</sub> laser, each spot has 150 laser shots. Over the entire image the laser fires approximately 1,336,650 times. If the laser lasts for  $6 \times 10^7$  shots before it reaches the end of its life span, at best this only allows ~45 sections of this size to be imaged before the laser requires replacing.

One of the most common alternatives to the N<sub>2</sub> laser are frequency tripled Nd:YAG lasers which have a wave length of 355nm and a repetition rate up to approximately 5KHz, these lasers have an average life span of over  $1 \times 10^9$  shots.

McLean *et al.*, 2003 presented work using a 1KHz Nd:YAG laser compared to a 30Hz N<sub>2</sub> laser, they showed that the 1KHz laser was capable of obtaining good

quality data within a 1 second acquisition time, they also found that in some cases the Nd:YAG 1KHz laser enhanced the signal for angiotensin II by up to a factor of 80. Moskovets *et al.*, 2006 have presented work using a 2KHz rep rate frequency tripled Nd:YAG laser for high throughput spot analysis of liquid chromatography mass spectrometric spot analysis, using the 2KHz laser and a rapid plate movement allowed Moskovets *et al.*, 2006 to achieve acquisition times much faster than commercially available instruments allowing the analysis of 625 LC-MS spots within a total run time of just 12 mins.

There are several things that are important when considering a laser for MALDI, the significance of the wavelength of the laser is one of the most important. The term matrix assisted laser desorption was first coined by Karas *et al.*, 1985, within this work the authors looked at the laser desorption ionisation mass spectra of amino acid using two laser wavelengths one generated by a frequency quadrupled Nd:YAG laser i.e. 266nm and the other generated by a frequency tripled Nd:YAG laser i.e. 355nm. Within this work the observation was noted that a mass spectrum of alanine could be obtain with the addition of tryptophan at an irradiance almost a tenth of that required to obtain a mass spectra of alanine on its own, hence the authors deduced that tryptophan must be acting as an absorbing matrix resulting in the desorption of the non absorbing alanine. Modern UV-MALDI lasers are selected such that their wavelength is in the absorbing region of common matrices that are used but are not at a wavelength that is commonly

Trim P.J. Chapter 6

absorbed by analyte molecules because this can cause considerable analyte fragmentation.

Another important consideration is the laser pulse length used within MALDI experiments. This has been shown to affect the internal energy transfer between matrix and analyte molecules (Vertes *et al.*, 2004).

There are three main factors affecting the internal energy (IE) content of analyte ions within MALDI these are, the laser fluence ( $J/m^2$ ), the nature of the matrix and the analyte molecular type.

Different types of matrix can have significant effects on the IE of analyte molecules,  $\alpha$ CHCA as a matrix can lead to increased fragmentation of peptide ions and is referred to as a "hot" matrix where as DHB leads to much fewer peptide fragment ions and hence has been referred to as a "cold" matrix for MALDI (Medzihradzky *et al.*, 2000). Vertes *et al.*, 2004 demonstrated that the opposite is true for preformed ions. Matrix with preformed analyte ions desorbed with ns pulse length laser irradiation has shown that  $\alpha$ CHCA imparts the least amount of energy on the analyte ions followed by SA and then DHB each imparting  $3.69 \pm 0.21\text{eV}$ ,  $4.04 \pm 0.27\text{eV}$  and  $4.3 \pm 0.29\text{eV}$  respectively.

Survival Yield (SY) is a parameter that can be calculated to compare different data sets in order to obtain information about the amount of analyte fragmentation. SY is calculated from the following simple equation, where  $I_m$  is the molecular ion abundance and  $I_f$  is the abundance of the fragment ion.

$$SY = \frac{\sum I_m}{(\sum I_m + \sum I_f)}$$

Equation 6.3 Calculation of survival yield (SY), where  $I_m$  is the ion count for the molecular ion and  $I_f$  is the ion count for the fragment ion.

It has been shown that using a picosecond (ps) pulse duration with a frequency tripled Nd:YAG laser gave an increase in the SY compared to the use of a nano second (ns) pulse duration N<sub>2</sub> laser (Vertes *et al.*, 2004). The N<sub>2</sub> laser also showed increased matrix suppression effects. A higher laser fluence was required for the ps pulse Nd:YAG laser before desorption/ionisation occurred. With both lasers increased fluence resulted in a decrease in the ion count for the molecular ion ( $I_m$ ) most likely due to the increased deposition of IE to the analyte ions from the matrix. The Nd:YAG laser showed a slower rate of decrease in  $I_m$  compared to the N<sub>2</sub> laser as the fluence was increased. Within this case study it was observed that the IE of analytes depended on the matrix and followed the trend of  $\alpha$ CHCA < SA < DHB for the IE of the analytes or put another way the SY for each matrix for the analysis of 3-methoxy-benzylpyridinium salt was  $\alpha$ CHCA > SA > DHB. Previous findings (Medzihradzky *et al.*, 2000) found  $\alpha$ CHCA to be a hot matrix, Vertes *et al.*, 2004 proposed that this difference was caused by the ionisation pathways for each analyte. The 3-methoxy-benzylpyridinium salt studied by Vertes *et al.*, 2004 are thought to be preformed ions. In contrast to the previous study on the analysis of peptides where the ionisation process would be



likely to occur via proton transfer. Vertes *et al.*, 2004 stated that the different results were possibly due to the ns pulse length excitation resulting in "ladder switching" or energy pooling by excitons, whereas the ps pulse length promotes ladder climbing. This would result in an increase in the number of electronically excited states within the matrix. The late onset of phase transition may be an indication of reduced exciton-phonon (vibrational energy) coupling.

Dreisewerd 2003 states that longer laser pulse durations can have a negative effect in MALDI. UV lasers used for MALDI generally have a pulse duration of 0.5-10ns, within this work the Nd:YVO<sub>4</sub> laser used has a pulse duration of 1.5ns. Long pulse durations do have a negative effect on MALDI and this is thought to be due to excessive thermal excitation of the analytes. Rapid excitation is key in MALDI experiments so that the desorption/ablation event predominantly occurs before analyte decay due to thermal degradation. If this is not the case this is called in source decay (ISD). This ISD requires fragmentation channels to occur within the time scale of the initial phase transition. Post source uni molecular decay (PSD) occurs at longer time scales than ISD, both ISD and PSD are analyte and matrix dependent, as previously mentioned  $\alpha$ CHCA is thought to be a hot matrix for certain analytes because this matrix causes a higher degree of fragmentation compared to DHB for certain analytes such as peptides, due to their physiochemical properties.

Holle *et al.*, 2006 have shown that the beam profile of the laser also has a marked effect on the efficiency of Nd:YAG lasers within MALDI experiments. Conventional  $N_2$  lasers have a beam profile with multiple maxima throughout the laser spot these maxima shift position randomly with every laser shot and this is depicted in figure 6.5 which has been reproduced from Holle *et al.*, 2006.

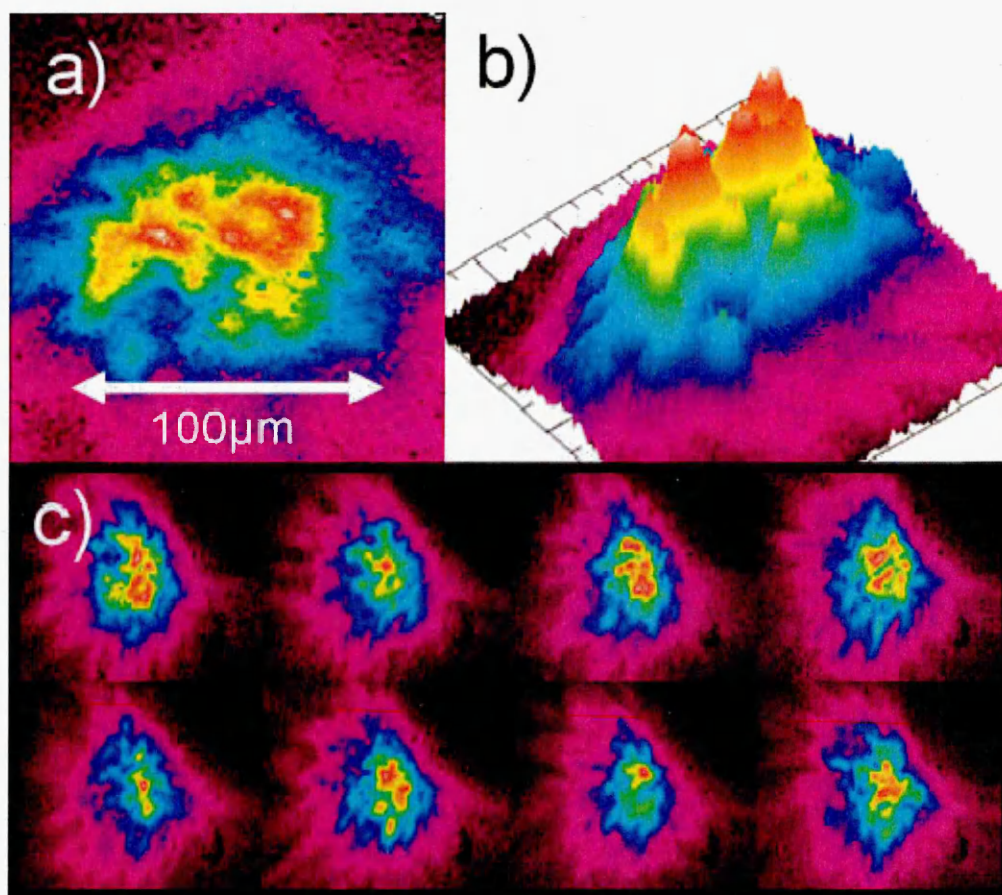


Figure 6.5 A typical  $N_2$  laser spot, showing multiple maxima throughout the laser spot a) in a 2d plane showing laser spot b) showing a laser spot in 3D also showing the multiple maxima throughout the laser spot and c) showing the random nature of the maxima as they change over 8 consecutive shots (Holle *et al.*, 2006)

Typical frequency tripled Nd:YAG lasers have a typical Gaussian distribution within the laser spot as shown in figure 6.6.

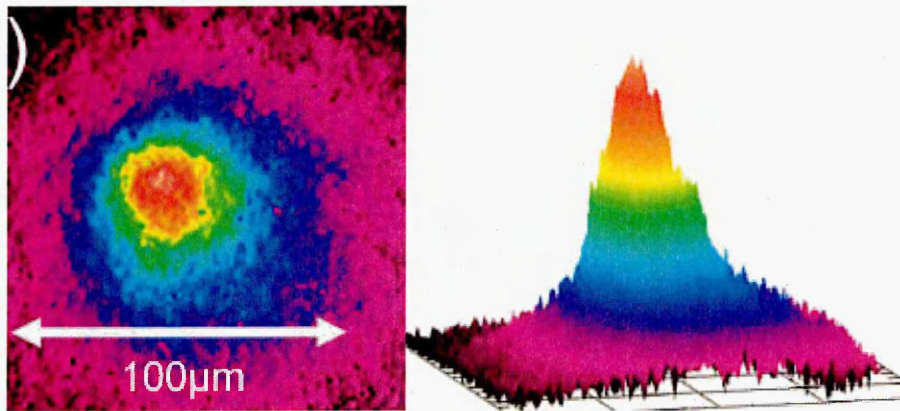


Figure 6.6 The Gaussian distribution of a typical Nd:YAG laser. (Holle et al., 2006)

This typical Gaussian distribution is disrupted when an Nd:YAG laser is fired through a fibre-optic cable. When this is done the spot profile of the Nd:YAG laser loses its Gaussian distribution and forms a spot with multiple maxima, however these do not vary like the  $N_2$  laser distribution figure 6.7 shows the distribution of maxima of a Teem Nd:YAG laser fired through a 100 $\mu\text{m}$  diameter fibre optic.

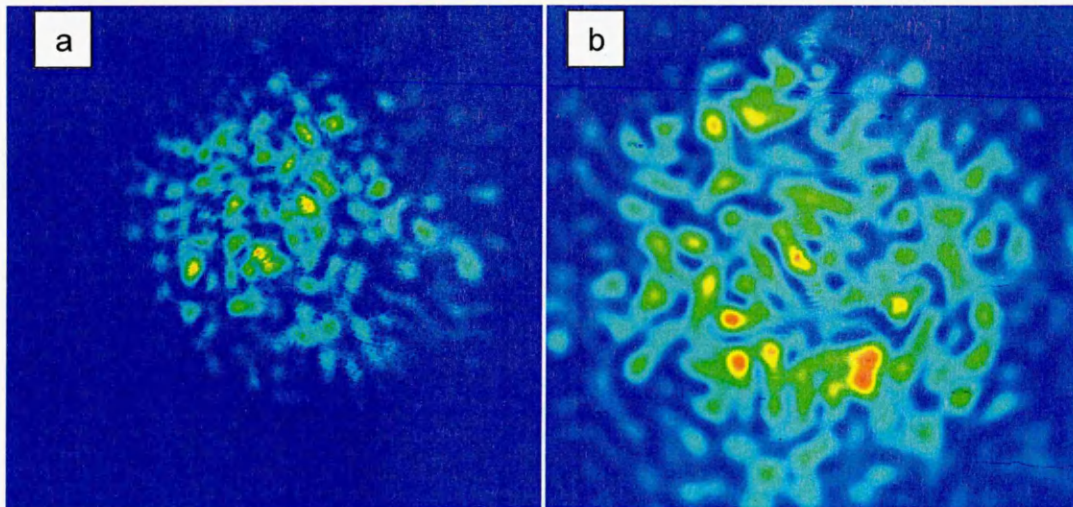


Figure 6.7 Teem (Teem Photonics, MA, USA) Nd:YAG laser spot profiles at (a) 25% and (b) 100% laser power, showing multiple maxima throughout the laser spot after it has been passed through a 100 $\mu$ m fiberoptic.

Holle *et al.*, 2006 present data on the Bruker Daltonik (Bremen, Germany) laser system that is employed on the Bruker Ultraflex III MALDI TOF/TOF. This laser system is a frequency tripled Nd:YAG laser at 355nm, but the important difference is the structured beam profile that is generated using a modulator. This results in the generation of a structured beam with multiple maxima this pattern as shown in figure 6.8. This pattern is then moved by a few micrometers after each laser shot.



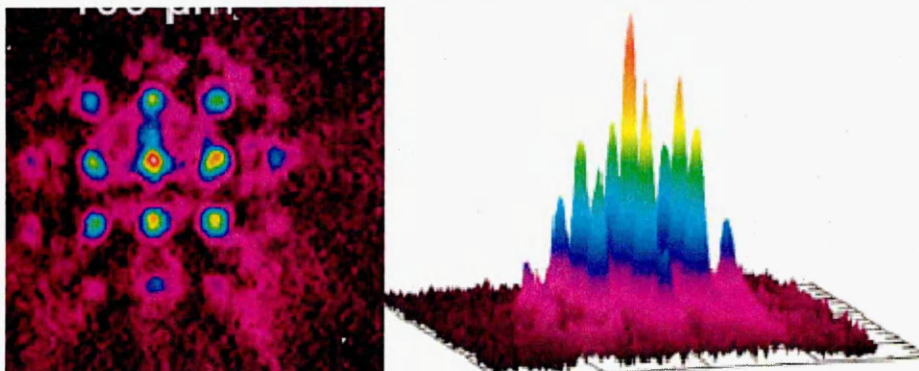


Figure 6.8 The structured beam profile of a single shot from the Nd:YAG “smart beam™” laser (Holle *et al.*, 2006).

Holle *et al.*, 2006 have shown that a structured beam profile that moves after every laser shot can markedly increase the performance of the Nd:YAG laser for MALDI.

The laser used for the work reported in this chapter is a frequency tripled Nd:YVO<sub>4</sub> which is a Neodymium doped Yttrium ortho Vanadate laser at 355nm wavelength. This laser allows for the use of a much higher repetition rates than the conventional lasers employed for MALDI. The Nd:YVO<sub>4</sub> laser allows for repetition rates up to approximately 100KHz, but within this work the highest repetition rate used will be 20KHz this is a hundred fold increase on the 200Hz Nd:YAG lasers and an increase of nearly a thousand fold on the traditional N<sub>2</sub> lasers. The Nd:YVO<sub>4</sub> laser suffers from the same matrix limitations as the Nd:YAG laser, and also has a Gaussian distribution the same as the Nd:YAG laser as can be seen in figure 6.9

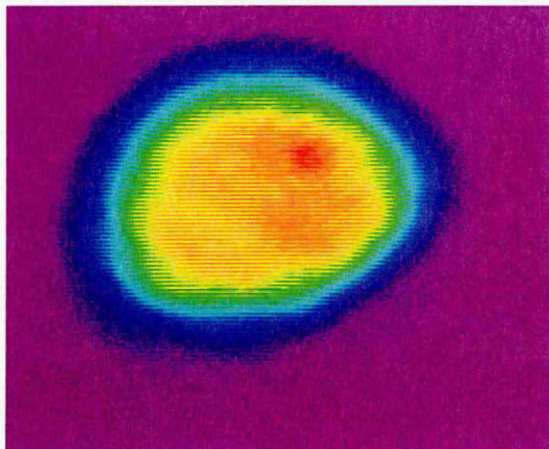


Figure 6.9 The Gaussian spot profile of an Nd:YVO<sub>4</sub> laser before entering the fiberoptic cable.

### 6.1.3 Raster imaging V's Conventional imaging

Conventional MALDI imaging is achieved by firing the laser onto the target in a stationary position and acquiring data at a number of discrete spots. The distance between each spot is defined by the user as the spatial resolution of the acquired image. A slight variation with this method is the use of "Dynamic Pixel" (Applied Biosystems/MDS Sciex, Concord, Ontario, Canada). Dynamic pixel moves the target plate during each acquisition within the defined spatial resolution, this improves the sensitivity for this instrument because more material is desorbed and ionised per acquisition. This method still takes the same time per image to acquire because the laser is fired for the same duration per spot. A further advancement of this technique is the introduction of raster imaging (Simmon 2008). When imaging using continuous raster imaging is performed the laser is fired at the sample and the sample is moved in a straight line from one side of the designated sample area to the other. The laser is then turned off and the target

moved to the start of the next row where the process is repeated. The distance between these rows is manually set as the vertical axis resolution, the horizontal resolution is also set manually. Within this method the software bins the data at calculated time points based on the distance travelled by the laser. Using this method the image acquisition time can be reduced by several fold.

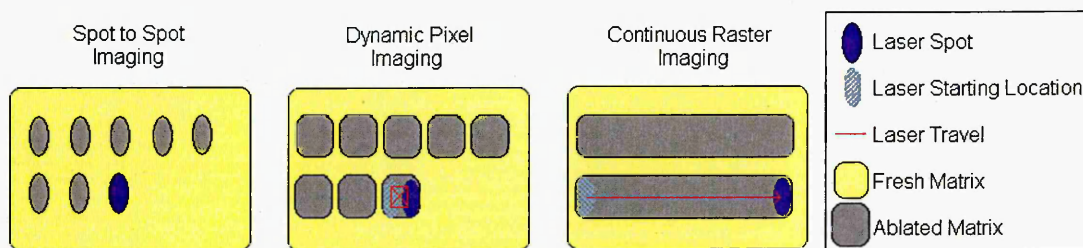


Figure 6.10 The three imaging modes that can be used within the oMALDI Server 5.1 software (Applied Biosystems/MDS Sciex, Concord, Ontario, Canada).

Simmons (Simmons 2008) also demonstrate how this technique could also improve the sensitivity of the technique due to the increased surface area sampled by continuous raster imaging figure 6.11 shows a brain section after imaging with conventional spot to spot imaging and raster imaging, it can be clearly seen that there is still areas of matrix left on the sample that has not been used for imaging on the spot to spot method, however, the entire matrix coating has been used for the image acquisition using the continuous rastering.

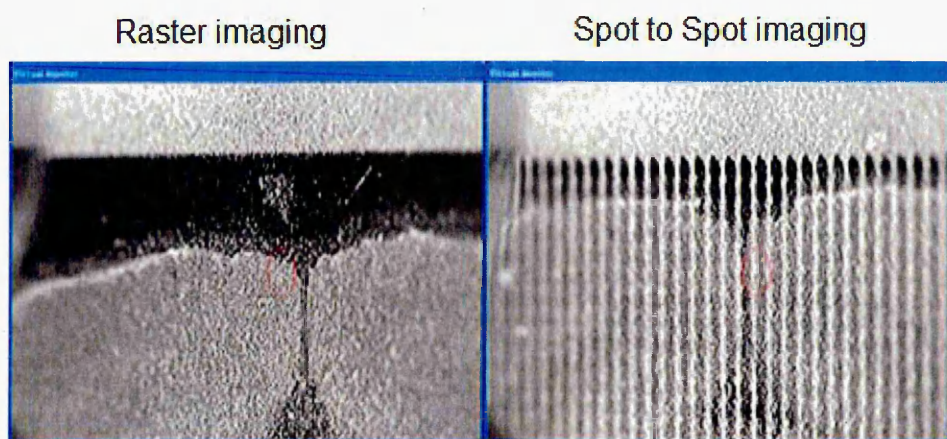


Figure 6.11 The differences between the matrix ablation using raster imaging compared to conventional spot to spot imaging. Reproduced from Simmons 2008

## 6.2 Methodology

### 6.2.1 Sample Preparation (Numbers)

A column of numbers 1-10 and 10-20 were printed onto plain paper using a HP LaserJet 4250n (Hewlett-Packard, Bracknell, UK). The columns were cut to size and mounted onto an Opti-Tof<sup>®</sup> LC MALDI target plate (Applied Biosystems/MDS Sciex, Concord, Ontario, Canada) using double sided carbon conductive tape (Figure 6.12).



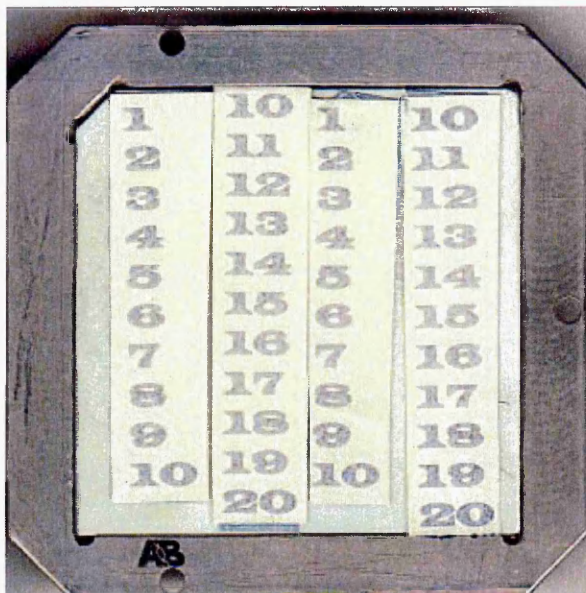


Figure 6.12, The printed numbers mounted on to an Opti TOF target plate, after being coated in  $\alpha$ CHCA matrix, prior to imaging.

The numbers were then manually spray coated with 10ml of  $25\text{mgml}^{-1}$   $\alpha$ -CHCA in ethanol with 0.1% TFA, spray coating was achieved using a gravity fed pneumatic air spray gun, Iwata studio series compressor fitted with an Iwata Eclipse gravity feed airgun (Iwata-Media Inc., Portland, OR, USA) set at 40psi. The samples were spray coated at a distance of 20cm, for 20 series of 2 passes of the air brush, with 20 second intervals, this was carried out to obtain an even matrix coating whilst avoiding sample over wetting which would result in analyte migration.

### 6.2.2 Sample Preparation (Brain tissue)

A brain was harvested from a male Wistar rat which was sacrificed by schedule one method according to Home Office (UK) regulations. The harvested tissue was

immediately snap frozen for 15 seconds in liquid nitrogen cooled iso-pentane, the frozen tissue was then stored at  $-80^{\circ}\text{C}$  until required.

When required the tissue was mounted onto cork in the desired orientation and held in place with a minimal amount of optimum cutting temperature (OCT) embedding medium, ensuring that no OCT embedding medium is near the region to be sampled. Tissue sections ( $12\mu\text{m}$ ) were cut using a Leica CM1510 cryostat (Leica Microsystems, Wetzlar, Germany) set at  $-12^{\circ}\text{C}$ , each section was thaw mounted onto glass slides.

### ***6.2.3 Vinblastine Profile and fragmentation due to laser repetition rate.***

$\alpha\text{CHCA}$  50:50:0.1(v:v:v) ethanol : water : TFA (20mg/ml) was made up and mixed 10:1 ratio Matrix to vinblastine (1mg/ml) to give a final concentration of 0.1mg/ml vinblastine, this was then spotted onto an opti TOF target plate (Applied biosystems) and allowed to air dry before analysis at 1, 5, 10, 15 and 20KHz laser repetition rates at a laser power of 50%.

### ***6.2.4 Mass spectrometric profiling and imaging***

The samples were analysed in positive ion mode using a Q-Star Pulsar-*i* / quadropole time-of-flight mass spectrometer (Applied Biosystems/MDS Sciex, Concord, Ontario, Canada) fitted with an orthogonal MALDI ion source, using the

oMALDI server 5.1 software. The laser was a Neodymium : Yttrium ortho Vanadate laser or Nd:YVO<sub>4</sub> (Elforlight Ltd, Daventry, Northants, UK) with a manually variable repetition rate between 1-20KHz, images were obtained by continuous raster imaging with a spatial resolution of 150µm.

Profiles were obtained by firing the laser at a defined area for 1min and summing the obtained spectra together.

### **6.2.5 Image Processing**

The imaging data sets were then converted into Analyze 7.5 file format using oMALDI server 5.1 software

All images were processed using 'BioMap' ion imaging software (<http://www.maldi-msi.org>) resulting in the production of a 2D ion density map.

### **6.3 Results and discussion.**

Whilst the ability to perform MALDLI imaging experiments on whole tissue sections or even whole body sections (Stoeckli *et al.*, 2007) has been shown to be hugely beneficial there are two major draw backs with trying to implement MALDLI imaging as a high throughput methodology. The major issue is time, to obtain a high resolution whole body image requires acquisition times of tens of hours or even several days. One whole body image obtained on the Bruker Ultraflex III

(Bruker Daltonik GmbH, Bremen, Germany) took over 72 hours of continuous acquisition (data not shown) and to obtain a high resolution image of individual organ sections requires hours of instrument time conventionally.

Applied Biosystems have recently introduced a new update for their oMALDI server 5.1 software (Applied Biosystems/MDS Analytical Technologies, Concord, ON). One of the key additions to the software is the inclusion of continuous laser raster image acquisition capabilities.

Shown in figure 6.13 is a sagittal rat brain section imaged using raster imaging, the image was acquired with a spatial resolution of  $150\mu\text{m}$ . The entire image acquisition took only approximately 37 mins to complete, using conventional imaging a comparable image at  $150\mu\text{m}$  resolution would have taken approximately 4 hours, this is a massive improvement in the acquisition time.

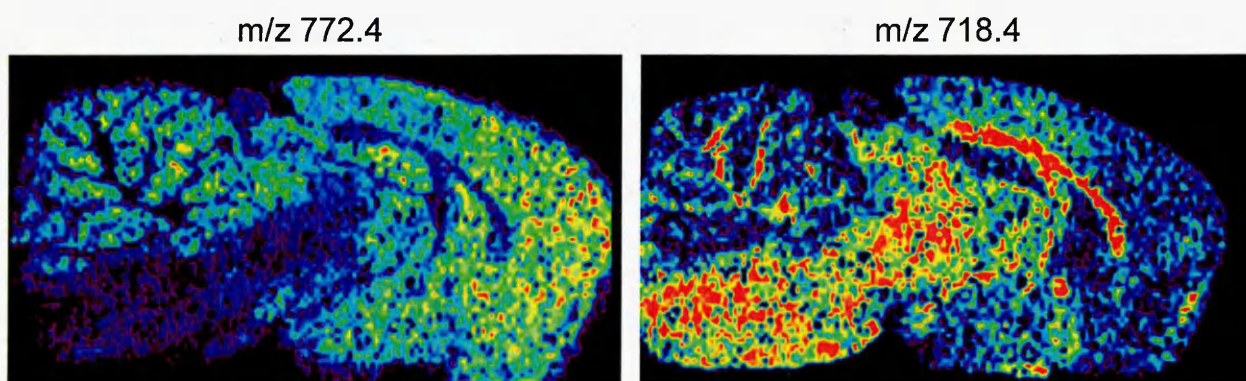


Figure 6.13 Brain image, imaged using raster imaging. Total acquisition time for the image at  $150\mu\text{m}$  resolution took ~37mins.

The brain image was acquired with a 10KHz laser repetition rate, as can be seen from the image white and grey matter associated ions have been shown at a spatial resolution of 150 $\mu\text{m}$  in a fraction of the conventional time this would have required to acquire. Although the laser spot size is above 100 $\mu\text{m}$  it is still possible to obtain higher resolution images with the use of over sampling (Jurchen *et al.*, 2005). Conventionally this would be achieved by firing the laser in one position until the matrix is fully ablated then the laser would be moved a fraction of its size and hence the matrix contributing to the next pixel will only be from an area smaller than the size of the laser beam. This has also been shown to be possible for raster imaging using the same principle, Simmons (Simmons 2008) showed that for the experimental conditions that they used the ion intensity for several ions reduced to less than 5% of the initial ion count after approximately 200 laser shots, and this could be recalculated using equation 6.4 to show the distance from the front edge of the spot at which the ion count reduces to less than 5% of the original ion count in raster imaging for these instrument settings, this meant that they could image down to a spatial resolution of 30 $\mu\text{m}$ .

$$\text{Distance from front edge of laser} = \text{number of laser shots} \times \left( \frac{\text{Raster Rate } (\mu\text{m}^{-1})}{\text{Laser Rep Rate } (\text{s}^{-1})} \right)$$

*Equation 6.4 Calculation for the minimum spatial resolution obtainable by raster imaging.*

To assess the effects of the laser repetition rate on MALDI imaging experiments a series of printed numbers spray coated with  $\alpha$ CHCA matrix, were imaged using a variable rep rate Nd:VVO<sub>4</sub> laser (Elforlight Ltd, Northants, UK) fitted to a Q-Star Pulsar-i (Applied Biosystems/MDS Sciex, Concord, Ontario, Canada).

Figure 6.14 shows images from ion signals commonly observed with  $\alpha$ CHCA as a matrix these are, a) the distribution of the molecular ion of the matrix  $\alpha$ CHCA  $(M+H)^+$  at  $m/z$  190, b) the distribution of the ion of matrix minus water  $(M-H_2O)^+$  at  $m/z$  172, c) the distribution of the sodiated matrix adduct  $(M+Na)^+$  at  $m/z$  212 and d) the distribution of the potassiated matrix adduct  $(M+K)^+$  at  $m/z$  228. There appears to be a distinct difference as the repetition rate increases. The 2D ion map for the molecular ion shows a distinct area of high signal from 2KHz upto and including approximately 8KHz. The other matrix related ions show a area of high intensity around 2-4KHz laser rep rate. These results may be caused by unhomogeneity in the matrix coating, but as can be seen in figure 6.12 the matrix appears to be a relatively uniform covering on the paper. Therefore it is reasonable to assume that the differences observed are due to the laser repetition rate and not solely due to matrix coating.



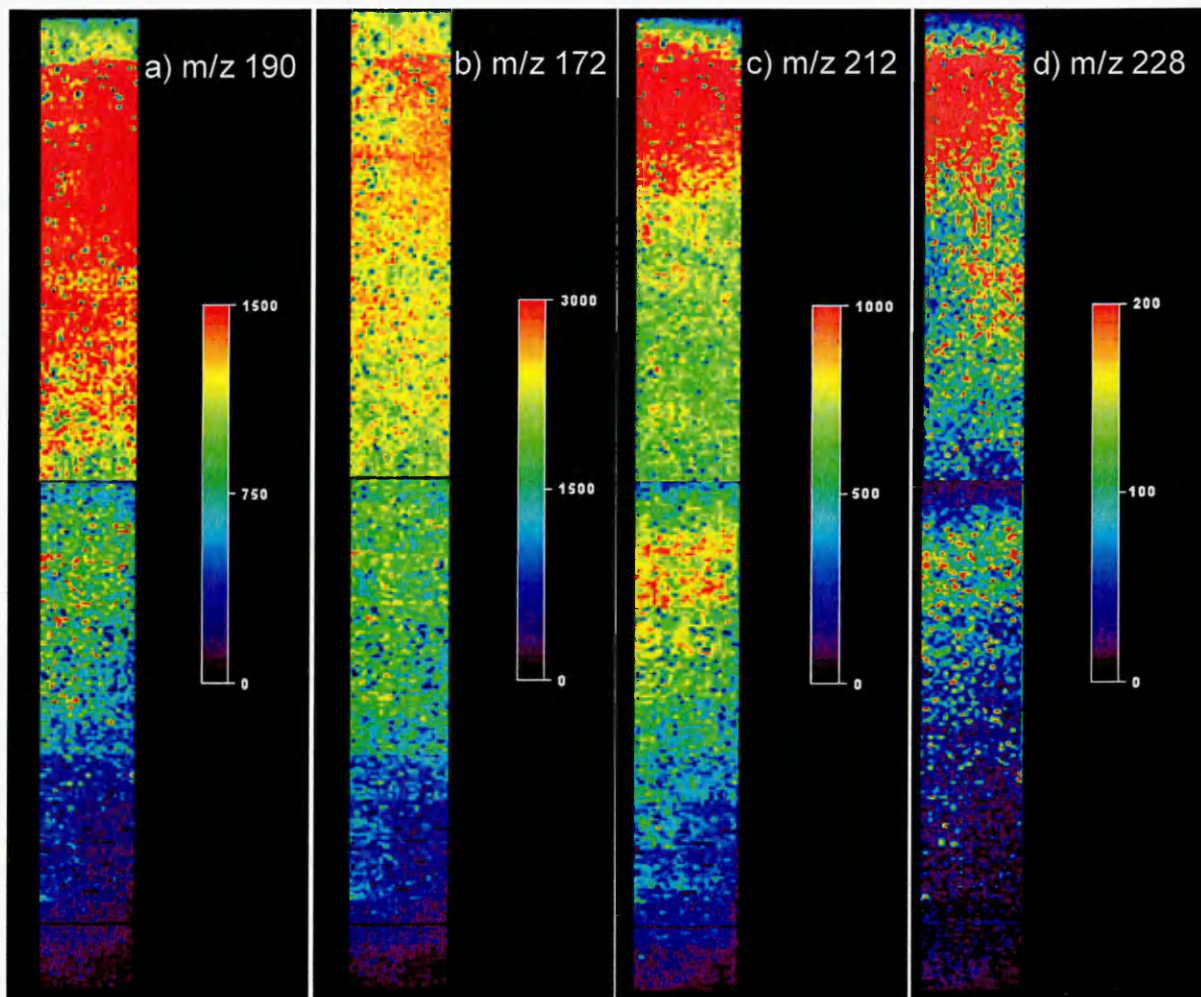


Figure 6.14 The distribution of matrix related ions over 1-20KHz laser repetition rate, a) the distribution of the molecular ion of the matrix  $\alpha$ CHCA  $(M+H)^+$  at  $m/z$  190, b) the distribution of the ion of matrix minus water  $(M-H_2O)^+$  at  $m/z$  172, c) the distribution of the sodiated matrix adduct  $(M+Na)^+$  at  $m/z$  212 and d) the distribution of the potassiated matrix adduct  $(M+K)^+$  at  $m/z$  228.

Figure 6.15 shows two ions with almost opposite distributions a) shows the distribution of  $m/z$  134. The identity of this ion is not known. This ion is either an ion related to the paper, which has been used, or it is matrix related showing possible suppression effects from ink. The ion has a range of high intensity

covering 3-9KHz laser repetition rates. The ink related ion  $m/z$  325, is shown in figure 6.15, also shows a maximum intensity in the 2-10KHz laser repetition rates, and as for nearly all the images, the ion intensity seems to reduce when the laser repetition rate is increased above 15KHz.

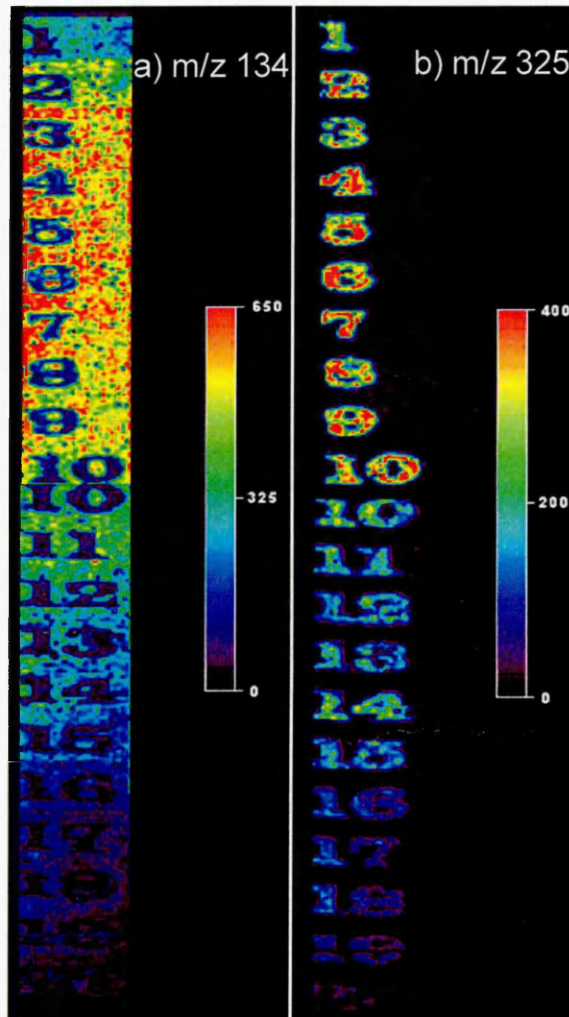


Figure 6.15 The distribution of two different ions over 1-20KHz laser repetition rates. a) The distribution of  $m/z$  134 this ion demonstrates the effect of matrix suppression. b) The distribution of the ink related ion  $m/z$  325.



Figure 6.16 shows ion map images of the two ions shown in figure 6.15 normalised to the matrix ion  $m/z$  190. This is common practice within many laboratories and is performed to try and compensate for possible matrix suppression effects caused by certain analytes and tissues. In this experiment it does not appear that the normalisation of the data against the matrix aids in decision making. This is due to the fact that we are looking for the difference within the ionisation of the matrix and possible analytes with the variation of laser repetition rate, and hence to normalise the data against the matrix only serves to remove the effect of reduced ionisation as can be seen by the intensity within these images being fairly constant

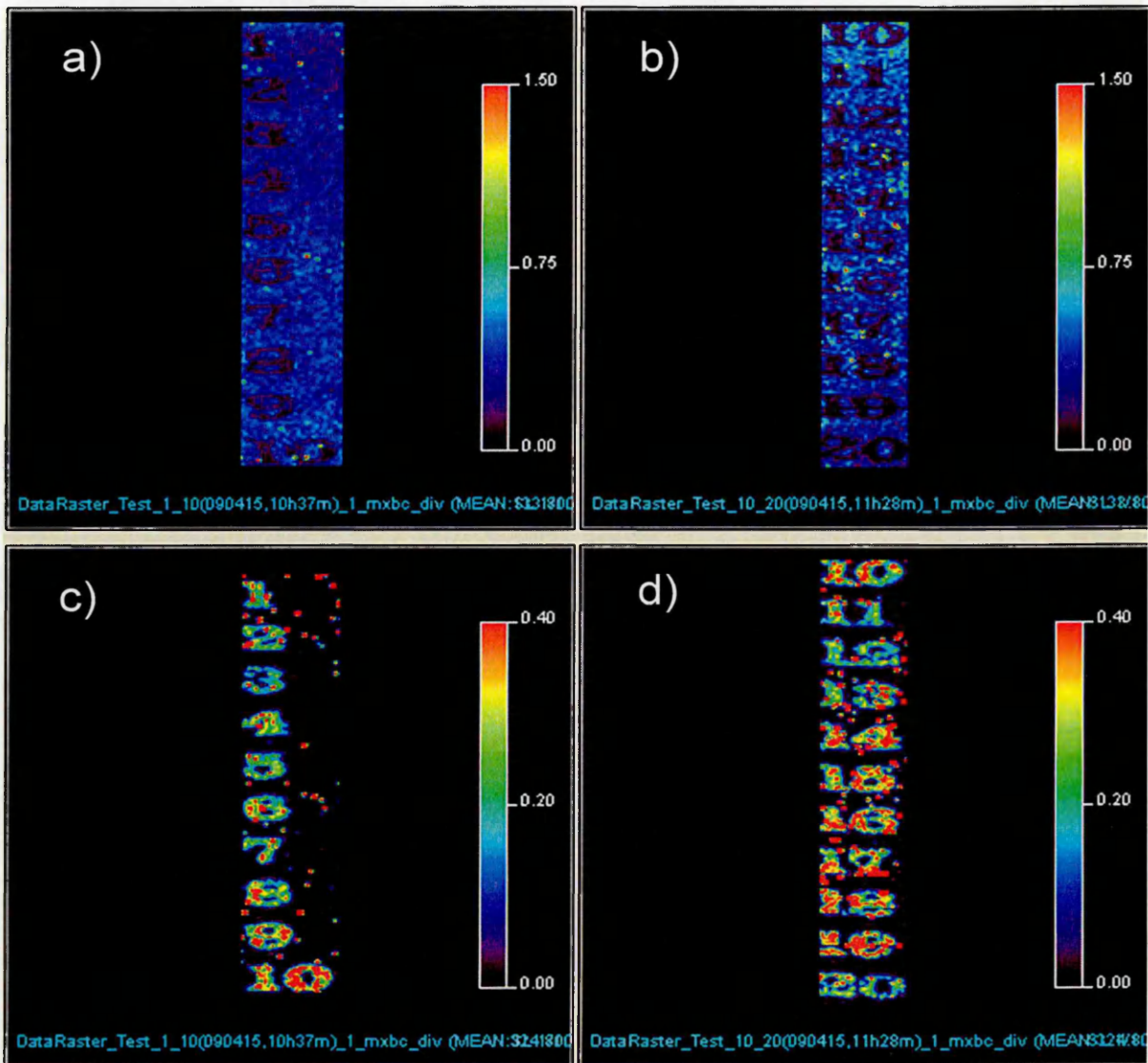


Figure 6.16 The distribution of a)  $m/z$  134 normalised against the matrix ion  $m/z$  190 at laser repetition rates 1-10KHz, b)  $m/z$  134 normalised against the matrix ion  $m/z$  190 at laser repetition rates 10-20KHz, c)  $m/z$  325 normalised against the matrix ion  $m/z$  190 at laser repetition rates 1-10KHz and d)  $m/z$  325 normalised against the matrix ion  $m/z$  190 at laser repetition rates 10-20KHz.

The results obtained within this work can be predominantly explained by the graph shown in figure 6.17. This graph shows the effect laser repetition rate has on the average power and energy output of the laser. It can be seen that as the repetition rate of the laser is increased the power also increases until it reaches its

maxima at 81mW at a repetition rate of 13-15KHz. After this repetition rate the power starts to decrease as repetition rate increases. The graph also shows the effect of the repetition rate on the energy it can be seen that as the repetition rate increases the energy decreases after approximately 6KHz and the energy peaks at 8.3 $\mu$ J at a laser repetition rate of 3KHz. The images shown in figure 6.14 and figure 6.15 follow this trend of the energy graph peaking at a similar repetition rate, at high repetition rates around 15-20KHz the energy is not enough to achieve a good ionisation of the matrix or analyte hence the markedly reduced signal at these repetition rates.

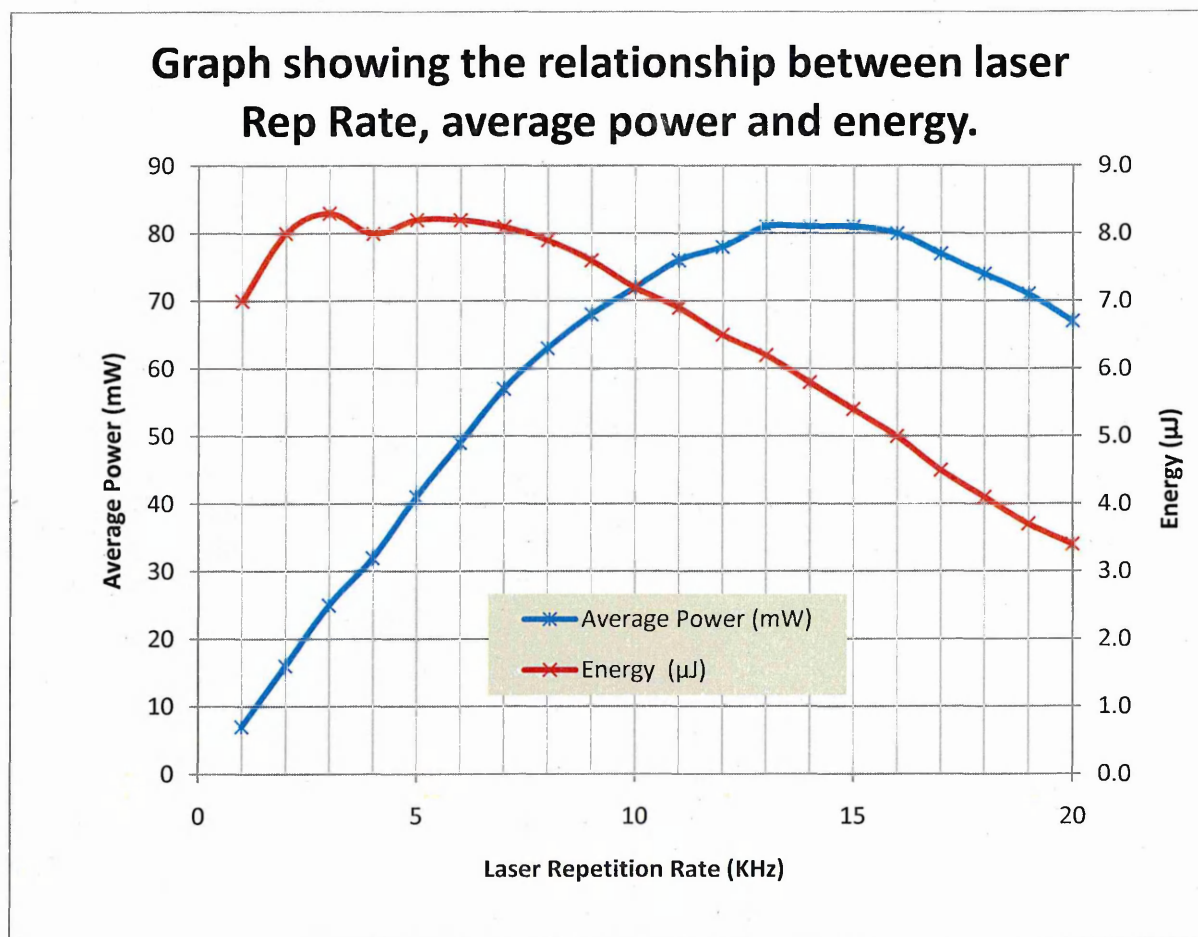


Figure 6.17. The relationship between the laser repetition rate, average power and energy for the Elforlight spot series laser (Elforlight Ltd. Daventry, UK. Private communication).

These results indicate that ionisation in this experiment is related to energy and possibly independent of laser repetition rates, to test this theory the percentage laser power was changed by an attenuator, to try and obtain similar intensity results for the base peak from the profile analysis of a matrix spot of  $\alpha$ CHCA on a target plate, the results of this work are shown below (figure 6.18).

### Comparison of laser power required to obtain similar ion count over laser rep rate

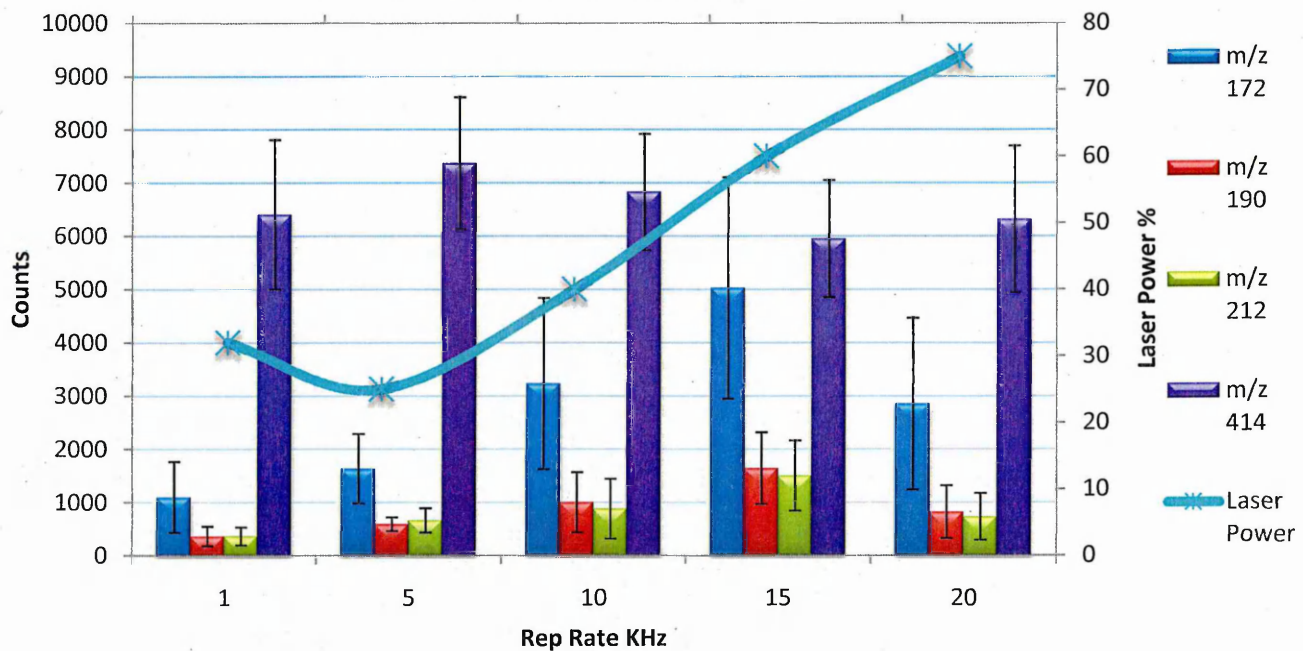


Figure 6.18 Chart showing the laser power selected for the conventional MALDI analysis of  $\alpha$ CHCA. An attempt was made to maintain a similar signal for ion m/z 414, also shown are the ion counts for a series of matrix related ions at m/z 172, 190 and 212.

Laser Rep Rate (KHz)	Power level (%)	Counts 12 Seconds (4 Scans 3Sec/Scan)			
		m/z 172	m/z 190	m/z 212	m/z 414
1	32	900	400	310	6397
		295	135	160	4160
		1950	600	590	7338
		740	230	285	6314
		1600	450	475	7810
1	Mean	1097	363	364	6403.8
5	25	1500	750	1050	6832
		1090	470	450	8600
		1200	445	590	7325
		1640	610	570	5600
		2735	675	650	8480
5	Mean	1633	590	662	7367.4
10	40	2130	700	750	6199
		1460	420	250	5210
		5450	1910	1800	7450
		2910	870	800	7500
		4200	1100	800	7785
10	Mean	3230	1000	880	6828.8
15	60	7832	2600	2400	6700
		4400	1400	1200	4250
		2200	800	700	5600
		6000	1950	1900	7070
		4700	1450	1300	6125
15	Mean	5026.4	1640	1500	5949
20	75	1770	430	380	6003
		2150	640	750	6100
		4950	1600	1450	7240
		4150	1000	700	7930
		1230	420	375	4315
20	Mean	2850	818	731	6317.6

Table 6.1 The values for each of the 5 acquisitions for each laser repetition rate used and the laser power selected.

It can be seen from figure 6.18 and table 6.1 that a lower laser power of 25% was required for the generation of similar ion signals of m/z 414 at 5KHz repetition rate compared to the laser power required for other repetition rates, to the point that at 20KHz it required 75% laser power to produce a similar ion count. The results



show that in this case for MALDI analysis using a high repetition rate Nd:VYO<sub>4</sub> laser the best repetition rate at lower laser powers is approximately between 3-8KHz. The effect of laser repetition rate on fragmentation was also investigated. To investigate this conventional MALDI-MS analysis of vinblastine was carried out at five repetition rates; 1, 5, 10, 15 and 20 KHz using the same laser power. The αCHCA matrix ions at m/z 190 and m/z 172 which are the molecular ion of the matrix [M+H]<sup>+</sup> and the dehydrated molecular ion [M+H-H<sub>2</sub>O]<sup>+</sup> respectively, and several known fragment ions of vinblastine were recorded.

Rep Rate	Laser Power	Ion Counts for each m/z													
		172	190	811.4	809.4	793.4	751.4	733.4	719.4	691.4	649.4	542.3	524.3	355.2	337.2
1	50	1900	415	7162	4193	1835	540	167	49	26	272	52	7	135	22
		1710	373	5957	3600	1687	470	145	42	24	210	40	4	135	26
		1236	278	7513	4346	2100	545	210	54	37	266	74	10	270	45
		1500	340	7226	4140	1825	525	190	45	27	277	52	8	187	25
		1046	248	6971	4125	2200	558	239	58	32	269	50	9	154	21
	Mean	1478.4	330.8	6965.8	4080.8	1929.4	527.6	190.2	49.6	29.2	258.8	53.6	7.6	176.2	27.8
5	50	4162	950	13000	8414	5527	1410	650	180	83	605	210	44	624	120
		4010	899	15000	9929	6505	1761	855	200	105	800	266	52	792	140
		3536	860	12700	8369	5346	1400	645	155	90	650	190	47	682	125
		3840	936	17000	11500	7863	1910	1030	197	128	943	217	51	598	99
		6354	1743	21000	14000	9844	3200	1538	376	218	1450	645	149	1400	260
	Mean	4380.4	1077.6	15740	10442	7017	1936.2	943.6	221.6	124.8	889.6	305.6	68.6	819.2	148.8
10	50	2050	600	8225	4770	2425	610	240	45	21	250	45	8	245	32
		1180	280	5825	3210	1860	420	177	54	19	177	45	10	260	40
		2059	500	8303	4925	2700	690	287	74	35	280	65	13	278	39
		2010	480	7640	4200	2555	646	270	71	47	270	66	16	260	94
		1744	412	8813	5200	3072	800	380	75	55	335	70	15	238	42
	Mean	1808.6	454.4	7761.2	4461	2522.4	633.2	270.8	63.8	35.4	262.4	58.2	12.4	256.2	49.4
15	50	792	230	4640	2999	1963	351	230	55	21	211	32	8.5	76	23
		1547	420	5731	3519	2600	460	315	85	36	270	42	12	134	37
		1883	520	6294	4050	2671	560	391	79	41	349	40	19	180	46
		2970	787	4788	2800	2053	420	256	239	34	239	45	11	160	120
		3702	972	7961	4800	3520	750	499	105	67	382	78	23	375	220
	Mean	2178.8	585.8	5882.8	3633.6	2561.4	508.2	338.2	112.6	39.8	290.2	47.4	14.7	185	89.2
20	50	209	67	906	599	400	56	45	10	4	46	4	2	13	8
		310	88	1186	689	480	73	67	13	7	52	7	3	21	25
		92	44	871	560	380	64	54	13	4	37	4	4	12	2
		192	89	722	458	309	61	42	6	3	31	2	2	10	6
		255	87	885	599	357	56	44	7	4	38	2	2	22	10
	Mean	211.6	75	914	581	385.2	62	50.4	9.8	4.4	40.8	3.8	2.6	15.6	10.2

Table 6.2 The intensity values of some matrix ions and vinblastine associated ions over 5 replicate measurements over 5 different laser repetition rates.

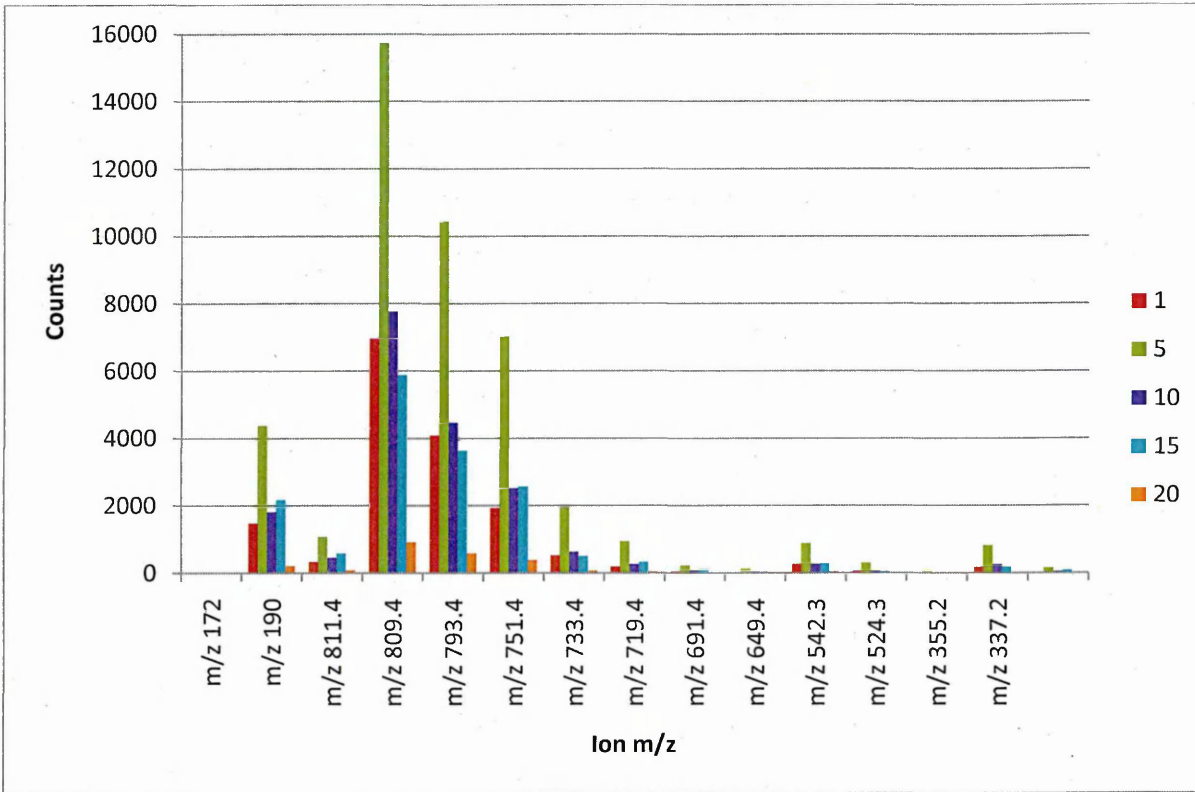


Figure 6.19 graph showing the mean ion count of 5 replicate measurements showing matrix ions and vinblastine associated ions.

As can be seen from figure 6.19 the ion intensity is consecutively higher for a laser repetition rate of 5KHz. To determine if the laser repetition rate affected the fragmentation of vinblastine the ratios of the parent ion m/z 811.4 and all the fragment ions m/z 809.4, 793.4, 751.4, 733.4, 719.4, 691.4, 649.4, 542.3, 524.3, 355.2 and 337.2 have been plotted in figure 6.20.

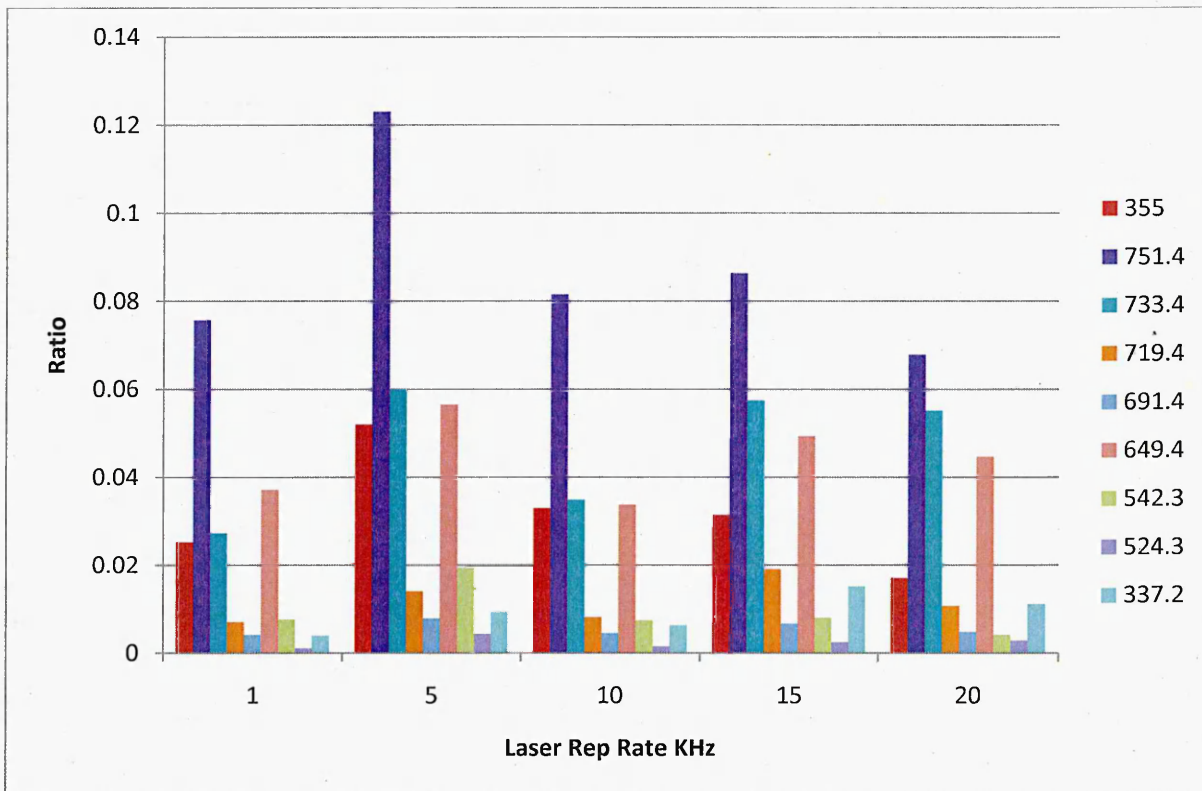


Figure 6.20 The ratio of  $m/z$  811.4 the protonated molecule of vinblastine compared to possible fragment ions. Little difference between different laser repetition rates, is observed.

Note:  $m/z$  809 has not been shown due to the possibility that this ion is not a fragment of the parent but a vinblastine related ion.

Survival yields of vinblastine at different laser repetition rates using the parent ion  $m/z$  811.4 as the  $I_m$  and the fragment ion  $m/z$  355 as  $I_f$ , have been calculated using equation 6.3.



An example of this is shown below for the 1KHz data.

$$SY = \frac{\sum I_m}{(\sum I_m + \sum I_f)}$$

$$SY = \frac{6965.8}{(6965.8 + 176.2)}$$

$$SY = 0.975329$$

The SY for each repetition rate is given in Table 6.3.

Rep Rate	SY
1	0.975329
5	0.950529
10	0.968045
15	0.969511
20	0.983219

*Table 6.3 The survival yields of vinblastine using different laser repetition rates using the parent ion  $m/z$  811.4 as the  $I_m$  and the fragment ion  $m/z$  355 as  $I_f$ .*

As can be seen from the survival yields for each of the repetition rates, the 5KHz laser repetition rate causes the most fragmentation. This is most likely due to this being around the repetition rate where the laser energy peaks, and hence at this repetition rate more energy is transferred to the matrix and hence to the analyte. This causes a slight increase in the analyte fragmentation and hence decreases the survival yield. This result needs to be considered in relation to the total observed ions for the analyte of interest at this laser repetition rate.

## 6.4 Conclusion

A High repetition rate MALDI Q-TOF instrument has been demonstrated with the capability of imaging samples at laser repetition rates up to and including 20KHz. This is a nearly a thousand fold increase on the traditional N<sub>2</sub> laser and a hundred fold increase on the 200Hz Nd:YAG lasers widely commercially employed. The introduction of raster imaging allows this laser to be utilised for high throughput MALDI imaging experiments. This results in faster turnaround times for imaging experiments, and opens the possibility of routine whole body imaging at reasonable acquisition times. This has great potential within pharma because currently during the drug development process the distribution of drugs throughout the body is studied by whole body autoradiography, a technique that does not have the specificity of MALDI imaging. MALDI Imaging could be employed to track the distribution of drugs and their metabolites as well as endogenous markers of efficacy or toxicity. This would reduce the cost for pharma because the expensive development of active radiolabelled compounds could be avoided.

The high repetition rate laser demonstrated here could also further increase the speed of MALDI profiling. This will require enhanced instrumentation and build on the work of Moskovets *et al.*, 2006, who used a 2KHz laser for high throughput LC-MALDI showing they could profile 625 MALDI spots in 12mins using 800 laser spots per spot.

Further evaluation of this laser compared to the commercially available  $N_2$  and Nd:YAG lasers is required in order to assess the LOD of analytes with each laser and to assess the extent to which imaging speed could be increased whilst maintaining sensitivity, specificity and spatial resolution.

Theoretically from equation 6.4 an increase in the repetition rate of the laser makes it possible to achieve high spatial resolutions with raster imaging. In practice this is unlikely to any significant extent. Due to the beam profile of the lasers and the instrumental limitations this would also cause a reduction in the sensitivity of the instrument due to the limited amount of sample per pixel. However the increase of the rastering speed is a much more likely possibility based on this equation.

## 6.5 References

Berkenkamp S; Menzel C; Karas M; Hillenkamp F. **1997**, *Rapid Commun. Mass Spectrom.* 11, 26.

Dreisewerd K. **2003**, *Chem. Rev.* 103, 395-425.

Dreisewerd K; Berkenkamp S; Leisner A; Rohlfing A; Menzel C. **2003**, *Int. J. Mass Spectrom.* 266, 189-209.

Holle A; Haase A; Kayser M; Höhdorf J. **2006**; *J. Mass Spectrom.* 41; 705-716.

Horneffer V; Dreisewerd K; Luedemann H.C; Hillenkamp F; Laege M; Strupat K. **1999**, *Int. J. Mass Spectrom.* 185/186/187, 859.

Huang F; Fan X; Murry K.K. **2008**, *Int. J. Mass Spectrom.* 274, 21-24.

Jurchen J. C; Rubakhin S. S; Sweedler J. V. **2005**, *J. Am. Soc. Mass Spectrom.* 16, 1654-1659.

Karas M; Bachmann D; Hillenkamp F; **1985**, *Anal. Chem.* 57, 2935-2939.

Trim P.J; Atkinson S.J; Princivalle A.P; Marshall P.S; West A; Clench M.R. **2008b**, *Rapid Comm. Mass Spectrom.* 22, 1503-1509.

Trim P.J; Henson C.M; Avery J.L; McEwen A; Snel M.F; Claude E; Marshall P.S; West A; Princivalle A.P; Clench M.R. **2008a**, *Analytical Chemistry.* 80, 8628-8634.

McLean J.A; Russell W.K; Russell D.H. **2003**, Anal. Chem. 75, 648-654.

Medzihradzky K.F; Campbell J.M; Baldwin M.A; Falick A.M; Juhasz P; Vestal M.L; Burlingame A.L. **2000**, Anal. Chem. 72, 552.

Moskovets E; Preisler J; Chen H.S; Rejtar T; Andreev V; Karger B.L. **2006**, Anal. Chem. 78, 921-919.

Simmons D. A. **2008**, ABI Technical Note, improved MALDI-MS imaging performance using continuous laser rastering.

Vertes A; Luo G; Ye L; Chen Y; Marginean I. **2004**, Appl. Phys. A. 79, 823-825.

Woods A.S; Ugarov M; Jackson S.N; Egan T; Wang H-Y. J; Murry K.K; Schultz J.A. **2006**, J Proteome Research 5, 1484-1487.

Wu K.J; Steding A; Becker C.H. **1993**, Rapid Commun. Mass Spectrum. 7, 142-146.

## CHAPTER 7

---

### Conclusions & Future Work

## 7.1 Conclusions

MALDI-MSI has a wide range of applications within both the biological and chemical fields. The specificity, sensitivity and spatial information obtainable from MALDI-MSI experiments are unique. The increasing interest in MALDI mass spectrometry has allowed the expansion of this technique into several fields. The further development of the technique, will allow increases in the spatial resolution most likely eventually allowing the imaging of analyte distributions within single cells, whilst maintaining some level of realistic acquisition time. Increased sensitivity for a wider range of analytes will allow the further expansion of this technique into a wider range of analytes, and also by removing some of the current limitations in ionisation efficiencies with the use of new matrices and improved sample preparation.

The added separation step obtained by the inclusion of ion mobility within MALDI-MSI has been shown in Chapter 3 to be beneficial within several applications for various analytes. With the continued improvement of this technology the possible information now obtainable within a single experiment is huge due to the possibility of separating previously overlooked isobaric ions. This new dimension of imaging data acquisition may redefine the way MALDI-MSI data is interpreted. The benefit of MALDI-IMS-MSI for the study of xenobiotic distribution has been demonstrated in Chapter 4 and 5 of this thesis. IMS allowed for the removal of interfering ions from the mass spectrum allowing clearly enhanced image quality of the distribution of vinblastine within tissues.



Lipidomics has gained a huge amount of interest over recent years. Despite electrospray ionisation mass spectrometry still being the method of choice for many applications, this technique does not have spatial information. With the recognition of the involvement of lipids within a wide range of cellular and disease processes, the use of MALDI-MSI within the field of lipidomics will serve to assist other techniques in the understanding of the diverse roles lipids have within biological systems. Shown within chapters 2, 3 and 5 of this thesis are some of the applications of MALDI-MSI within lipidomics. Shown in chapter 2 MALDI-MSI data processing using PCA statistical analysis has been able to identify ions accounting for some of the differences between tissue types. This has also been demonstrated within chapter 5 where PCA was applied to MALDI-MSI data from tumour xenografts, using this technique. Ions associated with the viable tumour and surrounding tissues were identified and some ions which altered with administration of vinblastine were observed.

MALDI imaging has been shown to be a very powerful technique for the identification and localisation of many different analytes. There is a large scope for MALDI-MSI within the drug development process, allowing the spatial distribution and characterisation of analytes within a single experiment. The current standard is QWBA for drug distribution studies. MALDI-MSI has several advantages over QWBA including the ability to identify the compound of interest,

and MALDI-MSI does not require expensive radiolabelled compounds to be developed, which is a large expense within the development process.

The advancement of technology within this field is constantly improving, within chapter 6 of this thesis an Nd:YVO<sub>4</sub> laser has been evaluated for MALDI-MSI. One of the benefits of this laser is the high repetition rates it is capable of operating at. Within this work up to 20KHz has been employed, the increase laser repetition rate and the use of raster imaging has allowed the massive reduction in sample acquisition time whilst maintaining a suitable number of laser shots per pixel.

## **7.2 Future work**

In order to further develop the applications of MALDI-MSI and the technology itself within small molecule analysis, it is required to:

- Increase the use of MALDI-IMS-MSI for a wide variety of applications and improve the data processing and interpretations, with further software development via collaborations with instrument manufacturers.
- Expand the separation of compounds especially lipids using MALDI-IMS-MS to allow species identification without the need for ms/ms identification, but by using the drift time information for each compound class within the ion mobility cell, and accurate mass information. Using the increased ion mobility resolution of the new Synapt G2 (Waters Corporation, Manchester)

this is a realistic possibility. This would allow for the tentative identification of compounds within a single experiment, and could reduce the time required for compound identification when trying to analyse a wide range of compounds within a single experiment. This would be especially relevant for the identification of new drug compound distributions and their metabolites, streamlining drug discovery and development and by reducing the cost and the number of animal experiments.

- Improved MS<sup>3</sup> information using TAP (Time Aligned Parallel) fragmentation within the Tri-Wave of a Synapt HDMS system, TAP fragmentation allows for the initial fragmentation of an ion in the trap region of the Tri-Wave followed by fragment ion mobility separation, and further fragmentation within the transfer region. Using this, the technique the initial fragments are drift time separated so form a diagonal line within the DriftScope plot and the MS<sup>3</sup> Fragment align vertically under their precursor ions.
  
- Optimisation of high repetition rate lasers allowing the improvement in sample acquisition time whilst maintaining sensitivity and spatial resolution.
  
- Further identification of the peaks which are associated within the different regions of the tumour xenographs and identification of any endogenous induced changes caused by chemotherapeutic drugs to aid in the discovery of possible new drug targets or help in the reduction of drug resistance.

## CHAPTER 8

---

**Publications,  
Posters and  
Attendance.**      **Presentations,  
and  
Conference**

## **8.1 Peer Review Publications**

1. Trim P.J; Atkinson S.J; Princivalle A.P; Marshall P.S; West A; Clench M.R. *Rapid Comm. Mass Spectrom.* **2008**, 22, 1503-1509. **MALDI-MS Imaging of Lipids in Rat Brain Tissue with Integrated Unsupervised and Supervised Multivariant Statistical Analysis.**
2. Trim P.J; Henson C.M; Avery J.L; McEwen A; Snel M.F; Claude E; Marshall P.S; West A; Princivalle A.P; Clench M.R. *Analytical Chemistry.* **2008**, 80, 8628-8634. **Matrix Assisted Laser Desorption Ionisation - Ion Mobility Separation - Mass Spectrometry Imaging of Vinblastine in Whole Body Tissue Sections.**
3. Trim P.J; Francese S; Clench M.R. *Bioanalysis.* **2009**, 1 (2), **Imaging Mass Spectrometry for the Assessment of Drugs and Metabolites in Tissue**

## 8.2 Presentations

1. Trim P.J; Claude E; McEwen A; Marshall S.P; Clench R.M. *Italian Chemical Society, Division of Mass Spectrometry, Workshop on High Resolution, Imaging and Ion Mobility, 16th December 2009, Milan. MALDI - Ion Mobility Separation - Mass Spectrometry Imaging for Direct Drug Distribution Analysis.*

### 8.3 Poster Presentations

1. Trim P.J; Atkinson S.J; Princivalle A.P; Marshall P.S; West A; Clench M.R.  
*55th American Society for Mass Spectrometry Conference on Mass Spectrometry and Allied Topics, Indianapolis, June 3<sup>rd</sup> - June 7<sup>th</sup> 2007;*  
**MALDI-MS Imaging of Lipids in Rat Brain Tissue with Integrated Unsupervised and Supervised Multivariant Statistical Analysis.**
2. Trim P.J; Atkinson S.J; Princivalle A.P; Marshall P.S; West A; Clench M.R.  
*Royal Society for Chemistry, Analytical Research Forum, Glasgow, July 16<sup>th</sup> - July 18<sup>th</sup> 2007;*  
**MALDI-MS Imaging of Lipids in Rat Brain Tissue with Integrated Unsupervised and Supervised Multivariant Statistical Analysis. (Awarded Best Poster)**
3. Trim P.J; Atkinson S.J; Princivalle A.P; Marshall P.S; West A; Clench M.R.  
*British Mass Spectrometry Society, Annual Meeting, Edinburgh, September 9<sup>th</sup> - September 12<sup>th</sup> 2007;*  
**MALDI-MS Imaging of Lipids in Rat Brain Tissue with Integrated Unsupervised and Supervised Multivariant Statistical Analysis.**
4. McCollin A; Henson C.M; Lathall A; Bird H; McEwen A; Wood S; Trim P.J;  
Clench M.R. *British Mass Spectrometry Society, Annual Meeting, Edinburgh,*

September 9<sup>th</sup> - September 12<sup>th</sup> 2007; **Beyond QWBA: Evaluation of a Novel Method of Direct Tissue Analysis.**

5. Snel M.F; Trim P.J; Claude E; McKenna T; Langridge J.I; *The Association of Biomolecular Resource Facilities, February 9<sup>th</sup> - February 12<sup>th</sup> 2008; MALDI Quadrupole Orthogonal Acceleration - TOF Mass Spectrometry Enhanced with Ion Mobility Spectrometry for Tissue Imaging.*
6. Avery J.L; Henson C.M; Read H; McEwen A; Trim P.J; Clench M.R; *10th European International Society for the Study of Xenobiotics Meeting, Vienna, May 18<sup>th</sup> - May 21<sup>st</sup> 2008; Tissue Distribution of Vinblastine and its Metabolites Using MALDI Imaging.*
7. Trim P.J; Avery J.L; McEwen A; Snel M.F; Claude E; Marshall P.S; West A; Princiville A.P; Clench M.R. *56th American Society for Mass Spectrometry Conference on Mass Spectrometry and Allied Topics, Denver, June 1<sup>st</sup> - June 5<sup>th</sup> 2008; MALDI - Ion Mobility Separation - MS Imaging of Vinblastine and its Metabolites in Rat Tissue.*
8. Claude E; Trim P.J; Snel M.F; McKenna T; Langridge J.I; *56th American Society for Mass Spectrometry Conference on Mass Spectrometry and Allied Topics, Denver, June 1<sup>st</sup> - June 5<sup>th</sup> 2008; MALDI Quadrupole Orthogonal Acceleration - TOF Mass Spectrometry Enhanced with Ion Mobility*



## **Spectrometry for Tissue Imaging.**

9. Trim P.J; Henson C.M; Avery J.L; McEwen A; Snel M.F; Claude E; Marshall P.S; West A; Princivale A.P; Clench M.R. *Royal Society for Chemistry, Analytical Research Forum, Hull, July 21<sup>st</sup> - July 23<sup>rd</sup> 2008; MALDI - MS/MS Imaging of Vinblastine in Whole Body Tissue Sections.*
  
10. Trim P.J; Henson C.M; Avery J.L; McEwen A; Snel M.F; Claude E; Marshall P.S; West A; Princivale A.P; Clench M.R. *British Mass Spectrometry Society, Annual Meeting, York, September 7<sup>th</sup> - September 10<sup>th</sup> 2008; Matrix Assisted Laser Desorption Ionisation - Ion Mobility Separation - Mass Spectrometry Imaging of Vinblastine in Whole Body Tissue Sections.*
  
11. Avery J.L; Henson C.M; Read H; McEwen A; Trim P.J; Clench M.R; *British Mass Spectrometry Society, Annual Meeting, York, September 7<sup>th</sup> - September 10<sup>th</sup> 2008; Tissue Distribution of Vinblastine and its Metabolites Using MALDI Imaging.*
  
12. Trim P.J; Henson C.M; Avery J.L; McEwen A; Snel M.F; Claude E; Marshall P.S; West A; Princivale A.P; Clench M.R. *Faculty of Health and Wellbeing Research Day, Sheffield, December 17<sup>th</sup> 2008; MALDI - Ion Mobility Separation - MS Imaging of Vinblastine in Whole Body Tissue Sections. (Awarded Best Poster)*

13. Trim P.J; Hearne K; Brown C; McEwen A; Claude E; Marshall P.S; Princivale A.P; Clench M.R. *57<sup>th</sup> American Society for Mass Spectrometry Conference on Mass Spectrometry and Allied Topics, Philadelphia, May 31<sup>st</sup> - June 4<sup>th</sup>, 2009; MALDI - MS Imaging of Tumour Lipids in DU145 and HCT116 Tumour Xenographs and the Effects of Vinblastine.*
14. Trim P.J; Hearne K; Brown C; McEwen A; Claude E; Marshall P.S; Princivale A.P; Clench M.R. *18<sup>th</sup> International Mass Spectrometry Conference, Bremen, August 30<sup>th</sup> – September 4<sup>th</sup>, 2009; MALDI - MS Imaging of Tumour Lipids in DU145 and HCT116 Tumour Xenographs and the Effects of Vinblastine.*
15. Avery J; Trim P.J; McEwen A; Wood S; Clench M.R. *American Association of Pharmaceutical Scientists Annual Meeting and Exposition 2009, Los Angeles, 8<sup>th</sup> November – 12<sup>th</sup> November 2009. MALDI-MS Imaging of Imipramine HCL and Metabolites in Rat Tissues.*
16. Avery J; Hearn K; Trim P.J; McEwen A; Wood S; Clench M.R. *Drug Metabolism Discussion Group Open Meeting, Nottingham, 17<sup>th</sup> September – 19<sup>th</sup> September 2009. MALDI-MS Imaging of Imipramine HCL in Rat Tissue and Reconstituted Human Epidermis.*

#### **8.4 Conference Attendance.**

1. 55th American Society for Mass Spectrometry Conference on Mass Spectrometry and Allied Topics, Indianapolis, June 3rd - June 7th 2007.
2. Royal Society for Chemistry, Analytical Research Forum, Glasgow, July 16th - July 18th 2007.
3. British Mass Spectrometry Society, Annual Meeting, Edinburgh, September 9th - September 12th 2007.
4. 56th American Society for Mass Spectrometry Conference on Mass Spectrometry and Allied Topics, Denver, June 1st - June 5th 2008.
5. Royal Society for Chemistry, Analytical Research Forum, Hull, July 21st - July 23rd 2008.
6. British Mass Spectrometry Society, Annual Meeting, York, September 7th - September 10th 2008.
7. 57<sup>th</sup> American Society for Mass Spectrometry Conference on Mass Spectrometry and Applied Topics, Philadelphia, May 31<sup>st</sup> – June 4<sup>th</sup> 2009.
8. 18<sup>th</sup> International Mass Spectrometry Conference, Bremen, August 30<sup>th</sup> – September 4<sup>th</sup> 2009.